Universidade do Minho
Escola de Engenharia

Liliana Sofia Correia Fernandes

Magnetic ionic liquid/polymer composites for printable sensors and actuators

junho de 2024

Magnetic ionic liquid/polymer composites for printable sensors and actuators
Liliana Sofia Correia Fernandes
UMinho | 2024

Universidade do Minho
Escola de Engenharia

Liliana Sofia Correia Fernandes

Magnetic ionic liquid/polymer composites for printable sensors and actuators

Tese de Doutoramento
Doutoramento em Engenharia de Materiais

Trabalho efetuado sobre a orientação de
Professor Doutor Senentxu Lanceros-Méndez
Investigador Auxiliar Pedro Martins
Investigadora Júnior Daniela Correia

junho 2024

Diretos de autor e condições de utilização do trabalho por terceiros

Este é um trabalho académico que pode ser utilizado por terceiros desde que respeitadas as regras e boas práticas internacionalmente aceites, no que concerne aos direitos de autor e direitos conexos.

Assim, o presente trabalho pode ser utilizado nos termos previstos na licença abaixo indicada.

Caso o utilizador necessite de permissão para poder fazer um uso do trabalho em condições não previstas no licenciamento indicado, deverá contactar o autor, através do RepositóriUM da Universidade do Minho.

Licença concedida aos utilizadores deste trabalho



Atribuição-NãoComercial
CC BY-NC

https://creativecommons.org/licenses/by-nc/4.0/

Acknowledgments

I want to express my profound gratitude to everyone who has contributed to and supported me over the past four years in the development of this work, whether directly or indirectly.

First and foremost, my heartfelt thanks go to the Foundation for Science and Technology (FCT) for their financial support through the grant SFRH/BD/145345/2019, which made this project possible.

The guidance and assistance from my supervisors and co-supervisors were invaluable, and this work would not have been achievable without them. I am grateful for the opportunity to work with Professor Senentxu Lanceros-Méndez, Assistant Researcher Pedro Martins, and Junior Researcher Daniela Correia. Thank you for your availability, guidance, vast scientific knowledge, and for your patience, support, encouragement, and kindness, which were indispensable throughout this journey.

To the Electroactive Smart Materials Group, thank you all for the camaraderie and unwavering encouragement. Special thanks to Nelson Pereira and Bárbara Cruz for their much-needed help and friendship.

Lastly, on a personal note, I extend my gratitude to my family and friends. A special mention to my parents, brothers and husband, who have been my pillars from the very beginning, providing unconditional love and support without which I would not have been able to realize my full potential.

To each and every one of you, heartfelt thanks!

Statement of integrity

I hereby declare having conducted this academic work with integrity. I confirm that I have not used plagiarism or any form of undue use of information or falsification of results along the process leading to its elaboration.

I further declare that I have fully acknowledged the Code of Ethical Conduct of the University of Minho.

Compósitos de líquidos iónicos magnéticos/polímeros para sensores e atuadores imprimíveis

Resumo

Num mundo governado digitalmente, intimamente ligado aos conceitos da Internet das Coisas e da Indústria 4.0, há necessidade de tecnologias de deteção e atuação universais e multifuncionais. Consequentemente, a procura pelo desenvolvimento de dispositivos flexíveis, leves, económicos e eficientes está a aumentar. Portanto, há uma necessidade crescente de explorar uma variedade de materiais inteligentes que tenham o potencial de responder a diferentes estímulos externos de maneira controlada e repetitiva.

Polímeros eletroativos (PEAs) são adequados para o desenvolvimento de sensores e atuadores por a sua capacidade de gerar uma resposta elétrica quando estimulados externamente e vice-versa. Frequentemente, os dispositivos baseados em PEAs incorporam materiais ativos como nanopartículas e nanofios para melhorar seu desempenho. No entanto, estas cargas apresentam tipicamente fraca dispersão e aglomeração. Os líquidos iónicos (LIs) oferecem uma alternativa promissora com vantagens como excelente dispersão e capacidade de serem adaptados para aplicações específicas devido à sua diversificada gama de espécies iónicas.

O principal objetivo deste trabalho é investigar, adaptar e otimizar as propriedades de novos PEAs iónicos multifuncionais de alto desempenho. Estes PEAs são baseados em LIs magnéticos (LIMs) e diferentes matrizes poliméricas, como poli(fluoreto de vinilideno) (PVDF) e copolímeros, poliuretano (PUA) e carragenina, visando aplicações em sensores (termocrómicos, humidade e magnéticos) e atuadores para telas sensíveis ao toque com propriedades táteis. Os materiais foram preparados em várias condições e suas propriedades magnéticas, elétricas, mecânicas, termocrómicas, eletromecânicas, magnetoiónicas (MI) determinadas. As propriedades foram relacionadas às propriedades físico-químicas, permitindo otimizar a resposta funcional.

Inicialmente, foram investigados compósitos à base de PVDF e seus copolímeros e diversos LIMs, explorando seu potencial para sensores e atuadores. A análise incluiu não só a avaliação da compatibilidade entre diferentes LIMs, mas também a adaptação dos parâmetros de processamento para obter respostas ideais nos compósitos. Foi realizado um exame minucioso das propriedades estruturais, físico-químicas, térmicas, elétricas e magnéticas. Posteriormente, foram avaliadas as respostas eletromecânicas e MI. Explorando a multifuncionalidade dos compósitos, a deteção de humidade e o termocromismo foram investigados, utilizando vários LIs à base de imidazólio. Simultaneamente, foram exploradas alternativas mais ecológicas para os polímeros, como a resina epóxi curável por UV e o polímero natural carragenina.

Em conclusão, novos compósitos LIM/polímero foram desenvolvidos e sua aplicabilidade para aplicações em sensores e atuadores foi demonstrada. Além disso, os materiais desenvolvidos são compatíveis com o processamento por técnicas de fabricação aditiva.

Palavras chave: Líquidos iónicos magnéticos, materiais termocrómicos, polímeros eletroativos, sensores e atuadores

Abstract

In a digitally governed world closely tied to the concepts of the Internet of Things and Industry 4.0, there is a need for universal and multifunctional sensing and actuating technologies. Consequently, the development of flexible, lightweight, cost-effective, and efficient devices is rising in demand. Hence, there is a growing need to explore a variety of smart materials that have the potential to respond to different external stimuli in a controlled and repetitive manner.

Electroactive polymers (EAPs) are well-suited for sensor and actuator development by their ability to generate an electrical response when stimulated externally and vice versa. Often, EAP-based devices incorporate active materials like nanoparticles and nanowires to enhance their performance. However, these fillers typically present poor dispersion and agglomeration. Ionic liquids (ILs) offer a promising alternative with advantages such as excellent dispersion and the ability to be tailored for specific applications owing to their diverse range of ionic species.

The main goal of this work is to investigate, tailor, and optimize the properties of novel high-performance multifunctional ionic EAPs. These EAPs are based on magnetic ionic liquids (MILs) and different polymer matrices such as poly (vinylidene fluoride) (PVDF) and copolymers, polyurethane (PUA), and carrageenan, targeting applications in sensor (thermochromic, humidity, and magnetic) and actuators for touch screens with haptic properties. The materials were prepared under various conditions, and their magnetic, electrical, mechanical, thermochromic, electromechanical, and magnetoionic (MI) properties were determined. These properties were related to the physical-chemical properties, allowing to optimize the functional response.

Initially, composites based on PVDF and its copolymers with various MILs were investigated, exploring their potential for sensors and actuators. Our analysis included not only assessing the compatibility between different MILs but also adapting processing parameters to achieve optimal responses in the composites. It was conducted a thorough examination of the structural, physical-chemical, thermal, electrical, and magnetic properties. Subsequently, the electromechanical and MI responses were evaluated. Exploring the multifunctionality of the composites, the humidity sensing and thermochromism was investigated, utilizing several imidazolium-based ILs. Simultaneously, it was explored more environmentally friendly alternatives for the polymers, such as UV-curable epoxy resin and the natural polymer carrageenan.

In conclusion, a novel MIL/polymer composites were developed and their applicability for sensors and actuator applications demonstrated. Further, the developed materials are compatible with processing by additive manufacturing techniques.

Keywords: Magnetic ionic liquids, thermochromic materials, electroactive polymers, sensors and actuators.

Table of contents

Acknowledgments ..... **iii**

Statement of integrity ..... **iv**

Resumo ..... **v**

Abstract ..... **vi**

Table of contents ..... **vii**

List of figures ..... **xiii**

List of tables ..... **xx**

List of abbreviations ..... **xxi**

Ionic liquids designation ..... **xxiii**

1 Introduction **1**

1.1 Industry 4.0 and Internet of Things 2

1.2 Smart responsive materials 3

1.2.1 Electroactive polymers 5

1.2.1.1 Poly (vinylidene fluoride) and co-polymers 6

1.2.2 Functional fillers 8

1.2.2.1 Ionic liquids 9

1.3 Ionic liquid/polymer composites and their applications 12

1.3.1 Magnetic ionic liquid/polymer based composites as sensors and actuators 15

1.4 Printing technologies and sustainable materials 17

1.5 Objectives and thesis structure 19

1.6 References 20

2 Experimental section **25**

2.1 Materials 26

2.1.1 Polymeric matrices 27

2.1.1.1 PVDF and copolymers 27

2.1.1.2 UV curable and natural polymers 27
2.1.2 Functional fillers 28
2.2 Characterization Methods 29
2.2.1 Morphological characterization 29
2.2.2 Physical-chemical characterization 29
2.2.3 Thermal characterization 30
2.2.4 Optical characterization 32
2.2.5 Mechanical characterization 33
2.2.6 Electrical characterization 33
2.2.7 Magnetic characterization 34
2.3 References 35
3 Magnetic Ionic liquid/polymer composites: Tailoring physico-chemical properties by ionic liquid content and solvent evaporation temperature 36
3.1 Introduction 37
3.2 Experimental section 37
3.2.1 Preparation of the composite films 37
3.2.2 Sample characterization 38
3.3 Results and discussion 38
3.3.1 Morphological characterization 38
3.3.2 Physical-chemical characterization 39
3.3.3 Thermal characterization 41
3.3.4 Magnetic properties of the nanocomposites 44
3.4 Conclusions 45
3.5 References 45
4 Structural organization of ionic liquids embedded in fluorinated polymers 47
4.1 Introduction 48

4.2 Experimental section 49
4.2.1 Sample preparation 49
4.2.2 Sample characterization 49
4.3 Results and discussion 50
4.3.1 Morphological features 50
4.3.2 Physical-chemical and thermal characterization 51
4.3.3 Structural organization of the IL within the polymer matrix 53
4.4 Conclusions 57
4.5 References 58
5 Design of ionic liquid based hybrid polymer materials with magnetoactive and electroactive multifunctional response 60
5.1 Introduction 61
5.2 Experimental section 62
5.2.1 Preparation of the hybrid films 62
5.2.2 Sample characterization 62
5.2.3 Functional electromechanical characterization 63
5.3 Results and discussion 64
5.3.1 Morphological features 64
5.3.2 Physical-chemical and thermal characterization 65
5.3.3 Magnetic and magnetoionic characterization 67
5.3.4 Electrical and electromechanical characterization 69
5.4 Conclusion 72
5.5 References 73
6 Multifunctional magnetoelectric sensing and bending actuator response of polymer-based hybrid materials with magnetic ionic liquids 75
6.1 Introduction 76
6.2 Experimental section 76

6.2.1 Preparation of the samples 76
6.2.2 Morphological and functional characterization 77
6.3 Results and Discussion 78
6.3.1 Morphology 78
6.3.2 Functional ME response 79
6.4 Conclusions 82
6.5 References 82
7 Ionic-triggered magnetoelectric coupling for magnetic sensing applications ..84
7.1 Introduction 85
7.2 Experimental section 88
7.2.1 Sample preparation 88
7.2.2 Sample characterization 89
7.3 Results and discussion 91
7.3.1 Material evaluation 91
7.3.2 Ionic conductivity and magnetic/ME response 94
7.3.3 Electronically optimized speedometer 99
7.4 Conclusions 100
7.5 References 101
8 Humidity sensors based on magnetic ionic liquids blended in poly (vinylidene fluoride-co-hexafluoropropylene) 104
8.1 Introduction 105
8.2 Experimental section 105
8.2.1 Preparation of the samples 105
8.2.2 Sample characterization 106
8.2.3 Humidity sensor response characterization 106
8.3 Results and discussion 108

8.3.1 Morphology 108
8.3.2 Polymer phase content, thermal and mechanical properties 110
8.3.3 Magnetic response and ionic conductivity 114
8.3.4 Humidity sensing response and proof of concept device 115
8.4 Conclusions 119
8.5 References 119
9 Photocurable temperature activated humidity hybrid sensing materials for multifunctional coatings 122
9.1 Introduction 123
9.2 Experimental section 124
9.2.1 Preparation of composite films 124
9.2.2 Sample characterization 125
9.3 Results and discussion 126
9.3.1 UV curing process 126
9.3.2 Morphological and contact angle characterization 128
9.3.3 Thermal and chemical characterization 130
9.3.4 Mechanical and electrical properties 133
9.3.5 Temperature-activated humidity-sensitive materials 135
9.3.5.1 UV-Vis characterization 135
9.3.5.2 Temperature-humidity-colour change characterization 137
9.3.5.3 Colour changing mechanism 139
9.4 Conclusions 140
9.5 References 140
10 Environmental-friendly carrageenan based ionic-liquid driven soft actuators 143
10.1 Introduction 144
10.2 Experimental section 145

10.2.1 Preparation of the neat and IL/carrageenan films 145
10.2.2 Sample characterization 146
10.3 Results and discussion 146
10.3.1 Morphological features 146
10.3.2 Infrared vibrational bands and mechanical properties 148
10.3.3 Thermal properties 152
10.4 Ionic conductivity 154
10.4.1 Electromechanical functional response 156
10.5 Conclusions 158
10.6 References 159
11 Conclusions and future work 161
11.1 Conclusions 162
11.2 Future work 164

List of figures

Figure 1.1 – Industry 5.0 core values [3]. 2

Figure 1.2 – Overview of smart materials inputs and outputs [8]. 4

Figure 1.3 – Schematic Illustration of the three main crystalline phases of PVDF: α, β and γ [36]..... 6

Figure 1.4 - Schematic representation of PVDF-based polymer and copolymers morphologies/structures for different advanced application areas. Adapted from [30]. 7

Figure 1.5 - Schematic representation of the a) P(VDF-TrFE) and b) P(VDF-HFP) repeat units. Adapted from [28] 8

Figure 1.6 - Most relevant physical-chemical properties of ILs [7]. 10

Figure 1.7 - General classification of ILs with an indication of a representative application area [7]..... 10

Figure 1.8 - Schematic representation of the most common cations and anions described in the literature [7]. 11

Figure 1.9 - Schematic representation of the production of IL-based polymer composites for different processing methods [7]. 13

Figure 1.10 - IL/polymer-based multifunctional materials application areas [7]. 15

Figure 1.11 - Schematic representation of the ion migration and bending response [90]. 16

Figure 1.12 – Schematic representation of the main printing techniques compatible with polymer-based composites: (a-c) contact and (d-g) non-contact methods [94]. 18

Figure 2.1 - Schematic representation of the chain conformation of β-PVDF and the repeat units of P(VDF-TrFE) and P(VDF-HFP) [1]. 27

Figure 2.2 - Chemical structure of ι-carrageenan. 28

Figure 3.1 - SEM images of the P(VDF-TrFE)/[Bmim][$FeCl_4$] composite films with 40 wt. % of MIL prepared at different solvent evaporation temperature: room temperature (a), 90 °C (b) and (c), and 210 °C (d). 38

Figure 3.2 – FTIR-ATR spectra for the P(VDF-TrFE)/[Bmim][$FeCl_4$] composites obtained at different solvent evaporation temperatures with 40 wt. % of MIL (a) and with different MIL contents at 210 °C (b). 40

Figure 3.3 - DSC thermograms of the P(VDF-TrFE)/[Bmim][$FeCl_4$] composites obtained at different solvent evaporation temperatures and a MIL content of 40 wt. % (a) and with different contents of MIL (b). 41

Figure 3.4 - TGA (a,c) and DTG (b,d) curves of the P(VDF-TrFE)/[Bmim][$FeCl_4$] composites for: different solvent evaporation temperatures with 40 wt % of MIL (a,b); for a solvent evaporation temperatures of 210 °C and different IL contents (c,d). 43

Figure 3.5 - Magnetization of (a) P(VDF-TrFE)/[Bmim][$FeCl_4$] composites obtained at different temperatures for an IL content of 40 wt. % Inset: pure IL [Bmim][$FeCl_4$]; and (b) for the composites with different IL contents as a function of applied magnetic field. 44

Figure 4.1 - Representative SEM cross-section images of the composite films comprising 40 wt. % of the ILs: a) PVDF/[Pmim][TFSI] (inset: unmodified initial PVDF cross-section film), b) PVDF/[Pmpip][TFSI], c) PVDF/[Bmim][$FeCl_4$] and d) PVDF/[$Bmim]_2[NiCl_4$]. 50

Figure 4.2 - a) FTIR spectra, b) electroactive β-phase content, c) DSC scans and d) TGA curves of the different PVDF/IL film composites: PVDF/[Pmim][TFSI], PVDF/[Pmpip][TFSI], PVDF/[Bmim][$FeCl_4$] and PVDF/[$Bmim]_2[NiCl_4$]. 51

Figure 4.3 - SANS data for polymer-IL based nanocomposties: PVDF/[Pmim][TFSI], PVDF/[Pmpip][TFSI], PVDF/[Bmim][$FeCl_4$] and PVDF/[$Bmim]_2[NiCl_4$]. Solid lines are fits according to various structural models. 54

Figure 4.4 - Sketches of the different structural organizations of the IL in: PVDF/[Pmim][TFSI], PVDF/[Pmpip][TFSI], PVDF/[Bmim][$FeCl_4$], and PVDF/[$Bmim]_2[NiCl_4$]. 56

Figure 5.1 - Schematic representation of the procedure used for the preparation of the PVDF/[$C_n$mim][$FeCl_4$] films. 62

Figure 5.2 - Cross-section SEM images of the PVDF/MIL films with a) [C_2mim][$FeCl_4$], b) [C_4mim][$FeCl_4$], c) [C_8mim][$FeCl_4$] and d)[C_{14}mim][$FeCl_4$]. 64

Figure 5.3 - Physical-chemical and thermal characterization of the PVDF/[$C_n$mim][$FeCl_4$] films: a) FTIR-ATR spectra, b) DSC thermograms, c) β-phase content and degree of crystallinity, d) TGA thermograms. 66

Figure 5.4 - a) Magnetization, b) MI voltage as a function of H_{AC} intensity at 10 kHz, c) MI coefficient as a function of frequency and d) MI coefficient at 10 kHz for the PVDF/[$C_n$mim][$FeCl_4$] films. 68

Figure 5.5 - a) Current-voltage intensity (I-V) curves and b) DC electrical conductivity of the different PVDF/MIL composites. As a reference, the electrical DC conductivity of PVDF is 5×10^{-14}

S cm^{-1} [31]. c) Displacement, δ, of the PVDF/MIL composite actuator tip as a function of time under different applied voltages at a frequency of 100 mHz for: [C_4mim][$FeCl_4$] and d) maximum displacement for the different PVDF/[$C_n$mim][$FeCl_4$] films as a function of the applied voltage. . 70

Figure 5.6 - a) Schematic representation of the bending response of the PVDF/MIL films. b) Bending motion as a function of time for the PVDF/[C_4mim][$FeCl_4$] composite at 100 mHz frequency and 4 V_{pp}. 72

Figure 6.1 - Schematic representation of the procedure used for the development of PVDF-TrFE and PVDF-TrFE/[Bmim][$FeCl_4$] films. 77

Figure 6.2 - Representative SEM images of P(VDF-TrFE) and P(VDF-TrFE)/[Bmim][$FeCl_4$] prepared with 40 wt.% content of MIL at different solvent evaporation temperatures: (a) room temperature P(VDF-TrFE); P(VDF-TrFE)/[Bmim][$FeCl_4$] at (b) 210 ºC, (c) 90 ºC and (d) room temperature. 78

Figure 6.3 - ME response of P(VDF-TrFE)/[Bmim][$FeCl_4$] films: (a) ME voltage as a function of H_{AC} intensity at 500 kHz; (b) ME voltage as a function of H_{AC} frequency with H_{AC} intensity at 2 Oe; (c) ME coefficient as a function of solvent evaporation temperature with H_{AC} intensity of 2 Oe and frequency of 10 MHz and (d) ME coefficient as a function of the pore size with H_{AC} intensity of 2 Oe and frequency of 10 MHz. 80

Figure 6.4 - (a) Displacement and (b) bending response of the P(VDF-TrFE)/ [Bmim][$FeCl_4$] composite as a function of time (f = 0.1 Hz) and DC magnetic field intensity, respectively. As a scale reference, the size of the small squares in the images is 1 mm. The schematic inset represents the ions (cations and anions) movement into the polymer matrix upon the applied DC magnetic field. 81

Figure 7.1 – Main connectivities found in polymer based ME materials: a) (0–3) particulate nanocomposites; b) (2–2) laminate composites and, c) (1–3) fiber/rod composites. 86

Figure 7.2 – Schematic representation of the ME coupling proposed in this work: i) A magnet will induce the bending of the composite due to the interaction with the CFO nanoparticles. Ii) The bending of the sample leads to an ionic charge separation through migration of the bigger IL [Bmim]+ cations to the direction of the surface with lower bending angle and the smaller Cl– anions to the direction of the surface with higher bending angle. Iii) The ionic charge separation leads to generation of the voltage across the sample. 88

Figure 7.3 – a) Photograph exhibiting the different components of the magnetic testing apparatus. B) Schematic representation of the electronic circuit for filtering (f_{cl} and f_{ch}) and amplification (A): 90

Figure 7.4 – Representative cross section SEM images of different samples: a) P(VDF-TrFE); b) P(VDF-TrFE)/IL; c) P(VDF-TrFE)/IL/CFO10; and d) P(VDF-TrFE)/IL/CFO30 with different magnifications. EDS analysis for the P(VDF-TrFE)/IL/CFO30: e) Fe mapping and; f) Cl mapping. 91

Figure 7.5 – a) FTIR-ATR spectra, and b) DSC thermograms of the different nanocomposites.92

Figure 7.6 – a) Stress strain curves, and b) Young's modulus (E_Y) for the different samples... 93

Figure 7.7 – a) Impedance spectroscopy for the different samples (no magnetic field applied). Comparison of the impedance spectroscopy with and without applied magnetic field for: b) P(VDF-TrFE)/IL; c) P(VDF-TrFE)/IL/CFO10; d) P(VDF-TrFE)/IL/CFO20; and e) P(VDF-TrFE)/IL/CFO30. f) Conductivity as a function of the CFO wt.% (with and without applied magnetic field)..... 94

Figure 7.8 – Schematic representation of the conduction mechanism on the P(VDF-TrFE)/IL/CFO nanocomposites. 95

Figure 7.9 – a) Room-temperature magnetic hysteresis cycles for the P(VDF-TrFE)/IL/CFO composites with different CFO wt. % (the magnetization curve of the pure CFO nanoparticles is also shown for comparison). B) Magnetic saturation (MagnetizationSAT) and remanent magnetization (MagnetizationREM) as a function of the CFO wt. %. 96

Figure 7.10 – ME-flexoelectric behaviour for composites with CFO content of: a) 10 wt. %; b) 20 wt. %, and c) 30 wt. % for a fixed IL content of 20 wt. %. D) ME-flexoelectric voltage response as a function of the CFO wt. % for different frequencies..... 98

Figure 7.11 – Comparison of the voltage response/magnetic sensing capability of: a) Hall sensor and P(VDF-TrFE)/IL/CFO10, b) Hall sensor and P(VDF-TrFE)/IL/CFO20, c) Hall sensor and P(VDF-TrFE)/IL/CFO30, d) Hall sensor and P(VDF-TrFE)/IL, e) Hall sensor and P(VDF-TrFE)/CFO20, and f) Voltage response of the P(VDF-TrFE)/IL sample submitted to mechanical bending. 99

Figure 7.12 – a) Electronic speedometer based on the P(VDF-TrFE)/IL/CFO30 nanocomposite. B) Relation between the motor frequency and the sensor frequency. The insets shows a photograph of the P(VDF-TrFE)/IL/CFO30 nanocomposite. 100

Figure 8.1 - Schematic representation of the procedure used to develop the IL/P(VDF-HFP) composites. 106
Figure 8.2 - a) Custom-built humidity characterization setup b) Representation of the humidity ionic and water content varation with the variation of RH. 107
Figure 8.3 – SEM images of the different IL/P(VDF-HFP) composites: a) P(VDF-HFP) surface; b) P(VDF-HFP) cross section; c) $[Bmim]_2[CoCl_4]$; d) $[Bmim][FeCl_4]$; e) $[Bmim]_2[Co(SCN)_4]$; and f) $[Emim]_2[Co(SCN)_4]$. 108
Figure 8.4 - SEM-EDX images showing the dispersion of Co and Fe elements into the different P(VDF-HFP)/IL composites a) $[Bmim]_2[CoCl_4]$, b) $[Bmim][FeCl_4]$, c) $[Bmim]_2[Co(SCN)_4]$ and d) $[Emim]_2[Co(SCN)_4]$. 109
Figure 8.5 - a) FTIR-ATR spectra for neat P(VDF-HFP) and for the different P(VDF-HFP)/IL composites incorporating imidazolium based ILs with different anions. b) Corresponding β-phase content for the samples. 110
Figure 8.6 - a) DSC curves, b) TGA thermograms, c) Stress-strain mechanical curves and d) magnetic room-temperature hysteresis loops for neat P(VDF-HFP) and for the different P(VDF-HFP)/IL composites incorporating imidazolium based ILs with different anions. 112
Figure 8.7 - a) Nyquist plots of the 40 wt. % P(VDF-HFP)/IL composites with $[Bmim][FeCl_4]$ at different temperatures (30, 60 and 90 °C) and b) Arrhenius plots for the ionic conductivities of the P(VDF-HFP)/IL composites with different ILs. 114
Figure 8.8 - Cycling sensing response for varying relative humidities between 35 and 85 % for the different P(VDF-HFP)/IL composites incorporating imidazolium based ILs with different anions: a) P(VDF-HFP)/$[Bmim]_2[CoCl_4]$, b) P(VDF-HFP)/$[Bmim]_2[Co(SCN)_4]$, c) P(VDF-HFP)/$[Emim]_2[Co(SNC)_4]$ and d) P(VDF-HFP)/$[Bmim][FeCl_4]$. 116
Figure 8.9 - Humidity sensing sensitivity of the P(VDF-HFP)/$[Bmim]_2[CoCl_4]$ composite..... 117
Figure 8.10 - a) Schematic representation of the breathing monitoring prototype, b) real photography of the breathing mask with component identification, including electronic system and humidity sensor, c) screen print of the Bluetooth application for breathing detection, d) schematic representation of the electronic acquisition board and e) response of the P(VDF-HFP)/$[Bmim]_2[CoCl_4]$ composite based monitoring device at different breathing rates. 118
Figure 9.1 - Representation of the development of the PUA and PUA/IL composite films (5, 10, 20 and 40 wt.%): 1 – ultrasonication, 2 – magnetic stirring at 45 °C, 3 – film processing by Doctor Blade, 4 – UV cure, 5 – flexible films. 125

Figure 9.2 - Curing conversion (C(α)) as a function of time of the pristine photoresin and the PUA/IL samples (a), and photopolymerization rate (R_p)(b). 127
Figure 9.3 - Representative SEM images of the PUA (a) and PUA/IL hybrid samples comprising different IL contents (b-e) at magnification of 300×. Thermochromism resulting from the dehydration process of PUA/IL with 10 wt. % IL content (f). 129
Figure 9.4 - Representative images of the water surface contact angle for neat PUA film (a) and PUA/IL samples containing 5 wt. % (b), 10 wt. % (c), 20 wt. % (d) and 40 wt. % (e). Evolution of the contact angle values as a function of time for the mentioned samples (f). 130
Figure 9.5 - DSC thermograms of neat PUA and PUA/IL samples for the first (a) and second (b) scans. 131
Figure 9.6 - FTIR spectra of neat PUA and PUA/IL samples containing different IL contents (a) and FTIR spectra at room temperature (hydrated) and at 80 °C (dehydrated) of 20 wt.% PUA/IL sample (b). 132
Figure 9.7 - Stress vs. strain mechanical characteristic curves (a) and Young modulus (b) for neat PUA and for PUA/IL samples containing different $[Bmim]_2[NiCl_4]$ contents. I-V curves (c) and electrical conductivity (d) for the same samples. 134
Figure 9.8 - UV-Vis spectra for the IL/PUA samples containing 20 wt. % of $[Bmim]_2[NiCl_4]$ content in the temperature range from 30 to 70 °C (a) and UV-Vis curves for the different samples at 70 °C (b). 136
Figure 9.9 - Colour variation of the films (initial and final state) with increasing relative humidity at constant temperature of 25 °C (a) and with increasing temperature at constant relative humidity of 60 % (b), increasing relative humidity at constant temperature of 45 °C (d) and 10 °C (e), and with increasing temperature at constant relative humidity of 40 % (f). 137
Figure 9.10 - Chemical modifications occurring during the heating and cooling process of the $[Bmim]_2[NiCl_4]$ IL (a) and changes in the coordination number of Ni(II) from octahedral to tetrahedral structure (b). Reproduced with permission [11]. Copyright 2019, ACS Publications. 139
Figure 10.1 - Schematic representation of the procedure used for the preparation of the carrageenan/IL hybrid materials. 146
Figure 10.2 – Cross-section images of the IL/carrageenan composites with different IL contents obtained at different solvent evaporation temperatures: a) 0 wt. % at 25 °C, b) 20 wt.%

of [Ch][DHP] at room temperature, c) 40 wt.% of [Ch][DHP] at 80 °C and d) 40 wt. % of [Bmim][$FeCl_4$] at 80°C. 147

Figure 10.3 - EDS cross section images for the carrageenan/IL samples containing different ILs: (a) 40 wt. % of [Ch][DHP], b) 40 wt. % of [Ch][$FeCl_4$], b) 40 wt. % of [Bmim][$FeCl_4$] and d) 40 wt. % of [Bmim][$C(CN)_3$]). All the samples were obtained at a solvent evaporation temperature of 80 °C. 148

Figure 10.4 - a-b) FTIR-ATR spectra and c-d) stress-strain curves for: carrageenan/[Ch][DHP] samples containing different IL contents (10, 20 and 40 wt. %) obtained at different drying temperatures (25 and 80 °C) and for carrageenan/IL samples comprising different ILs obtained at a solvent evaporation temperature of 80 °C, respectively. 150

Figure 10.5 - a-b) DSC and c-d) TGA thermograms for: carrageenan/[Ch][DHP] samples containing different IL contents (10, 20 and 40 wt. %) and obtained at different drying temperatures (25 and 80 °C) and for carrageenan/IL samples comprising different ILs obtained at a solvent evaporation temperature of 80 °C, respectively. 153

Figure 10.6 - Nyquist plots at 30 and 60 °C for the IL/carrageenan samples comprising 40 wt .% of the different ILs: (a) [Ch][DHP], b) [Ch][$FeCl_4$], c) [Bmim][$FeCl_4$] and d) [Bmim][$C(CN)_3$]). All the samples were obtained at a solvent evaporation temperature of 80 °C..... 155

Figure 10.7 - Arrhenius plots for the ionic conductivity of the Carrageenan/IL composites: a) carrageenan/[Ch][DHP] samples containing different IL contents (10, 20 and 40 wt. %) and obtained at different drying temperatures (25 and 80 °C) and b) carrageenan/IL samples comprising different ILs obtained at a solvent evaporation temperature of 80 °C. 155

Figure 10.8 - a) Displacement of the carrageenan/[Ch][DHP] composites containing 10, 20 and 40 wt. % of IL at same maximum applied voltage (9 V) under an DC field. b) Bending motion as a function of time for 40 wt. % [Ch][DHP]/carrageenan films prepared at solvent evaporation temperatures of 25 °C and 80 °C for an applied voltage of 9 V at. c) Schematic representation of bending actuation mechanism and d) optical pictures of the [Ch][DHP]/carrageenan films prepared at solvent evaporation temperatures of 25 °C and 80 °C for an applied voltage of 9V. 157

List of tables

Table 1.1 - ILs functionalities for the development of smart and multifunctional applications [7]. 14

Table 2.1 - Overview of materials and main processing parameters. 26

Table 3.1 - Relevant thermal parameters for pristine P(VDF-TrFE) and for the polymer within the P(VDF-TrFE)/[Bmim][$FeCl_4$] composites. 42

Table 7.1 - - Curie temperature, melting temperature and degree of crystallinity of the different samples. 92

Table 7.2 – Comparation of the α, α' and α_{DC} reported in ME and MI composites. 98

Table 8.1- Degree of crystallinity ($\Delta\chi$), stress at yield (σ_y) and Young modulus (E') for the P(VDF-HFP)/IL samples 112

Table 9.1 - Experimental details for thermochromic and relative humidity (RH) variation assays. 126

Table 9.2 - UV curing process characteristic parameters of the pristine resin and the PUA/IL samples for the different IL contents. 127

Table 9.3 - Glass transition temperature for first (T_{g1}) and second (T_{g2}) scans, strain at break (ε_b) and elastic modulus (E) for PUA and IL/PUA films. 131

Table 10.1 - Thickness of the IL/carrageenan films 145

Table 10.2 - Young modulus and glass transition temperature of the different carrageenan/IL composites. 152

List of abbreviations

C

CFO	Cobalt ferrite

D

DMF	Dimethylformamide
DSC	Differential scanning calorimetry

E

EAP	Electroactive polymer
EDX	Energy dispersive X-Ray spectroscopy
EIS	Electrochemical impedance spectroscopy

F

FDM	Fused deposition modelling
FTIR	Fourier transform infrared spectroscopy

I

IoT	Internet of Things
IL	Ionic liquid

M

ME	Magnetoelectric
MIL	Magneto ionic liquid
MI	Magnetoionic

N

NP	Nanoparticle

P

P3HT	Poly (3-hexylthiophene)
PE	Polyethylene
PEG	Poly (ethylene glycol)
PEO	Poly (ethylene oxide)
PET	Poly (ethylene terephthalate)
PHB	Poly (3-hydroxybutyrate)
PLA	Poly (lactic acid)
PMMA	Poly (methyl methacrylate)
PNIPAM	Poly (M-isopropylacrylamide)
PU	Polyurethane
PUA	Poly (urethane acrylate)

PVDF	Poly (vinylidene fluoride)
P(VDF-HFP)	Poly (vinylidene fluoride-co-hexafluoropropene)
P(VDF-TrFE)	Poly (vinylidene fluoride-trifluoroethylene)
S	
SANS	Small angle neutron scattering
SEM	Scanning electron microscopy
SQUID	Superconducting quantum interference device
T	
TEAPU	Triethanolamine cross-linked polyurethane
TFSI	Bis(trifluoromethylsulfonyl)imide
TGA	Thermogravimetric analysis
TrFE	Trifluoroethylene
U	
UV-Vis	Ultraviolet-Visible
V	
VDF	Vinylidene fluoride
VSM	Vibrating sample magnetometer

Ionic liquids designation

B

[Bmim][$C(CN)_3$]	1-butyl-3-methylimidazolium tricyanomethanide
[Bmim][Cl]	1-butyl- 3-methylimidazolium chloride
[Bmim]$_2$[$CoCl_4$]	(bis(1-butyl-3-methylimidazolium)) tetrachlorocobaltate(II)
[Bmim]$_2$[$Co(SCN)_4$]	(bis(1-butyl-3-methylimidazolium)) tetrathiocyanocobaltate(II)
[Bmim][$FeCl_4$]/[C_4mim][$FeCl_4$]	1-butyl-3-methylimidazolium tetrachloroferrate(III)
[Bmim]$_2$[$NiCl_4$]	(bis(1-butyl-3-methylimidazolium)) tetrachloronickelate(II)

C

[C_2mim][$FeCl_4$]	1-ethyl-3-methylimidazolium tetrachloroferrate(III)
[C_8mim][$FeCl_4$]	1-octyl-3-methylimidazolium tetrachloroferrate(III)
[C_{14}mim][$FeCl_4$]	1-tetradecyl-3-methylimidazolium tetrachloroferrate(III)
[Ch][DHP]	Choline dihydrogen phosphate
[Ch][$FeCl_4$]	Choline tetrachloroferrate

E

[Emim]$_2$[$Co(SCN)_4$]	(bis(1-ethyl-3-methylimidazolium)) tetrathiocyanocobaltate(II)

P

[Pmim][TFSI]	1-methyl-3-propylimidazolium (bis(trifluoromethylsulfonyl) imide)
[Pmpip][TFSI]	1-methyl-1-propylpiperidinium (bis(trifluoromethylsulfonyl) imide)

1 Introduction

Stable, safe and high performance (multi)functional materials are major concerns for technological applications in today's society. In this chapter, the main concepts, terms and advances in smart functional materials are presented, focusing on ionic liquid/polymer composites. Further, their implementation in the development of responsive materials in sensor and actuator applications is reviewed. Finally, the general objectives of the thesis are indicated.

This chapter is based on the following publication: Correia, D.M., Fernandes, L.F., Martins, P.M., García-Astrain, C., Costa, C.M., Reguera, J., Lanceros-Méndez, S., *Ionic liquid-polymer composites: a new platform for multifunctional applications.* Advanced Functional Materials, 2020. **30**: p. 1909736

1.1 Industry 4.0 and Internet of Things

Concepts such and *Industry 4.0* and Internet of Things (IoT) have been a part of today's generation and drive for society and technology evolution. IoT mostly refers to a network of interconnected and interrelated devices, objects and other items that have the capacity to communicate between each other collecting and exchanging data, creating a vast ecosystem of interconnected devices [1]. This concept goes hand in hand with the Fourth Industrial Revolution (i.e. Industry 4.0) which had its origin in 2011 at the Hannover Fair and its used to describe the transformation of manufacturing and industrial processes using the integration of digital technologies, automation, data analytics and IoT [2]. Recently, in 2021, the European commission, announced Industry 5.0. This concept aligns with the social paradigm of Industry 4.0, fostering research and innovation for a sustainable shift from a human-centric to a resilient industry. It envisions the collaboration of smart machines and robots with people, promoting a sustainable and resilient approach with shared core values (**Figure 1.1**) [3]. This paves the way for a vision of enhanced, interconnected manufacturing and industrial processes.



Figure 1.1 – Industry 5.0 core values [3].

As such, Industry 4.0 an IoT play key roles in predictive maintenance, smart manufacturing, quality control, energy efficiency, worker safety, customized production, environmental

monitoring, data analytics, and more, revolutionizing industrial processes, creating a more efficient, data-driven, and adaptable, with enhanced productivity and competitiveness manufacturing sector [3].

As a consequence, the demand for stable, safe and high performance (multi)functional materials has been a growing concern for technological applications in today's society [4]. However, geometrical and manufacturing complexity and the cost of commonly used materials and systems can be a drawback to their implementation. Electroactive polymers (EAPs) and composites based on such materials are increasingly being used in technological applications to solve some of these problems [5]. Nonetheless, improvements in (multi)functionality, materials performance and stability are needed to reach their full potential for the implementation in advanced technologies.

Polymer composites based on ionic liquids (ILs) have been emerging as promising candidates for sensors and actuators, environmental applications, energy storage and generation, and biomedicine, among others, due to their unique and easily tuneable properties. In particular, composites based on magnetic ILs (MILs) are an attractive possibility for sensors and soft actuators due to their ability to respond to magnetic and electric stimuli [6]. Furthermore, in the area of soft actuators, with the currently available processes there is no accurate control between the interplay of processing and response (whether this response is in strength, bending or frequency). Here, a finer tuning of the soft actuator behaviour is needed, thus reducing processing time and the misuse of materials [7].

In this context, the synthesis of polymeric/MIL composite materials has the potential to develop a new generation of multifunctional magnetic sensors and actuators with improved and accurate performance.

1.2 Smart responsive materials

Smart and multifunctional materials are materials with the ability of adapting to different environments, by means of altering their intrinsic properties in a controlled and repetitive manner as a reaction response to external physical stimuli such as, stress, temperature, electric, magnetic and electromagnetic fields, pH, among others (**Figure 1.2**) [8]. Due to their interesting

properties, they have been applied in different fields, including but not limited to, sensors, actuators and transducers.

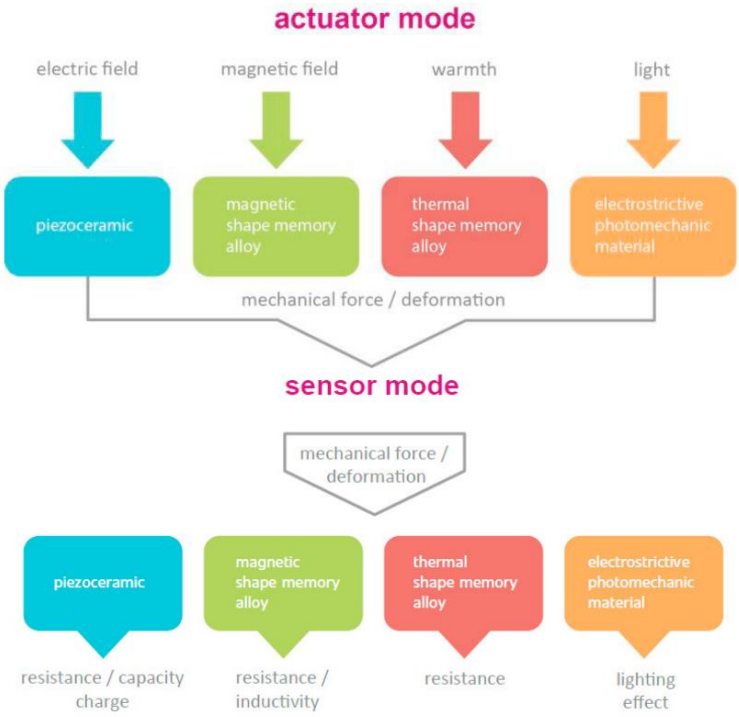


Figure 1.2 – Overview of smart materials inputs and outputs [8].

There are several types of smart materials, however some examples are piezoelectric, electro- and magneto-strictive, magnetoelectric (ME), shape memory materials, dielectric elastomers, pH and temperature sensitive polymers, and EAPs [8, 9].

Another relevant class of smart materials are ME responsive materials, which have the ability to provide coupling between magnetic and dipolar orders, being capable to generate an electric response upon magnetic stimulation or vice-versa [10]. The coexistence of magnetization and electric polarization will allow an additional degree of freedom showing their suitability for implementation in technological applications as multifunctional materials such as, transducers, storage devices, sensors and actuators, among others [11-17]. They can be divided into single-phase and composite ME materials. Single-phase materials can present this ME effect inherently. However, the effect is typically small and at low temperatures [18]. Different composite materials comprising magnetostrictive and piezoelectric phases have been developed capable of displaying a high ME response [19]. Among the many ME composites, when compared to ceramic

composites, polymer-based ones are characterized by simple fabrication, robustness and flexibility [16-18].

1.2.1 Electroactive polymers

EAPs are capable of working as smart responsive polymers, responding to stimuli such as electric field [20, 21] making them promising materials for applications in the areas of sensors and actuators [22, 23]. When compared to other smart materials systems, EAPs show clear advantages such as, wide range of response speed (μs to min), lower density (1-2 g/cm^3) larger resilience and higher actuation strains (over 300 - 400 %), as well as the fact that they are lightweight, cost effective, easy to process, flexible and tolerant to fracture [6, 24]. EAPs are classified as electronic and ionic [20, 24], both with different response times, force and bending [25, 26]. Electronic EAPs are mainly based on piezoelectric polymers [27, 28], and represent a more mature technology than ionic EAPs due to the drawback in durability of the later under open atmosphere conditions [29]. The development of systems composed of electronic EAPs and ILs can overcome such limitations [21, 30].

In particular, piezoelectric polymers are interesting, as they can generate electric signals by the application of a mechanical force, called the direct piezoelectric effect, or undergo a mechanical deformation when subjected to an electric field, named converse piezoelectric effect [28]. The direct piezoelectric effect is of importance for sensor applications and the converse piezoelectric effect for actuator applications [30].

The most interesting polymers for developing electronic EAPs are Nafion, poly (vinylidene fluoride) (PVDF) and its copolymers [28, 31, 32]. It has been reported that the incorporation of ILs into a PVDF matrix leads/promotes an actuation strain upon application of low voltages < 3.0 V and high voltages (up to 10 V) [5, 33]. In addition, EAPs doped with ILs exhibit high ionic conductivity under dry conditions which is one of the major requirements for actuator applications [34].

The main challenges in EAP actuators with ILs are related to tailoring the ionic mobility of the cations and anions of the IL in order to achieve better response times and stability. However, new developments must be achieved before reaching real applications: morphological, mechanical, magnetic, electrical and electromechanical properties must be properly tailored/optimized [6].

1.2.1.1 Poly (vinylidene fluoride) and co-polymers

PVDF is a semi-crystalline biocompatible polymer with interesting intrinsic properties, such as high electroactive response, dielectric constant, ionic conductivity and polarity [28]. This polymer shows a complex structure and can present five distinct crystalline phases related to different chain conformations designed as all trans (TTT) planar zigzag for the β-phase, TGTG' (trans-gauche–trans-gauche) for the α and δ phases and T_3GT_3G' for γ and ε phases, with the β-phase being the main responsible for its piezoelectric properties, with the highest dipolar moment ($8x10^{-30}$ C m^{-1}) [35]. **Figure 1.3** shows the three main PVDF crystalline phases that are relevant for advanced applications: α, β and γ.

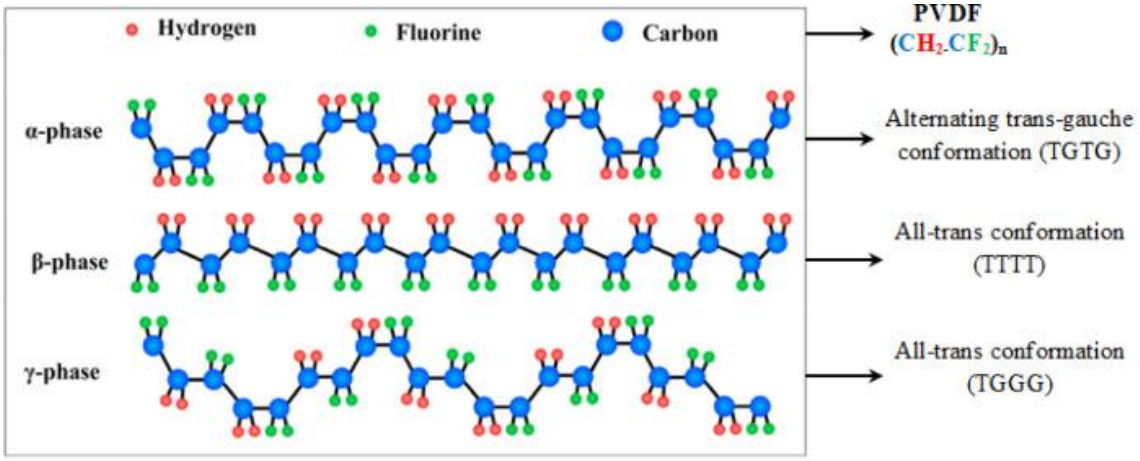


Figure 1.3 – Schematic Illustration of the three main crystalline phases of PVDF: α, β and γ [36]

Being the most electrically active phases, β and γ, they have been targeted with great interest for various applications such as sensors and actuators, biomedical and energy, ME devices, among others [28, 30, 37].

Additionally, PVDF and its copolymers can be processed in different forms and shapes and applied in several areas, such as tissue engineering, sensors and actuators, among others as it can be seen in **Figure 1.4** [30, 38, 39].

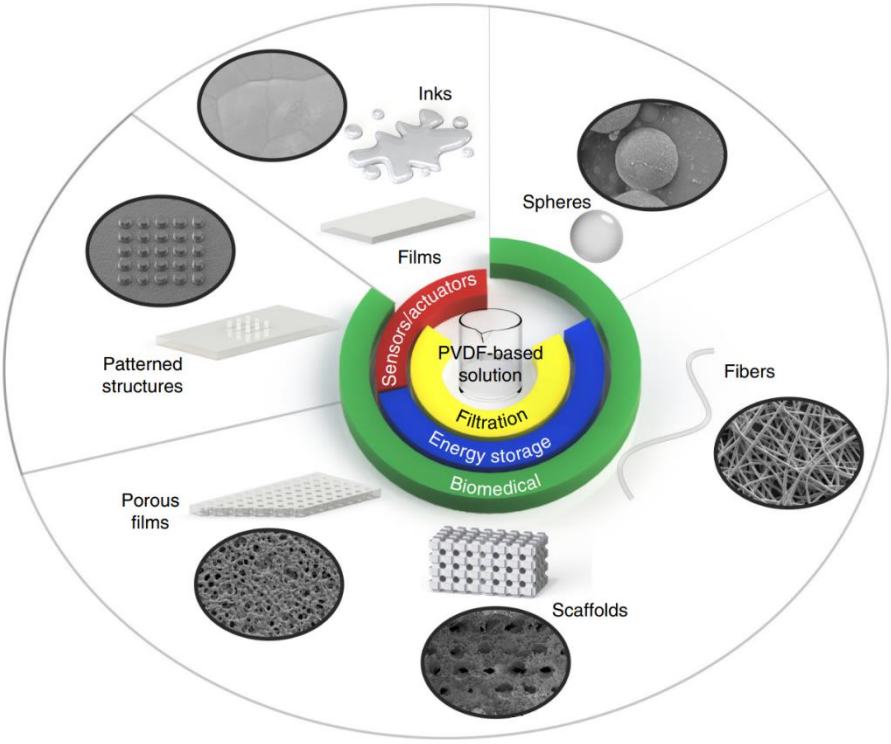


Figure 1.4 - Schematic representation of PVDF-based polymer and copolymers morphologies/structures for different advanced application areas. Adapted from [30].

Apart from PVDF, in the area of sensors and actuators, the copolymers poly (vinylidene fluoride-trifluoroethylene) (P(VDF-TrFE)) and poly (vinylidene fluoride-co-hexafluoropropene) (P(VDF-HFP)) are also extensively used [6, 30, 40] (**Figure 1.5**).

P(VDF-TrFE) can be synthesized by polymerization of VDF (vinylidene fluoride) and TrFE (trifluoroethylene), obtaining the crystalline structure shown in **Figure 1.5a**. The Addition of TrFE modifies the crystal structure of PVDF due to the increase of the unit cell size and interplanar distance of the ferroelectric phase [41]. Compared to PVDF, P(VDF-TrFE) exhibits lower Curie temperature (T_c) (between 55 and 128 °C), attributed to the reduction of the interactions between each unit and dipole moments [28]. The notable difference between PVDF and P(VDF-TrFE) is that, for P(VDF-TrFE), the ferroelectric to paraelectric phase transition occurs at T_c below the melting temperature [28]. P(VDF-TrFE) has enhanced crystallinity and promotes the growth of a preferred orientation, TrFE addition leads to easy formation of the ferroelectric β-phase), improving the electromechanical coupling factor [6]. The piezoelectricity is also greatly influenced by the mass ratio of VDF/TrFE and the synthesis conditions [28].

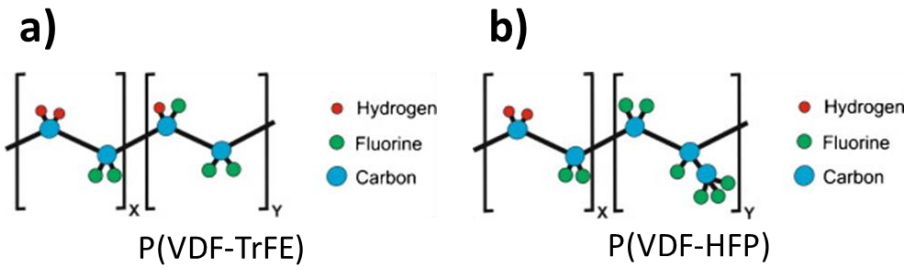


Figure 1.5 - Schematic representation of the a) P(VDF-TrFE) and b) P(VDF-HFP) repeat units. Adapted from [28]

P(VDF-HFP) can be synthetized by polymerization of VDF and HFP (hexafluoropropylene), with the final crystalline structure shown in **Figure 1.5b**. The copolymerization process with HFP reduces the crystallinity degree significantly because of the bulky CF_3 groups, which has a negative impact in the high piezoelectricity. The addition of HFP increases flexibility and hydrophobicity due to the elevated fluorine content, surpassing those of pure PVDF [42, 43]. In this copolymer, the piezoelectric coefficient (d_{31}) is comparable to PVDF, however, the pyroelectric coefficient is higher [44, 45].

1.2.2 Functional fillers

Advancements in polymer composites have predominantly focused on developing materials with improved properties, where fillers play a crucial role in enhancing the properties of the polymer matrix. This enhancement encompasses electrical properties, including both electric and ion conductivity, or the introduction of additional functionalities, such as magnetism. The incorporation of materials, such as nanoparticles (NPs), nanowires, and ionic liquids, among others, is carefully done to ensure compatibility with polymers. As a result, the characteristics of polymer-based composites are heavily influenced by the intrinsic properties of the filler, the compatibility between components, and the uniform dispersion of the active material within the polymeric network.

Concerning magnetically responsive materials, they typically result from combining magnetic nanoparticles (MNPs) with polymeric matrices. In such systems, the influence of an external magnetic field on magnetic particles induces a physical transformation in the polymer's structure.

Notably, in this context, MILs have emerged as a novel generation of magnetically responsive materials, addressing certain limitations associated with other conventional materials.

1.2.2.1 Ionic liquids

ILs have emerged as a novel class of chemical compounds for the development of advanced (multi)functional materials with outstanding potential in applications of several areas due to the ILs unique properties and functionalities.

ILs are typically defined as liquid electrolytes composed uniquely by ions and with a melting point below 100 °C (criteria to distinguish molten salts and ILs) [46, 47]. They can include a vast number of organic cations and organic or inorganic anions. The first reported IL, the ethylammonium nitrate, was discovered in 1914 by Walden [48], being the first generation of ILs reported in the 1970s–80s with the development of the alkylimidazolium halogenoaluminate ILs by mixing aluminium halides with imidazolium halides [49, 50].

ILs are characterized by their unique profiles based on an interplay between hydrogen bonding, coulombic and van-der-Waals interactions of their ions [46]. These compounds also exhibit a low vapor pressure, usually below the decomposition temperature, and the majority of them are liquid at room temperature [51]. Overall, ILs present unique characteristics (**Figure 1.6**) such as negligible vapor pressure [52], high ionic conductivity (~10^{-3}-10^{-2} S cm^{-1}) [53], or viscosities from 2 to 3 orders of magnitude higher than organic solvents [54]. Additionally, due to their excellent solubility and miscibility with many compounds (organic, inorganic and polymeric materials) ILs can replace traditional volatile organic solvents in different processes such as organic reactions, catalysis, extraction, and separation, promoting the development of green chemistry and clean technologies [50, 55]. Other advantages are their high thermal stability, usually with a decomposition temperature above 350 °C and excellent chemical and electrochemical stability [49, 52, 55], with an electrochemical window between 4 and 6 V [56]. ILs are also considered non-flammable and non-volatile [57].

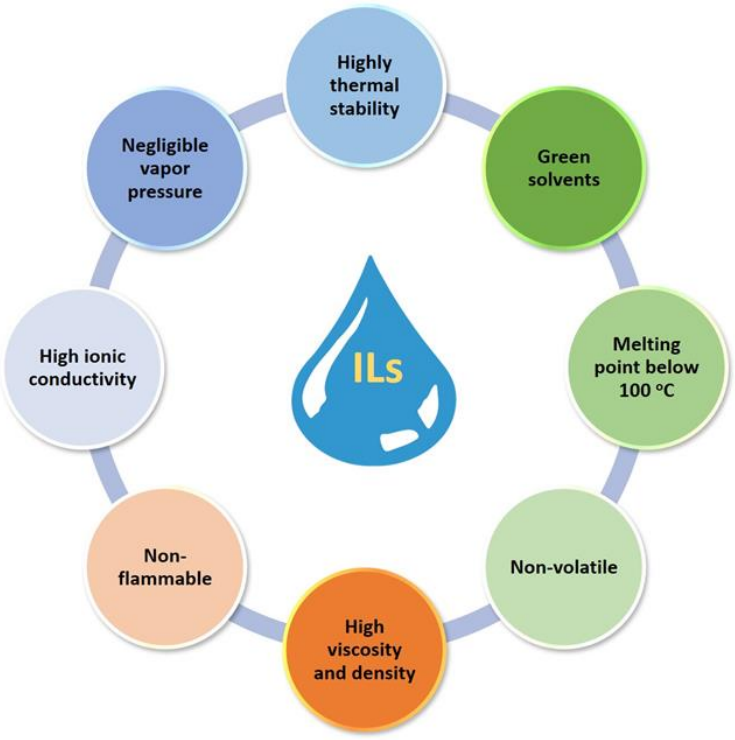


Figure 1.6 - Most relevant physical-chemical properties of ILs [7].

It has been reported the existence of ~10^{18} ILs involving the combination of different anions and cations [58]. Attending to the cation chemical composition, ILs are commonly classified into three subclasses: aprotic, protic and zwitterionic (**Figure 1.7**), each one being generally synthesized towards a specific application [59].

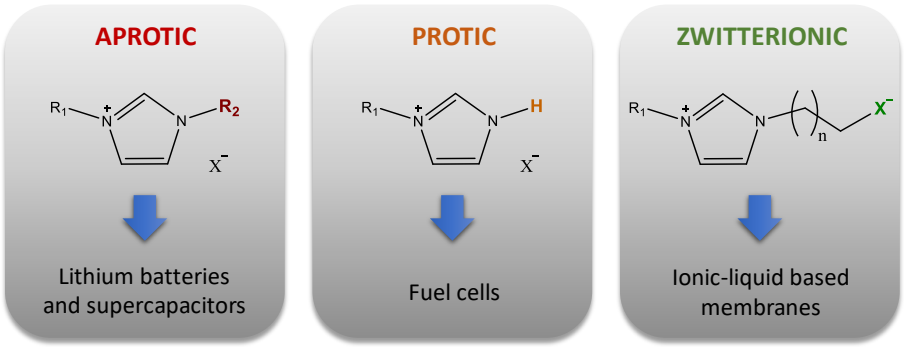


Figure 1.7 - General classification of ILs with an indication of a representative application area [7].

Aprotic ILs containing large cations such as pyridinium, imidazolium and phosphonium, and smaller anions are the most commonly used. Typical IL anions include inorganic anions (e.g. bromine (Br^-), chloride (Cl^-), sulfate (SO_4^{2-}), hexafluorophosphate (PF_6^-), tetrafluoroborate (BF_4^-)) and

organic anions such as bis(trifluoromethylsulfonyl)imide (TFSI), among others [60]. **Figure 1.8** represents the chemical composition of the most common cations and anions described in the literature.

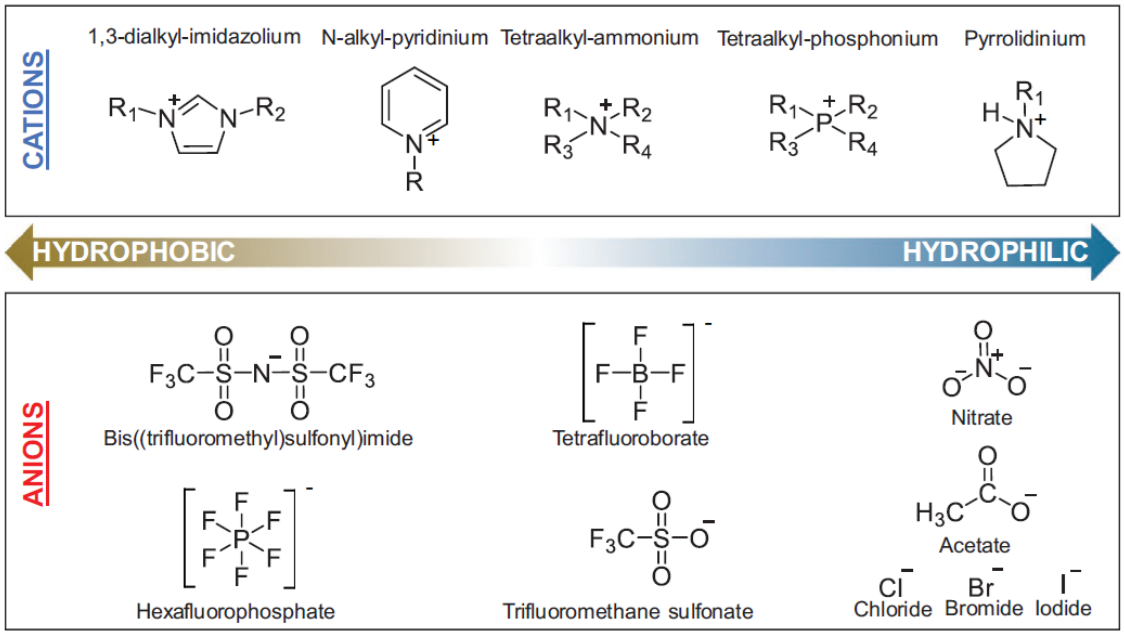


Figure 1.8 - Schematic representation of the most common cations and anions described in the literature [7].

Protic ILs are prepared by proton transfer through the combination of a Brönsted acid and a Brönsted base, leading to the presence of proton-donor and acceptor sites, which can be used to build up a hydrogen-bonded network [61]. This kind of ILs has attracted increasing attention for fuel cell applications as new proton conductors and n-doped carbon materials using protic ILs as novel small-molecule precursors via direct carbonization treatments instead of traditional polymer precursors, which require more complex procedures and can lead to more impurities on the materials [62].

Zwitterionic ILs results from the addition of ILs to surfactant systems, actuating the ILs as additives with the primary goal of modifying the properties of aqueous zwitterionic surfactants systems. The resulting properties of the system depend both on the type and the extent of the interaction between the cation/anion of the IL with the surfactant head group [52].

The functionalities of the ILs can be tailored through the incorporation of functional groups linked covalently into the cation, anion or both, tuning the ILs properties and increasing their

effectiveness towards specific applications such as catalysis, medicine, CO_2 capture, batteries, lubricants, or fuels, among others [46, 47, 49, 55]. The physical properties of ILs can be adjusted depending on the ionic constituents (alkyl chain length and functional groups) and also the IL properties (magnetic, luminescent and catalytic properties, among others), as well as by their incorporation into other constituents, such as polymers [55]. In this sense, the combination of the ILs functionality with polymers allows the development of smart materials with superior properties when compared with other nanocomposites, increasing the interest and potentiality for several areas of application.

In the development of magnetically responsive materials, magnetic fillers commonly in the form of NPs, like cobalt ferrite (CFO) or iron oxide (Fe_3O_4) [63], or nanowires and nanotubes, such as iron, cobalt, nickel, among others are incorporated into the polymer matrix [64]. The main drawbacks are associated with the formation of agglomerates and poor dispersion when incorporated into polymer matrix in which the addition of surfactants during the composite synthesis might be needed [65, 66]. Recently, MILs have emerged as a new alternative as they offer a solution to this problem due to their good dispersion and null agglomeration [7].

MILs possess the ability of responding to an external magnetic field due to the integration of magnetic elements, more commonly in the anion structure, such as transition, like iron and cobalt, or rare earth metals such as dysprosium [67-69]. When compared to other magnetic materials, MILs offer a major advantage since there is no need to add magnetic NPs to obtain a magnetic response [69]. Additionally, it is already known that the ionic species have higher mobility within the amorphous part of the polymeric matrix, which can give an enhanced effect of the IL in the composites .[70]

1.3 Ionic liquid/polymer composites and their applications

The combination of ILs with polymers, in a composite, allows developing smart materials, which synergistically combine the features of specific polymers and ILs. Moreover, ILs can be extensively modified by the incorporation of functional groups with specific properties into the cation, anion or both. Thus, it is possible to tune the IL, the polymer, or both to obtain a broad spectrum of multifunctional composites and address the specific requirements of many applications.

Besides being applied in electrochemistry due to their exciting properties (according to experimental studies, many ILs exhibit high electrochemical stability windows ranging between 4 and 7 V [71]), ILs have emerged as a new trend in materials science. The combination of ILs with specific polymers opens the possibility to develop novel stimuli-responsive materials with different morphologies (films, membranes, fibers and printed), **Figure 1.9**, with tailored functionality, as a new platform for advanced multifunctional materials, with advantages over traditional smart nanocomposite materials.

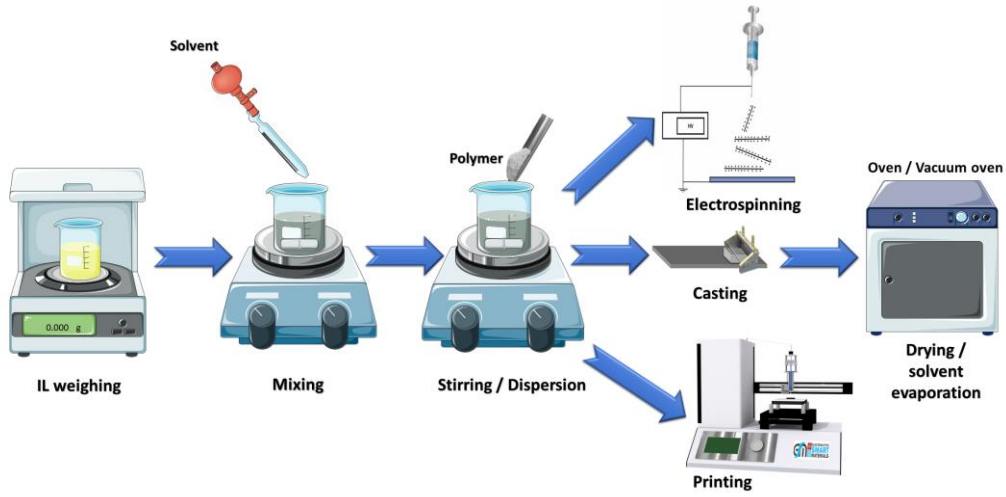


Figure 1.9 - Schematic representation of the production of IL-based polymer composites for different processing methods [7].

The main advantage is related to a large variety of ILs, which allows tuning materials responses to a large variety of external environmental stimuli, such as electrical and magnetic fields, heat or light, among others [8], based on the vast array of IL functional characteristics [72]. The material functionality is a result of the selection of the IL and its properties (e.g. size of cation/anion, viscosity, conductivity, density and molecular weight) and the polymer type. Furthermore, the interplay between the selected IL charges (cations and anions) with the polymer chains, also plays an essential role in the composite properties. As an example, IL with different anions and cations, when incorporated into a PVDF matrix will affect the percentage of β-phase (the most electroactive and polar phase) in the composite, and the mechanical properties (acts as a plasticizing agent) [73], due to the interaction of the positive CH_2 of PVDF with the negative anion charge and the interaction of the negative holding charge PVDF groups (CF_2 groups) with the IL cation charges [73, 74]. Another work devoted to evaluating the effect of ILs on PVDF-copolymer

morphology indicates that ILs can also induce a porous structure in the polymer matrix [6]. Additionally, IL may avoid the need for the addition of more than one filler (active material) to endow a nanocomposite with more than one functionality – altering its original properties negatively.

In **Table 1.1** it is summarized the ILs functionalities to develop IL-based smart and multifunctional materials.

Table 1.1 - ILs functionalities for the development of smart and multifunctional applications [7].

IL-based multifunctional materials	ILs functionality
Responsive and sensitive materials	Photo-responsive
	pH-sensitive
	Temperature-sensitive
	Gas-sensing
	Ion-responsive
	Moisture-sensitive
	Magnetic-responsive
	Electrochromic
	ILs with switchable polarity
Optical materials	Luminescent
	Nonlinear optical
	Photonic ILs
	ILs based structural color
Energetic materials	Energetic ILs
	Hydrogen-storage

The potential applications of such smart/multifunctional materials have been increasing significantly, including nowadays areas such as sensors and actuators [32, 74-76], tissue engineering [27, 32, 39], energy generation and storage, such as batteries [77-80], among others (**Figure 1.10**).

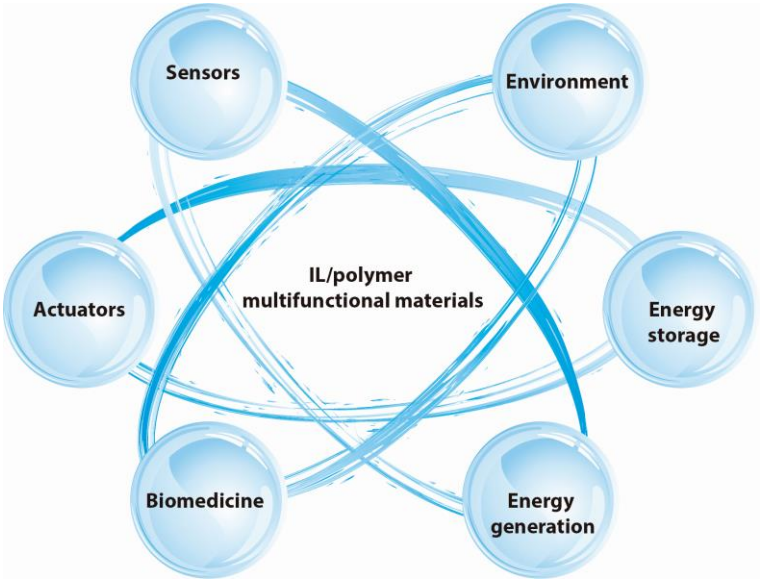


Figure 1.10 - IL/polymer-based multifunctional materials application areas [7].

1.3.1 Magnetic ionic liquid/polymer based composites as sensors and actuators

Composites based on MILs and EAPs [81] allow the development of an entirely new class of electroactive smart materials combining highly polar matrices with ionic mobile species [82], and exhibiting suitable magnetic, electric, mechanical and electromechanical properties [30]. However, being such an innovative area, only a few studies have been reported on the development of composites combining polymers with MILs, as the examples given ahead [76, 83-89].

Magnetic composites based on the MIL 1-butyl-3-methylimidazolium tetrachloroferrate ([Bmim][$FeCl_4$]) and the electroactive polymer P(VDF-TrFE) where synthetized with different contents of the MIL (10, 20 and 40 wt. %) to study the magnetoionic (MI) effect. The maximum obtained MI response was 10 $V.cm^{-1}.Oe^{-1}$ for the sample containing 40 wt. % of [Bmim][$FeCl_4$] showing their suitability as magnetic sensors and applicability by printing technologies [83].

Another study, with the same MIL and PVDF explored the influence of the MIL content (5,10 and 20 wt%) in the composites to perform as humidity sensors. It was shown that all composites exhibited a linear resistance variation with the relative humidity, the sensitivity to humidity variations increasing linearly with the IL content, evidencing the potential of the composites in this area [76].

Also with PVDF, the thermochromic properties of the bis(1-butyl-3-methylimidazolium) tetrachloronickelate ($[Bmim]_2[NiCl_4]$)/PVDF films revealed a potentiality to be applied as printable sensors [84]. The capacity of these materials to change from transparent to a dark blue color has been attributed to the tetrahedral complex $NiCl_4^{2-}$, after a dehydration process. As a result of the dehydration process that takes place, decreasing the number of ions into the matrix leading to a conductivity decrease. Hence, the high potential of these materials for thermosensitive and thermochromic printable sensors in different areas such as temperature sensors, water level sensors, smart windows, among others.

For a more sustainable approach, composites based on the natural polymer carrageenan and the MIL $[Bmim][FeCl_4]$ were produced with different MIL contents (10, 20 and 40 wt. %), for the development of pressure printable sensors while also accessing the recyclability of the materials [86] The sensor resistance response and sensitivity (711 to 27 Ω/g) was tuned by the IL concentration.

In the area of electromechanical actuators, IL/polymer composites have already been successfully used for low voltage and large deformation actuators. For this, the design of the actuators consists in the IL/polymer composite and two conductive flexible electrodes at the sides. The working mechanism is as follows, when an electric field is applied, ionic diffusion within the polymer matrix occurs and, consequently, a bending motion is produced (**Figure 1.11**) [90].

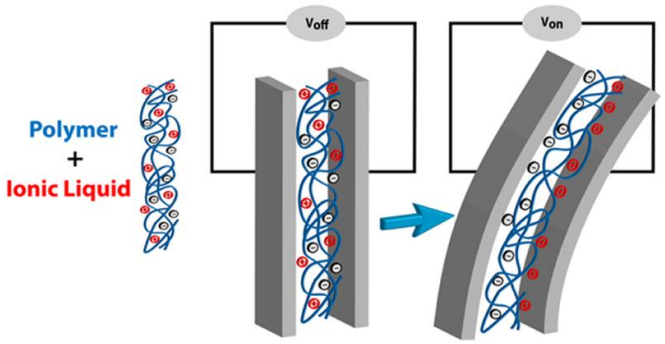


Figure 1.11 - Schematic representation of the ion migration and bending response [90].

By far, the most commonly used polymer in this type of composites its PVDF and its copolymers [5, 75, 81, 90-92], due to its high dielectric constant, polarity and ionic conductivity, where the influence of the polymer matrix, anion and cation type have been studied [30].

The use of MIL/polymer composites as electric/magnetic actuators, is till scarce, however the potentiality of these materials as multifunctional sensors and actuators cannot be overlooked [7].

A thermochromic actuator was designed with the MILs $[Bmim]_2[NiCl_4]$ and bis(1-butyl-3-methylimidazolium) tetrachlorocobaltate $[Bmim]_2[CoCl_4]$ and a thermally induced shape-memory triethanolamine cross-linked polyurethane (TEAPU) [89]. The shape–color-switchable thermochromic actuators showed a change in the color and shape quickly in a narrow temperature range (30–70 °C), thus showing potential in artificial muscle actuators and intelligent camouflages.

1.4 Printing technologies and sustainable materials

During the last decade, additive manufacturing, has been emerging as an alternative to classic methods for the development of polymer composite materials. These printing techniques allow to overcome several drawbacks encountered such as scalability, processing time, cost effectiveness, shape accuracy and easy assembly of layered composites [93]. Manufacturing of devices with active elements on flexible substrates using printing technologies means the possibility of using environmentally friendly processes with a large printing area, defined shape and high throughput being compatible with polymer-based materials [94]. Printing methods can be classified as contact or non-contact methods, as shown in **Figure 1.12**.

Flexography, gravure and screen printing are the most common contact method printing techniques, using a roller or a screen that is in contact with the ink in the deposition moment (**Figure 1.12a-1.12c**). From these three techniques, screen printing is a fast, cost effective and easily scalable process ideal for mechanically flexible substrates using a predefined pattern [95]. As such, it makes this technique ideal for electrode design (as in this work) and water-soluble materials.

AS for non-contact techniques, they use a head or nozzle to deposit the ink directly onto the substrate or above a previously printed material. The most prevalent techniques are inkjet printing, aerosol jet, fused deposition modelling (FDM), and 3D dispensing (**Figure 1.12d-g**) [94]. In sensor and actuator design, commonly, a coupling of both techniques can be used for the electrical part design and active material deposition [96].

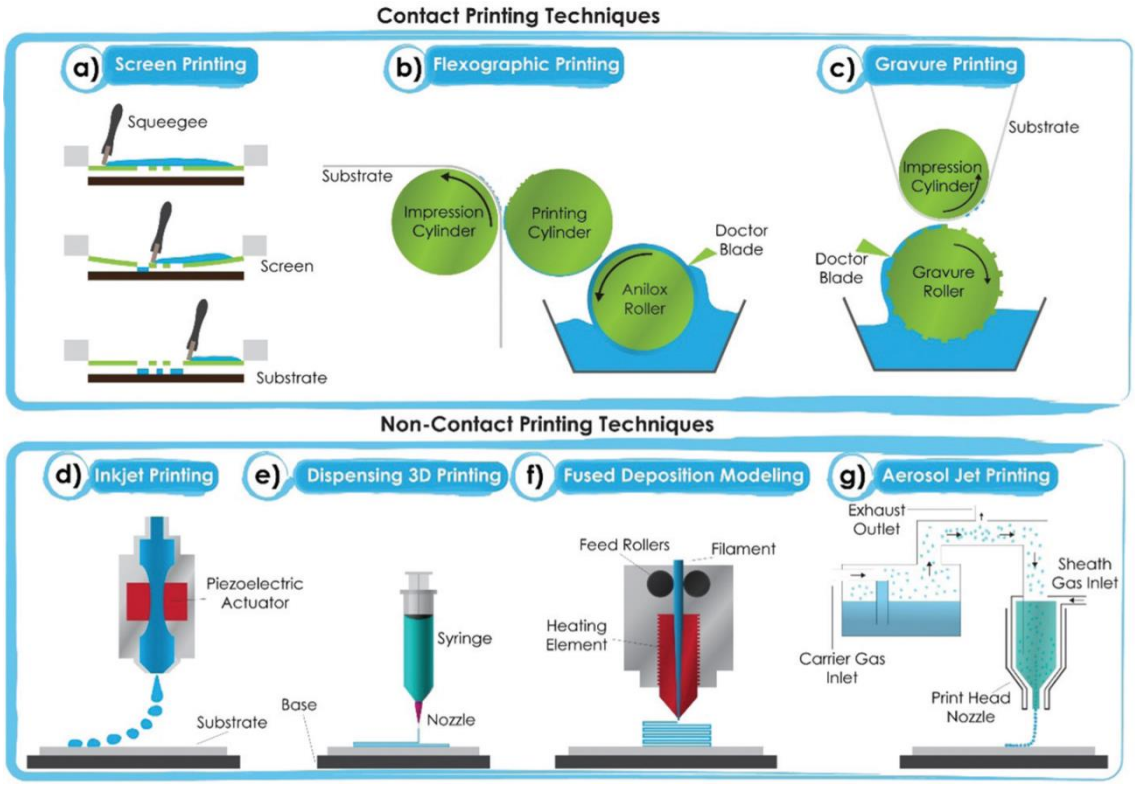


Figure 1.12 – Schematic representation of the main printing techniques compatible with polymer-based composites: (a-c) contact and (d-g) non-contact methods [94].

Overall, printing techniques give the opportunity to more sustainable and eco-friendly approaches, in flexible devices design. This can also be easily couple with greener alternative in polymer-based composites, an urgent need, with the use of curable (such as polyurethane (PU) epoxy resins) and/or natural polymers.

Natural polymers are a class of materials produced by biological and renewable resources (plants and animals), many of them being biodegradable and/or biocompatible, allowing also to improve reuse and recyclability [97]. Natural materials can be classified in six different groups: lignin, polyesters, polyisoprenes, polynucleotides, polysaccharides and proteins, giving rise to different types of natural polymers such as, agar, alginates, carrageenan, cellulose, chitin, galactomannans, gelatin, hyaluronan, pectin or xanthan, that can be selected for applications based on its different physical-chemical, thermal and mechanical properties [98].

Carrageenan's are sulphated polysaccharides extracted from red marine algae and they allow to form stiff and thermoreversible gels at room temperature [99]. Carrageenan's are linear polymers composed of 1,3-linked β-d-galactose and 1,4-linked α-d-galactose [100, 101]. All

carrageenan's show high molecular flexibility and in high concentrations they can form a double-helical structure [102]. There are different types of carrageenan which are designated by the Greek alphabet letters (kappa (κ-), iota (ι-), lambda (λ-), nu (ν-), mu (μ-) and teta (θ-)) [103]. The most used are the first three and differ in the number of sulphate groups and in the content of 3,6- anhydro-galactose. Thus, κ- carrageenan has one, ι- carrageenan has 2 and λ- carrageenan has 3 of these sulphate groups [104, 105]. I-carrageenan is one of the natural polymers with large abundance in nature, biodegradability and low cost [106, 107]. This type of carrageenan is considered a promising and environmentally friendly material for electronic devices but has a low ionic conductivity when compared with other types of carrageenan [108]. Recently, the potential of carrageenan hydrogels as actuators has been demonstrated [108], the use of different types of carrageenan (κ, ι, and λ) combined with poly (3-hexylthiophene) (P3HT) allowing to tailor the electrical and electrochemical properties of neat carrageenan hydrogels [108].

1.5 Objectives and thesis structure

The main objective of the thesis is the development, understanding, processing and application of advanced multifunctional ionic EAPs using MILs and diverse polymer matrices. The goal is to enhance their performance for applications including sensors and actuators.

This document is structured in eleven different chapters, with eight chapters reporting the preparation, characterization, and performance of the developed materials. The current chapter (Chapter 1) introduces a context and overview of the subject, allowing the comprehension of the works motivation. Chapter 2 provides an overview on the materials and the characterization techniques which are common in the following chapters, whereas the characterizations and/or proofs of concept specific for each chapter are provided in those chapters.

Chapters 3 and 4 provide an understanding of fundamental composite properties, in particular related to morphology, structural, physical-chemical, electric, and magnetic properties. Chapter 5 presents the study of the electromechanical and magnetoactive response of composites, providing an insight of these composites' behavior for the development of advanced devices. The exploration of IL/polymer composite materials as magnetic actuators are presented in chapter 6. Chapter 7 explores the potential of tri-composites with the incorporation of magnetic NPs to improve the potential of IL/polymer composites as MI devices., whereas the demonstration of the

suitability of IL/polymer composites as humidity sensors is provided in chapter 8, taking advantage of the hygroscopic nature of the ILs. Looking into a different approach for the development of IL/polymer composites for advanced sensor applications, a more sustainable approach is introduced in chapters 9 and 10, investigating the use of a solvent free UV-curable alternative and a natural polymer matrix for actuators and thermochromic materials, respectively.

The final chapter (Chapter 11) addresses the main conclusions of the work as well as future perspectives opened by this thesis.

1.6 References

1. Botta, C., L. Pierangelini, and L. Vollero. *IoT Gateways for Industrial and Medical Applications: Architecture and Performance Assessment*. in *2020 IEEE International Workshop on Metrology for Industry 4.0 & IoT*. 2020.
2. Vaidya, S., P. Ambad, and S. Bhosle, *Industry 4.0 – A Glimpse.* Procedia Manufacturing, 2018. **20**: p. 233-238.
3. Xu, X., et al., *Industry 4.0 and Industry 5.0—Inception, conception and perception.* Journal of Manufacturing Systems, 2021. **61**: p. 530-535.
4. Lendlein, A. and R.S. Trask, *Multifunctional materials: concepts, function-structure relationships, knowledge-based design, translational materials research.* Multifunctional Materials, 2018. **1**(1): p. 010201.
5. Dias, J.C., et al., *Electromechanical actuators based on poly(vinylidene fluoride) with N-1112(OH) NTf_2 and C_2mim C_2SO_4.* Journal of Materials Science, 2016. **51**(20): p. 9490-9503.
6. Correia, D., et al., *Magnetic ionic liquid/polymer composites: Tailoring physico-chemical properties by ionic liquid content and solvent evaporation temperature.* Composites Part B: Engineering, 2019. **178**: p. 107516.
7. Correia, D.M., et al., *Ionic Liquid–Polymer Composites: A New Platform for Multifunctional Applications.* Advanced Functional Materials, 2020. **30**(24): p. 1909736.
8. Drossel, W.G., et al., *Smart materials for smart production – a cross-disciplinary innovation network in the field of smart materials.* Procedia Manufacturing, 2018. **21**: p. 197-204.
9. Schwartz, M., *Smart Materials*. 2008: CRC Press.
10. Eerenstein, W., N.D. Mathur, and J.F. Scott, *Multiferroic and magnetoelectric materials.* Nature, 2006. **442**(7104): p. 759-765.
11. Malleron, K., et al., *Experimental study of magnetoelectric transducers for power supply of small biomedical devices.* Microelectronics Journal, 2019. **88**: p. 184-189.
12. Rupp, T., et al., *Magnetoelectric Transducer Designs for Use as Wireless Power Receivers in Wearable and Implantable Applications.* Materials (Basel, Switzerland), 2019. **12**(3): p. 512.
13. Cheng, Y., et al., *Recent development and status of magnetoelectric materials and devices.* Physics Letters A, 2018. **382**(41): p. 3018-3025.
14. Leung, C.M., et al., *A review on applications of magnetoelectric composites: from heterostructural uncooled magnetic sensors, energy harvesters to highly efficient power converters.* Journal of Physics D: Applied Physics, 2018. **51**(26): p. 263002.
15. Wang, Y. and J. Atulasimha, *A Dexterous Surgical Manipulation Tool Using Self-Sensing Magnetoelectric Actuators*. 2010. p. 767-771.
16. Martins, P. and S. Lanceros-Méndez, *Polymer-based magnetoelectric materials: To be or not to be.* Applied Materials Today, 2019. **15**: p. 558-561.

17. Martins, P. and S. Lanceros-Méndez, *Polymer-Based Magnetoelectric Materials.* Advanced Functional Materials, 2013. **23**(27): p. 3371-3385.
18. Nan, C.W., et al., *Multiferroic magnetoelectric composites: Historical perspective, status, and future directions.* Journal of Applied Physics, 2008. **103**(3).
19. Liang, X., H. Chen, and N.X. Sun, *Magnetoelectric materials and devices.* APL Materials, 2021. **9**(4).
20. Yoseph, B.-C. *EAP as artificial muscles: progress and challenges*. in *Proc.SPIE*. 2004.
21. Li, Y., et al., *Novel multi-responsive polymer materials: When ionic liquids step in.* European Polymer Journal, 2015. **69**: p. 441-448.
22. Bar-Cohen, Y., *Electroactive Polymer (EAP) Actuators as Artificial Muscles: Reality, Potential, and Challenges*. Press Monograph Series. 2004: Society of Photo Optical.
23. Hong, W., A. Almomani, and R. Montazami, *Influence of ionic liquid concentration on the electromechanical performance of ionic electroactive polymer actuators.* Organic Electronics, 2014. **15**(11): p. 2982-2987.
24. Cheng, Z.Y. and Q.M. Zhang, *Field-activated electroactive polymers.* Mrs Bulletin, 2008. **33**(3): p. 183-187.
25. Shankar, R., T.K. Ghosh, and R.J. Spontak, *Dielectric elastomers as next-generation polymeric actuators.* Soft Matter, 2007. **3**(9): p. 1116-1129.
26. O'Halloran, A., F. O'Malley, and P. McHugh, *A review on dielectric elastomer actuators, technology, applications, and challenges.* Journal of Applied Physics, 2008. **104**(7): p. 071101.
27. Correia, D.M., et al., *Strategies for the development of three dimensional scaffolds from piezoelectric poly(vinylidene fluoride).* Materials & Design, 2016. **92**: p. 674-681.
28. Martins, P., A.C. Lopes, and S. Lanceros-Mendez, *Electroactive phases of poly(vinylidene fluoride): Determination, processing and applications.* Progress in Polymer Science, 2014. **39**(4): p. 683-706.
29. Zhao, Y. and T. Boström, *Ionic liquid and nanoparticle based magnetic electrolytes: Design, preparation, and electrochemical stability characterization.* Journal of Molecular Liquids, 2016. **213**: p. 268-272.
30. Ribeiro, C., et al., *Electroactive poly(vinylidene fluoride)-based structures for advanced applications.* Nature Protocols, 2018. **13**(4): p. 681-704.
31. Liu, Y., et al., *Enhanced Electromechanical Response of Ionic Polymer Actuators by Improving Mechanical Coupling between Ions and Polymer Matrix.* Macromolecules, 2012. **45**(12): p. 5128-5133.
32. Dias, J.C., et al., *Development of poly(vinylidene fluoride)/ionic liquid electrospun fibers for tissue engineering applications.* Journal of Materials Science, 2016. **51**(9): p. 4442-4450.
33. Imaizumi, S., H. Kokubo, and M. Watanabe, *Polymer Actuators Using Ion-Gel Electrolytes Prepared by Self-Assembly of ABA-Triblock Copolymers.* Macromolecules, 2012. **45**(1): p. 401-409.
34. Kim, S.-S., et al., *Electro-active hybrid actuators based on freeze-dried bacterial cellulose and PEDOT:PSS.* Smart Materials and Structures, 2013. **22**(8): p. 085026.
35. Nunes-Pereira, J., et al., *Poly(vinylidene fluoride) composites with carbon nanotubes decorated with metal nanoparticles.* Composites Part B: Engineering, 2018. **142**: p. 1-8.
36. Veved, A., G.W. Ejuh, and N. Djongyang, *Review of emerging materials for PVDF-based energy harvesting.* Energy Reports, 2022. **8**: p. 12853-12870.
37. Costa, C.M.S., et al., *Electroactive poly (vinylidene fluoride) based materials: recent progress, challenges and opportunities.* 2020.
38. Nunes-Pereira, J., et al., *Energy harvesting performance of BaTiO3/poly(vinylidene fluoride-trifluoroethylene) spin coated nanocomposites.* Composites Part B-Engineering, 2015. **72**: p. 130-136.
39. Ribeiro, C., et al., *Piezoelectric polymers as biomaterials for tissue engineering applications.* Colloids and Surfaces B-Biointerfaces, 2015. **136**: p. 46-55.
40. Serra, J.P., et al., *Humidity Sensors Based on Magnetic Ionic Liquids Blended in Poly(vinylidene fluoride-co-hexafluoropropylene).* ACS Applied Polymer Materials, 2023. **5**(1): p. 109-119.

41. Mao, L., et al., *Conjugated polyfluorene imidazolium ionic liquids intercalated reduced graphene oxide for high performance supercapacitor electrodes.* Nano Energy, 2014. **6**: p. 119-128.
42. Shi, L., R. Wang, and Y. Cao, *Effect of the rheology of poly(vinylidene fluoride-co-hexafluropropylene) (PVDF–HFP) dope solutions on the formation of microporous hollow fibers used as membrane contactors.* Journal of Membrane Science, 2009. **344**(1): p. 112-122.
43. Neese, B., et al., *Piezoelectric responses in poly(vinylidene fluoride/hexafluoropropylene) copolymers.* Applied Physics Letters, 2007. **90**(24): p. 242917.
44. Huan, Y., et al., *Influence of extrusion, stretching and poling on the structural and piezoelectric properties of poly (vinylidene fluoride-hexafluoropropylene) copolymer films.* Journal of Applied Polymer Science, 2007. **104**(2): p. 858-862.
45. Künstler, W., et al., *Preparation and assessment of piezo- and pyroelectric poly (vinylidene fluoride-hexafluoropropylene) copolymer films.* Applied Physics A, 2001. **73**(5): p. 641-645.
46. Vekariya, R.L., *A review of ionic liquids: Applications towards catalytic organic transformations.* Journal of Molecular Liquids, 2017. **227**: p. 44-60.
47. Lei, Z., et al., *Introduction: ionic liquids.* Chemical Reviews, 2017. **117**(10): p. 6633-6635.
48. Wang, A.L., et al., *Electrochemical performances of a new solid composite polymer electrolyte based on hyperbranched star polymer and ionic liquid for lithium-ion batteries.* Journal of Solid State Electrochemistry, 2017. **21**(8): p. 2355-2364.
49. Dong, K., et al., *Multiscale Studies on Ionic Liquids.* Chemical Reviews, 2017. **117**(10): p. 6636-6695.
50. Wang, B., et al., *Are Ionic Liquids Chemically Stable?* Chemical Reviews, 2017. **117**(10): p. 7113-7131.
51. Rogers, R.D. and K.R. Seddon, *Ionic Liquids–Solvents of the Future?* Science, 2003. **302**(5646): p. 792.
52. Ye, Y.-S., J. Rick, and B.-J. Hwang, *Ionic liquid polymer electrolytes.* Journal of Materials Chemistry A, 2013. **1**(8): p. 2719-2743.
53. Marsh, K.N., J.A. Boxall, and R. Lichtenthaler, *Room temperature ionic liquids and their mixtures—a review.* Fluid Phase Equilibria, 2004. **219**(1): p. 93-98.
54. Yu, G., et al., *Viscosity of ionic liquids: Database, observation, and quantitative structure-property relationship analysis.* Aiche Journal, 2012. **58**(9): p. 2885-2899.
55. Zhang, S., et al., *Beyond solvents and electrolytes: Ionic liquids-based advanced functional materials.* Progress in Materials Science, 2016. **77**: p. 80-124.
56. Endres, F., *Ionic Liquids: Promising Solvents for Electrochemistry*. Vol. 218. 2004. 255-284.
57. Yoo, C.G., Y.Q. Pu, and A.J. Ragauskas, *Ionic liquids: Promising green solvents for lignocellulosic biomass utilization.* Current Opinion in Green and Sustainable Chemistry, 2017. **5**: p. 5-11.
58. Taherifard, H. and S. Raeissi, *Estimation of the Densities of Ionic Liquids Using a Group Contribution Method.* Journal of Chemical and Engineering Data, 2016. **61**(12): p. 4031-4038.
59. Correia, D.M., et al., *Ionic and conformational mobility in poly(vinylidene fluoride)/ionic liquid blends: Dielectric and electrical conductivity behavior.* Polymer, 2018. **143**: p. 164-172.
60. Luczak, J., et al., *Ionic liquids for nano- and microstructures preparation. Part 1: Properties and multifunctional role.* Advances in Colloid and Interface Science, 2016. **230**: p. 13-28.
61. Mai, N.L., K. Ahn, and Y.M. Koo, *Methods for recovery of ionic liquids-A review.* Process Biochemistry, 2014. **49**(5): p. 872-881.
62. Watanabe, H., et al., *Hydrogen bond in imidazolium based protic and aprotic ionic liquids.* Journal of Molecular Liquids, 2016. **217**: p. 35-42.
63. Kudr, J., et al., *Magnetic Nanoparticles: From Design and Synthesis to Real World Applications.* Nanomaterials (Basel), 2017. **7**(9).
64. Staňo, M. and O. Fruchart, *Chapter 3 - Magnetic Nanowires and Nanotubes*, in *Handbook of Magnetic Materials*, E. Brück, Editor. 2018, Elsevier. p. 155-267.
65. Fang, W., et al., *Optimization of the magnetic properties of aligned Co nanowires/polymer composites for the fabrication of permanent magnets.* Journal of Nanoparticle Research, 2014. **16**(2): p. 2265.

66. Nana, A.B.A., et al., *Multifunctional Magnetic Nanowires: Design, Fabrication, and Future Prospects as Cancer Therapeutics.* Cancers (Basel), 2019. **11**(12).
67. Xie, Z.-L. and A. Taubert, *Thermomorphic Behavior of the Ionic Liquids [C4mim][FeCl4] and [C12mim][FeCl4].* ChemPhysChem, 2011. **12**(2): p. 364-368.
68. Joseph, A., et al., *Paramagnetic Ionic Liquids for Advanced Applications: A Review*. Vol. 218. 2016. 319-331.
69. Santos, E., J. Albo, and A. Irabien, *Magnetic ionic liquids: synthesis, properties and applications.* RSC Advances, 2014. **4**(75): p. 40008-40018.
70. Correia, D.M., et al., *Molecular relaxation and ionic conductivity of ionic liquids confined in a poly(vinylidene fluoride) polymer matrix: Influence of anion and cation type.* Polymer, 2019. **171**: p. 58-69.
71. Kazemiabnavi, S., et al., *Electrochemical Stability Window of Imidazolium-Based Ionic Liquids as Electrolytes for Lithium Batteries.* The Journal of Physical Chemistry B, 2016. **120**(25): p. 5691-5702.
72. Kitazawa, Y., K. Ueno, and M. Watanabe, *Advanced Materials Based on Polymers and Ionic Liquids.* The Chemical Record, 2018. **18**(4): p. 391-409.
73. Correia, D.M., et al., *Influence of Cation and Anion Type on the Formation of the Electroactive β-Phase and Thermal and Dynamic Mechanical Properties of Poly(vinylidene fluoride)/Ionic Liquids Blends.* The Journal of Physical Chemistry C, 2019. **123**(45): p. 27917-27926.
74. Correia, D., et al., *Ionic liquid cation size-dependent electromechanical response of ionic liquid/poly (vinylidene fluoride)-based soft actuators.* The Journal of Physical Chemistry C, 2019. **123**(20): p. 12744-12752.
75. Dias, J.C., et al., *Improved response of ionic liquid-based bending actuators by tailored interaction with the polar fluorinated polymer matrix.* Electrochimica Acta, 2019. **296**: p. 598-607.
76. Fernandes, L., et al., *Highly sensitive humidity sensor based on ionic liquid-polymer composites.* ACS Applied Polymer Materials, 2019.
77. Costa, C.M., et al., *Electroactive Poly(Vinylidene Fluoride-Trifluorethylene) (PVDF-TrFE) Microporous Membranes for Lithium-Ion Battery Applications.* Ferroelectrics, 2012. **430**(1): p. 103-107.
78. Costa, C.M., M.M. Silva, and S. Lanceros-Méndez, *Battery separators based on vinylidene fluoride (VDF) polymers and copolymers for lithium ion battery applications.* RSC Advances, 2013. **3**(29): p. 11404-11417.
79. Ferrari, S., et al., *Lithium ion conducting PVdF-HFP composite gel electrolytes based on N-methoxyethyl-N-methylpyrrolidinium bis(trifluoromethanesulfonyl)-imide ionic liquid.* Journal of Power Sources, 2010. **195**(2): p. 559-566.
80. Ye, H., et al., *Li ion conducting polymer gel electrolytes based on ionic liquid/PVDF-HFP blends.* Journal of the Electrochemical Society, 2007. **154**(11): p. A1048-A1057.
81. Mejri, R., et al., *Imidazolium-based ionic liquid type dependence of the bending response of polymer actuators.* European Polymer Journal, 2016. **85**: p. 445-451.
82. Smiglak, M., et al., *Ionic liquids for energy, materials, and medicine.* Chemical Communications, 2014. **50**(66): p. 9228-9250.
83. Correia, D.M., et al., *Low-field giant magneto-ionic response in polymer-based nanocomposites.* Nanoscale, 2018. **10**(33): p. 15747-15754.
84. Fernandes, L.C., et al., *Ionic-Liquid-Based Printable Materials for Thermochromic and Thermoresistive Applications.* ACS Applied Materials & Interfaces, 2019. **11**(22): p. 20316-20324.
85. Fernandes, L.C., et al. *Electrospun Magnetic Ionic Liquid Based Electroactive Materials for Tissue Engineering Applications*. Nanomaterials, 2022. **12**, DOI: 10.3390/nano12173072.
86. Serra, J.P., et al., *Carrageenan-Based Hybrid Materials with Ionic Liquids for Sustainable and Recyclable Printable Pressure Sensors.* ACS Sustainable Chemistry & Engineering, 2022. **10**(26): p. 8631-8640.
87. Ikake, H., et al., *Development of a magnetic hybrid material capable of photoinduced phase separation of iron chloride by shape memory and photolithography.* Journal of Materials Chemistry C, 2022. **10**(20): p. 7849-7856.

88. Karzarjeddi, M., et al., *Adjustable hydro-thermochromic green nanofoams and films obtained from shapable hybrids of cellulose nanofibrils and ionic liquids for smart packaging.* Chemical Engineering Journal, 2022. **443**: p. 136369.
89. Wang, Z., et al., *Shape- and Color-Switchable Polyurethane Thermochromic Actuators Based on Metal-Containing Ionic Liquids.* ACS Applied Materials & Interfaces, 2021. **13**(24): p. 28878-28888.
90. Correia, D.M., et al., *Ionic Liquid Cation Size-Dependent Electromechanical Response of Ionic Liquid/Poly(vinylidene fluoride)-Based Soft Actuators.* The Journal of Physical Chemistry C, 2019. **123**(20): p. 12744-12752.
91. Mejri, R., et al., *Effect of anion type in the performance of ionic liquid/poly(vinylidene fluoride) electromechanical actuators.* Journal of Non-Crystalline Solids, 2016. **453**.
92. Sugino, T., et al., *Actuation mechanism of dry-type polymer actuators composed by carbon nanotubes and ionic liquids.* Sensors and Actuators B-Chemical, 2018. **273**: p. 955-965.
93. Saroia, J., et al., *A review on 3D printed matrix polymer composites: its potential and future challenges.* The International Journal of Advanced Manufacturing Technology, 2020. **106**(5): p. 1695-1721.
94. Merazzo, K.J., et al., *Magnetic materials: a journey from finding north to an exciting printed future.* Materials Horizons, 2021. **8**(10): p. 2654-2684.
95. Oliveira, J., et al., *Polymer-based smart materials by printing technologies: Improving application and integration.* Additive Manufacturing, 2018. **21**: p. 269-283.
96. Correia, D.M., et al., *All printed soft actuators based on ionic liquid/polymer hybrid materials.* Applied Materials Today, 2021. **22**: p. 100928.
97. Rudin, A. and P. Choi, *The elements of polymer science and engineering*. 2012: Academic press.
98. Olatunji, O., *Natural polymers: industry techniques and applications*. 2015: Springer.
99. Mangione, M., et al., *K+ and Na+ effects on the gelation properties of κ-carrageenan.* Biophysical Chemistry, 2005. **113**(2): p. 129-135.
100. Tang, C.-H., et al., *Formation and properties of glycinin-rich and β-conglycinin-rich soy protein isolate gels induced by microbial transglutaminase.* Food Research International, 2006. **39**(1): p. 87-97.
101. Ahmed, A.B.A., et al., *Chapter Ten - Pharmaceutical, Cosmeceutical, and Traditional Applications of Marine Carbohydrates*, in *Advances in Food and Nutrition Research*, S.-K. Kim, Editor. 2014, Academic Press. p. 197-220.
102. Bartkowiak, A. and D. Hunkeler, *Carrageenan–oligochitosan microcapsules: optimization of the formation process.* Colloids and surfaces B: Biointerfaces, 2001. **21**(4): p. 285-298.
103. Khotimchenko, M., et al., *Antitumor potential of carrageenans from marine red algae.* Carbohydrate Polymers, 2020: p. 116568.
104. Geonzon, L.C., et al., *Gelation mechanism and network structure in gels of carrageenans and their mixtures viewed at different length scales–A review.* Food Hydrocolloids, 2020: p. 106039.
105. Zia, K.M., et al., *A review on synthesis, properties and applications of natural polymer based carrageenan blends and composites.* International journal of biological macromolecules, 2017. **96**: p. 282-301.
106. Soleimani, F., M. Sadeghi, and H. Shahsavari, *Preparation and swelling behavior of carrageenan-graft-polymethacrylamide superabsorbent hydrogel as a releasing drug system.* Indian Journal of Science and Technology, 2012. **5**(2): p. 2143-2147.
107. Jayaramudu, T., et al., *Iota-Carrageenan-based biodegradable Ag0 nanocomposite hydrogels for the inactivation of bacteria.* Carbohydrate polymers, 2013. **95**(1): p. 188-194.
108. Kim, M.-K. and J.-S. Lee, *Short-term plasticity and long-term potentiation in artificial biosynapses with diffusive dynamics.* ACS nano, 2018. **12**(2): p. 1680-1687.

2 Experimental section

The materials, equipment specifications and the main characterisation techniques and conditions common to the different works are provided. Specific characterization techniques and the experimental development of applications are provided in the different chapters.

The goal behind this chapter is to provide an overview of the materials, and most common characterization techniques used in the duration of this thesis, apart from the synthesis methods and any specific characterization techniques for an aim application (such as the study of the MI/ME effect, electromechanical behavior, thermochromic and humidity sensing), which are described in each corresponding chapter. This chapter aims to supports an easier and more objective reading of the work.

2.1 Materials

Table 2.1 summarizes the materials used in the different chapters/works, as well as the main processing parameters for each. In the following, the corresponding characteristics of each material will be reviewed.

Table 2.1 - Overview of materials and main processing parameters.

Chapter	Polymer	Functional Filler(s)	Processing parameters	
			Filler content (wt. %)	Solvent evaporation temperature (ºC)
3	P(VDF-TrFE)	[Bmim][$FeCl_4$]	10, 20, 40	25, 90, 210
4	PVDF6010	[Pmim][TFSI]	40	210
		[Pmpip][TFSI]		
		[Bmim][$FeCl_4$]		
		[Bmim]$_2$[$NiCl_4$]		
5	PVDF6010	[C_2mim][$FeCl_4$]	20	210
		[C_4mim][$FeCl_4$]		
		[C_8mim][$FeCl_4$]		
		[C_{14}mim][$FeCl_4$]		
6	P(VDF-TrFE)	[Bmim][$FeCl_4$]	40	25, 90, 210
7	P(VDF-TrFE)	CFO	20/0 (IL/CFO), 20/10, 20/20, 20/30	90
		[Bmim][Cl]		
8	P(VDF-HFP)	[Bmim][$FeCl_4$]	40	210
		[Bmim]$_2$[$CoCl_4$]		
		[Emim]$_2$[$Co(SCN)_4$]		
		[Bmim]$_2$[$Co(SCN)_4$]		
9	PUA	[Bmim]$_2$[$NiCl_4$]	5, 10, 20, 40	-
10	ι-carrageenan	[Ch][DHP]	10,20,40	25, 80
		[Ch][$FeCl_4$]		
		[Bmim][$FeCl_4$]		
		[Bmim][$C(CN)_3$]		

2.1.1 Polymeric matrices

2.1.1.1 PVDF and copolymers

PVDF: PVDF (Solef6010, M_w 300 000–330 000 Da) was purchased from Solvay. In **Figure 2.1** is represented the chain conformation of β-PVDF and the repeat units of the P(VDF-TrFE) and PVDF-HPF copolymers.

P(VDF-TrFE): P(VDF-TrFE) (Piezotech® FC30) (30 % TrFE content) was obtained from Piezotech-Arkema (Pierre-Benite, France).

P(VDF-HFP): P(VDF-HFP) (Solef 21216; 12 wt% of HFP content) was supplied by Solvay.

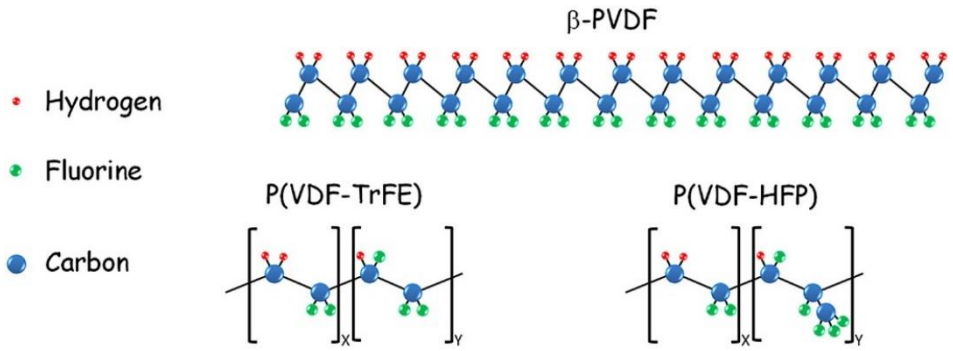


Figure 2.1 - Schematic representation of the chain conformation of β-PVDF and the repeat units of P(VDF-TrFE) and P(VDF-HFP) [1].

2.1.1.2 UV curable and natural polymers

Poly (urethane acrylate) (PUA): SPOT-ETM, a commercial PUA photoresin with great elongation (>65%), low shrinkage (1.5%) and a viscosity of 300 $mPa.s^{-1}$ was purchased from SPOT-A Materials®.

ι-carrageenan: Carrageenan (iota-ι type) (**Figure *2.2***) was purchased from Alfa Aesar (Kandel, Germany) (M_w 946.75 g/mol, impurity content of heavy metals <20 ppm).

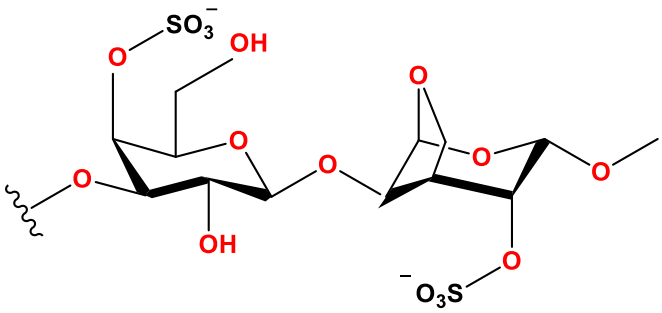


Figure 2.2 - Chemical structure of ι-carrageenan.

2.1.2 Functional fillers

Cobalt ferrite (CFO) nanoparticles: CFO nanoparticles (98% purity and 35-55 nm particle size) were purchased from Nanoamor (Texas, USA).

Ionic liquids: The ILs bis(1-butyl-3-methylimidazolium) tetrachlorocobaltate $[Bmim]_2[CoCl_4]$, 1-butyl-3-methylimidazolium tetrachloroferrate (III) >97% $[Bmim][FeCl_4]$, bis(1-butyl-3-methylimidazolium) tetrathiocyanatocobaltate $[Bmim]_2[Co(SCN)_4]$, bis(1-ethyl-3-methylimidazolium) tetrathiocyanotocobaltate, >99% $[Emim]_2[Co(SCN)_4]$, 1-propyl-3-methylimidazolium bis(trifluoromethylsulfonyl) imide ([Pmim][TFSI]), 1-methyl-1-propylpiperidinium bis(trifluoromethylsulfonyl) imide ([Pmpip][TFSI]), Choline dihydrogen phosphate >98% ([Ch][DHP]) and 1-butyl-3-methylimidazolium tricyanomethanide 98% $[Bmim][C(CN)_3]$ were purchased from Iolitec. 1-butyl- 3-methylimidazolium chloride [Bmim][Cl] (98% purity) was purchased from Solvionic (Toulouse, France).

Bis(1-butyl-3-methylimidazolium) tetrachloronickelate $([Bmim]_2[NiCl_4])$ was synthetized as described in [2, 3]. The ILs 1-ethyl-3-methylimidazolium tetrachloroferrate (III) $[C_2mim][FeCl_4]$, 1-bthyl-3-methylimidazolium tetrachloroferrate (III) $[C_4mim][FeCl_4]$, 1-octyl-3-methylimidazolium tetrachloroferrate (III) $[C_8mim][FeCl_4]$ and 1-tetradecyl-3-methylimidazolium tetrachloroferrate (III) $[C_{14}mim][FeCl_4]$ with purity >99% were synthetized as described in [4]. Choline tetrachloroferrate ($[Ch][FeCl_4]$), purity >99% was prepared as described in [2] with the change of the initial IL from [Bmim][Cl] to [Ch][Cl].

2.2 Characterization Methods

2.2.1 Morphological characterization

Scanning electron Microscopy (SEM) is a high depth focus technique that provides an insight into the observation and characterization of materials in a scale ranging from nanometers (nm) up to micrometers (μm). With this imaging instrument, different features can be analyzed, such as, surface roughness, as well as the presence of pores and voids or fractures. Additionally, in the presence of fillers it represents an important tool in observing their size, distribution and the presence of agglomerates. When analyzing polymeric-based films, surface and cross-section micrographs imaging is an important tool to aid in the analysis of other film properties.

The morphology of composite polymer films was analyzed using a SEM, NanoSEM – FEI Nova 200, with an accelerating voltage of 5 kV, (Chapter 5), 10 kV (Chapters 3, 4, 6, 9) or 10 kV (Chapters 7, 8, 10). The samples were previously coated with a thin gold layer using a sputter coating (Polaron, model SC502).

Energy dispersive X-Ray spectroscopy (EDX) technique is often coupled with SEM and is used for a chemical characterization of the materials. As such, EDX a mapping allows to obtain the elemental distribution across the sample surface.

In chapters 8 and 10, EDX analysis were carried out using Hitachi Tabletop Microscope TM 3000.

2.2.2 Physical-chemical characterization

Contact Angle is a technique often used to study the hydrophobic/hydrophilic behavior of the film materials. With the static drop method, the angle formed between the liquid–solid interface and the liquid–vapor interface is the contact angle that characterizes the nature of the sample.

The Ossila Contact Angle Goniometer was used in Chapter 9, to measure the contact angle of each sample over time (3 experiments per sample). Drops of Mili-Q water were deposited on each sample (10 μL/drop) and the evolution of the contact angle over time was measured.

Fourier transform infrared spectroscopy in attenuated total reflectance mode (FTIR-ATR) is a technique that provides information in relation to the chemical structure and molecular conformation of the materials at a molecular level.

FTIR-ATR measurements (Chapters 3-5, 7-10) were performed at room temperature in a Thermo Nicolet Nexus 670 in attenuated total reflectance (ATR) mode from 4000 to 400 cm^{-1}, using 64 scans at a resolution of 4 cm^{-1}. From the FTIR-ATR spectra, the electroactive β-phase content of the PVDF-based samples was evaluated using **equation 2.1**:

$$F(\beta) = \frac{A_\beta}{\left(K_\beta / K_\alpha\right)\left(A_\alpha + A_\beta\right)} \quad (2.1)$$

Where A_α and A_β are the absorbances at 766 and 840 cm^{-1}, respectively, and K_α and K_β are the corresponding absorption coefficients (6.1×10^4 and 7.7×10^4 $cm^2 mol^{-1}$) [5].

Small angle neutron scattering (SANS) uses elastic neutron scattering at small scattering angles to investigate the structure of various substances at a mesoscopic scale of about 1–100 nm.

In Chapter 4, SANS experiments were performed in the small-angle spectrometer YuMO at the IBR-2 pulsed reactor (JINR, Dubna, Russia) in the time-of-flight mode [29]. The differential cross section per sample volume (scattering intensity) was obtained as a function of the scattering vector module, $q=(4\pi/\lambda)\sin(\theta/2)$, where λ is the incident neutron wavelength and θ is the scattering angle. SANS curves were obtained using a wavelength range of λ=0.05÷0.8 nm. The absolute calibration of the scattered intensity was carried out by using vanadium standard and raw data were averaged using the SAS program [30]. The analysis of the SANS data was performed using SasView software [SasView version 5.0, http://www.sasview.org/].

2.2.3 Thermal characterization

Differential scanning calorimetry (DSC) is used to determine thermal events related to phase transitions such as, glass transitions temperature (T_g), melting temperature (T_m) and crystallisation temperature (T_c), which provides an insight in the materials operating temperatures as well as on the crystallinity of the materials.

DSC measurements were performed in a Perkin-Elmer DSC 8000 apparatus between 30 and 200 °C using a heating rate of 10 °C.min^{-1} under nitrogen purge. The degree of crystallinity (Xc) of each P(VDF-TrFE)-based sample was evaluated using **equation 2.2** [6]:

$$\chi_c = \frac{\Delta H_f}{\Delta H_{100}} \times 100 \quad (2.2)$$

where ΔH_f is the melting enthalpy of the sample and ΔH_{100} is the melting enthalpy for a 100% crystalline sample (ΔH_{100} = 103.4 J.g^{-1} for P(VDF-TrFE) [6]).

Similarly, for PVDF-based samples, the degree of crystallinity (X_c) of the samples was calculated using **Equation 2.3** [7]:

$$X_c = \frac{\Delta H}{x\Delta H_\alpha + y\Delta H_\beta} \quad (2.3)$$

where ΔH is the polymer melting enthalpy, ΔH_α and ΔH_β are the melting enthalpies of pure α and β phase PVDF, being 93.07 J g^{-1} and 103.4 J g^{-1} respectively, and x and y are the α- and β-phase contents of each sample [8], calculated from the FTIR spectra.

In Chapter 9, for the PUA composite, DSC was measured under nitrogen atmosphere in two successive scans from -50 to 250 °C at 20 °C.min^{-1} in the first scan and from -50 to 150°C at 20 °C.min^{-1} in the second scan (DSC 822e, Mettler Toledo). The cooling process between the first and second scans, from 250 °C to -50 °C was made with a cooling rate of 20 °C.min^{-1}. The glass transition temperature was obtained as the extrapolated endset of the baseline shift in both heating processes. In addition, the water absorption capability of the samples was also evaluated in the first scan. Additionally, the effect of the introduction of the IL within the polymer in the UV curing process was quantified by photo-differential scanning calorimetry (photo-DSC) using a DSC 2920 Modulated DSC equipment coupled to a differential photocalorimetry from TA Instruments®. All samples were irradiated with UV light at room temperature for 5 minutes while the heat flow was measured. The results were normalized by the weight of the photoresin included in each sample, which depends on the IL content within them.

The C=C double bonds conversion (C(α)) was obtained according to **Equation 2.4** [9]**:**

$$C(\alpha) = \frac{\Delta H_t}{\Delta H_0^{theor}} \quad (2.4)$$

where ΔH_t is the enthalpy at time t (calculated from the integration of the area under the peak of the DSC curves), and ΔH_0^{theor} is the theoretical enthalpy for the full conversion; both in J/g. Due

to fact that a commercial photoresin was used, the enthalpy of the pure resin after complete UV cure was considered as the theoretical enthalpy for total conversion [10, 11][11,45].

The photopolymerization rate (R_p) was obtained applying **Equation 2.5**:

$$R_p = \frac{dC(\alpha)}{dt} = \frac{dH/dt}{\Delta H_0^{theor}} \quad (2.5)$$

Thus, the maximum photopolymerization rate (R_p^{max}) and the time to reach R_p^{max}, named t^{max}, were obtained.

Thermogravimetric analysis (TGA) is a technique that measures the mass loss profile as a function of time for a specific temperature, or vice versa, under a controlled atmosphere. This thermal analysis technique can be used not only to evaluate the thermal stability of the materials, but also the moisture absorption and the amount of organic and inorganic compounds and residues.

TGA was used to study the thermal degradation of the samples using a Mettler Toledo TGA/SDTA 851e apparatus operating between and 800 °C. For experiments, the samples were placed in α-Al_2O_3 sample holders, and the measurements were performed at a heating rate of 10 °C min^{-1} under nitrogen atmosphere.

2.2.4 Optical characterization

Ultraviolet-visible (UV-Vis) spectroscopy is a technique whose wavelengths are in the ultraviolet (100–400 nm), visible (400–750 nm) and near infrared (750–1400 nm) range, allowing to quantitatively measure the materials transparency at those wavelengths.

In chapter 9, the thermochromic response was investigated by ultraviolet–visible (UV-Vis) spectroscopy as a function of temperature. UV–Vis spectra were recorded with an Agilent Cary 60 UV/vis spectrophotometer with an external temperature controller. The spectra were obtained in the range of 300-800 nm, with a resolution of 1 nm, from 30 to 70 °C (temperature range in which sample colour changes) every 5 °C after 2 min stabilization before each measurement. Further, the effect of temperature and relative humidity (RH) variation on the colour of the films was measured within a climate chamber Challenge 250E from ACS Company by recording photographs while RH and temperature were varied. This analysis was carried out for the IL/PUA

sample (2.5 x 2.5 cm square) with 20 wt.% IL content. In order to obtain the blue (dehydrated) initial state, the sample was kept at 70 °C for 5 minutes, while for the colourless (hydrated) state, the sample was kept under ambient conditions during 24 hours.

2.2.5 Mechanical characterization

Uniaxial tensile tests are carried out to study the materials behaviour under mechanical stimulation. Particularly stress-strain measurements are performed to explore the materials mechanical nature before deformation and/or breakage when in use. With such measurements different properties can be obtained such as, Young's modulus or elasticity modulus (E), maximum tensile stress or yield stress (σ_y), and elongation at break (ε_b), which are dependent on the temperature, applied forces, and the speed of deformation [12].

Mechanical tests, in Chapters 7 and 9, in the tensile mode were carried in a universal testing machine (Shimadzu model AG-IS) at room temperature using a load cell of 50 N. Rectangular shaped (30 x 10 mm) samples with thicknesses ranging from ~22 μm to ~150 μm were analyzed at a test velocity of 10 mm/min.

Mechanical stress-strain curves (Chapters 8 and 10) were obtained with a TST350 tensile testing set up from Linkam Scientific Instruments using a strain rate of 15 $\mu m.s^{-1}$. All experiments were performed at room temperature.

2.2.6 Electrical characterization

Volume electrical conductivity allows to measure the materials capacity for electric current conduction.

The DC electrical conductivity of the samples was obtained using a Keithley 6430 picoammeter/voltage source. Previous to the measurements, the samples were prepared in the form of a parallel plate condenser with circular gold electrodes of 5 mm diameter deposited by magnetron sputtering (Polaron SC502). The volume electrical conductivity was obtained at room temperature by the characteristic I-V curves in the -10 to 10 voltage range. The DC electrical conductivity (σ) of the polymer-based composites, was calculated from the slope of the I-V curves taken into consideration the geometrical factors of the samples, according to **Equation 2.6**:

$$\sigma = {}^{1}\Big/\left({}^{RA}\Big/_{L}\right) \tag{2.6}$$

where R is the electrical resistance, L the sample thickness and A the area of the electrodes.

Ionic conductivity represents the materials electrical conductivity due to ionic charge motion.

In chapters 7 and 8, electrochemical impedance spectroscopy (EIS) measurements were performed using an Autolab PGSTAT 12-30 device between 25 °C and 100 °C by varying the frequency between 0.5 mHz and 1MHz. The ionic conductivity was measured by placing the sample between two gold electrodes inside a Buchi TO-51 oven and was calculated according to the following equation [13]:

$$\sigma_i = \frac{d}{R_b * A} \tag{2.7}$$

where, d is the thickness, R_b is the bulk resistance and A is the area of the film.

Similar to Chapter 8, the ionic conductivity of the different IL/carrageenan samples (Chapter 10) was determined at frequencies between 500 mHz and 65 kHz and a temperature range from 25 to 70 °C and σ was obtained after **equation 2.7.**

2.2.7 Magnetic characterization

Vibrating sample magnetometer (VSM) device is used to measure the magnetic properties of magnetic materials. From such measurements, typically a magnetic hysteresis loop is obtained from the applied external magnetic field (H) vs sample magnetization (M).

The magnetic behavior of the MIL and corresponding composites, in Chapters 3 and 5, was measured at room temperature using a Quantum Design's MPMS 3 superconducting quantum interference device (SQUID) from -20 kOe to 20 kOe.

In Chapter 7, room-temperature magnetic hysteresis loops were measured from – 20000 Oe to 20000 Oe using a Microsenses ADE 3473-70 Technologies VSM

The magnetic response, in chapter 8, of the IL/PVDF composites was obtained with a Micro-Sense EZ7 VSM, by measuring room temperature hysteresis loops from -6.0 kOe to 6.0 kOe.

2.3 References

1. Nunes-Pereira, J., et al., *Poly(vinylidene fluoride) and copolymers as porous membranes for tissue engineering applications.* Polymer Testing, 2015. **44**: p. 234-241.
2. Chongmin, Z., et al., *Syntheses, Structures, and Properties of a Series of Metal Ion-Containing Dialkylimidazolium Ionic Liquids.* 2007. **80**(12): p. 2365-2374.
3. Meredith, M.B., et al., *Ambient temperature imidazolium-based ionic liquids with tetrachloronickelate(II) anions.* Polyhedron, 2009. **28**(12): p. 2355-2358.
4. Zhong, C., et al., *Syntheses, structures, and properties of a series of metal ion-containing dialkylimidazolium ionic liquids.* Bulletin of the Chemical Society of Japan, 2007. **80**(12): p. 2365-2374.
5. Correia, D., et al., *Magnetic ionic liquid/polymer composites: Tailoring physico-chemical properties by ionic liquid content and solvent evaporation temperature.* Composites Part B: Engineering, 2019. **178**: p. 107516.
6. Nunes-Pereira, J., et al., *Li-ion battery separator membranes based on poly(vinylidene fluoride-trifluoroethylene)/carbon nanotube composites.* Solid State Ionics, 2013. **249**: p. 63-71.
7. Fernandes, L.C., et al., *Ionic-Liquid-Based Printable Materials for Thermochromic and Thermoresistive Applications.* ACS Applied Materials & Interfaces, 2019. **11**(22): p. 20316-20324.
8. Martins, P., A.C. Lopes, and S. Lanceros-Mendez, *Electroactive phases of poly(vinylidene fluoride): Determination, processing and applications.* Progress in Polymer Science, 2014. **39**(4): p. 683-706.
9. Llorente, O., et al., *Study of the crosslinking process of waterborne UV curable polyurethane acrylates.* Progress in Organic Coatings, 2016. **99**: p. 437-442.
10. Mendes-Felipe, C., et al., *Stimuli responsive UV cured polyurethane acrylated/carbon nanotube composites for piezoresistive sensing.* European Polymer Journal, 2019. **120**: p. 109226.
11. Mendes-Felipe, C., et al., *UV curable nanocomposites with tailored dielectric response.* Polymer, 2020. **196**: p. 122498.
12. Davis, J.R., *Tensile Testing, 2nd Edition*. 2004: ASM International.
13. Correia, D., et al., *All printed soft actuators based on ionic liquid/polymer hybrid materials.* Applied Materials Today, 2021. **22**: p. 100928.

3 Magnetic Ionic liquid/polymer composites: Tailoring physico-chemical properties by ionic liquid content and solvent evaporation temperature

MIL/polymer composites show great potential regarding the development of sensors and actuators. However, a better understanding of the composites fundamental properties is needed in order to improve and adapt to the envisioned application. This chapter presents the study of the influence of IL content and solvent evaporation temperature in the P(VDF-TrFE)/[Bmim][$FeCl_4$] composites morphological, physical-chemical, thermal and magnetic properties.

This chapter is based on the following publication: Correia, D.M., Fernandes, L.C., García-Astrain, C., Tariq, M., Esperança, J.M.S.S., de Zea Bermudez, V., Lanceros-Méndez, S., *Magnetic ionic liquid/polymer composites: Tailoring physico-chemical properties by ionic liquid content and solvent evaporation temperature.* Composites Part B: Engineering, 2019. **178**: p.107516

3.1 Introduction

Smart materials are materials with the ability to adapt to different surrounding conditions by changing their intrinsic properties upon application of an external stimuli, such as stress, temperature, pH, electromagnetic fields, among others [1].

Recently, a great interest has been devoted to MILs such as [Bmim][$FeCl_4$] [2]. The major advantage of MILs is associated with their ability to respond to an external magnetic field upon incorporation of magnetic constituents, such as, transition (iron and cobalt) or rare earth metal ions [3-6].

Composites based on MILs and EAPs [7] allow the development of an entirely new class of electroactive smart materials combining highly polar matrices with ionic mobile species [8], and exhibiting suitable magnetic, electric, mechanical and electromechanical properties [9]. Different IL/polymer composites have been developed targeting different fields, such as biomedicine, and sensor and actuator applications [10]. However, to the best of our knowledge, few studies have been reported on the development of composites combining piezoelectric polymers with MILs [11-13].

In this work, magnetically responsive P(VDF-TrFE)/[Bmim][$FeCl_4$] composites were synthesized by solvent casting. The composites were prepared at different solvent evaporation temperatures (room temperature, 90 and 210 °C) and various MIL concentrations (10, 20 and 40 wt. %). The morphology, physical-chemical and thermal properties were evaluated. The magnetic properties of all composites were also analysed.

3.2 Experimental section

3.2.1 Preparation of the composite films

P(VDF-TrFE) was dissolved in dimethylformamide (DMF) in a ratio of 15/85 wt. % under mechanical agitation at room temperature. After complete dissolution of the polymer, different contents of the [Bmim][$FeCl_4$] MIL (10, 20 and 40 % wt. %) were added to the solution. P(VDF-TrFE)/[Bmim][$FeCl_4$] films with a thickness of ≈50 μm were obtained after spreading the solution at room temperature on a clean glass substrate, followed by solvent evaporation at different

temperatures (room temperature, 90 and 210 °C in an air oven). The study of effect of the solvent evaporation temperature was performed for composites with 40 wt. % of MIL.

3.2.2 Sample characterization

The structure of the P(VDF-TrFE)/[Bmim][$FeCl_4$] films was examined through SEM analysis. The FTIR-ATR, DSC, and TGA techniques were employed to assess their physical-chemical and thermal properties. Additionally, the magnetic behavior was investigated using the VSM technique. Detailed information on the experimental conditions can be referenced in chapter 2.

3.3 Results and discussion

3.3.1 Morphological characterization

To evaluate the influence of the solvent evaporation temperature on the morphology of the composites, samples with the highest content of MIL (40 wt. %) were analysed by SEM (**Figure 3.1**).

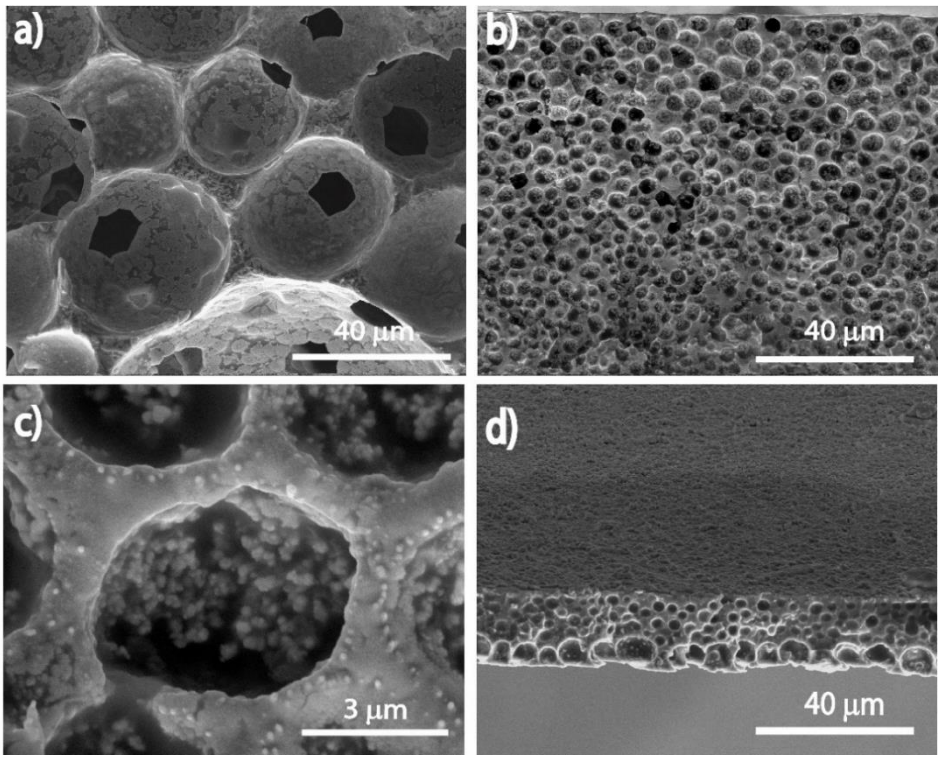


Figure 3.1 - SEM images of the P(VDF-TrFE)/[Bmim][$FeCl_4$] composite films with 40 wt. % of MIL prepared at different solvent evaporation temperature: room temperature (a), 90 °C (b) and (c), and 210 °C (d).

Figure 3.1 shows that the preparation of the composites at different evaporation temperatures led to different porous structures with different pore size and degree of porosity. **Figure 3.1a** allows observing that when the solvent evaporation occurs at room temperature, the P(VDF-TrFE)/[Bmim][$FeCl_4$] composites present the characteristic porous structure of β-P(VDF-TrFE) crystalline phase originating from the spinodal liquid-liquid phase separation [14] with a porous mean dimeter of 36 ± 7 μm. The presence of the MIL within the polymer matrix and in its walls is also detected. The number of interconnected pores increases, and the size of the pores decreases with an increase in the solvent evaporation temperature. For a solvent evaporation temperature of 90 °C a higher number of porous with a mean diameter of 4.2 ± 0.9 μm can be observed. Under these conditions the MIL is entrapped in the polymer matrix and in and out of the pores of the polymer matrix (**Figure 3.1b-c**).

The same tendency is observed for the P(VDF-TrFE)/[Bmim][$FeCl_4$] composites obtained at a solvent evaporation temperature of 210 °C. Generally, at this temperature the P(VDF-TrFE) polymer chains acquire the necessary mobility to occupy the free space left by solvent evaporation, leading to a more compact structure [11, 15]. It is also noticed that the pore sizes decrease (mean diameter of 2.6±0.6 μm) with increasing solvent evaporation temperature from 90 to 210 °C. This result indicates that the inclusion of the MIL into the polymer matrix induces the observed porosity, the number of pores being thus associated with the solvent evaporation temperature. When the solvent starts to evaporate, the MIL is encapsulated in the P(VDF-TrFE) polymer structure since it tends to move to the space previously occupied by DMF [11].

A more compact structure is formed when the solvent evaporation increases because a higher amount of MIL is encapsulated inside to the polymer matrix. This induced us to study in further detail the effect of MIL content in the polymer matrix in composites in which the solvent evaporation occurred at 210 °C.

3.3.2 Physical-chemical characterization

The influence of the solvent evaporation temperature and [Bmim][$FeCl_4$] content on the chemical properties of P(VDF-TrFE) was evaluated by FTIR-ATR measurements.

Figure 3.2 shows the FTIR-ATR spectra of the P(VDF-TrFE)/[Bmim][$FeCl_4$] composites obtained at different solvent evaporation temperatures with an IL content of 40 wt. % (**Figure 3.2a**) and with different MIL contents (**Figure 3.2b**).

The bands at 1432 and 1398 cm^{-1} are assigned to the bending and wagging vibrational modes of CH_2, and to the symmetric stretching vibration of C-C group, respectively [16]. The bands at approximately 1171, 882, 842, 502, 465 and 411 cm^{-1} can be assigned to the stretching vibration of the group CF_2. The feature at 842 cm^{-1} is the band assigned to the β-phase of the polymer [16]. No other polymer characteristic phases were observed since, it is known that for solvent evaporation temperatures up to 80 °C, the chain entanglements of the polymer chain lead to an oriented packing of CH_2–CF_2 dipoles promoting the nucleation of the β-phase [17].

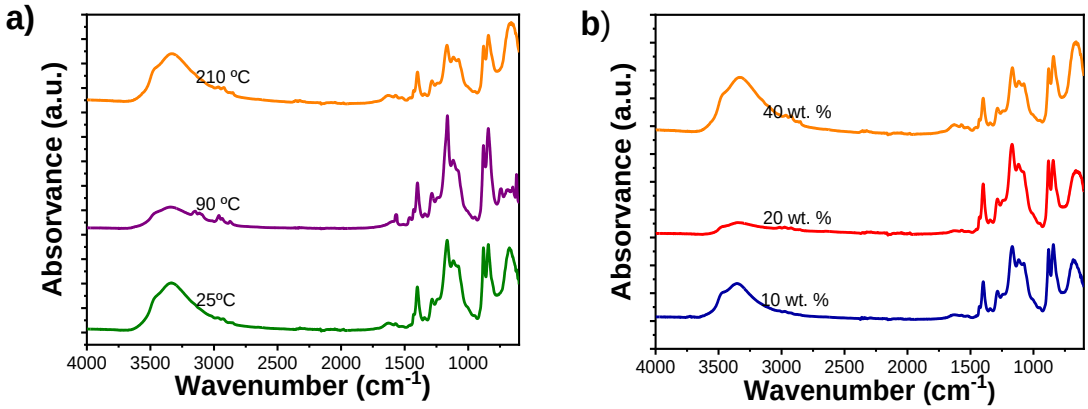


Figure 3.2 – FTIR-ATR spectra for the P(VDF-TrFE)/[Bmim][$FeCl_4$] composites obtained at different solvent evaporation temperatures with 40 wt. % of MIL (a) and with different MIL contents at 210 °C (b).

The FTIR-ATR spectra of **Figure 3.2a and b** demonstrate that the main characteristics absorption bands of the P(VDF-TrFE) are not suppressed after the incorporation of the MIL. It is also possible to conclude from these spectral data that, independently of the solvent evaporation temperature and IL content, the P(VDF-TrFE)/[Bmim][$FeCl_4$] composites crystallize mainly in the ferroelectric β-phase. This finding is in perfect agreement with the fact that, no matter the processing method, P(VDF-TrFE) crystallizes in the electroactive β-phase for PVDF contents ranging from 50 to 80 % [10]. The absorption bands observed in the composites at approximately 3150, 3110, 1162, 638, and 613 cm^{-1} are assigned to aromatic C-H vibrations of the $[Bmim]^+$ cations [18]. The bands at 2961, 2932, 1459, 829, and 736 cm^{-1} are assigned to aliphatic C–H

vibrations of the $[Bmim]^+$ cations [18]. The C–C and C–N stretching vibrations of $[Bmim]^+$ are found at 1564 cm^{-1} [18].

Figure 3.2b reveals that, as expected, the intensity of the characteristic absorption bands of [Bmim][$FeCl_4$] increases with the increase of MIL content. Furthermore, it is also possible to detect a decrease in the intensity of absorption bands characteristic of the P(VDF-TrFE) polymer. These results indicate a very weak chemical interaction between P(VDF-TrFE) and [Bmim][$FeCl_4$], suggesting the occurrence of physical interactions.

3.3.3 Thermal characterization

The DSC thermograms of the P(VDF-TrFE)/[Bmim][$FeCl_4$] composites obtained at different temperatures and with different MIL contents are shown in **Figure 3.3**.

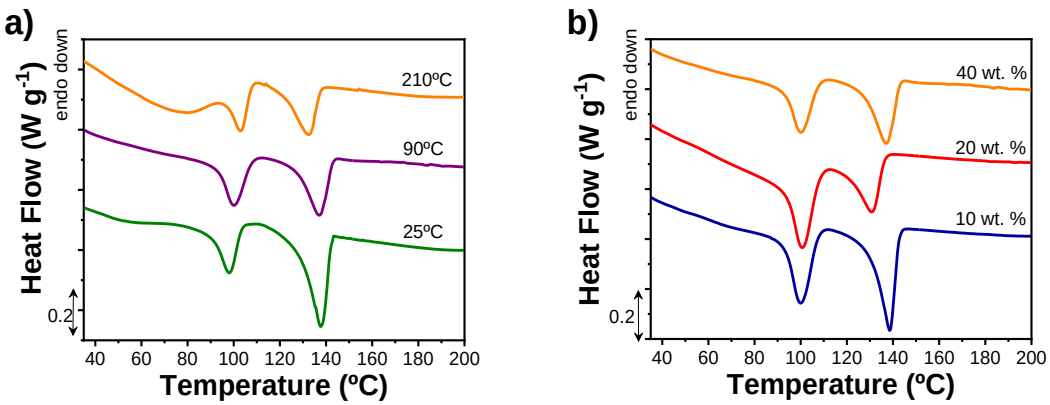


Figure 3.3 - DSC thermograms of the P(VDF-TrFE)/[Bmim][$FeCl_4$] composites obtained at different solvent evaporation temperatures and a MIL content of 40 wt. % (a) and with different contents of MIL (b).

As expected, two endothermic peaks are observed in the composites. The lower temperature peak centred around 93 °C corresponds to the ferroelectric-paraelectric phase transition (Curie temperature, T_c) and the higher temperature peak centred between 120 and 145 °C corresponds to the melting temperature (T_m) of the polymer [19].

As shown in **Table 3.1**, the incorporation of [Bmim][$FeCl_4$] into the P(VDF-TrFE) matrix promotes a slight shift of T_c to lower temperatures and a larger decrease in the Tm value with respect to the pure copolymer, being both nearly independent of the IL content. Both shifts are indicative of

the miscibility and compatibility between the polymer chains and the MIL [20] as well as on the destabilization of the ferroelectric and crystalline phases due to the defects introduced by the filler.

Table 3.1 - Relevant thermal parameters for pristine P(VDF-TrFE) and for the polymer within the P(VDF-TrFE)/[Bmim][$FeCl_4$] composites.

		T_c (ºC)	T_m (ºC)	$\chi_c \pm 3$ (%)
P(VDF-TrFE)		105[15]	150[15]	28[21]
P(VDF-TrFE)/[Bmim][$FeCl_4$]				
Solvent evaporation temperature	25 °C	98	137	16
	90 °C	103	132	24
	210 °C	100	137	20
MIL content (solvent evaporation at 210ºC)	10 wt. %	100	138	18
	20 wt. %	100	131	12
	40 wt. %	100	137	20

The influence of the temperature and MIL content on the Xc value of the P(VDF-TrFE) within the samples was determined from the DSC curves using **Equation 2.2** (**Table 3.1**).

Table 3.1 reveals that the degree of crystallinity of the samples is significantly lower for the composite samples, indicating that the [Bmim][$FeCl_4$] acts as defect during the crystallization process. The addition of [Bmim][$FeCl_4$] changes the nucleation process inducing a growth in its kinetics, which leads to a defective crystallization of the P(VDF-TrFE) at the zones in contact to the MIL [11]. It is to notice that this effect is nearly independent of IL content or solvent evaporation temperature. The crystallization process around 90 °C leads to slightly higher degrees of crystallinity, when compared to the other crystallization temperatures. This effect may be related to proximity of the ferroelectric-paraelectric transition that occurs near this temperature, modifying the crystallization energetic landscape [22, 23].

Figure 3.4 shows the TGA curves and the 1st derivate (DTG) curves of the P(VDF-TrFE)/[Bmim][$FeCl_4$] composite films. For all composites the weight loss is a multi-stage process.

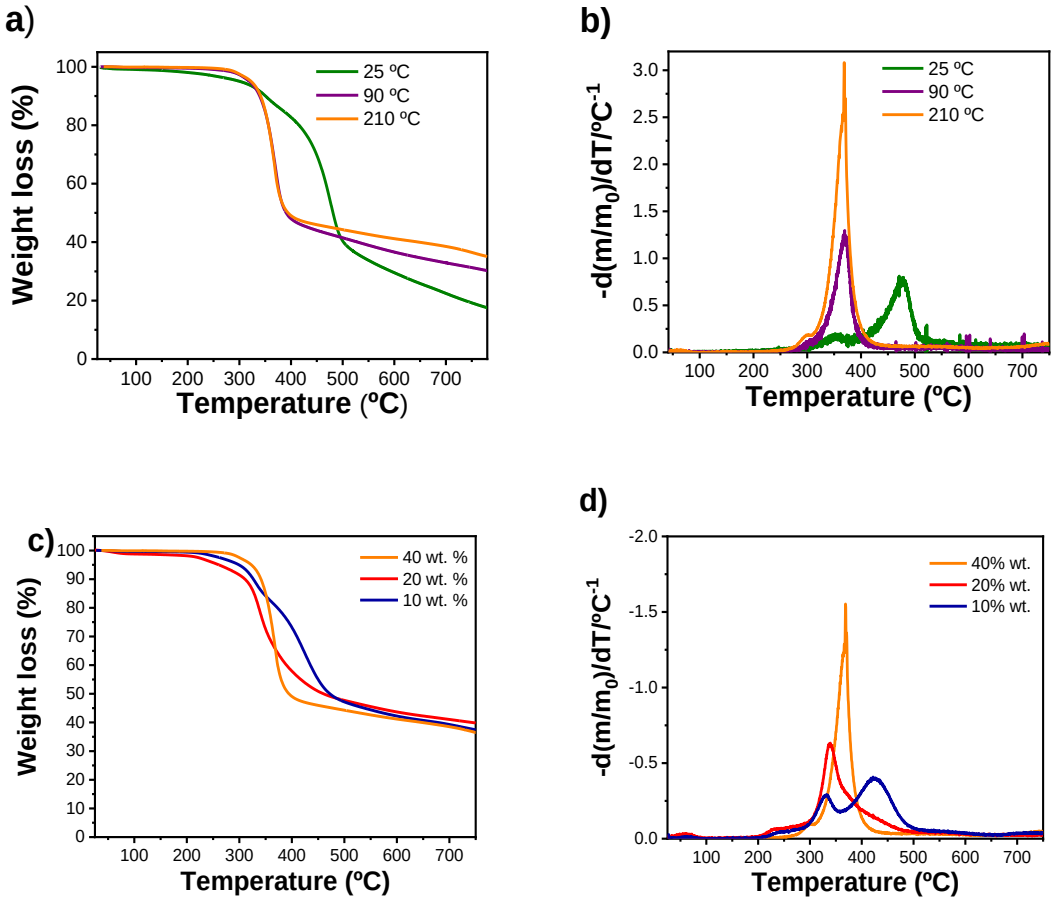


Figure 3.4 - TGA (a,c) and DTG (b,d) curves of the P(VDF-TrFE)/[Bmim][$FeCl_4$] composites for: different solvent evaporation temperatures with 40 wt % of MIL (a,b); for a solvent evaporation temperatures of 210 °C and different IL contents (c,d).

A sharp weight loss with onset near 300 °C is detected for the P(VDF-TrFE)/[Bmim][$FeCl_4$] composites containing 40 wt. % of the MIL and for which the solvent was evaporated at 90 and 120 °C (violet and orange lines in **Figure 3.4a**, respectively), and also for the composite sample dried at 210 °C and incorporating 40 wt. % of MIL (orange line in **Figure 3.4c**). This thermal event is attributed to the thermal degradation of [Bmim][$FeCl_4$], which is known to thermally decompose in a single step at ~330 °C [18]. During the process the anions thermally decompose through dealkylation, whereas the cations mainly undergo alkyl migration and elimination reactions [24]. In the remaining samples the thermal decomposition starts at lower temperature. This effect is probably due to the progressive loss of occluded DMF (boiling temperature of 150 °C). At temperatures higher than 400-450 °C the degradation of P(VDF-TrFE) and the release of volatile compounds, such as hydrogen fluoride (HF), and small contents of 1,1,2-trifluoro-1,3-butadiene ($C_4H_3F_3$) and 1,2-difluoroethylene ($C_2H_2F_2$) [25], are responsible for

the weight loss observed. At 750 °C, about 30 % of the mass of practically all the samples remained to be thermally decomposed. The exception is the sample dried at room temperature and containing 40 wt. % of MIL, for which the degradation process was more efficient (green line in **Figure 3.4a**).

Figure 3.4c shows that the highest onset temperature was observed at the highest MIL content.

3.3.4 Magnetic properties of the nanocomposites

Figure 3.5 presents the magnetic properties of the composites evaluated from VSM. The variation of magnetization with the applied magnetic field was also evaluated for [Bmim][$FeCl_4$].

The inset of **Figure 3.5a** demonstrates that the IL exhibits a linear correlation with the applied magnetic field. This linear dependence on the magnetic field is also observed for the composites, both with varying IL content and solvent evaporation temperature. This behaviour has already been reported for polymeric ILs and was related to the paramagnetic nature of the materials [26]. The magnetic susceptibility, related with the extent of magnetization of a material in response to a magnetic field, is similar for the samples prepared at room temperature or 90 °C, but increases for samples prepared at 210 °C, which can be related to the more compact structure and improved entrapment/incorporation of the IL within the polymer structure. As expected, the magnetic susceptibility increase is proportional to the IL content, which allows to tune the magnetic response of the polymeric IL composites.

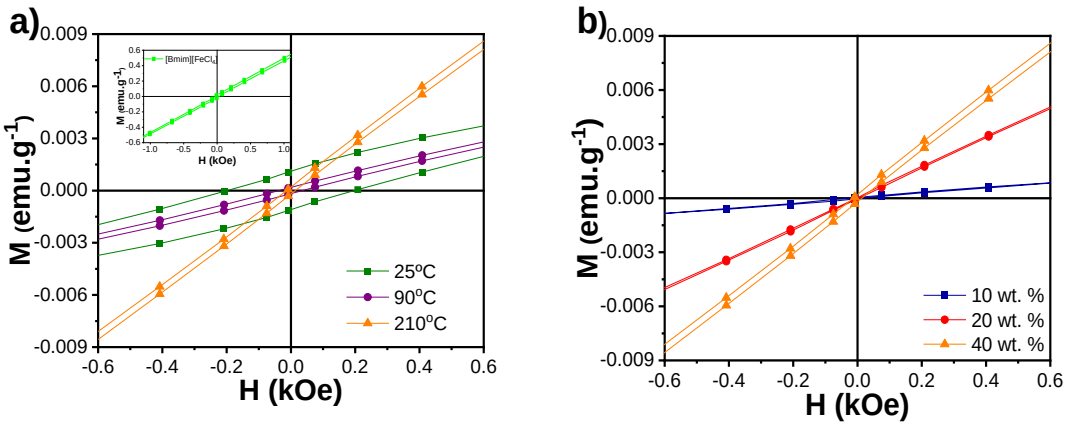


Figure 3.5 - Magnetization of (a) P(VDF-TrFE)/[Bmim][$FeCl_4$] composites obtained at different temperatures for an IL content of 40 wt. % Inset: pure IL [Bmim][$FeCl_4$]; and (b) for the composites with different IL contents as a function of applied magnetic field.

3.4 Conclusions

Magnetic P(VDF-TrFE)/[Bmim][$FeCl_4$] composites were synthesized at different solvent evaporation temperatures and at different [Bmim][$FeCl_4$] contents. The composites morphology is dependent on the evaporation temperature. No changes were detected in the chemical structure of the P(VDF-TrFE) polymer after incorporation of the MIL. The thermal characterization revealed a shift to lower temperatures of both the melting and Curie temperatures, indicating miscibility between the polymer and the MIL. Furthermore, the MIL incorporation led to a decrease in the degree of crystallinity (exceptionally for composites obtained at 90°C) and at high MIL content to an increase of thermal stability, independent of the solvent evaporation temperature used during the composite's preparation. Finally, an increase in the magnetic susceptibility was observed upon increasing IL content and solvent evaporation temperature.

3.5 References

1. Drossel, W.G., et al., *Smart materials for smart production – a cross-disciplinary innovation network in the field of smart materials.* Procedia Manufacturing, 2018. **21**: p. 197-204.
2. Zai-Lai, X. and T. Andreas, *Thermomorphic Behavior of the Ionic Liquids [C4mim][FeCl4] and [C12mim][FeCl4].* ChemPhysChem, 2011. **12**(2): p. 364-368.
3. Zhang, S., et al., *Beyond solvents and electrolytes: Ionic liquids-based advanced functional materials.* Progress in Materials Science, 2016. **77**: p. 80-124.
4. Joseph, A., et al., *Paramagnetic ionic liquids for advanced applications: A review.* Journal of Molecular Liquids, 2016. **218**: p. 319-331.
5. Santos, E., J. Albo, and A. Irabien, *Magnetic ionic liquids: synthesis, properties and applications.* RSC Advances, 2014. **4**(75): p. 40008-40018.
6. Cruz, M.M., et al., *Thermophysical and magnetic studies of two paramagnetic liquid salts: [C4mim][FeCl4] and [P66614][FeCl4].* Fluid Phase Equilibria, 2013. **350**: p. 43-50.
7. Mejri, R., et al., *Effect of anion type in the performance of ionic liquid/poly(vinylidene fluoride) electromechanical actuators.* Journal of Non-Crystalline Solids, 2016. **453**: p. 8-15.
8. Smiglak, M., et al., *Ionic liquids for energy, materials, and medicine.* Chemical Communications, 2014. **50**(66): p. 9228-9250.
9. Ribeiro, C., et al., *Electroactive poly(vinylidene fluoride)-based structures for advanced applications.* Nature Protocols, 2018. **13**(4): p. 681-704.
10. Martins, P., A.C. Lopes, and S. Lanceros-Mendez, *Electroactive phases of poly(vinylidene fluoride): Determination, processing and applications.* Progress in Polymer Science, 2014. **39**(4): p. 683-706.
11. Correia, D.M., et al., *Low-field giant magneto-ionic response in polymer-based nanocomposites.* Nanoscale, 2018. **10**(33): p. 15747-15754.
12. Fernandes, L.C., et al. *Electrospun Magnetic Ionic Liquid Based Electroactive Materials for Tissue Engineering Applications*. Nanomaterials, 2022. **12**, DOI: 10.3390/nano12173072.
13. Fernandes, L.C., et al., *Ionic-Liquid-Based Printable Materials for Thermochromic and Thermoresistive Applications.* ACS Applied Materials & Interfaces, 2019. **11**(22): p. 20316-20324.
14. Nunes-Pereira, J., et al., *Poly(vinylidene fluoride) and copolymers as porous membranes for tissue engineering applications.* Polymer Testing, 2015. **44**: p. 234-241.

15. Gonçalves, R., et al., *Evaluation of the Physicochemical Properties and Active Response of Piezoelectric Poly(vinylidene fluoride-co-trifluoroethylene) as a Function of Its Microstructure.* The Journal of Physical Chemistry C, 2018. **122**(21): p. 11433-11441.
16. Faria, L.O. and R.L. Moreira, *Infrared spectroscopic investigation of chain conformations and interactions in P(VDF-TrFE)/PMMA blends.* Journal of Polymer Science Part B-Polymer Physics, 2000. **38**(1): p. 34-40.
17. Ferreira, J.C.C., et al., *Variation of the physicochemical and morphological characteristics of solvent casted poly(vinylidene fluoride) along its binary phase diagram with dimethylformamide.* Journal of Non-Crystalline Solids, 2015. **412**: p. 16-23.
18. Xie, Z.-L., et al., *Transparent, flexible, and paramagnetic ionogels based on PMMA and the iron-based ionic liquid 1-butyl-3-methylimidazolium tetrachloroferrate(III) Bmim FeCl4.* Journal of Materials Chemistry, 2010. **20**(42): p. 9543-9549.
19. Nunes-Pereira, J., et al., *Li-ion battery separator membranes based on poly(vinylidene fluoride-trifluoroethylene)/carbon nanotube composites.* Solid State Ionics, 2013. **249**: p. 63-71.
20. Leones, R., et al., *Effect of Ionic Liquid Anion Type in the Performance of Solid Polymer Electrolytes Based on Poly (Vinylidene fluoride-trifluoroethylene).* Electroanalysis, 2015. **27**(2): p. 457-464.
21. Nunes-Pereira, J., et al., *A green solvent strategy for the development of piezoelectric poly(vinylidene fluoride–trifluoroethylene) films for sensors and actuators applications.* Materials & Design, 2016. **104**: p. 183-189.
22. Costa, C.M., et al., *Electroactive Poly(Vinylidene Fluoride-Trifluorethylene) (PVDF-TrFE) Microporous Membranes for Lithium-Ion Battery Applications.* Ferroelectrics, 2012. **430**(1): p. 103-107.
23. Legrand, J.F., *Structure and ferroelectric properties of P(VDF-TrFE) copolymers.* Ferroelectrics, 1989. **91**(1): p. 303-317.
24. Zhou, C., et al., *Properties and catalytic activity of magnetic and acidic ionic liquids: Experimental and molecular simulation.* Carbohydrate Polymers, 2014. **105**: p. 300-307.
25. Correia, D.M., et al., *Physicochemical properties of poly(vinylidene fluoride-trifluoroethylene)/poly(ethylene oxide) blend membranes for lithium ion battery applications: Influence of poly(ethylene oxide) molecular weight.* Solid State Ionics, 2014. **268**: p. 54-67.
26. Döbbelin, M., et al., *Synthesis of paramagnetic polymers using ionic liquid chemistry.* Polymer Chemistry, 2011. **2**(6): p. 1275-1278.

4 Structural organization of ionic liquids embedded in fluorinated polymers

Hybrid materials based on ILs and polymers are increasingly being used for the development of smart and multifunctional materials, allowing to tune polymer properties or introduce new ones. Nevertheless, the structural organization of ILs within the polymer matrix is not properly understood. This chapter reports the effect of different imidazolium based ILs incorporated into PVDF films. The obtained results are correlated to the observed variations in the morphological and physical-chemical properties.

This chapter is based on the following publication: Petrenko, V.I., Fernandes, L.C., Ivankov, O.I., Tubio, C.R., Tariq, M., Esperança, J.M.S.S., Correia, D.M., Lanceros-Méndez, S., *Structural organization of ionic liquids embedded in fluorinated polymers.* Journal of Molecular Liquids, 2022. **260:** p.119385

4.1 Introduction

Besides the high interest devoted to the development of IL-polymer based materials, there is a lack of studies concerning the materials characterization at nanoscale. Their characterization is mostly focused on the morphology, physical-chemical, electrical/ionic, and mechanical characterization techniques [1, 2]. The study of the ILs structural organization into the polymer matrix will allow a better understanding of the IL-polymer matrix chain interactions, stability and macroscopic response. In this context, SANS or small-angle X-ray (SAXS) scattering techniques are among the most suitable techniques. In fact, recently SANS and SAXS were successfully used for the detailed structural characterization at the nanoscale of native and modified (by magnetic nanoparticles) woven cotton textiles and different structural organization of nanoparticles were observed [3]. With respect to ILs, SANS studies have been reported, often relying on the study of the solvent and/or IL influence in the polymeric matrix structure/conformation, solvation and dispersion [4-6]. The combination of poly(ethylene glycol) (PEG) and poly (ethylene oxide) (PEO) with imidazolium-based ILs has been studied [6-12]. In particular, the solubility and conformability of PEG in cholinium amino acid-based (glycinate, prolinate and argininate) ([Ch][AA]) ILs and water mixtures was tested and it has been found that the hydrogen bond capacity of the anion plays a key role in the salting out effect of PEG and that the radius of gyration is dependent on the anions species and water concentration [7]. The solvation of PEO in different protic ionic liquids (PILs) was also studied by dissolving PEO in pure propylammonium nitrate (PAN) and PAN with a 10 % mole fraction of propylammonium chloride (PACl) or propylammonium bromide (PABr). A reduction in the solvation quality was observed by the addition of the halide salt in the order PAN>PABr>PACl, as well as an increase in the charge density (NO^{3-} to Br^- to Cl^-), leading to a larger ionic interaction and, therefore, to a poorer solvation [6].

Attending to the previously mentioned and to the lack of studies concerning the IL-polymer interactions and structural organization at a nanoscale, this work reports on hybrid films based on PVDF with different ILs types (different anions and cations), in order to access the influence structural organization of the IL types within the polymer matrices and their effect in the properties of the composites. An IL content of 40 wt. % has been incorporated in the polymer matrix, since higher concentrations lead to mechanically less stable samples and also limits incorporation of IL with the matrix. The morphological and physical-chemical properties of the

developed materials were studied, together with SANS technique, in order to access the composite structure at a nano- and micro-scale.

4.2 Experimental section

4.2.1 Sample preparation

The films were prepared by solvent casting following the general guidelines presented in [13]. For the preparation of the pristine polymer films, after completely PVDF dissolution in DMF (ratio of 15/85 % w/w polymer/solvent) under magnetic stirring at room temperature, the solution was spread into a glass, the solvent was evaporated at 210 °C (P-Selecta model 2000208 oven) during 10 min and let to cool down to room temperature. After this procedure, PVDF crystallizes into the non-polar α-phase [13]. The polymer/IL composites were prepared after a similar procedure: prior to the polymer dissolution, 40 wt. % of the corresponding IL ([Pmim][TFSI]), [Pmpip][TFSI], $[Bmim]_2[NiCl_4]$ or [Bmim][$FeCl_4$]) was dispersed in DMF, under magnetic agitation, until a homogenous solution was obtained. Then, PVDF was added in a ratio of 15:85 wt. % (PVDF/DMF). After polymer dissolution, the solution was spread on a glass at room temperature, the solvent was evaporated at 210 °C for 10 min. For the composites PVDF/$[Bmim]_2[NiCl_4]$, and PVDF/[Bmim][$FeCl_4$], incorporating magnetic IL anions, mechanical agitation was used instead of magnetic agitation. After those procedures, films with 40 wt. % of IL and an average thickness of ~33 μm were obtained.

4.2.2 Sample characterization

The samples' morphology was assessed utilizing the SEM technique, while the chemical characterization of the developed materials was conducted through the FTIR-ATR technique. Analysis of thermal properties was carried out using the DSC and TGA techniques. Furthermore, the structural organization of the samples was investigated using SANS experiments (refer to chapter 2.2.2). Detailed experimental conditions are provided in chapter 2.

4.3 Results and discussion

4.3.1 Morphological features

The morphology of neat PVDF polymers and the corresponding IL based composites is presented in the representative SEM images shown in **Figure 4.1**. The morphology of PVDF and hybrid composites strongly depend on the processing conditions, the obtained morphology being compatible with the used processing conditions of solvent evaporation at 210 °C prior to polymer crystallization [13] PVDF is obtained in the form of compact dense films, as corresponding to the used processing conditions [14].

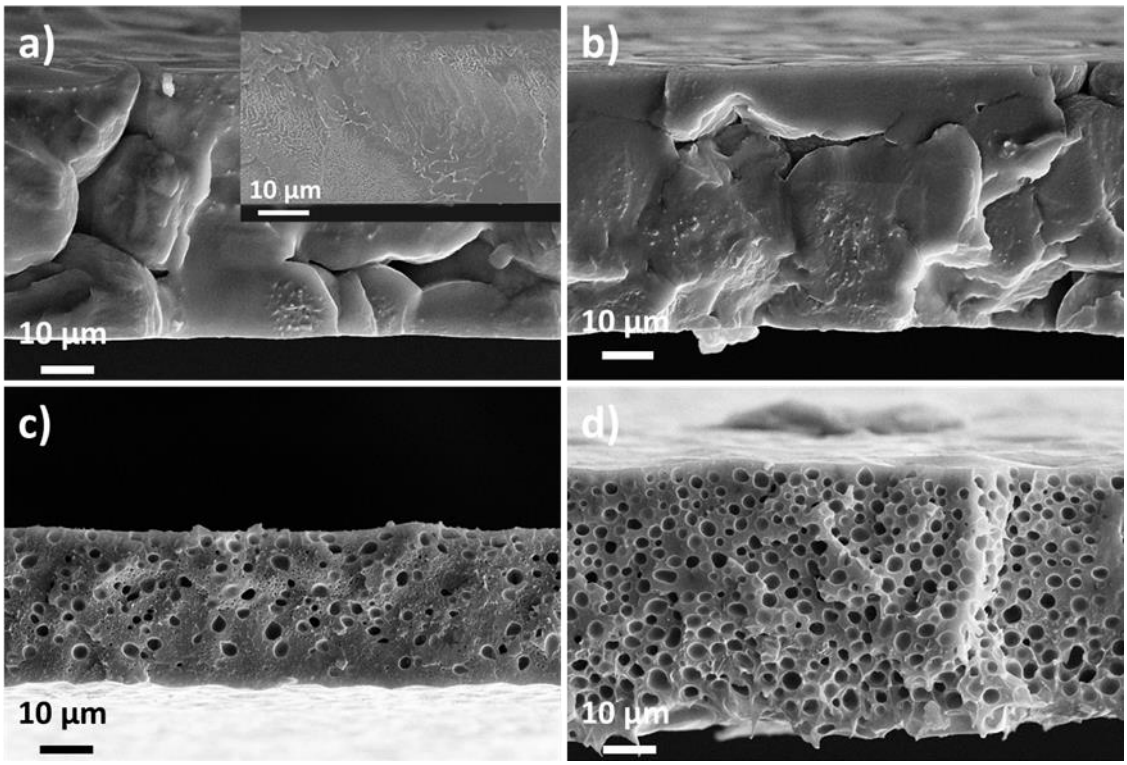


Figure 4.1 - Representative SEM cross-section images of the composite films comprising 40 wt. % of the ILs: a) PVDF/[Pmim][TFSI] (inset: unmodified initial PVDF cross-section film), b) PVDF/[Pmpip][TFSI], c) PVDF/[Bmim][$FeCl_4$] and d) PVDF/$[Bmim]_2[NiCl_4]$.

The films are characterized by a homogeneous and non-porous surface (see inset of **Figure 4.1a**) [13]. Upon the [Pmim][TFSI] and [Pmpip][TFSI] incorporation, PVDF/[Pmim][TFSI] and PVDF/[Pmpip][TFSI] films present a spherulitic structure characteristic of neat PVDF polymer films [15, 16], as shown in **Figure 4.1a and b**, the result being independent of the IL cation type. On the other hand, the incorporation of [Bmim][$FeCl_4$] and $[Bmim]_2[NiCl_4]$ promotes the development of a well-defined porous structure (**Figure 4.1c and d**), which is a characteristic of

magnetic ILs incorporation into PVDF matrix [2]. This porous structure is a consequence of the solvent-IL interactions, leading to a phase separation process. Further, due to the high dipole moment of DMF and the interaction with the IL, once solvent evaporation takes place, the ILs remains encapsulated in the pores left by the migration of the phase-separated solvent + IL [2, 14, 17]. These results are an indicative that the interactions between the solvent and the [Bmim][$FeCl_4$] and [Bmim]$_2$[$NiCl_4$] are stronger than the interactions that occurs with [Pmim][TFSI] and [Pmpip][TFSI].

4.3.2 Physical-chemical and thermal characterization

The influence of the IL type into the vibrational spectra of the PVDF based films was evaluated by FTIR-ATR measurements (**Figure 4.2a**).

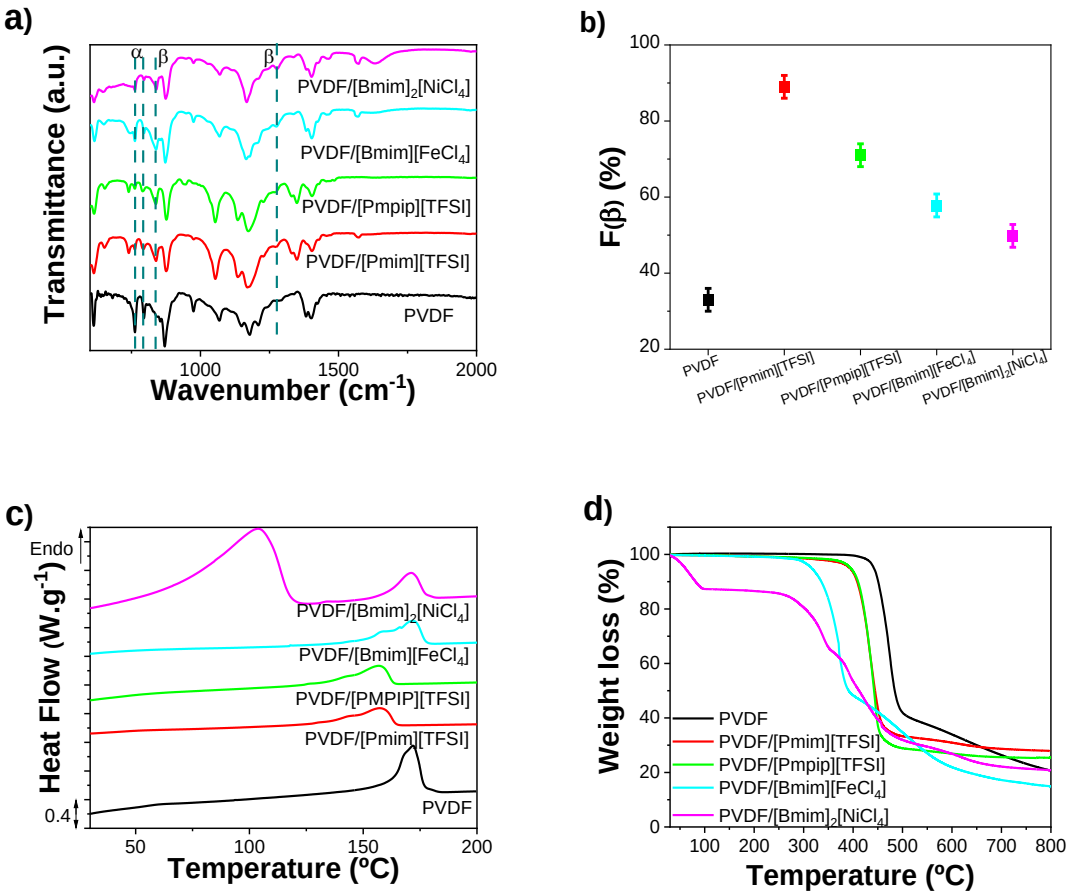


Figure 4.2 - a) FTIR spectra, b) electroactive β-phase content, c) DSC scans and d) TGA curves of the different PVDF/IL film composites: PVDF/[Pmim][TFSI], PVDF/[Pmpip][TFSI], PVDF/[Bmim][$FeCl_4$] and PVDF/[Bmim]$_2$[$NiCl_4$].

The FTIR-ATR spectra of the PVDF and PVDF based composites show the main characteristic PVDF absorption bands, namely the α-phase bands at 795 and 976 cm^{-1}. Additionally, for all samples, the β-phase absorption band is observed at 840 cm^{-1} and 1275 cm^{-1} [16]. It is to notice that, after the selected processing conditions, neat PVDF crystallizes mainly in the α phase (67%) [18]. Upon ILs incorporation into PVDF matrix, and independently of the IL type, an increase in the intensity of the β-phase characteristics absorption bands occur, described as an all-trans (TTT) planar zigzag conformation of PVDF chain, acting ILs as β-phase nucleating agents due to the electrostatic interactions between the PVDF polymer chain with the positive and negative charges from the IL [17]. The β-phase content quantification of all the samples (**Figure 4.2b**) was evaluated **using equation 2.1**. As observed, independently of the IL type, the inclusion of an IL into the PVDF matrix induces the PVDF crystallization majorly in the electroactive β-phase. The highest β-phase content is observed for PVDF/[Pmim][TFSI] composite (89%), followed by the composites PVDF/[Pmpip][TFSI] (71%), PVDF/[Bmim][$FeCl_4$] (58%) and PVDF/$[Bmim]_2[NiCl_4]$ (50%). The observed differences indicate that the interaction between the polymer chains and the IL charges is influenced by the IL type, namely the cation and anion, displaying the [Pmim][TFSI] strong interactions with PVDF polymer chain comparatively with the other ILs. Further, it is also to notice that for the composites comprising the ILs [Bmim][$FeCl_4$] and $[Bmim]_2[NiCl_4]$, the presence of two [Bmim]+ cations in the IL $[Bmim]_2[NiCl_4]$ leads to slight decrease of the electroactive phase as a result of the hinderance of interaction between the CF_2 groups of PVDF with the imidazolium [Bmim]+ charges.

The presence of the IL within the polymer matrix is confirmed by the corresponding absorption bands: For the composites comprising the $[TFSI]^-$ anion, the absorption band present at 740 cm^{-1} is attributed to the cis $[TFSI]^-$ conformation, and at 1135 cm^{-1} and 1149 cm^{-1} due to the asymmetric and symmetric stretching vibration modes from the SO_2 group [19]. For the composites comprising the ILs sharing the same cation $[Bmim]^+$, the absorption band at 1168 cm^{-1} is attributed to the C-N vibration and the skeleton vibrations between 1327 cm^{-1} and 1600 cm^{-1} [20].

The DSC spectra of the composite films are presented in **Figure 4.2c**. Independently of the IL type, the composite films containing PVDF as the polymeric matrix present a single endothermic peak at ~157 °C ascribed to the melting temperature of PVDF [16]. It is also to notice that, independently of the IL type, all the samples show a similar trend, with a single melting peak that

shifts to lower temperatures, when compared with the melting temperature of the pristine PVDF polymer. The decrease in the melting temperature with the incorporation of the ILs indicated a destabilization of the crystalline phase of PVDF as a result of the electrostatic interactions between the different ILs and the PVDF chain, hindering the crystallization process [21].

The influence of the IL type and polymer matrix in the thermal degradation of the samples was evaluated by TGA measurements (**Figure 4.2d**). The thermal degradation of PVDF occurs through C-H and C-F polymer chains decomposition in a single degradation step starting at ~450 °C. Upon ILs incorporation into the PVDF matrix, it is observed that the PVDF composite films with [Pmim][TFSI] and [Pmpip][TFSI] display a single degradation step at ~400 °C with a residual weight of 28 % and 25 %, respectively, associated to the thermal degradation of the polymer [16]. For PVDF/$[Bmim]_2[NiCl_4]$ the first weight loss, is attributed to water loss ascribed to the hydrophilic IL behavior [14]. The degradation step at ~330 °C is attributed to the IL imidazolium cation through dealkylation degradation, finalizing with the PVDF polymer degradation. PVDF/$[Bmim][FeCl_4]$ samples display two degradation steps at ~330 °C and 430 °C associated to the $[Bmim]^+$ and PVDF thermal degradation, respectively [17]. In this context, independently of the IL type, a decrease in the thermal stability of PVDF matrix occurs upon the different ILs incorporation.

4.3.3 Structural organization of the IL within the polymer matrix

Small-angle neutron scattering measurements were conducted for the detailed structural characterization of the polymer-based composites with addition of various ILs as a filler. Experimental SANS curves for all PVDF/IL samples are presented in **Figure 4.3**, showing that all SANS data can be grouped in two categories. SANS from pure film is very low, almost at the background level (data not shown), being not possible to conclude the nanoscale structure of neat PVDF film. The SANS data for PVDF/[Pmim][TFSI] and PVDF/[Pmpip][TFSI] show a scattering plateau at low q-values (reaching so-called Guinier regime [22]) and the PVDF/$[Bmim][FeCl_4]$ and PVDF/$[Bmim]_2[NiCl_4]$ composites show a power-law decay at small q-values, reflecting the presence of large, extended structures with fractal-like organization [23, 24]. SANS curves are thus depending on the IL type, indicating the formation of various structures at the nanoscale. It should be noted that scattering objects for all samples are highly polydisperse, as smoothed curves are observed, which is typical for polydisperse systems, unlike the case of a

highly symmetric system of monodisperse particles, which should give characteristic oscillations [22].

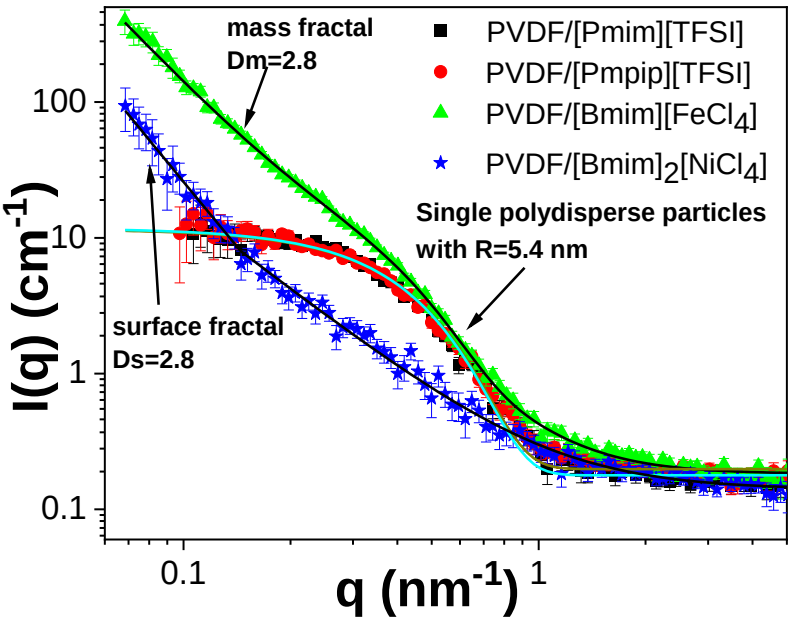


Figure 4.3 - SANS data for polymer-IL based nanocomposties: PVDF/[Pmim][TFSI], PVDF/[Pmpip][TFSI], PVDF/[Bmim][$FeCl_4$] and PVDF/[Bmim]$_2$[$NiCl_4$]. Solid lines are fits according to various structural models.

At sufficiently small q-values (qRg < 1), the scattered intensity can be described by the Guinier approximation [22]:

$$\boldsymbol{I(q) = I(0)exp(-(qRg)^2/3)} \qquad \textbf{(2.1)}$$

with just two parameters, which are the forward scattered intensity, I(0) (which is proportional to the concentration; square of the contrast in scattering length density between matrix and inhomogeneity; and square of the particles volume), and the radius of gyration, Rg (characteristic size of the scattering objects).

The power-law decay of the SANS data was fitted by $I(q)=B\,q^{-p}$ and the value of the P exponent reflects the inner structure of the scattering units and characterizes the type of their mass or surface organization according to the following classification [25]:

$1 < P < 3$; mass fractal with fractal dimension, $D_m = P$.

$3 < P < 4$; surface fractal with fractal dimension, $D_s = 6 - P$.

$4 < P < 6$; diffusive surface with exponent, $b = (P - 4)/2$.

For mass fractal aggregates the following relation between aggregates volume, V, and its linear size, L, is obtained: $V \sim L^{Dm}$. And in the case of surface fractal, the surface, S, is proportional to the linear size as $S \sim L^{Ds}$.

The analysis of the SANS data presented in **Figure 4.3** allow to conclude that only single polydisperse "particles" (strictly speaking nanoinhomogeneities in the polymer matrix) are detected for composites PVDF/[Pmim][TFSI] and PVDF/[Pmpip][TFSI]. The radius of gyration of such particles, Rg = 4.2 nm, are the same for both samples and in case of spherical shape it can be estimated the average radius of such polydisperse spheres as R = 5.4 nm. Thus, some nanoinhomogeneities are identified in the polymer matrix with characteristic size about 5 nm.

At the same time, single highly polydisperse nanoparticles with gyration radius R_g = 4.9 nm and large fractal-type aggregates (mass fractal dimension Dm = 2.74) were observed by SANS for PVDF/[Bmim][$FeCl_4$]. The average radius of single particles for this composite, R = 6.3 nm, is larger than the one obtained for PVDF/[Pmim][TFSI] and PVDF/[Pmpip][TFSI] composites (there we have R = 5.4 nm). More complex and multiscale structures were observed for PVDF/[Bmim]$_2$[$NiCl_4$] composite. Transition from mass fractal (power law exponent P = 2.8 which corresponds to mass fractal dimension $D_m = P = 2.8$) to surface fractal (power law exponent P = 3.2 which corresponds to surface fractal dimension D_s = 6-P = 2.8) is observed for PVDF/[Bmim]$_2$[$NiCl_4$] composites, correspondingly. Complex structural organization of structural units at lower size scale is also observed for such samples. The structural organization of the IL within the PVDF polymer matrix is summarized in **Figure 4.4**.

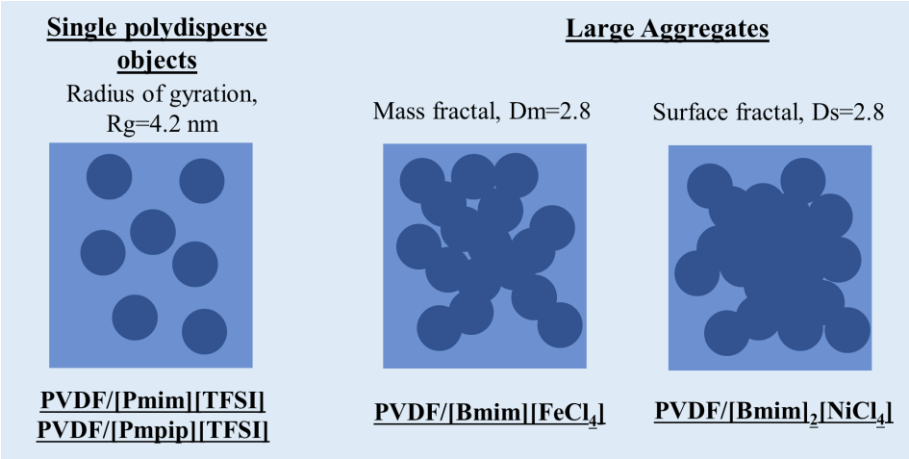


Figure 4.4 - Sketches of the different structural organizations of the IL in: PVDF/[Pmim][TFSI], PVDF/[Pmpip][TFSI], PVDF/[Bmim][$FeCl_4$], and PVDF/$[Bmim]_2[NiCl_4]$.

Thus, the SANS results are in good agreement with the SEM images and macroscales. As observed from SEM images, the composites PVDF/[Pmim][TFSI] and PVDF/[Pmpip][TFSI] do not present a porous structure upon their processing into films. This fact is corroborated from SANS results in which only a single polydisperse objects are observed. The same behavior trend is not observed for the other IL-polymer based composites. Independently of the IL type both [Bmim][$FeCl_4$] and $[Bmim]_2[NiCl_4]$ induce a porous structure, attributed to their structural organization with large aggregates. These results allow to infer that the interaction between these types of ILs with the DMF solvent during the evaporation process is higher when compared with the interaction with the [Pmim][TFSI] and [Pmpip][TFSI], resulting the presence of a porous structure. Thus, different structure organization at nanoscale which affect macroscopic properties of the composites are evidenced in the IL-polymer based films. These results corroborate the reported possible explanations concerning the porous morphology, the influence of ILs into the β-phase content as a result of the strong interactions that occurs during the films processing between the polymer chains, the DMF solvent and the ILs. For this specific fluorinated matrix, the ion-dipole interactions occur through the interaction of the IL cation with the negative CF_2 groups present in PVDF matrix and also from the IL anion interactions with the PVDF holding CH_2 groups holding a positive charge [1, 26]. As briefly discussed, PVDF/[Pmim][TFSI] and PVDF/[Pmpip][TFSI] composites presented the high β contents, indicating that a single dispersion of the IL into the PVDF matrix favors the strong ion-dipole interactions (since the smaller particles size the larger specific surface to interact with environmental medium) between the PVDF chain and the IL charges, and in this sense the crystallinity of the developed materials.

Thus, the present work allows a fundamental understanding of IL-polymer systems, namely the IL-polymer interactions and the structuring of the IL within the polymer matrix, which in turn influences the different material properties such as morphological, physical-chemical, thermal, mechanical, and electrical. It is to notice that, in the last years, the main efforts in this field have been devoted to develop IL-polymer based functional materials with tailored responses based on IL intrinsic characteristics and on the interaction between the polymer matrix and ILs. Based on this strategy, highly efficient materials have been developed for a new generation of applications such as piezo-ionic, and thermochromic, as well as for ionic- conductive materials, among others [1].

Further, polymer-based nanocomposites and, in particular, the ones with the incorporation of ILs also present strong potential for novel application areas. As an example, by tuning the proper IL type and content, the reported variations at the nanostructure and morphology levels can find applications in the area of ferroelectric materials and devices for energy harvesting applications, since pore structure are essential in determining the final electrical properties and in the energy harvesting processes [27-29].

Thus, attending to the future perspectives in the area of IL-polymer based materials, this work emerges as a necessary step in the development of advanced IL-polymer based materials with tailored properties.

4.4 Conclusions

The present work reports on the effect of IL type in the structural, physical-chemical and ILs structural organization into the polymer matrix to a better understanding of the IL-polymer matrix chain interactions, stability and macroscopic response. For this purpose, different composites comprising different ILs were prepared.

The morphology depends both on IL type and IL/polymer/solvent interactions during the solvent evaporation process, displaying the samples comprising the magnetic ILs $[Bmim]_2[NiCl_4]$ and $[Bmim][FeCl_4]$ a porous structure. For IL-PVDF composites, an increase in the electroactive phase content occurs, being independent of the IL type. Additionally, no significant changes were observed in the thermal transitions of the composites, but a decrease in the melting temperature and thermal stability of PVDF matrix occurs upon the different ILs incorporation.

Different structural organization at nanoscale was observed by SANS for studied nanocomposites. Namely, just single polydisperse objects with Rg = 4.2 nm was detected after addition of [Pmim][TFSI] or [Pmpip][TFSI] to PVDF and more complex structures were obtained for the composites PVDF/[Bmim][FeCl4] and PVDF/$[Bmim]_2[NiCl_4]$. Transition from just single polydisperse particles to mass fractal like or to surface like aggregation were concluded when [Pmim][TFSI] or [Pmpip][TFSI] was substituted by $[Bmim]_2[NiCl_4]$ or $[Bmim][FeCl_4]$ during synthesis process. Complex aggregation of particles observed in both PVDF/$[Bmim]_2[NiCl_4]$ and PVDF/$[Bmim][FeCl_4]$ composites indicate a strong interaction between these types of ILs with the DMF solvent during the evaporation process, resulting in the presence of a porous structure. In contrast, [Pmim][TFSI] and [Pmpip][TFSI] promotes strong interactions with PVDF polymer chain as revealed by the higher β phase contents observed for this composite when compared to the composites incorporating $[Bmim]_2[NiCl_4]$ and $[Bmim][FeCl_4]$.

4.5 References

1. Correia, D.M., et al., *Ionic Liquid–Polymer Composites: A New Platform for Multifunctional Applications.* Advanced Functional Materials, 2020. **30**(24): p. 1909736.
2. Correia, D., et al., *Magnetic ionic liquid/polymer composites: Tailoring physico-chemical properties by ionic liquid content and solvent evaporation temperature.* Composites Part B: Engineering, 2019. **178**: p. 107516.
3. Safarik, I., et al., *Cotton Textile/Iron Oxide Nanozyme Composites with Peroxidase-like Activity: Preparation, Characterization, and Application.* ACS Applied Materials & Interfaces, 2021. **13**(20): p. 23627-23637.
4. Yang, M., et al., *Dimethyl sulfoxide assisted dissolution of cellulose in 1-ethyl-3-methylimidazoium acetate: small angle neutron scattering and rheological studies.* Cellulose, 2019. **26**(4): p. 2243-2253.
5. Fedosse Zornio, C., et al., *Ionic PMMA/nanosilica interfaces from grafting ionic liquids under supercritical CO2 conditions.* European Polymer Journal, 2018. **109**: p. 82-92.
6. Stefanovic, R., et al., *Effect of halides on the solvation of poly(ethylene oxide) in the ionic liquid propylammonium nitrate.* Journal of Colloid and Interface Science, 2019. **534**: p. 649-654.
7. Brunner, M., et al., *Conformation of poly(ethylene glycol) in aqueous cholinium amino acid hybrid solvents.* Journal of Colloid and Interface Science, 2021. **602**: p. 334-343.
8. Hashimoto, K., et al., *Ion Gel Network Formation in an Ionic Liquid Studied by Time-Resolved Small-Angle Neutron Scattering.* The Journal of Physical Chemistry B, 2018. **122**(40): p. 9419-9424.
9. Apostolides, D.E., et al., *Near-Model Amphiphilic Polymer Conetworks Based on Four-Arm Stars of Poly(vinylidene fluoride) and Poly(ethylene glycol): Synthesis and Characterization.* Macromolecules, 2018. **51**(7): p. 2476-2488.
10. Kharel, A. and T.P. Lodge, *Coil Dimensions of Poly(ethylene oxide) in an Ionic Liquid by Small-Angle Neutron Scattering.* Macromolecules, 2017. **50**(21): p. 8739-8744.
11. Asai, H., et al., *Structural Analysis of High Performance Ion-Gel Comprising Tetra-PEG Network.* Macromolecules, 2012. **45**(9): p. 3902-3909.

12. Lee, H.-N., et al., *Unusual Lower Critical Solution Temperature Phase Behavior of Poly(ethylene oxide) in Ionic Liquids.* Macromolecules, 2012. **45**(8): p. 3627-3633.
13. Ribeiro, C., et al., *Electroactive poly(vinylidene fluoride)-based structures for advanced applications.* Nature Protocols, 2018. **13**(4): p. 681-704.
14. Fernandes, L.C., et al., *Ionic-Liquid-Based Printable Materials for Thermochromic and Thermoresistive Applications.* ACS Applied Materials & Interfaces, 2019. **11**(22): p. 20316-20324.
15. Silva, M.P., et al., *α- and γ-PVDF: Crystallization kinetics, microstructural variations and thermal behaviour.* Materials Chemistry and Physics, 2010. **122**(1): p. 87-92.
16. Mejri, R., et al., *Effect of anion type in the performance of ionic liquid/poly(vinylidene fluoride) electromechanical actuators.* Journal of Non-Crystalline Solids, 2016. **453**.
17. Fernandes, L., et al., *Highly sensitive humidity sensor based on ionic liquid-polymer composites.* ACS Applied Polymer Materials, 2019.
18. Ribeiro, C., et al., *Electroactive poly(vinylidene fluoride)-based structures for advanced applications.* Nature Protocols, 2018. **13**(4): p. 681-704.
19. Herstedt, M., et al., *Spectroscopic characterization of the conformational states of the bis(trifluoromethanesulfonyl)imide anion (TFSI–).* Journal of Raman Spectroscopy, 2005. **36**(8): p. 762-770.
20. Yassin, F.A., et al., *Highly effective ionic liquids for biodiesel production from waste vegetable oils.* Egyptian Journal of Petroleum, 2015. **24**(1): p. 103-111.
21. Correia, D.M., et al., *Ionic Liquid Cation Size-Dependent Electromechanical Response of Ionic Liquid/Poly(vinylidene fluoride)-Based Soft Actuators.* The Journal of Physical Chemistry C, 2019. **123**(20): p. 12744-12752.
22. Feigin, L. and D.I. Svergun, *Structure analysis by small-angle X-ray and neutron scattering*. Vol. 1. 1987: Springer.
23. Tomchuk, O.J.U.J.o.P., *The Concept of Fractals in the Structural Analysis of Nanosystems: A Retrospective Look and Prospects.* 2020. **65**(8): p. 709-709.
24. Tomchuk, O.V., M.V. Avdeev, and L.A. Bulavin, *Modeling fractal aggregates of polydisperse particles with tunable dimension.* Colloids and Surfaces A: Physicochemical and Engineering Aspects, 2020. **605**: p. 125331.
25. Schmidt, P.W.J.J.o.A.C., *Small-angle scattering studies of disordered, porous and fractal systems.* 1991. **24**(5): p. 414-435.
26. Correia, D., et al., *All printed soft actuators based on ionic liquid/polymer hybrid materials.* Applied Materials Today, 2021. **22**: p. 100928.
27. Zhang, Y., et al., *Ferroelectret materials and devices for energy harvesting applications.* Nano Energy, 2019. **57**: p. 118-140.
28. Mahanty, B., et al., *An effective flexible wireless energy harvester/sensor based on porous electret piezoelectric polymer.* Materials Chemistry and Physics, 2017. **186**: p. 327-332.
29. Ghosh, S.K., et al., *Self-poled Efficient Flexible "Ferroelectretic" Nanogenerator: A New Class of Piezoelectric Energy Harvester.* Energy Technology, 2015. **3**(12): p. 1190-1197.

5 Design of ionic liquid based hybrid polymer materials with magnetoactive and electroactive multifunctional response

Multifunctional materials with sensor and actuator capabilities play an increasing important role in modern technology. In this chapter, hybrid materials with magnetic sensing and an electromechanical actuator response based on magnetic ILs and PVDF have been developed. MILs comprising different cation alkyl chain lengths $[C_nmim]^+$ and sharing the same anion $[FeCl_4]^-$ were incorporated into the PVDF matrix and the morphological, physical, chemical, and functional (MI and electromechanical response) properties of the materials were evaluated.

This chapter is based on the following publication: Fernandes, L.C., Correia, D.M., Fernández, E., Tariq, M., Esperança, J.M.S.S., Lanceros-Méndez, S., *Design of ionic-liquid based hybrid polymer materials with magnetoactive and electroactive multifunctional response.* ACS Applied Materials & Interfaces, 2020. **12**: p.42089–42098

5.1 Introduction

ME responsive materials are attracting interest due to their ability to provide coupling between magnetic and dipolar orders, allowing to generate an electric response upon magnetic stimulation or vice-versa [1]. This ME coupling makes them suitable for implementation in technological applications including transducers, storage devices, sensors and actuators, among others [2-7].

Single-phase materials can present this ME effect inherently. However, they are not abundant, the effect ME coupling is small and occurs at low temperatures [8]. Thus, composite materials comprising magnetostrictive and piezoelectric phases have been developed exhibiting a high ME response [9]. Among the many ME composites, polymer-based ones are characterized by simple fabrication, robustness and flexibility when compared to ceramic-based composites [7, 8]. A step further in the development of magneto-electrically responsive materials, is the introduction of the MI effect reported for MILs within the semicrystalline and highly polar PVDF matrix, allowing high ionic mobility [10]. Consequently, a distinct ME effect, identified a MI effect, arises. This effect relies on the ionic movement within the polymer matrix instead of dipole variations, leading to the development of a voltage variation in the samples upon application of a magnetic field [10]. To the best of our knowledge, the MI effect in this type of composites has only been reported in [10]

Interestingly, the incorporation of IL into a polymer matrix is one of the most suitable ways to develop high-bending soft actuators [11], where the electromechanical response is governed by the migration of anions and cations to the electrodes under the application of an electric field [11]. Efforts have been performed in order to optimize maximum bending actuation by varying polymer matrix [12, 13], IL type [14], cation [15] and anion [16]. Despite its, this multifunctionality is rarely explored [17]. The combination of the two effects (electrical and magnetic) will allow to develop highly interesting hybrid materials with a double functional response, opening new and challenging opportunities in the development of magnetically and electrically responsive soft actuators.

In this context, this work reports the development of double responsive materials with both MI sensing and electromechanical actuation response. Hybrid materials based on imidazolium cations comprising different cation chain lengths and the same anion PVDF/[$C_n$mim][$FeCl_4$] (n= 2, 4, 8 and 14) with a 20 wt. % MIL content have been used to optimize both signals by tuning alkyl chain length of the MILs. It is to notice that the materials are prepared by solvent casting

and therefore their preparation is compatible with additive manufacturing technologies, such as screen or ink-jet printing [18].

5.2 Experimental section

5.2.1 Preparation of the hybrid films

The hybrid films were prepared following the general guidelines presented in [19]. Before PVDF dissolution, the different [$C_n$mim][$FeCl_4$] ILs (20 wt. %) were mixed with DMF. Then, PVDF was added in a proportion of 15/85 wt. % (PVDF/DMF) and dissolved under mechanical stirring at room temperature. After complete polymer dissolution, the PVDF/[$C_n$mim][$FeCl_4$] solutions were spread at room temperature in a glass substrate and the solvent was evaporated at 210 °C in an air oven for 10 minutes (**Figure 5.1**). It is to notice that these processing conditions provide homogeneous compact films mostly in the non-polar alpha phase in pristine PVDF [19]. After the solvent evaporation process, PVDF/[$C_n$mim][$FeCl_4$] films with a thickness of ≈50 µm were obtained.

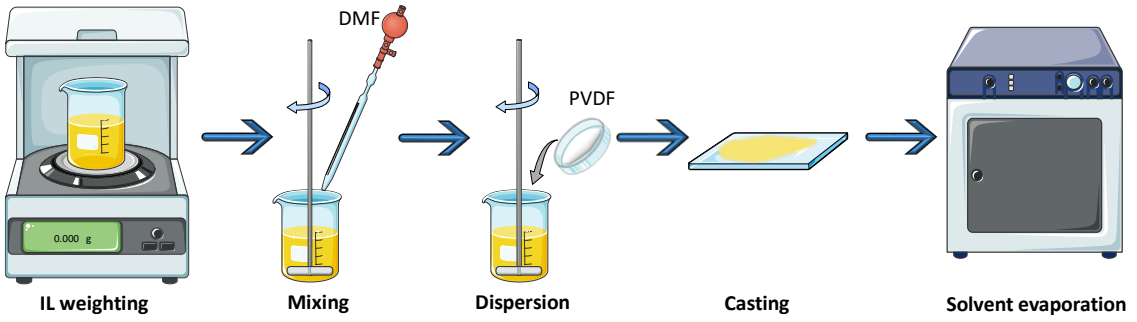


Figure 5.1 - Schematic representation of the procedure used for the preparation of the PVDF/[$C_n$mim][$FeCl_4$] films.

5.2.2 Sample characterization

To examine the cross-sectional morphology of the PVDF/[$C_n$mim][$FeCl_4$] films, the SEM technique was employed. The polymer phase within the films was assessed using the FTIR-ATR technique. Thermal properties were analysed through the DSC and TGA techniques. Additionally, the magnetic properties were evaluated using the VSM technique. A comprehensive description of the characterization techniques can be found in chapter 2.

To obtain the MI response, the samples were sputtered with gold (Polaron Coater SC502) on both sides with an electrode length of 25 mm and a width of 3 mm. A wire was glued to each

side for electrical contacts with silver paint and the sample was placed in the center of a solenoid. The magnetic field was applied along the long side of the electrical contact. The solenoid resonance frequency is on the range of the MHz, which allows characterizing the MI coefficient with AC magnetic fields up to 100 kHz. It is to notice that the MI voltage coefficient measurements were performed with no dc magnetic field applied. Further, the AC excitation coil was placed inside a magnetic shield to reduce the ambient magnetic field to less than 0.5 μT with a noise of a few nT.

A computer program designed and implemented in LabView controls the whole experiment, including data acquisition. During the experiments, the solenoid coil produces the AC magnetic field of 8.13 Oe per Ampere at the center. An Agilent 33210A signal generator feeds it and the current flowing on the solenoid is continuously measured in a non-inductive resistance connected in series with the solenoid. A PID control procedure was implemented to maintain the selected field with a resolution of 6.28×10^{-4} Oe rms. The AC magnetic field frequency was swept from 1 Hz to 100 kHz and at each frequency the AC magnetic field amplitude ranged from 6.28×10^{-2} Oe to 6.28×10^{-1} Oe in 6.28×10^{-2} Oe steps. Then the MI voltage generated by the sample was obtained using an AMTEK 7280 DSP Lock-in amplifier. The MI coefficient (α_{33}) was calculated after **Equation 5.1** [20]:

$$\alpha_{33} = \frac{\Delta V}{H_{AC} \times t} \tag{5.1}$$

where ΔV is measured output voltage, H_{AC} represents the amplitude of the AC magnetic field, and t the films thickness [20].

5.2.3 Functional electromechanical characterization

The actuator response of the films was evaluated by means of bending measurements carried out with a PC connected to a high-definition Logitech HD 1080p Webcam camera. Samples were prepared with a width of 2 mm and full length of 12 mm, leaving a free length of 10 mm after sample attachment to the sample holder. Two gold electrodes were deposited in both sides of the film by magnetron sputtering (Polaron SC502). The actuators were clamped by two needles and connected to an Agilent 33220A function generator. The displacement was measured by applying

a square wave signal with voltages from 2 Vpp to 5 Vpp at a frequency of 100 mHz to allow complete anion and cation migration to the electrodes [14].

The quantification of the bending (ε) actuation was achieved using the samples with the dimensions briefly described by analyzing the videos in 2 s steps, obtaining a full description of the displacement by measuring the displacement (δ) of the sample along the x axis. The bending strain ε was calculated taking into consideration the sample free length (L), thickness (d) and δ, according to **Equation 5.2** [15]:

$$\varepsilon = \frac{2d\delta}{L^2 + \delta^2} \tag{5.2}$$

5.3 Results and discussion

5.3.1 Morphological features

The morphology of the [$C_n$mim][$FeCl_4$]/PVDF films depends on the alkyl chain length of the imidazolium based ILs, as presented in the SEM images presented in **Figure 5.2**.

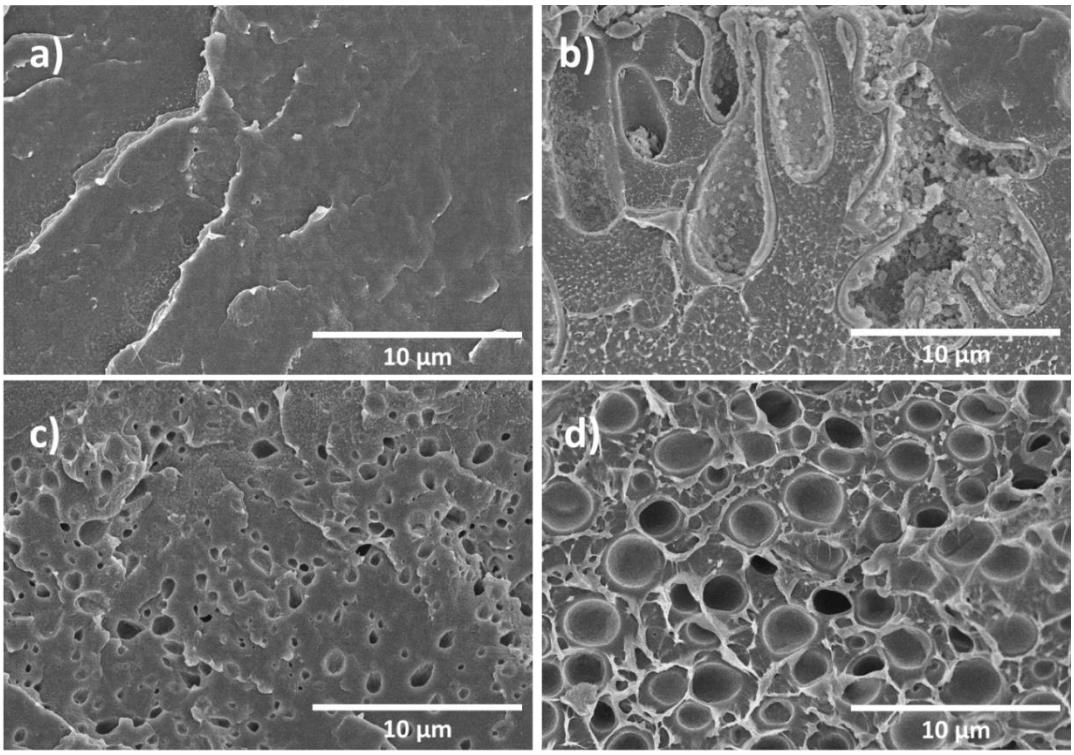


Figure 5.2 - Cross-section SEM images of the PVDF/MIL films with a) [C_2mim][$FeCl_4$], b) [C_4mim][$FeCl_4$], c) [C_8mim][$FeCl_4$] and d)[C_{14}mim][$FeCl_4$].

For neat PVDF at the used processing conditions the samples show a compact non-porous and homogeneous microstructure as no phase separation occurs during the solvent evaporation process [10, 19]. Similar results are observed upon $[C_2mim][FeCl_4]$ incorporation into the PVDF matrix (**Figure 5.2a**), being observed a non-porous film.

On the other hand, the same behaviour is not observed for the other PVDF/$[C_nmim][FeCl_4]$ (n=4, 8 and 14) (**Figure 5.2b-d**) films comprising different alkyl chain lengths and a tendency to the formation of a porous structure with increasing cation alkyl chain length is observed. This fact is indicative of a thermally induced phase separation process during solvent evaporation occurs leading to the pores formation. This fact results from the ILs $[C_nmim][FeCl_4]$ (n=4, 8 and 14) separation from the polymer rich regions together with the solvent, remaining the ILs in the pores once the DMF solvent is evaporated, in agreement with the results reported in [10]. Thus, the relation between the porosity and alkyl chain length demonstrates also that there is an increasing interaction between the MILs and the solvent with increasing alkyl chain length. In this sense, the observed porous structure is more noticeable for the films containing $[C_8mim][FeCl_4]$ and $[C_{14}mim][FeCl_4]$ with average pore sizes of 0.7 ± 0.2 μm and 2.0 ± 0.5 μm for the corresponding films.

5.3.2 Physical-chemical and thermal characterization

The introduction of different ILs in the PVDF/$[C_nmim][FeCl_4]$ films also influences the polymer phase and degree of crystallinity of the samples, as presented in **Figure 5.3**.

The influence of the cation chain length in the chemical properties of the films and in the electroactive β-phase content was evaluated by FTIR-ATR measurements (**Figure 5.3a**). Independently of the IL cation chain length, no significant differences are observed in the spectra, being possible to observe the main characteristic absorption bands of the PVDF α-phase at 855,795 and 763 cm^{-1} and of the electroactive β-phase at 840 cm^{-1} and 1275 cm^{-1} [21, 22]. It is to notice that the inclusion of the IL in the IL/PVDF films induces an increase of the absorption bands intensity characteristics of the electroactive β-phase and promotes a decrease in the bands identifying the α-phase of PVDF. Further, the absorption band intensity in the region 2800-3000 cm^{-1} increases with the alkyl chain length of the IL and, therefore, are attributed to CH_2 and CH_3 stretching vibrations of the alkyl groups of the imidazolium ring [23].

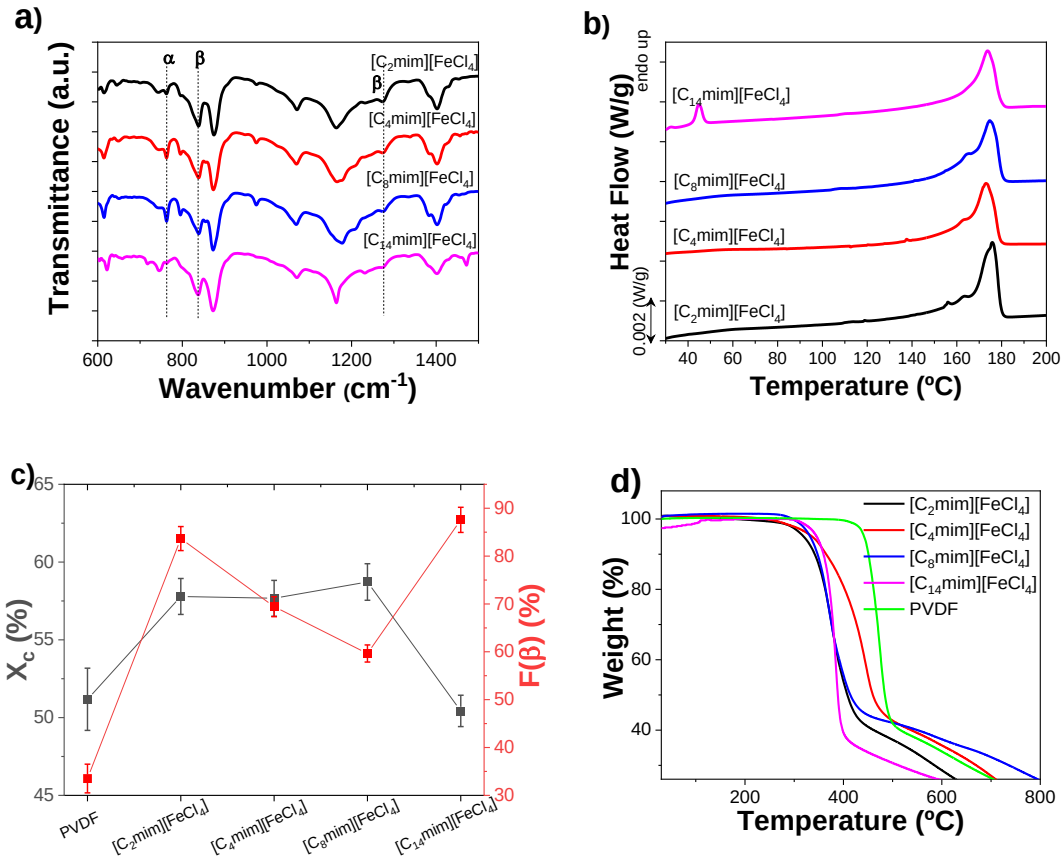


Figure 5.3 - Physical-chemical and thermal characterization of the PVDF/[$C_n$mim][$FeCl_4$] films: a) FTIR-ATR spectra, b) DSC thermograms, c) β-phase content and degree of crystallinity, d) TGA thermograms.

The influence of the cation alkyl chain length in the electroactive β-phase content was quantified using **Equation 2.1** (**Figure 5.3c**), showing an strong increase of the amount of β-phase with the introduction of the IL, from 33% for PVDF to 83% for the sample with 20% of PVDF/[C_2mim][$FeCl_4$]. Increasing the alkyl chain length of the cation leads to a decrease in the β-phase content from 83% (PVDF/[C_2mim][$FeCl_4$]) to 60% (PVDF/[C_8mim][$FeCl_4$]), which is reversed for the IL with the largest alkyl chain length ([C_{14}mim][$FeCl_4$]), indicating that, probably, alkyl chain lengths higher than C_n=8 leads to higher interactions between the positive PVDF charge and the negative anion charge. Thus, independently of the IL chain length, the incorporation of the ILs in the PVDF polymer matrix induces a polymer crystallization in β-phase, known for its high polarity and piezoelectric response. It is to notice that pristine PVDF films prepared in the same conditions, crystallize mainly in the α-phase (~33%). This fact allows to conclude that the electroactive β-phase is nucleated due to the electrostatic ion-dipole interactions between the IL anion and cation and the dipoles of the PVDF chain, promoting the orientation of the polymer

chains in the all-trans chain conformation of the β-phase [24]. As it has been demonstrated, the extent of this ion-dipole interaction also depends on the ion-ion interaction of the IL, which in turn depends on the alkyl chain length, among other factors, related to the observed nucleation differences among the IL used in the present work [14, 15].

Figure 5.3b shows the differential scanning calorimetry (DSC) scans obtained for the PVDF/IL films, characterized by a single endothermic peak between 150-190 °C, corresponding to the melting of the PVDF polymer [21]

The degree of crystallinity (**Figure 5.3c**) was evaluated after **Equation 2.3** and shows an increase from ~50% to 59% for the films containing the ILs, [C_2mim][$FeCl_4$], [C_4mim][$FeCl_4$] and [C_8mim][$FeCl_4$], due to the aforementioned ion-dipole interactions, the IL acting as nucleation centre for polymer crystallization [25]. No significant differences are observed between neat PVDF and the film PVDF/[C_{14}mim][$FeCl_4$].

The influence of the alkyl chain length of the ILs into the thermal degradation and stability of the films is shown in **Figure 5.3d**. As observed in the TGA curves, neat PVDF presents an onset temperature near 450 °C, corresponding to the PVDF chain bonds scission (carbon-fluorine and carbon hydrogen) [25]. Upon the ILs incorporation, a decrease in the thermal stability of the films is observed, as indicated by the decrease in the onset temperature. It is to notice that for [$C_n$mim][$FeCl_4$] ILs the onset temperature occurs in the range of 250 and 310 °C depending on the alkyl chain length. During the thermal degradation, the IL anions thermally decompose through dealkylation and the cations experience alkyl migration and elimination reactions [26]. The decrease in the thermal stability is more noticeable for the films containing the ILs with the lower alkyl chain length, the thermal stability varying in the following order: [C_2mim][$FeCl_4$]<[C_4mim][$FeCl_4$]<[C_8mim][$FeCl_4$]<[C_{14}mim][$FeCl_4$]. However, the influence of the imidazolium cation chain length in the thermal stability of PVDF is relatively small, as previously observed [27].

5.3.3 Magnetic and magnetoionic characterization

The influence of the alkyl chain length in the magnetic and MI properties of the PVDF/[$C_n$mim][$FeCl_4$] films is presented in **Figure 5.4**.

The magnetization of the films containing the magnetic anion $[FeCl_4]^-$ was measured in the magnetic field range from -20 to 20 KOe. **Figure 5.4a** shows a paramagnetic behaviour for all composites, characterized by a linear increase of the magnetization with the applied magnetic field. All samples show a similar response, the magnetic susceptibility being larger for the films containing the $[C_4mim][FeCl_4]$ and $[C_{14}mim][FeCl_4]$ ILs and not being observed large differences for the PVDF/$[C_nmim][FeCl_4]$ (n=2 and 8) composites. There is no correlation between the magnetization and the alkyl chain length increase, being the former determined for the magnetic anion $[FeCl_4]^-$.

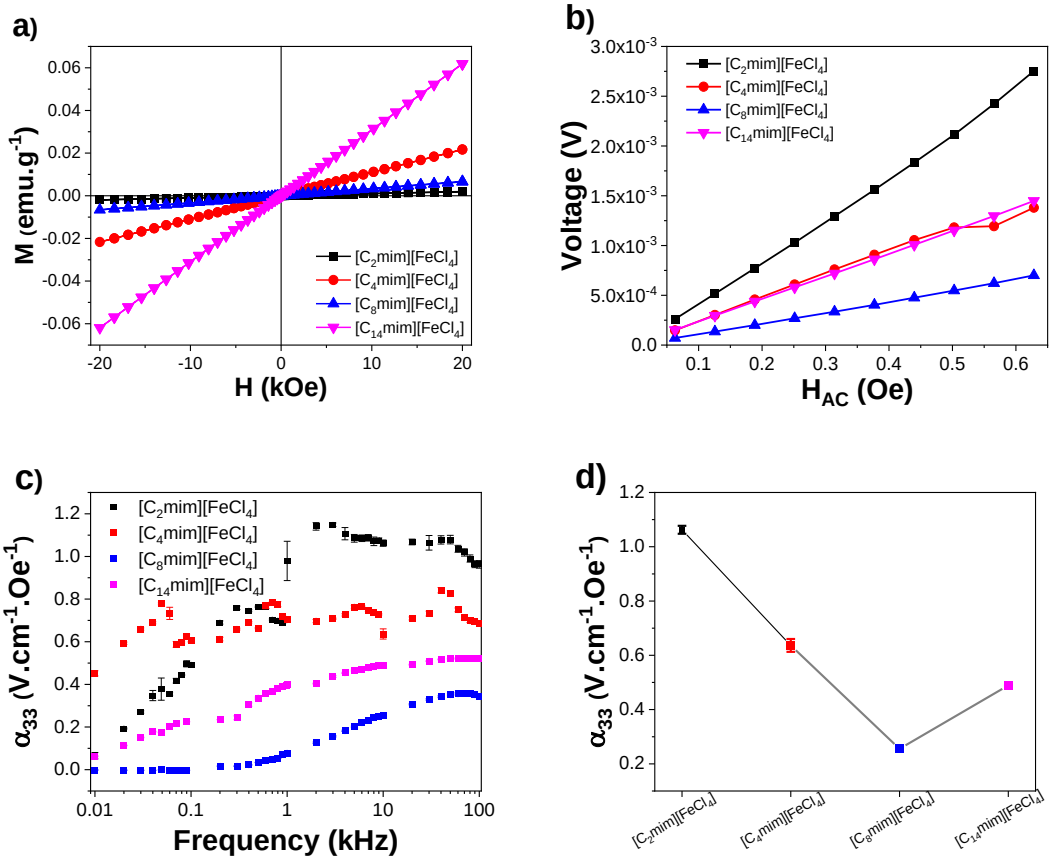


Figure 5.4 - a) Magnetization, b) MI voltage as a function of H_{AC} intensity at 10 kHz, c) MI coefficient as a function of frequency and d) MI coefficient at 10 kHz for the PVDF/$[C_nmim][FeCl_4]$ films.

The MI response of the PVDF/$[C_nmim][FeCl_4]$ films was evaluated by a semi-dynamic method, through the application of an alternating magnetic field (H_{AC}) and quantifying the corresponding output voltage response. **Figure 5.4b** shows the voltage generated by the films when an AC magnetic field is applied showing that the AC response increases with increasing frequency (**Figure 5.4c**). A maximum is reached with increasing frequency, due to the localized ionic

movement of the MIL, which leads to an increase of the electrical conductivity and dielectric losses with increasing frequency [10].

The MI coefficient (α_{33}) was calculated after **Equation 5.1**, being observed that the films with the shorter alkyl chain length (PVDF/[C_2mim][$FeCl_4$]) present the highest MI coefficient (1.06±0.015 V cm^{-1} Oe^{-1}) (**Figure 5.4d**), which can be related with the higher mobility of the ions into a non-porous structure. With increasing cation chain length, the MI coefficient tends to decrease to a minimum of 0.255±0.0026 V cm-^{1} Oe^{-1} for the PVDF/[C_8mim][$FeCl_4$] composite. Interestingly, a slight increase to 0.489 ±0.0019 V cm^{-1} Oe^{-1} is observed for the PVDF/[C_{14}mim][$FeCl_4$] film. By comparing these MI coefficients with the magnetoelectric coefficients of laminate and particulate composites, it is possible to conclude that the inclusion of MILs within a polymer matrix allows to develop materials with higher voltage variations under applied magnetic fields. In fact, ME laminate composite develops ME coefficients of e.g. 186 mV cm^{-1} Oe^{-1} at the H_{AC} frequency of ≈39 kHz [28] and magnetoelectric particulate composites ME coefficients from 0.4 to 40 mV cm^{-1} Oe^{-1} [29, 30].

The developed voltage can only be linked to the ionic displacement of the MIL due to the application of the magnetic field to the paramagnetic films. The application of the magnetic field leads to a interaction of the magnetic gradient forces with the [$FeCl_4$]- anions spin inducing the corresponding spins orientation and ionic displacement, following the applied external H_{AC} [10].

5.3.4 Electrical and electromechanical characterization

The electrical conductivity of the PVDF/[$C_n$mim][$FeCl_4$] films as well as the actuator response, i.e. the displacement of the actuator tip as a function of time in response to applied square voltages are shown in **Figure 5.5**.

The electrical DC conductivity of the PVDF/[$C_n$mim][$FeCl_4$] films was evaluated with **Equation 2.6** from the I-V curves presented in **Figure 5.5a**. From **Figure 5.5b** it is observed a strong increase of the electrical conductivity for the PVDF/[$C_n$mim][$FeCl_4$] films with respect to the one of PVDF. The electrical conductivity increases in the same order of magnitude, independently of the IL alkyl chain length, being the highest conductivity values observed for the PVDF/[C_2mim][$FeCl_4$] composite (4.54×10^{-8} ±4.80×10^{-9} S cm^{-1}), i.e. the one with the shorter chain length and therefore the larger mobility.

PVDF films incorporating ILs have been developed for large deformation soft actuators [11], the bending response depending on the degree of crystallinity of the polymer and the IL anion and cation characteristics. When subjected to an external electric field, the cations and ions move and redistribute within the polymer matrix leading to the bending actuation as a result of the different sizes of anions and cations and their accumulation closer to the electrodes (**Figure 5.6a**) [15]. Thus, the actuation response is dependent not just on the mechanical and electrical properties of the PVDF/MIL films but also on the intrinsic characteristics of the IL, such as the size of the ionic species and the chain length of the ILs [14].

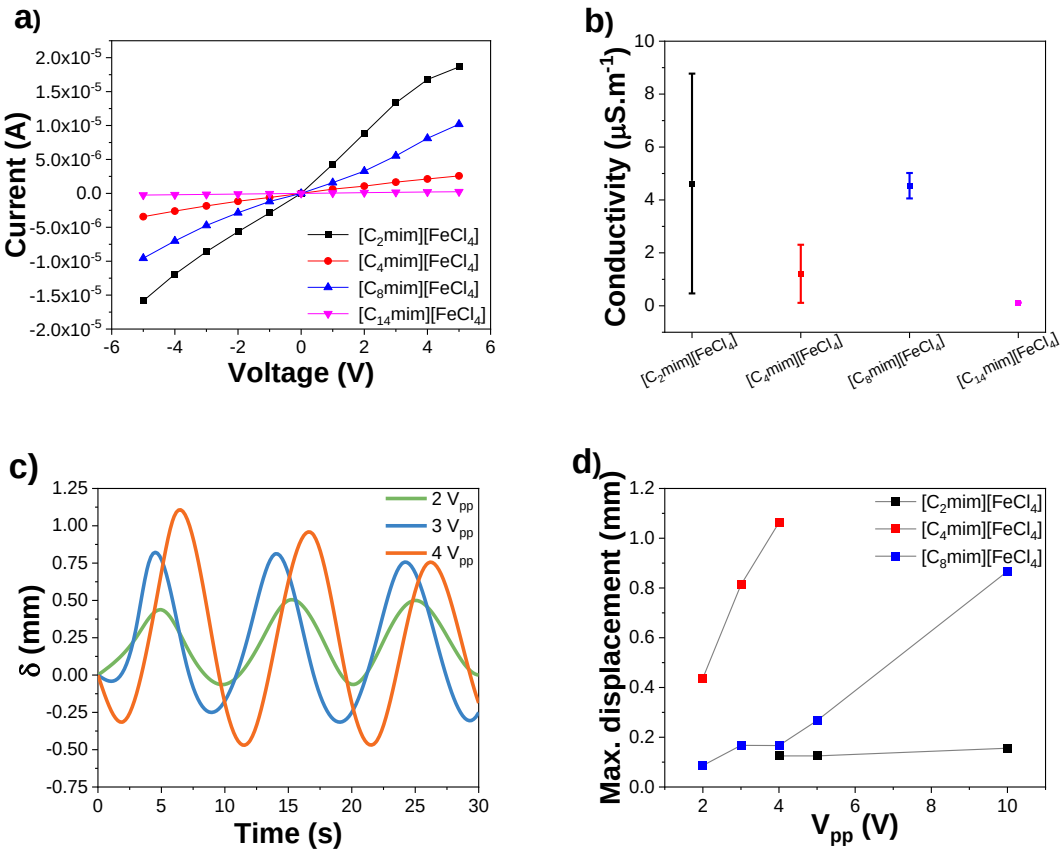


Figure 5.5 - a) Current-voltage intensity (I-V) curves and b) DC electrical conductivity of the different PVDF/MIL composites. As a reference, the electrical DC conductivity of PVDF is 5×10^{-14} S cm^{-1} [31]. c) Displacement, δ, of the PVDF/MIL composite actuator tip as a function of time under different applied voltages at a frequency of 100 mHz for: [C_4mim][$FeCl_4$] and d) maximum displacement for the different PVDF/[$C_n$mim][$FeCl_4$] films as a function of the applied voltage.

Figure 5.5c show the bending response as a function the time of the films containing [C_4mim][$FeCl_4$], the rest of the films showing a similar response, with the exception of the PVDF/[C_{14}mim][$FeCl_4$] composite in which no bending actuation was observed. The latter is

related to the higher cation alkyl chain length, leading to a porous structure and a large number of charge carriers (cations and anions) within of the porous structure, hindering their mobility across the polymer matrix, limiting the number of ionic species available to move when an electrical field is applied [10]. Additionally, it is also to notice that due to the smaller differences between the electroactive β phase content, the bending displacement is not higher affected by the ion-dipole interactions that occurs between the IL and PVDF.

For the rest of the IL and independently of the IL alkyl chain length, the bending response follow the periodic applied signal but are not symmetric, when compared to the initial position as a function of the applied voltage. This fact is explained by the imbalance of the ion transport, i.e. the different sizes of anion and cation result in a non-symmetrical ion dynamic with respect to positive or negative voltages. From **Figure 5.5d** it is observed that the maximum displacement of the actuator tip for all films increases with increasing applied voltage with a maximum of 0.16 mm for $[C_2mim][FeCl_4]$, 1.1 mm for $[C_4mim][FeCl_4]$ and 0.87 mm for $[C_8mim][FeCl_4]$ for applied voltages of 10 V, 4 V and 10 V, respectively. For applied voltages lower than 4 V, the PVDF/$[C_2mim][FeCl_4]$ composite does not show a bending response. Additionally, it is to notice that PVDF/$[C_4mim][FeCl_4]$ films do not show bending response for applied voltages higher than 4 V, due to actuator damage.

As a representative example, the observed displacement for the PVDF/$[C_4mim][FeCl_4]$ composite at a frequency of 100 mHz and at an applied voltage of 4 Vpp is presented in **Figure 5.6b**.

The maximum bending (ε) actuation was evaluated for the maximum observed displacement, using **Equation 5.2**, being observed a decreases from 0.13% at 10 Vpp for PVDF/$[C_8mim][FeCl_4]$ films to 0.09 % for PVDF/$[C_4mim][FeCl_4]$ at 4 V_{pp}. The lowest bending response being observed for the for PVDF/$[C_2mim][FeCl_4]$ at 10 V_{pp} (0.01%). These results allow to conclude that the cation size chain length does not have a significant effect in the actuators performance, being the bending response very similar for all films.

Thus, the electromechanical response of the studied materials is proven, which together with the MI response and the possibility of being implemented by additive manufacturing technologies [32] based on their solvent based processing, confirm these materials unique characteristics for the development of sensor and actuator applications.

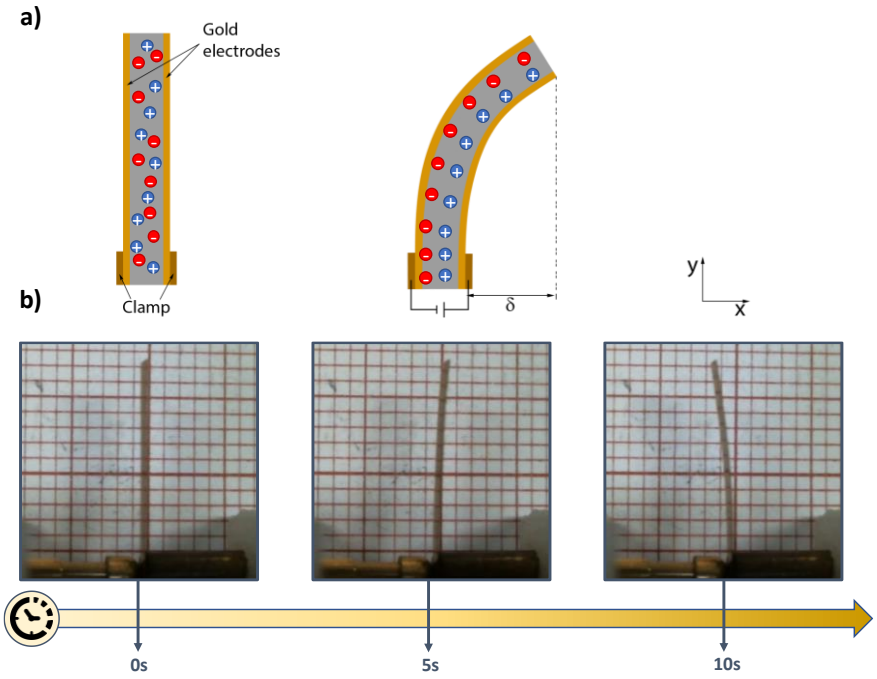


Figure 5.6 - a) Schematic representation of the bending response of the PVDF/MIL films. b) Bending motion as a function of time for the PVDF/[C_4mim][$FeCl_4$] composite at 100 mHz frequency and 4 V_{pp}.

5.4 Conclusion

Multifunctional MI sensing and electromechanical actuator materials have been developed based on imidazolium-based IL and PVDF. PVDF/[$C_n$mim][$FeCl_4$] (n=2, 4, 8 and 14) films have been developed by solvent casting using IL with different alkyl chain length and sharing the same anion.

The influence of the alkyl chain length on the morphological behavior reveals a tendency to the formation of a porous structure with increasing cation alkyl chain length, as a result of a thermally indicted phase separation process and the solvent-IL interaction. The incorporation of the different ILs into the PVDF polymer matrix also induces an increase in the electroactive β-phase from ~33% for neat PVDF up to to 87% (PVDF/[C_{14}mim][$FeCl_4$]), the amount of β-phase depending on the alkyl chain length of the IL. Further, also a slight variation in the degree of crystallinity is observed with the incorporation of the different IL.

The films show a paramagnetic behavior and a MI response, which is the highest (1.06±0.015 V cm^{-1} Oe^{-1}) for the composite with the lowest alkyl chain length (PVDF/[C_2mim][$FeCl_4$]).

Further, the materials show a suitable bending actuation with a maximum displacement of 1.1 mm for the PVDF/[C_4mim]ionic composite under application of 10 V at 100 mHz.

The combination of electromechanical and MI response represents a new generation of materials with multifunctional properties for a large variety of applications including, sensors, actuators and biomedicine. Further, simple solvent based processability allows facile integration into devices through additive manufacturing technologies.

5.5 References

1. Eerenstein, W., N.D. Mathur, and J.F. Scott, *Multiferroic and magnetoelectric materials.* Nature, 2006. **442**(7104): p. 759-765.
2. Malleron, K., et al., *Experimental study of magnetoelectric transducers for power supply of small biomedical devices.* Microelectronics Journal, 2019. **88**: p. 184-189.
3. Rupp, T., et al., *Magnetoelectric Transducer Designs for Use as Wireless Power Receivers in Wearable and Implantable Applications.* Materials (Basel, Switzerland), 2019. **12**(3): p. 512.
4. Cheng, Y., et al., *Recent development and status of magnetoelectric materials and devices.* Physics Letters A, 2018. **382**(41): p. 3018-3025.
5. Leung, C.M., et al., *A review on applications of magnetoelectric composites: from heterostructural uncooled magnetic sensors, energy harvesters to highly efficient power converters.* Journal of Physics D: Applied Physics, 2018. **51**(26): p. 263002.
6. Wang, Y. and J. Atulasimha, *A Dexterous Surgical Manipulation Tool Using Self-Sensing Magnetoelectric Actuators*. 2010. p. 767-771.
7. Martins, P. and S. Lanceros-Méndez, *Polymer-based magnetoelectric materials: To be or not to be.* Applied Materials Today, 2019. **15**: p. 558-561.
8. Nan, C.W., et al., *Multiferroic magnetoelectric composites: Historical perspective, status, and future directions.* Journal of Applied Physics, 2008. **103**(3).
9. Liang, W.I., et al., *Design of magnetoelectric coupling in a self-assembled epitaxial nanocomposite via chemical interaction.* Journal of Materials Chemistry C, 2014. **2**(5): p. 811-815.
10. Correia, D.M., et al., *Low-field giant magneto-ionic response in polymer-based nanocomposites.* Nanoscale, 2018. **10**(33): p. 15747-15754.
11. Correia, D.M., et al., *Ionic Liquid–Polymer Composites: A New Platform for Multifunctional Applications.* Advanced Functional Materials, 2020. **30**(24): p. 1909736.
12. Dias, J.C., et al., *Improved response of ionic liquid-based bending actuators by tailored interaction with the polar fluorinated polymer matrix.* Electrochimica Acta, 2019. **296**: p. 598-607.
13. Reizabal, A., et al., *Silk Fibroin Bending Actuators as an Approach Toward Natural Polymer Based Active Materials.* ACS Applied Materials & Interfaces, 2019. **11**(33): p. 30197-30206.
14. Mejri, R., et al., *Imidazolium-based ionic liquid type dependence of the bending response of polymer actuators.* European Polymer Journal, 2016. **85**: p. 445-451.
15. Correia, D.M., et al., *Ionic Liquid Cation Size-Dependent Electromechanical Response of Ionic Liquid/Poly(vinylidene fluoride)-Based Soft Actuators.* The Journal of Physical Chemistry C, 2019. **123**(20): p. 12744-12752.
16. Mejri, R., et al., *Effect of anion type in the performance of ionic liquid/poly(vinylidene fluoride) electromechanical actuators.* Journal of Non-Crystalline Solids, 2016. **453**.
17. Wang, Z., et al., *Shape- and Color-Switchable Polyurethane Thermochromic Actuators Based on Metal-Containing Ionic Liquids.* ACS Applied Materials & Interfaces, 2021. **13**(24): p. 28878-28888.

18. Oliveira, J., et al., *Polymer-based smart materials by printing technologies: Improving application and integration.* Additive Manufacturing, 2018. **21**: p. 269-283.
19. Ribeiro, C., et al., *Electroactive poly(vinylidene fluoride)-based structures for advanced applications.* Nature Protocols, 2018. **13**(4): p. 681-704.
20. Correia, D.M., et al., *Low-field giant magneto-ionic response in polymer-based nanocomposites.* Nanoscale, 2018. **10**(33): p. 15747-15754.
21. Martins, P., A.C. Lopes, and S. Lanceros-Mendez, *Electroactive phases of poly(vinylidene fluoride): Determination, processing and applications.* Progress in Polymer Science, 2014. **39**(4): p. 683-706.
22. Cai, X., et al., *A critical analysis of the α, β and γ phases in poly(vinylidene fluoride) using FTIR.* RSC Advances, 2017. **7**(25): p. 15382-15389.
23. Roth, C., et al., *Hydrogen bonding in ionic liquids probed by linear and nonlinear vibrational spectroscopy.* New Journal of Physics, 2012. **14**.
24. Dias, J.C., et al., *High performance electromechanical actuators based on ionic liquid/poly(vinylidene fluoride).* Polymer Testing, 2015. **48**: p. 199-205.
25. Meira, R., et al., *Ionic-liquid-based electroactive polymer composites for muscle tissue engineering.* ACS Applied Polymer Materials, 2019. **1**(10): p. 2649-2658.
26. Zhou, C., et al., *Properties and catalytic activity of magnetic and acidic ionic liquids: Experimental and molecular simulation.* Carbohydrate Polymers, 2014. **105**: p. 300-307.
27. Cao, Y. and T. Mu, *Comprehensive Investigation on the Thermal Stability of 66 Ionic Liquids by Thermogravimetric Analysis.* Industrial & Engineering Chemistry Research, 2014. **53**(20): p. 8651-8664.
28. Li, D., et al., *Construction of Magnetoelectric Composites with a Large Room-Temperature Magnetoelectric Response through Molecular–Ionic Ferroelectrics.* 2018. **30**(52): p. 1803716.
29. Prabhakaran, T. and J. Hemalatha, *Magnetoelectric investigations on poly(vinylidene fluoride)/$NiFe_2O_4$ flexible films fabricated through a solution casting method.* RSC Advances, 2016. **6**(90): p. 86880-86888.
30. Prabhakaran, T. and J. Hemalatha, *Poly(vinylidene fluoride)-Based Magnetoelectric Polymer Nanocomposite Films*, in *Magnetoelectric Polymer-Based Composites*. 2017. p. 87-113.
31. Fernandes, L., et al., *Highly sensitive humidity sensor based on ionic liquid-polymer composites.* ACS Applied Polymer Materials, 2019.
32. Fernandes, L.C., et al., *Ionic-Liquid-Based Printable Materials for Thermochromic and Thermoresistive Applications.* ACS Applied Materials & Interfaces, 2019. **11**(22): p. 20316-20324.

6 Multifunctional magnetoelectric sensing and bending actuator response of polymer-based hybrid materials with magnetic ionic liquids

The development of smart materials with ME properties, capable of wirelessly generating electrical signals in response to external magnetic fields, represents a suitable approach for the development of magnetic field sensors and actuators due to their ME coupling, flexibility, robustness and easy fabrication, compatible with additive manufacturing technologies. In this chapter is demonstrated the suitability of magnetoelectric responsive materials based on the magnetic IL [Bmim][$FeCl_4$] and P(VDF-TrFE) for magnetic sensing and actuation device development. An AC magnetic field sensor has been developed based on the obtained materials, showing frequency-dependent sensitivity.

This chapter is based on the following publication: Fernandes, L.C., Correia, D.M., Tariq, M., Esperança, J.M.S.S., Martins, P., Lanceros-Méndez, S., *Multifunctional magnetoelectric sensing and bending actuator response of polymer-based hybrid materials with magnetic ionic liquids.* Nanomaterials, 2023. **13**: p.2186

6.1 Introduction

In an era in which concepts such as the IoT and Industry 4.0 are key enabling technologies, miniaturized portable and multifunctional devices are becoming increasingly demanded. In this context, smart systems including sensors and actuators are essential components of the evolution of technology. However, geometrical and manufacturing complexity and the cost of commonly used materials and systems can be a drawback to their implementation [1, 2].

The combination of EAPs with ILs provides the opportunity to develop hybrid materials with improved and/or new functionalities such as electromechanical, mechanical, magnetic and electric properties considering specific target applications [3, 4].

Hybrid IL/polymer materials have been developed for implementation in different areas such as sensors and actuators, biomedicine and energy storage, but few studies concerning the combination of MILs with piezoelectric polymers with both MI and ME effects have been reported [4-6]. Additionally, and to the best of our knowledge, few studies concerning the use of piezoelectric MIL/polymer-based composites as magnetic sensors and actuators have been reported, in which the influence of the IL concentration or the cationic chain size of imidazolium-based ILs has been explored, but never the influence of the solvent evaporation temperature [7, 8].

In this work, P(VDF-TrFE)/[Bmim][$FeCl_4$] hybrid materials were developed via solvent casting, and their functional ME and bending actuation response was demonstrated.

6.2 Experimental section

6.2.1 Preparation of the samples

P(VDF-TrFE) was dissolved in DMF at room temperature under mechanical agitation with a ratio of 15/85 weight percentage (wt.%). After complete polymer dissolution, [Bmim][$FeCl_4$] (40 wt.%) was added to the solution. This concentration was selected based on [5], because of the higher value of magnetization. Hybrid films with a thickness of ~50 μm were obtained after spreading the solution on a clean glass substrate followed by the solvent evaporation in an oven (P-Selecta) at room temperature (~30 °C), 90 °C and 210 °C. The films thickness was 52.8 ± 5.0 μm, 158.2 ± 4.1 μm and 208.8 ± 22.2 μm with solvent evaporation temperatures of 210 °C, 90 °C and

room temperature, respectively (**Figure 6.1**). Samples were prepared at different solvent evaporation temperatures, as this process strongly influences a sample's morphology and functional response [3].

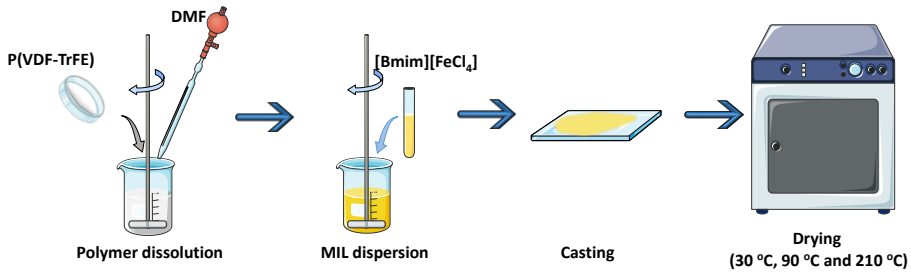


Figure 6.1 - Schematic representation of the procedure used for the development of PVDF-TrFE and PVDF-TrFE/[Bmim][$FeCl_4$] films.

6.2.2 Morphological and functional characterization

The morphology of the [Bmim][$FeCl_4$]/PVDF-TrFE films was analyzed with the SEM technique, with details provided in chapter 2.

The ME effect was evaluated with Helmholtz coils powered with an AC current (Agilent 33220A signal generator, Keysight Technology, Santa Clara, CA, USA) to reach AC magnetic fields ranging from 0 to 2 Oe. The AC fields were applied along the thickness direction of the samples, and a Rigol DS1074Z (Rigol, Suzhou, China) oscilloscope was used to record the induced output voltage. Prior to the analysis, the samples were coated by 5 mm diameter gold electrodes, deposited on both sides of the samples via magnetron sputtering (Polaron SC502, Quorum, Laughton, UK). The determination of the transversal ME coefficient (a) was performed measuring the induced voltage using **Equation 5.1** (previously mentioned in Chapter 5).

The actuator bending response of the materials was obtained with a high-definition Logitech HD 1080p Webcam camera, (Logitech, Lausanne, Switzerland) connected to a PC with 200 μm accuracy. The film actuator was clamped with two needles and submitted to the magnetic stimulation of a moving magnet (BX0C8-N52—K&J Magnetics, Pipersville, PA, USA—with a periodic movement from a maximum distance to the composite sample dmax = 2.2. mm to a minimum distance dmin = 0.1 mm, f = 0.1 Hz). Alternating current displacement measurements were performed by applying a square wave signal with voltages from 2 V_{pp} to 4 V_{pp} and a frequency of 100 mHz, allowing complete anion and cation migration to the electrodes. To evaluate the

actuation, the displacement of the films displacement was analysed every 2 s. The quantification of the bending (ε) was calculated using **Equation 5.2** (previously mentioned in Chapter 5). Results and discussion

6.3 Results and Discussion

6.3.1 Morphology

The morphology variations in the MIL/polymer materials with solvent evaporation temperature were evaluated via SEM (**Figure 6.2**).

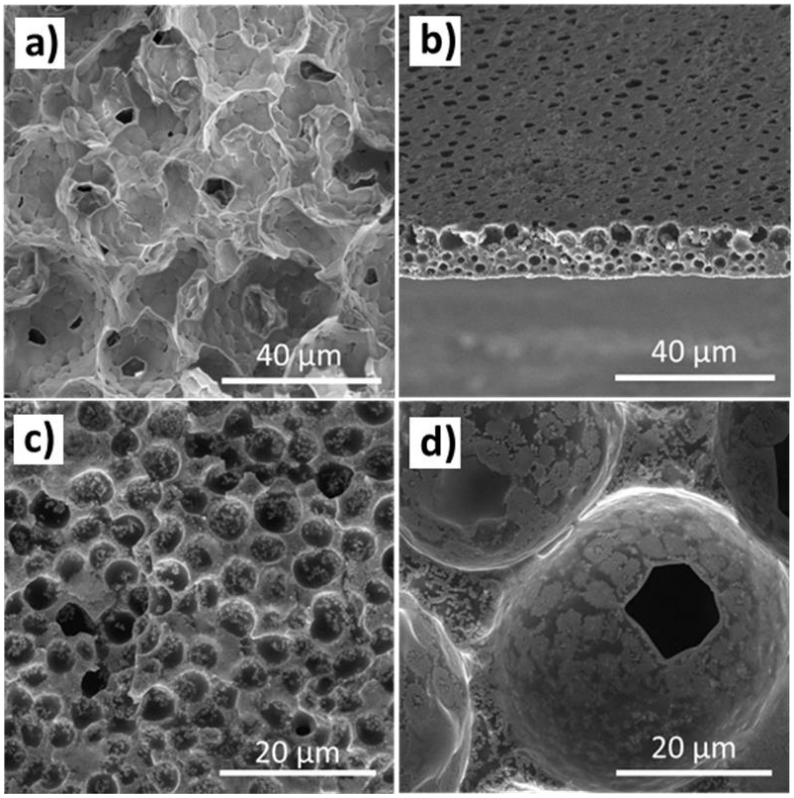


Figure 6.2 - Representative SEM images of P(VDF-TrFE) and P(VDF-TrFE)/[Bmim][$FeCl_4$] prepared with 40 wt.% content of MIL at different solvent evaporation temperatures: (a) room temperature P(VDF-TrFE); P(VDF-TrFE)/[Bmim][$FeCl_4$] at (b) 210 ºC, (c) 90 ºC and (d) room temperature.

Figure 6.2a shows the characteristic porous structure of electroactive P(VDF-TrFE) with an average pore size of 10.3 ± 2.2 µm [9]. Increasing the solvent evaporation temperature in pristine P(VDF-TrFE) leads to a more compact structure with the absence of pores due to the higher mobility of the polymer chains during solvent evaporation [10]. On the other hand,

independently of the presence of the MIL and the solvent evaporation temperature used during the processing method, a porous structure is observed after the IL incorporation. This fact is an indication that the inclusion of the MIL in the polymer matrix induces porosity in the films, based on the strong interaction of the IL with the DMF solvent, the phase separation of the polymer and solvent phases and the solvent evaporation, with the free spaces left by the solvent occupied by the IL being dragged to the pores due to their interaction with the solvent [11]. Additionally, **Figure 6.2** shows that the solvent evaporation temperature influences the pore size of the polymer matrix. As observed, the pore size decreases with increasing solvent evaporation temperature (**Figure 6.2b–d**) from a mean diameter of 2.2 ± 0.8 μm for solvent evaporation at 210 ºC (**Figure 6.2b**) to 35 ± 6 μm for room-temperature-prepared materials (**Figure 6.2d**). Additionally, the pore size of the P(VDFTrFE)/[Bmim][$FeCl_4$] samples increase with decreasing solvent evaporation temperature, with the temperature influencing the solvent evaporation rate. Higher solvent evaporation temperatures lead to quick solvent removal, resulting in a higher number of spherulites with smaller porous radii during polymer crystallization. Further, increasing temperature leads to the polymer chains acquiring enough mobility to occupy the free spaces left by the solvent [10]. Contrarily, lower solvent evaporation rates lead to a phase separation process [9], and the low mobility of the polymer chains at low temperature does not allow them to occupy the free space left by the solvent, leading to a final microstructure with spherulites with small radii and higher porosity.

6.3.2 Functional ME response

The effect of the solvent evaporation temperature on the ME sensing response of the P(VDF-TrFE)/ [Bmim][$FeCl_4$] composites with 40 wt.% of MIL is shown in **Figure 6.3**. Previous studies have shown the effect of different MIL contents in samples prepared at 210 °C [8, 11].

Figure 6.3a shows a linear increase in the ME output voltage with increasing H_{AC}, with fitting R^2 > 0.998, characteristic of composites containing MILs composed with paramagnetic ions [12]. This effect is based in the interaction of the $[FeCl_4]^-$ anions with the applied H_{AC}, where the anions move in the direction of the applied magnetic field. With a continuous variation in the direction of the magnetic field, the movement of the ions will generate the AC voltage signal in the electrodes of material. Thus, the materials show voltage responses in the mV range, suitable for the development of magnetic field sensors with a highest sensitivity (s) of 76 mV Oe^{-1}.

As shown in **Figure 6.3b**, at lower frequencies, there is a high voltage increase with increasing frequency, while for higher frequencies, the opposite effect is observed. This fact is explained based on the dynamics and mobility of the ions within the pores of the polymer matrix. For lower frequencies, the ions have enough time to move within the pores, with this movement being maximized at ≈10 MHz. With increasing frequency, the ions' mobility is reduced, and complete displacement does not occur, leading to ion relaxation processes and causing them to lag behind the fast excitation dynamics due to the increasing frequency [7, 13].

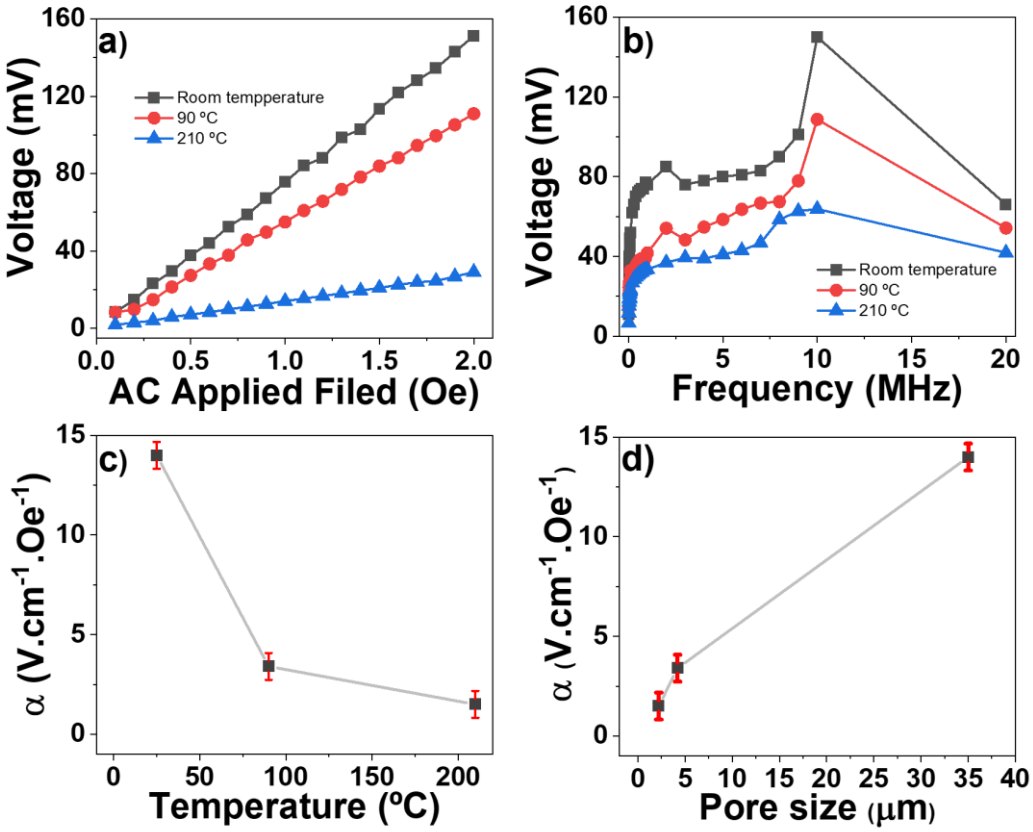


Figure 6.3 - ME response of P(VDF-TrFE)/[Bmim][$FeCl_4$] films: (a) ME voltage as a function of H_{AC} intensity at 500 kHz; (b) ME voltage as a function of H_{AC} frequency with H_{AC} intensity at 2 Oe; (c) ME coefficient as a function of solvent evaporation temperature with H_{AC} intensity of 2 Oe and frequency of 10 MHz and (d) ME coefficient as a function of the pore size with H_{AC} intensity of 2 Oe and frequency of 10 MHz.

The increase in the ME response with decreasing solvent evaporation temperature is shown in **Figure 6.3c**. As a consequence, the ME voltage coefficient increases from 1.5 V·cm^{-1}·Oe^{-1} to 14.1 V·cm^{-1}·Oe^{-1} when the pore size increases from 2.2 μm to 35 μm (**Figure 6.3d**), which is explained by the reduced motion capability of the MILs in the smaller pores and the larger degree

of confinement [14]. When such an ME response is compared to other P(VDF-TrFE)-based systems without MILs, it is observed that it is 3 orders of magnitude higher than the value reported for P(VDF-TrFE)/CFO nanocomposites (35 $mV \cdot cm^{-1} \cdot Oe^{-1}$) and in the same order of magnitude as the values reported for P(VDF-TrFE)/Vitrovac bi-layer laminates (66 $V \cdot cm^{-1} \cdot Oe^{-1}$) [15, 16].

Further, the magnetomechanical bending actuation response was evaluated in the hybrid materials, with the largest pore sizes and highest ME response observed for P(VDF-TrFE)/ [Bmim][$FeCl_4$] with 40 wt.% of MIL (**Figure 6.4**).

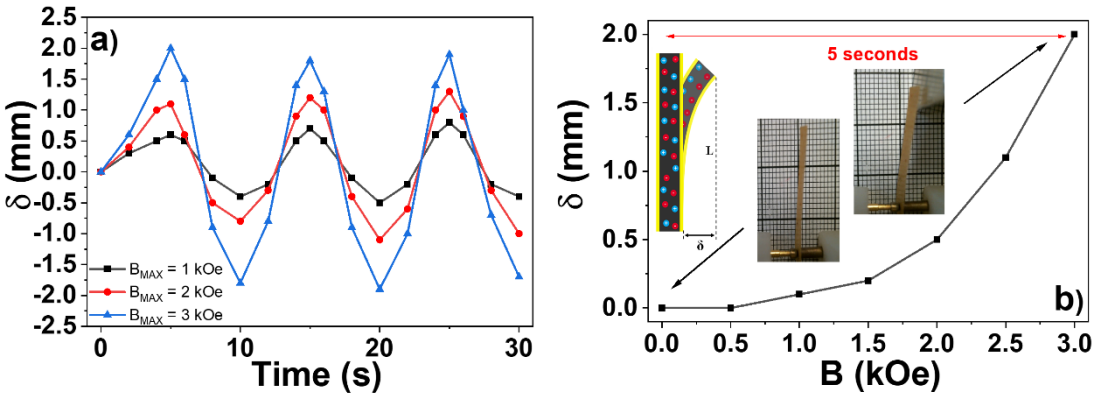


Figure 6.4 - (a) Displacement and (b) bending response of the P(VDF-TrFE)/ [Bmim][$FeCl_4$] composite as a function of time (f = 0.1 Hz) and DC magnetic field intensity, respectively. As a scale reference, the size of the small squares in the images is 1 mm. The schematic inset represents the ions (cations and anions) movement into the polymer matrix upon the applied DC magnetic field.

Figure 6.4a,b show the displacement of the actuator tip with respect to the initial position and the bending response of the materials, respectively. It is also observed that the displacement, and consequently, the bending response of the sample increases with an increasing applied DC magnetic field. The maximum displacement (2.1 mm) is observed when the moving magnet is at the minimum distance to the sample (0.1 mm). In such a situation, the magnet applies to the P(VDF-TrFE)/ [Bmim][$FeCl_4$] sample an H_{DC} = 3 kOe. The periodic movement of the magnet also induces a periodic displacement of the samples, leading to bending of 0.2% and an actuation capability (c) of 0.7 $mm \cdot kOe^{-1}$. Thus, the highest bending response is achieved for a DC applied magnetic field of 3 kOe , with it being possible to tune the bending response for a specific application depending on the applied DC magnetic field.

The response of the samples to the applied magnetic field is generated by the number and diffusion of the cations and anions near to the electrodes, as shown in the schematic representation of **Figure 6.4b**, with the bending response thus being governed by the mobility and ionic charge [3].

6.4 Conclusions

Hybrid films based on the magnetic ionic liquid [Bmim][$FeCl_4$] and P(VDF-TrFE) with 40 wt.% filler content were prepared using the solvent casting technique at different solvent evaporation temperatures in order to tune samples' morphologies. The morphologies of the P(VDF-TrFE)/[Bmim][$FeCl_4$] composites depend on the solvent evaporation temperature, increasing the pore size with decreasing solvent evaporation temperature. The developed materials exhibit a double functional response: a magnetoelectric response of 14.1 V cm^{-1} Oe^{-1} and a bending actuator response with a displacement of 2.1 mm and bending of 0.2%, which are maximized for the samples with the larger average pore size of 35 μm. Such results demonstrate the suitability of the MILs to be implemented in different polymeric matrices as innovative magnetic sensors and magnetically driven soft actuators, able to be prepared using additive manufacturing technologies.

6.5 References

1. Garbie, I. and A. Garbie. *Outlook of Requirements of Manufacturing Systems for Industry 4.0*. in *2020 Advances in Science and Engineering Technology International Conferences (ASET)*. 2020.
2. Botta, C., L. Pierangelini, and L. Vollero. *IoT Gateways for Industrial and Medical Applications: Architecture and Performance Assessment*. in *2020 IEEE International Workshop on Metrology for Industry 4.0 & IoT*. 2020.
3. Correia, D.M., et al., *Ionic Liquid–Polymer Composites: A New Platform for Multifunctional Applications.* Advanced Functional Materials, 2020. **30**(24): p. 1909736.
4. Lu, J., F. Yan, and J. Texter, *Advanced applications of ionic liquids in polymer science.* Progress in Polymer Science, 2009. **34**(5): p. 431-448.
5. Smiglak, M., et al., *Ionic liquids for energy, materials, and medicine.* Chemical Communications, 2014. **50**(66): p. 9228-9250.
6. Mejri, R., et al., *Effect of anion type in the performance of ionic liquid/poly(vinylidene fluoride) electromechanical actuators.* Journal of Non-Crystalline Solids, 2016. **453**.
7. Correia, D.M., et al., *Low-field giant magneto-ionic response in polymer-based nanocomposites.* Nanoscale, 2018. **10**(33): p. 15747-15754.
8. Fernandes, L.C., et al., *Design of Ionic-Liquid-Based Hybrid Polymer Materials with a Magnetoactive and Electroactive Multifunctional Response.* ACS Applied Materials & Interfaces, 2020. **12**(37): p. 42089-42098.

9. Nunes-Pereira, J., et al., *Poly(vinylidene fluoride) and copolymers as porous membranes for tissue engineering applications.* Polymer Testing, 2015. **44**: p. 234-241.
10. Gonçalves, R., et al., *Evaluation of the Physicochemical Properties and Active Response of Piezoelectric Poly(vinylidene fluoride-co-trifluoroethylene) as a Function of Its Microstructure.* The Journal of Physical Chemistry C, 2018. **122**(21): p. 11433-11441.
11. Oliveira, J., et al., *Polymer-based smart materials by printing technologies: Improving application and integration.* Additive Manufacturing, 2018. **21**: p. 269-283.
12. Schadewald, U., et al., *The Manipulation of Paramagnetic Ions by Magnetic Field Gradient Forces*, in *Modelling for Material Processing*. 2010: Riga. p. 127-133.
13. Kowalczuk, J., M. Bielejewski, and J. Tritt-Goc, *Ionic liquid dynamics and electrical conductivity under confinement within micro and nanocellulose ionogels.* Cellulose, 2023. **30**(6): p. 3551-3567.
14. Monk, J., R. Singh, and F.R. Hung, *Effects of Pore Size and Pore Loading on the Properties of Ionic Liquids Confined Inside Nanoporous CMK-3 Carbon Materials.* The Journal of Physical Chemistry C, 2011. **115**(7): p. 3034-3042.
15. Lima, A.C., et al., *Greener Solvent-Based Processing of Magnetoelectric Nanocomposites.* ACS Sustainable Chemistry & Engineering, 2022. **10**(13): p. 4122-4132.
16. Reis, S., et al., *Electronic optimization for an energy harvesting system based on magnetoelectric Metglas/poly(vinylidene fluoride)/Metglas composites.* Smart Materials and Structures, 2016. **25**(8): p. 085028.

7 Ionic-triggered magnetoelectric coupling for magnetic sensing applications

Conventional magnetoelectric nanocomposites exhibit low magnetoelectric responses, involve electric poling, and AC magnetic excitation after fabrication. In this chapter all those technological/scientific issues are jointly addressed through the nanoengineering of a new type of magnetoelectric coupling, whose voltage response is ionic triggered. Polymer-based nanocomposites with the IL [Bmim][Cl] and CFO nanoparticles were explored with respect to their fundamental properties and magnetoelectric response. Finally, an electrically optimized speedometer was developed as a proof of concept with the obtained materials.

This chapter is based on the following publication: Fernandes, L.C., Correia, D.M., Pereira, N., Ribeiro, C., Tubio, C.R., Martins, P., Lanceros-Méndez, S., *Ionic-triggered magnetoelectric coupling for magnetic sensing applications.* Applied Materials Today, 2022 **29**: p.101590

7.1 Introduction

Progress in energy, information and communication technologies largely relies on an optimized use of magnetic smart materials [1-4]. Such materials have largely contributed to the digital revolution by radically increasing data storage capacity, energy management/harvesting and data processing speeds [1, 5]. Thus, magnetic smart materials became fundamental in a large variety of electronic applications, ranging from the huge hard magnets in wind turbines to magnetic nanostructures for processing devices, sensing, actuation and data storage [6-9]. Among the different magnetic smart materials and over the past decade, ME materials and devices have been extensively investigated due to their applicability as multifunctional sensing devices with improved design variability and high ME coupling, making this field one of the most dynamic and promising research topics in the area of magnetism [10-14]. The ME effect usually refers to the interaction between ferromagnetic and ferroelectric order parameters in the same material, that make possible the modification of the magnetization (M_i) by electric fields (E_j) or, conversely, the control the polarization (P_i) by magnetic fields (H_j) [15-17], as quantified by **Equations 7.1** and **7.2**:

$$P_i = \alpha_{ij}.H_i \tag{7.1}$$

$$M_i = \frac{\alpha_{ij}}{\mu_0}E_j \tag{7.2}$$

being μ_0 the magnetic permeability of free space ($4\pi \times 10^{-7}$ N·A^{-2}) and the ME coefficient tensor [18]. The second rank tensor describes the interaction between the magnetic and electric orders of the matter, acting as the figure of merit for ME coupling, being calculated experimentally through **Equation 7.3**:

$$\alpha_{ij} = \frac{V_i}{tH_{ACj}} \tag{7.3}$$

where V_i is the induced voltage on the I direction, t is the thickness of the material and H_{Acj} is the amplitude of the AC magnetic field along the j direction [19].

The reported on single-phase ME materials such as Cr_2O_3, Gd_2CuO_4 and $BiFeO_3$ in the 1970's was very low (some mV.cm^{-1}.Oe^{-1}) and occurring at very low temperatures (<10 K), with below-room temperature Curie temperature. Further, the limited composition variations limited the opportunities for the successful tailoring the ME response [20, 21], hindering their incorporation into applications [16] and leading to a scientific numbness of the field [20, 22]. With the change of the millennium, multiferroic composite ME materials experienced a sharp increase in research

activities due to the improved ME conversion efficiency, two orders or magnitude higher than for single-phase materials [23, 24]. Among ME multiferroic composites, typically composed of a piezoelectric and a magnetostrictive phase, piezoelectric-ceramic based ME materials allow improved (three orders of magnitude higher) ME voltage responses when compared to the polymer-based systems, but they lack of flexibility, are difficult to process into specific shapes and large areas, are mechanically fragile and exhibit high leakage current density [16, 25]. On the other hand, polymer-based ME composites show suitable characteristics for applications such as flexibility, light weight, low power consumption, ability to conform into a variety of forms, simple integration into devices and compatibility with additive manufacturing technologies [25, 26].

Polymer-based ME composites can be classified according to their connectivity [16, 27] into (0–3) particulate nanocomposites; (2–2) laminate composites and (1–3) fiber/rod composites (**Figure 7.1**).

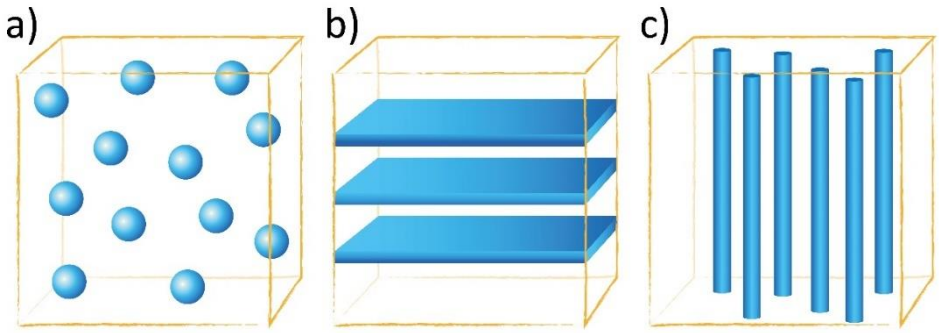


Figure 7.1 – Main connectivities found in polymer based ME materials: a) (0–3) particulate nanocomposites; b) (2–2) laminate composites and, c) (1–3) fiber/rod composites.

In (1–3) fiber/rod composites, the magnetic component can originate leakage currents during polarization [28] and for such reason very few attempts have been carried out to fabricate this type of ME composites. With respect to (0–3) particulate nanocomposites, the final properties of the developed ME composite can be easily designed by a careful selection of both magnetic and electric phases, by the tailoring of the magnetic/electric particle size, and by an adjustment of the processing parameters, being the main drawback of this type of composites the low ME response (just one order of magnitude higher than the one observed in single-phase ME materials and two orders of magnitude lower than the one found on laminated structures) [29]. Finally, in (2–2) laminate composites, the active layers (piezoelectric + magnetostrictive) are often connected by a coupling agent, causing the reduction or even removal of the undesired

leakage currents, leading to a higher ME coupling, but with deteriorated mechanical properties in the bonding area that harms their long-term use [21]. In order to obtain higher ME voltages (similar to the ones reported on ME laminates) with the advantages of the (0–3) particulate composites, new materials and approaches are urgently needed [16, 29, 30].

Further, two additional issues associated to composite ME materials with the aforementioned connectivities need to be addressed: i) the need to use superimposed DC and AC magnetic fields [16, 20, 30, 31] to obtain a suitable functional response [1]; and ii) the need of electric poling of the piezoelectric component of the composite [32]. In particular, the piezoelectric polarization processes hinders simple integration into devices and limits their service life [33].

In this context, MI materials appear as a suitable approach to tackle those challenges [20, 30, 34]. In those materials, the coupling between the magnetic and the electric order is mediated by the movement of ions as a response to a strain gradient: the flexoelectricity [16, 35]. The magneto-ionic modulation of electroactive materials is a recent strategy in the field of Mes and has large potential across a broad range of nanotechnology areas including nanobatteries, data storage and processing, sensing, and actuation [6, 36]. Several works have been reported regarding the voltage-control of magnetism in magnetoelectric/MI nanocomposites, in turn the magnetic-control of electric field in magnetoelectric/MI composites is still in its infancy [31], despite being pointed out [6, 20, 30, 37] that such approach could revolutionize the area, broadening the application range of the ME coupling, in particular in the scope of the IoT [20, 38].

This work reports on the ME response resulting from ionic migration in a nanocomposite composed of P(VDF-TrFE) [39, 40], [Bmim][Cl] (selected due to the solubility in the solvent, DMF, that also dissolves the P(VDF-TrFE) and high ionic conductivity) [41, 42] and $CoFe_2O_4$ – CFO nanoparticles (a ferromagnetic material that through its magnetic interaction with the external magnetic field will lead to the bending of the composite and consequently to the ionic migration of the IL [43, 44]): **Figure 7.2**.

This new type of ME coupling does not need an additional AC excitation magnetic field and the ME voltage coefficient can be therefore obtained after **Equation 7.3**, but just considering the applied DC magnetic field, the thickness of the composite and the maximum output voltage [45].

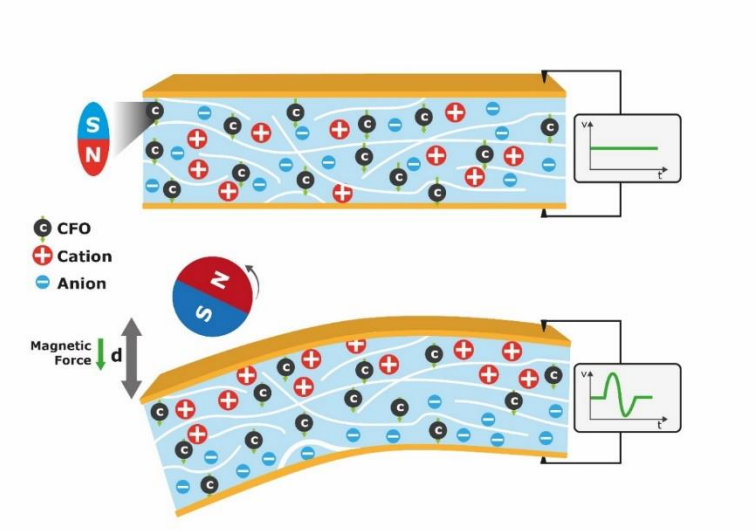


Figure 7.2 – Schematic representation of the ME coupling proposed in this work: i) A magnet will induce the bending of the composite due to the interaction with the CFO nanoparticles. Ii) The bending of the sample leads to an ionic charge separation through migration of the bigger IL [Bmim]+ cations to the direction of the surface with lower bending angle and the smaller Cl– anions to the direction of the surface with higher bending angle. Iii) The ionic charge separation leads to generation of the voltage across the sample.

7.2 Experimental section

7.2.1 Sample preparation

P(VDF-TrFE)/[Bmim][Cl] film

20 % in weight (wt. %) of IL [Bmim][Cl] was initially dispersed in DMF, under magnetic agitation, until a homogenous solution was obtained. Then, P(VDF-TrFE) was added in a P(VDF-TrFE)/DMF volume fraction of 15/85, until complete polymer dissolution. The solution was spread in a glass substrate at room temperature and solvent evaporation was performed at 90 ◦C for 30 minutes. Samples were allowed to cool until reaching room-temperature (≈30◦C).

P(VDF-TrFE)/[Bmim][Cl]/CFO films

Different contents of CFO nanoparticles (10, 20 and 30 wt. %) were dispersed in DMF in an ultrasound bath (ATU ATM 3LCD) for 1 hour. Under mechanical stirring, P(VDF-TrFE) was added in a P(VDF-TrFE)/DMF volume fraction of 15/85 until complete polymer dissolution. Finally, the IL was added at a 20 wt. %. The solution was spread in a glass substrate at room temperature and solvent evaporation was performed at 90 ◦C for 30 minutes. Samples were then allowed to cool until reaching room-temperature (≈30◦C).

7.2.2 Sample characterization

The samples morphological analysis was conducted through the SEM technique, while the physical-chemical properties were investigated using FTIR-ATR. Thermal properties were studied using the DSC technique. Additionally, the evaluation encompassed ionic conductivity, mechanical, and magnetic properties. Chapter 2 provides comprehensive details on the employed characterization techniques.

For the ME-flexoelectric characterization, the testing apparatus was composed by a neodymium disc magnet diametrically magnetized (6 mm of diameter and 3 mm of thickness, grade N35), connected to a stepper motor that controls the frequency from 0.1 Hz to 10 Hz. The composite films magnetized along the thickness direction at 2T were connected to a support with gold contacts allowing electrical characterization.

When the magnetic poles were coincident (between the magnet and the composite samples), there would be acting a repulsive force and the distance ***d*** between the magnet and the composite film increased; when the magnetic poles were opposite (between the magnet and the composite samples), there would be acting an attractive force and the distance ***d*** between the magnet and the composite film decreased. Thus the repeated action of attractive/repulsive forces lead to the bending of the film at the origin of the displacement of anions and cations of the IL (the largest moving to the gold surface with the largest curvature radius, and the smallest moving to the gold surface with the lowest curvature radius) leading therefore to the ME/flexoelectric voltage [46] across the sample.

Such movement results from the application of a magnetic field that bends the composite, as a result the differently sized ions or ion clusters inside the polymeric films will move from one side to the other as one side will have a larger volume expansion than the other.

The developed voltage response is thus based on the accumulation of the mobilized ions at the opposite electrodes in response to the externally-induced magnetic field. The application of the magnetic field and the interaction with the magnetic nanoparticles leads to a bending of the composite and the difference between the volumes of cations and anions results in a volume imbalance, leading to the differently sized ions or ion clusters within the polymeric film to move from one side or the other as one side will have a larger volume expansion than the other. The

ionic motion toward or away from each electrode can be reversed upon modulating the polarity of the magnetic field [39, 47, 48].

Signal acquisition was carried out with a band-pass filter with reference to half the supply voltage, ensuring to offset the negative part of the signal. The band-pass filter removed the DC component from the natural distribution of the ionic charges in the film and all the high frequencies contributions from the ambient noise (**Figure 7.3**).

The magnetic field produced by the rotation of the circular magnet was measured by a ratiometric linear Hall sensor (A1302 from allegro microsystems) with a sensibility of 2.5 mV.G^{-1}.

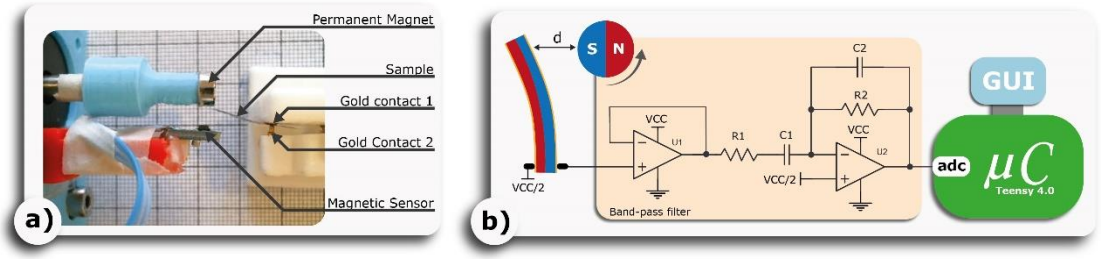


Figure 7.3 – a) Photograph exhibiting the different components of the magnetic testing apparatus. B) Schematic representation of the electronic circuit for filtering (f_{cl} and f_{ch}) and amplification (A):

$$A = -\frac{R_2}{R_1} \tag{7.4}$$

$$fc_l = \frac{1}{2\pi R_1 C_1} \tag{7.5}$$

$$fc_h = \frac{1}{2\pi R_2 C_2} \tag{7.6}$$

where R are the resistances and C capacitors.

The band-pass filter was designed for filtering frequencies between 0.08 Hz (fc_l) and (fc_h)15.9 Hz based on the following components, R_2= 1 GΩ, C_2=10 pF, R_1=20 kΩ, C_1=100 uF, and the operational amplifier MCP6V01 from microchip. An amplification gain (A) of 50000 was used in order to measure the signal by the 12-bit analog to digital converter (ADC) of the microcontroller Teensy 4.0, from PJRC. The microcontroller firmware sends the acquired signal of the films and Hall sensor to the PC for data visualization and storage in the graphic user interface (GUI). The GUI converts the raw data from the ADC to the proportional voltage and magnetic field.

7.3 Results and discussion

7.3.1 Material evaluation

Figure 7.4a-d show representative SEM images of the different nanocomposites (with and without IL and CFO) without substantial differences among them. The samples are characterized by a compact and smooth surface without micro-sized pores.

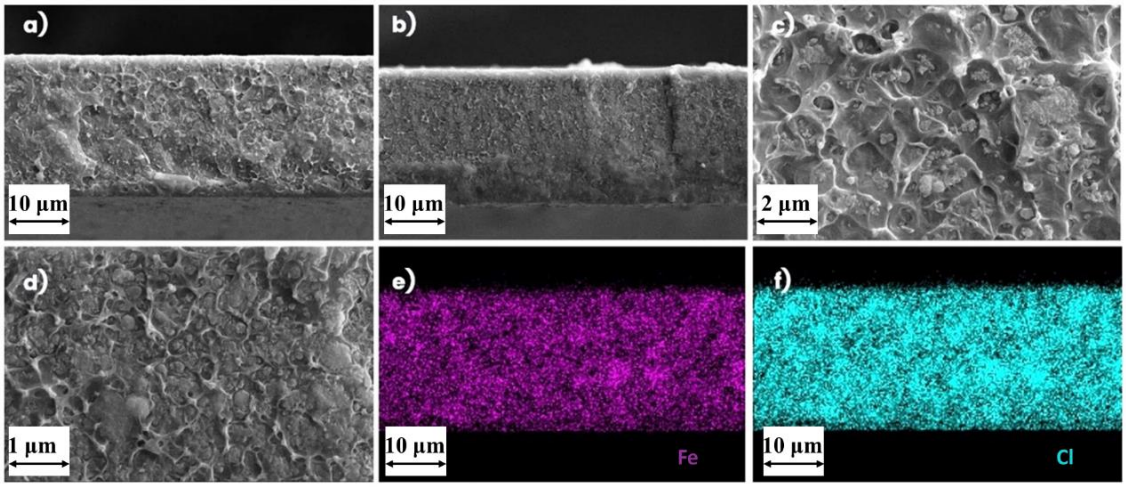


Figure 7.4 – Representative cross section SEM images of different samples: a) P(VDF-TrFE); b) P(VDF-TrFE)/IL; c) P(VDF-TrFE)/IL/CFO10; and d) P(VDF-TrFE)/IL/CFO30 with different magnifications. EDS analysis for the P(VDF-TrFE)/IL/CFO30: e) Fe mapping and; f) Cl mapping.

SEM images also allow to determine the thickness of the samples: P(VDF-TrFE) – 22 ± 2 µm; P(VDF-TrFE)/IL – 23 ± 2 µm; P(VDF-TrFE)/IL/CFO10 – 23 ± 3 µm; P(VDF-TrFE)/IL/CFO20 – 28 ± 3 µm; and P(VDF-TrFE)/IL/CFO30 – 34 ± 3 µm.

Thus, the thickness of the samples slightly increases with increasing CFO wt.% due to the increased viscosity. EDS mapping (**Figure 7.4e-f**) reveal that both CFO nanoparticles (Fe element) and IL (Cl element) are uniformly distributed throughout the composite and no agglomeration/sedimentation is detected.

The FTIR spectra shown in **Figure 7.5a** reveals that the characteristic vibration modes (851 cm^{-1}, 886 cm^{-1} and 1402 cm^{-1}) of the all-trans conformation of the polymer, indicating that the polymer fully crystallizes in the β-phase regardless the presence of the IL and the CFO nanoparticles [49].

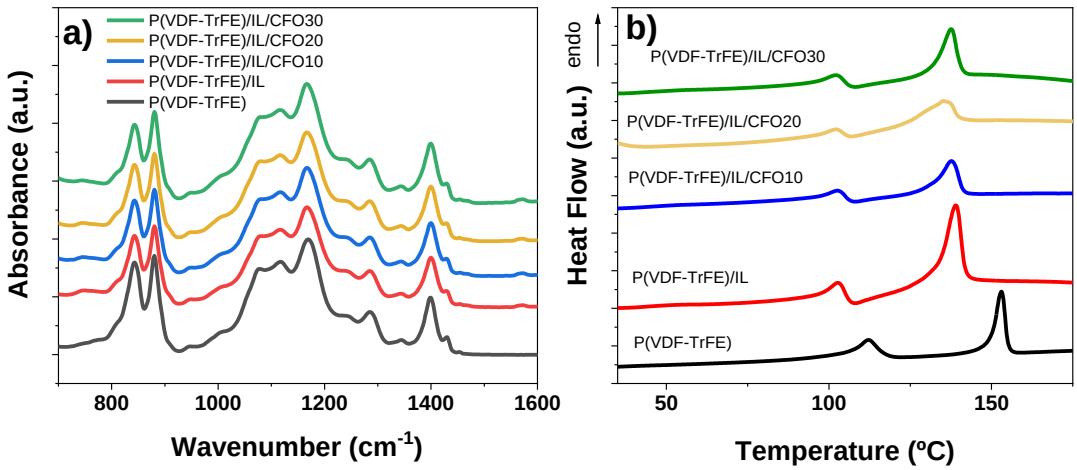


Figure 7.5 – a) FTIR-ATR spectra, and b) DSC thermograms of the different nanocomposites.

The DSC thermograms presented in **Figure 7.5b** show a lower temperature peak, around 102 – 112°C, corresponding to the ferroelectric–paraelectric transition (Curie transition-T_c), and the higher temperature transition peak, at 136–149°C, corresponding to the melting temperature, T_m, of the paraelectric phase [50].

The introduction of IL leads to a reduction of the polymer melting temperature from 149 °C to 139 °C and the Curie temperature from 112 °C to 103 °C, which is attributed to the ion-dipole electrostatic interactions between the polymer chains and the IL, determining the crystallization process [41]. Regardless the wt. % of CFO, no effect on both Curie temperature and melting temperature is observed. From DSC data of **Figure 7.5b**, the degree of crystallinity values were calculated through **Equation 2.2** and presented in **Table 7.1**.

Table 7.1 - - Curie temperature, melting temperature and degree of crystallinity of the different samples.

Sample	Curie Temperature (ºC ±1)	Melting Temperature (ºC ±1)	χ_c (%)
P(VDF-TrFE)	112	149	27
P(VDF-TrFE)/IL	103	139	50
P(VDF-TrFE)/IL/CFO10	102	138	31
P(VDF-TrFE)/IL/CFO20	102	136	33
P(VDF-TrFE)/IL/CFO30	102	138	32

Results from **Table 7.1** reveal that the addition of the IL almost doubles the degree of crystallinity of the neat P(VDF-TrFE) indicating that throughout the crystallization the IL leads to strong ion-dipole interactions supporting chain orientation and packaging, acting as a crystallization director [51]. CFO has the opposite effect (decreases the crystallinity) as large filler contents, as the ones used in this work, typically act as defective places during the crystallization process, hindering the growth and crystallization [52].

With respect to the mechanical characteristics, all samples reveal the usual characteristic of a thermoplastic polymer: a yielding separating the linear elastic region from the inelastic region (**Figure 7.6a**), being such behaviour independent of the presence of IL and/or CFO nanoparticles.

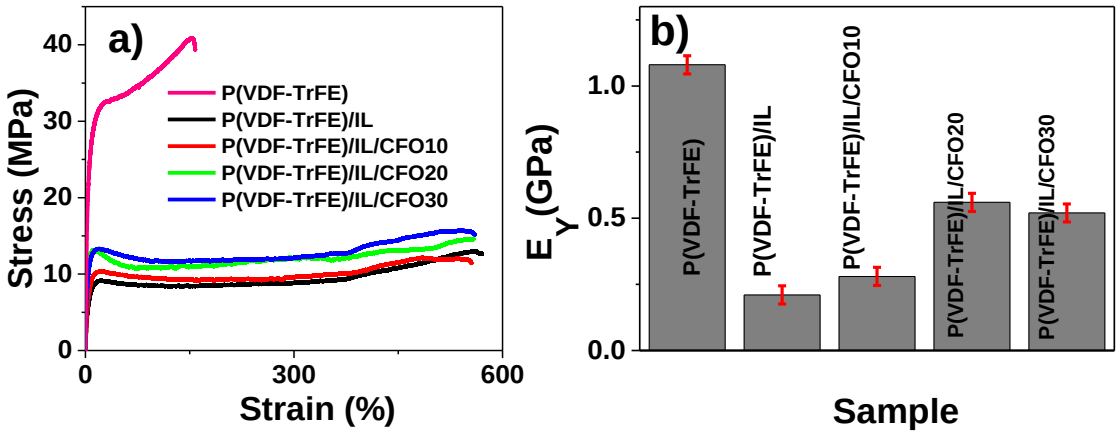


Figure 7.6 – a) Stress strain curves, and b) Young's modulus (E_Y) for the different samples.

Further, it is also verified that the yielding stress increases with increasing CFO content. The Young's modulus (E_Y) was evaluated (**Figure 7.6b**) from the linear elastic regime (**Figure 7.6a**) showing that the incorporation of the IL led to a substantial decrease of the elastic modulus, comparatively to neat P(VDF-TrFE), from 1.1 Gpa to 0.4 Gpa, as a result of the plasticizing effect of the IL [41]. On the other hand, the E_Y increases with the incorporation of the CFO fillers, being this increase more substantial for samples with higher CFO content (higher than 20 wt.%), fact that is related to the mechanical enhancement resulting from interaction of the magnetic nanoparticles and the P(VDF-TrFE) chains, and also with the higher E_Y of CFO (≈150 Gpa) [29, 53].

7.3.2 Ionic conductivity and magnetic/ME response

With the addition of IL into the P(VDF-TrFE) the flexibility of the polymer backbones increases, initiating the segmental motion of polymer chains (plasticizing effect), thus improving the frequency of ion hopping process within the polymer chains. Additionally, more mobile ions are added to the polymer matrix, and as a result a higher number of charge carrier are available for transportation, enhancing the ionic conductivity of the composite from ≈ 10^{-10} S·m^{-1} [54] to ≈ 1.7 × 10^{-5} S·m^{-1} (**Figure 7.7**) [55]. The ionic conductivity increases also with increasing CFO wt. %. (from 1.7 × 10^{-5} S·m^{-1} to 1.5 × 10^{-3} S·m^{-1}). In spinel ferrites such as CFO nanopowders the conduction process can be expressed by the Verwey mechanism, where the conduction is attributed to the hopping of electrons, between the ions of the same element but with different valence at the octahedral (B) site [56, 57]. Such electron exchange leading to local displacement of charges in the presence of an electric field is represented by the chemical **Equation 7.7** [57]:

$$Co^{2+} + Fe^{3+} = Co^{3+} + Fe^{2+} \tag{7.7}$$

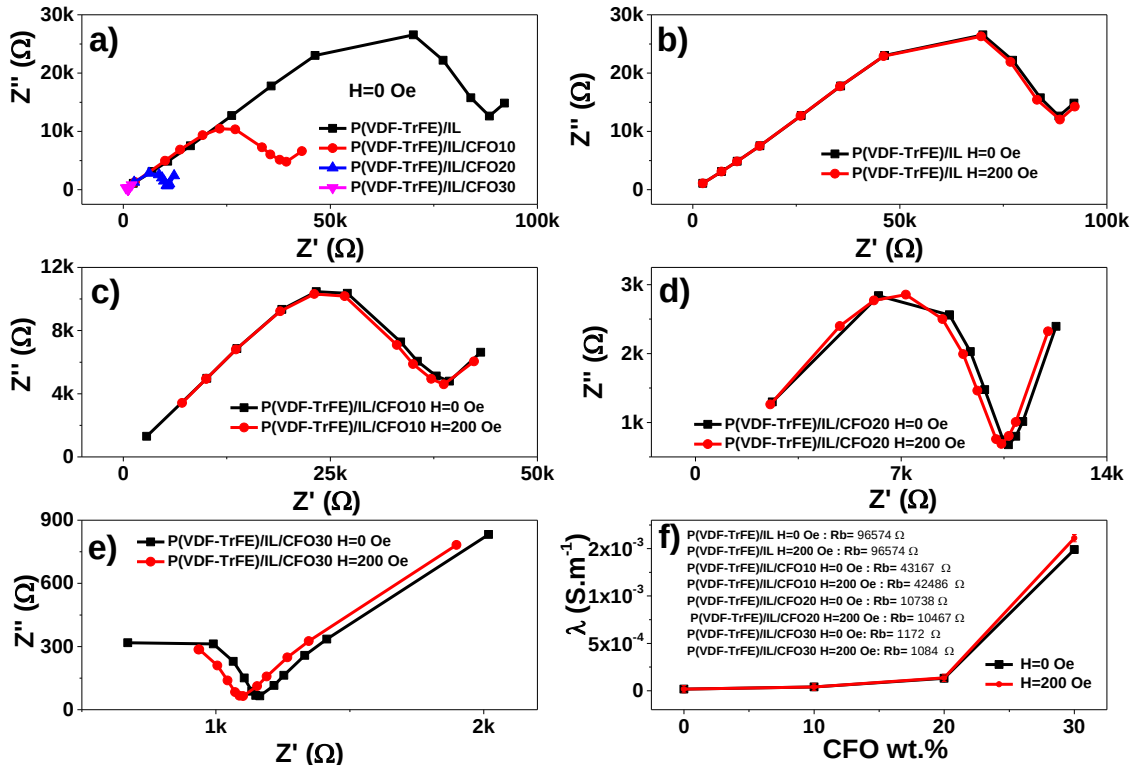


Figure 7.7 – a) Impedance spectroscopy for the different samples (no magnetic field applied). Comparison of the impedance spectroscopy with and without applied magnetic field for: b) P(VDF-TrFE)/IL; c) P(VDF-TrFE)/IL/CFO10; d) P(VDF-TrFE)/IL/CFO20; and e) P(VDF-TrFE)/IL/CFO30. f) Conductivity as a function of the CFO wt.% (with and without applied magnetic field).

Such hopping effect happens for CFO concentrations well below percolation (10 wt. % - 30 wt. %) once IL in their ionic migration can also act as charge carriers between adjacent CFO nanoparticles (**Figure 7.8**).

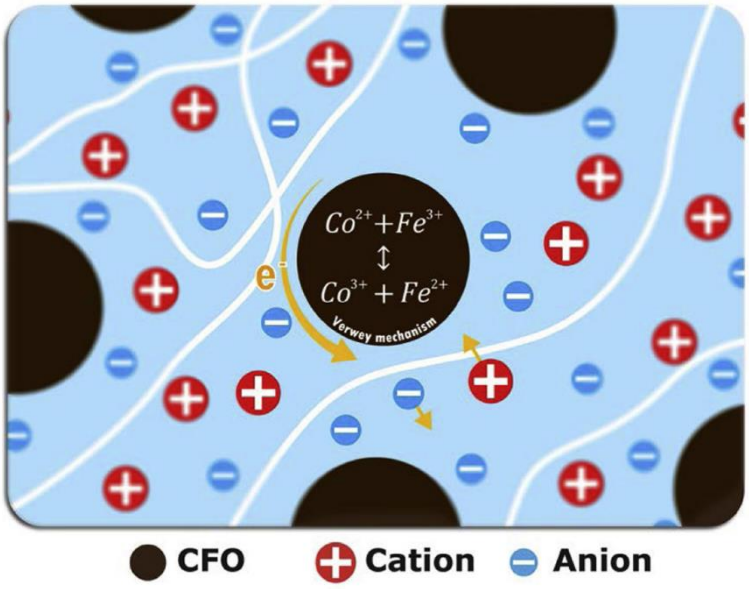


Figure 7.8 – Schematic representation of the conduction mechanism on the P(VDF-TrFE)/IL/CFO nanocomposites.

Thus, the lower degree of crystallinity, the ill-crystallization, and the interface charges as a result of the CFO addition, as well as the mentioned conduction process taking place in CFO, collectively favour the improvement in the ionic conductivity [58].

The small increase (≈ 8 %) on the ionic conductivity detected on samples with CFO when a magnetic field of 200 Oe was applied is explained by the action of the magnetic gradient force on the ions that are present on the composites [31].

The room-temperature magnetic properties of the P(VDF-TrFE)/IL/CFO composites has been evaluated as a function of the applied DC magnetic field and CFO wt. % (**Figure 7.9**).

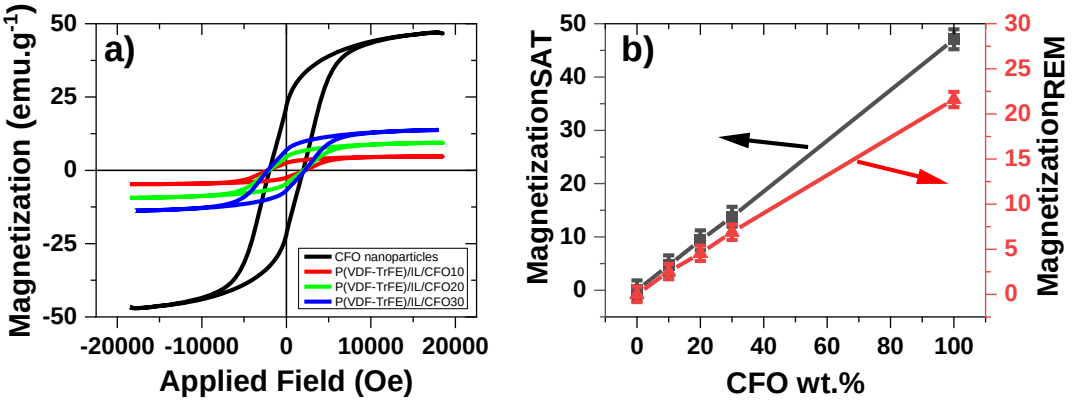


Figure 7.9 – a) Room-temperature magnetic hysteresis cycles for the P(VDF-TrFE)/IL/CFO composites with different CFO wt. % (the magnetization curve of the pure CFO nanoparticles is also shown for comparison). B) Magnetic saturation (MagnetizationSAT) and remanent magnetization (MagnetizationREM) as a function of the CFO wt. %.

The hysteresis loops presented in **Figure 7.9a** confirm the typical ferromagnetic behaviour of CFO with a coercivity of ≈2460 Oe and blocked magnetic moment in both CFO nanopowder and P(VDF-TrFE)/IL/CFO nanocomposites. Such ferromagnetic behaviour, that ensures a magnetization when the applied magnetic field is removed, will permit the magnetization of samples on the thickness direction that in turn will lead to the appearance of a magnetic force when the different samples are approached to the magnet with rotating polarity. **Figure 7.9b** demonstrates that the experimental fabrication of composites does not affect the magnetic properties of CFO. Finally, it is observed that the magnetic saturation and remanence values increase proportionally with increasing CFO wt. %, being the maximum values (47 emu·g^{-1} and 26 emu·g^{-1}) obtained for the composite with the highest (30 wt. %) filler content. This fact shows that the magnetic moment displayed by the P(VDF-TrFE)/IL/CFO nanocomposites turns out to be the sum of the different single contributions of the CFO nanoparticles within the polymer matrix, being also an indication of the suitable dispersion of the magnetic nanoparticles in the polymer matrix [59].Figure **7.10** shows the ME-flexoelectric behaviour of the samples with different CFO wt. % at frequencies of 0.5, 0.8, 2, 4 and 6 Hz.

The application of a magnetic field in the sample ranging from 0 mT to 500 mT through a rotating circular magnet originates a magnetic force proportional to the magnetic field shown in **Figure 7.10a-c** on the P(VDF-TrFE)/IL/CFO composites and, as a consequence, a bending movement. Such bending leads to the displacement of anions and cations (the largest moving to the gold surface electrodes with the largest curvature radius, and the smallest moving to the gold

surface with the lowest curvature radius) [39, 47, 48] creating an instantaneous ME/flexoelectric voltage (**Figure 7.10a-c**). Higher magnetic fields will create higher magnetic forces that will increase the voltage output until reaching the saturation.

Regarding the frequency response, the ME-flexoelectric voltage decreases when the frequency increases due to the smaller range of motion caused by the fast change of magnetic field polarities on the rotating magnet. At the highest frequencies (higher than 20 Hz) the sample will not be able to move, and the output voltage comes to zero. When the output voltage response is studied in the 0.5-6 Hz frequency range and as a function of time it is observed a nearly sinusoidal behaviour being the maximums and minimums explained by the mechanical/bending stimulus resulting from the movement triggered by the magnetic attraction and repulsion, respectively. Below 0.8 Hz the output voltage is already saturated once to those frequencies almost all anions and cations had time to move. Additionally, the ME-flexoelectric voltage increases with increasing CFO wt.% for all frequencies in the 0.5-10 Hz range once the magnetic force and consecutively bending is proportional to the CFO wt. %.

Aiming to compare the voltage generated in the proposed device (P(VDF-TrFE)/IL/CFO30 + electronic circuitry) with the ones reported for polymer composites with the highest ME coupling [60] and in a previous MI composite [31], such voltage has been divided on **Table 7.2** by the thickness (34×10^{-4} μm) of the composite (α') and by thickness (34×10^{-4} μm) and the DC magnetic field (α_{DC} – 400 Oe):

Table 7.2 reveals that the voltage output of the P(VDF-TrFE)/IL/CFO30 favourably compares with the ones reported in the literature, when it is normalized to the thickness of the composite and to the applied DC magnetic field.

Thus, all P(VDF-TrFE)/IL/CFO samples can detect the frequencies produced by the rotating magnetic field, with less noise being detected on the P(VDF-TrFE)/IL/CFO30 composite. For lower frequencies, the frequency detection decreases due to the fact that the samples need a bending strain for producing the ME-flexoelectric response.

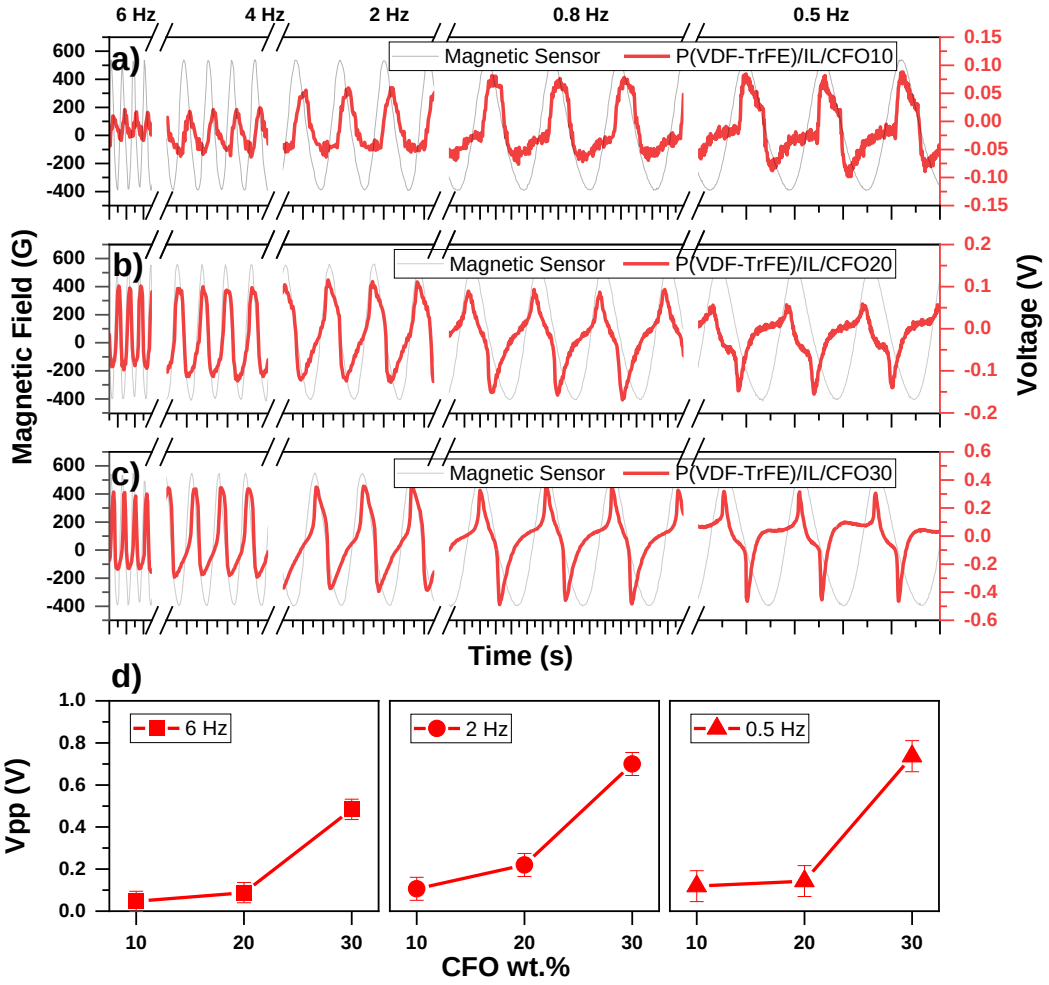


Figure 7.10 – ME-flexoelectric behaviour for composites with CFO content of: a) 10 wt. %; b) 20 wt. %, and c) 30 wt. % for a fixed IL content of 20 wt. %. D) ME-flexoelectric voltage response as a function of the CFO wt. % for different frequencies.

Table 7.2 – Comparation of the α, α' and α_{DC} reported in ME and MI composites.

Material/Figure of merit	α (V.cm^{-1}.Oe^{-1})	α' (V.cm^{-1})	α_{DC} (V.cm^{-1}.Oe^{-1})	Ref
P(VDF-TrFE)/Metglas	850	0.850	0.142	[60]
P(VDF-TrFE)/[Bmim][FeCl$_4$]	10	20	-	[31]
Proposed device	-	267	0.668	This

Tests were also performed on samples with IL and without CFO, and with CFO and without IL (**Figure 7.11**).

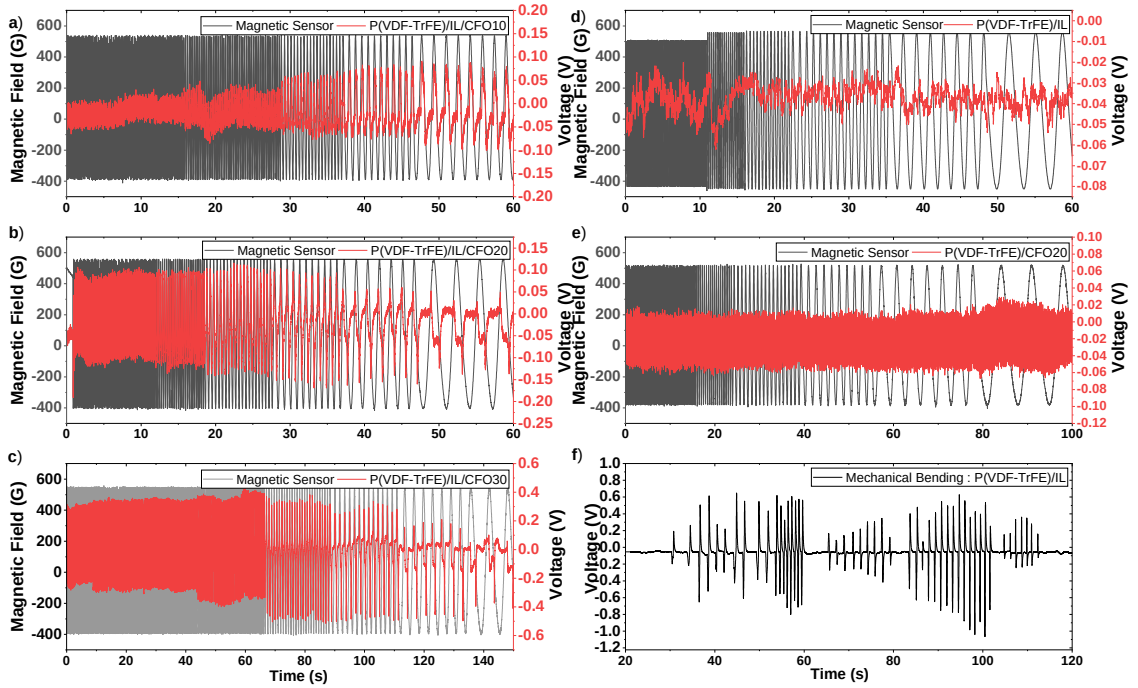


Figure 7.11 – Comparison of the voltage response/magnetic sensing capability of: a) Hall sensor and P(VDF-TrFE)/IL/CFO10, b) Hall sensor and P(VDF-TrFE)/IL/CFO20, c) Hall sensor and P(VDF-TrFE)/IL/CFO30, d) Hall sensor and P(VDF-TrFE)/IL, e) Hall sensor and P(VDF-TrFE)/CFO20, and f) Voltage response of the P(VDF-TrFE)/IL sample submitted to mechanical bending.

Only samples having CFO and IL on their composition exhibited linked (with matched frequency) voltage output response and magnetic input stimulation (**Figure 7.11a-c**). On the sample P(VDF-TrFE)/IL only noise can be detected on the output voltage response (**Figure 7.11d**). Results from P(VDF-TrFE)/CFO20 sample revealed an increased noise as a result of the CFO incorporation and IL removal from composite structure (**Figure 7.11e**). The mechanical bending of the P(VDF-TrFE)/IL/CFO composites led to an out voltage (**Figure 7.11f**) similar to the ones detected with magnetic stimulation.

7.3.3 Electronically optimized speedometer

Based on the obtained results, a frequency detector/speedometer was designed by connecting the sample with the higher output voltage (P(VDF-TrFE)/IL/CFO30) to the amplification circuit (**Figure 7.12a**). The software was developed in Qt Modeling Language (QML) using QT Creator for visualization of the speedometer application. The software detects the rising edge on the

crossover of a predefined voltage (0 V) that triggers the start of a timer, when another rising edge event occurs, the timer stops counting and saving the value. The result of the timer provides the signal period T, hence the frequency $f = T^{-1}$. The frequency value is associated in QML to the rotation of needle in the speedometer application. The proposed sensor exhibits (**Figure 7.12b**) higher linearity (r^2 =0.998) than some recently reported piezoelectric [61, 62], ME [63, 64] and speedometers based in magnetic composites [65, 66]. Such precise measurement of the rotational frequency allied to the contact-free way of sensing demonstrates the high application potential for the proposed sensor in a variety of IoT-related electronic applications including blocked rotor testing tools, automobile steering wheel sensors, angular positions sensors, position limit sensors, pulse counters, and robotics arm joints sensors, among others [66-68].

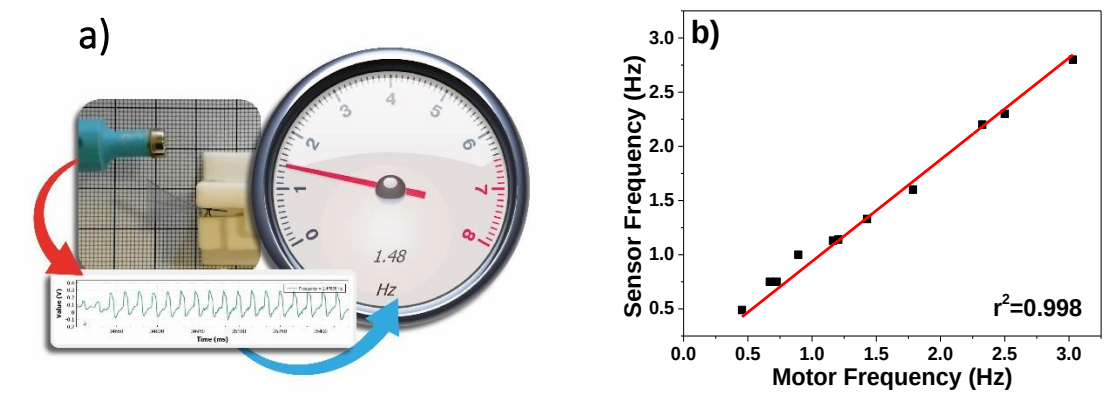


Figure 7.12 – a) Electronic speedometer based on the P(VDF-TrFE)/IL/CFO30 nanocomposite. B) Relation between the motor frequency and the sensor frequency. The insets shows a photograph of the P(VDF-TrFE)/IL/CFO30 nanocomposite.

7.4 Conclusions

In conclusion, this work offers a nanostructured route for the development of ME devices, suitable for application in the scope of the IoT and industry 4.0. The prepared P(VDF-TrFE)/IL/CFO (0-3) nanocomposites, obtained through a solvent casting method, exhibited an uniform structure, suitable thermal properties, improved ionic conductivity, tailored magnetic properties and a ≈0.6 V.cm^{-1}.Oe^{-1} ME voltage coefficient that allowed the development of a speedometer demonstrator with high linearity (r^2= 0.998). Specifically, the proposed ionic-triggered ME response can be used to overcome some of the applicability problems of the traditional ME materials, such as the need of electrical poling or the application of both AC and DC magnetic fields.

7.5 References

1. Wu, R., et al., *Self-biased magnetoelectric switching at room temperature in three-phase ferroelectric–antiferromagnetic–ferrimagnetic nanocomposites.* Nature Electronics, 2021. **4**(5): p. 333-341.
2. Yarali, E., et al., *Magneto-/ electro-responsive polymers toward manufacturing, characterization, and biomedical/ soft robotic applications.* Applied Materials Today, 2022. **26**: p. 101306.
3. H.R, L., et al., *Effect of cerium on structural, microstructural, magnetic and humidity sensing properties of Mn–Bi ferrites.* Nano-Structures & Nano-Objects, 2020. **24**: p. 100608.
4. Getzlaff, M., et al., *Magnetic nanoparticles in toner material.* Nano-Structures & Nano-Objects, 2020. **22**: p. 100462.
5. Takhsha Ghahfarokhi, M., et al., *Microfabricated ferromagnetic-shape-memory Heuslers: The geometry and size effects.* Applied Materials Today, 2021. **23**: p. 101058.
6. Nichterwitz, M., et al., *Advances in magneto-ionic materials and perspectives for their application.* APL Materials, 2021. **9**(3).
7. Liu, J., et al., *Magnetically propelled soft microrobot navigating through constricted microchannels.* Applied Materials Today, 2021. **25**: p. 101237.
8. Bichurin, M., et al. *Magnetoelectric Magnetic Field Sensors: A Review*. Sensors, 2021. **21**, DOI: 10.3390/s21186232.
9. Nazar, D.A.M., et al., *Boron nitride nanotubes decorated with magnetite nanoparticles for application as a multifunctional system in cancer treatment.* Nano-Structures & Nano-Objects, 2020. **24**: p. 100616.
10. Liang, X., H. Chen, and N.X. Sun, *Magnetoelectric materials and devices.* APL Materials, 2021. **9**(4).
11. Yue, Y., et al., *Buoy structural high-sensitive magnetoelectric sensors for soft robots' tactile sensing and avoiding obstacles.* Applied Materials Today, 2022. **27**: p. 101440.
12. Chen, X.-Z., et al., *Recent developments in magnetically driven micro- and nanorobots.* Applied Materials Today, 2017. **9**: p. 37-48.
13. Gao, J., et al. *Review of Magnetoelectric Sensors*. Actuators, 2021. **10**, DOI: 10.3390/act10060109.
14. Pradhan, D.K., S. Kumari, and P.D. Rack, *Magnetoelectric Composites: Applications, Coupling Mechanisms, and Future Directions.* Nanomaterials (Basel), 2020. **10**(10).
15. Gao, M., et al., *Magnetoelectricity in vertically aligned nanocomposites: Past, present, and future.* MRS Bulletin, 2021. **46**(2): p. 123-130.
16. Martins, P. and S. Lanceros-Méndez, *Polymer-based magnetoelectric materials: To be or not to be.* Applied Materials Today, 2019. **15**: p. 558-561.
17. Hu, J.-M., et al., *Understanding and designing magnetoelectric heterostructures guided by computation: progresses, remaining questions, and perspectives.* npj Computational Materials, 2017. **3**(1): p. 18.
18. Fiebig, M., *Revival of the magnetoelectric effect.* Journal of Physics D: Applied Physics, 2005. **38**(8): p. R123.
19. Karan, S.K., et al., *Small-Scale Energy Harvesting Devices for Smart Electronics*, in *Encyclopedia of Materials: Technical Ceramics and Glasses*, M. Pomeroy, Editor. 2021, Elsevier: Oxford. p. 391-425.
20. Pereira, N., et al., *Magnetoelectrics: Three Centuries of Research Heading towards the 4.0 Industrial Revolution.* Materials (Basel), 2020. **13**(18).
21. Martins, P., et al., *Theoretical optimization of magnetoelectric multilayer laminates.* Composites Science and Technology, 2021. **204**: p. 108642.
22. Yu, Z., et al., *Using magnetoelectric effect to reveal magnetization behavior of bulk and heavy ferromagnetic materials.* Applied Materials Today, 2021. **23**: p. 101051.
23. Yan, H., et al., *Electric-Field-Controlled Antiferromagnetic Spintronic Devices.* Advanced Materials, 2020. **32**(12): p. 1905603.

24. Nicolenco, A., et al., *Strain gradient mediated magnetoelectricity in Fe-Ga/P(VDF-TrFE) multiferroic bilayers integrated on silicon.* Applied Materials Today, 2020. **19**: p. 100579.
25. Pradhan, S., et al., *Magnetic field induced ferroelectric polarization voltage in compositional dependent (0–3) NFO/P(VDF-TrFE) nanocomposite film.* Smart Materials and Structures, 2021. **30**(7): p. 075034.
26. Mushtaq, F., et al., *Magnetoelectric 3D scaffolds for enhanced bone cell proliferation.* Applied Materials Today, 2019. **16**: p. 290-300.
27. Martins, P. and S. Lanceros-Méndez, *Polymer-Based Magnetoelectric Materials.* Advanced Functional Materials, 2013. **23**(27): p. 3371-3385.
28. Nan, C.-W., et al., *Multiferroic magnetoelectric composites: Historical perspective, status, and future directions.* Journal of Applied Physics, 2008. **103**(3): p. 031101.
29. Lima, A.C., et al., *Chapter 2 - Magnetic materials for magnetoelectric coupling: An unexpected journey*, in *Handbook of Magnetic Materials*, E. Brück, Editor. 2020, Elsevier. p. 57-110.
30. Liang, X., et al., *Roadmap on Magnetoelectric Materials and Devices.* IEEE Transactions on Magnetics, 2021. **57**(8): p. 1-57.
31. Correia, D.M., et al., *Low-field giant magneto-ionic response in polymer-based nanocomposites.* Nanoscale, 2018. **10**(33): p. 15747-15754.
32. Lázpita, P., et al., *Polarized Neutron Study of Ni-Mn-Ga Alloys: Site-Specific Spin Density Affected by Martensitic Transformation.* Physical Review Letters, 2017. **119**(15): p. 155701.
33. Shu, L., et al., *Flexoelectric materials and their related applications: A focused review.* Journal of Advanced Ceramics, 2019. **8**(2): p. 153-173.
34. Correia, D., et al., *All printed soft actuators based on ionic liquid/polymer hybrid materials.* Applied Materials Today, 2021. **22**: p. 100928.
35. Piedrahita, C.R., et al., *Flexoelectricity in Flexoionic Polymer Electrolyte Membranes: Effect of Thiosiloxane Modification on Poly(ethylene glycol) Diacrylate and Ionic Liquid Electrolyte Composites.* ACS Applied Materials & Interfaces, 2020. **12**(14): p. 16978-16986.
36. Wan, X., et al., *Bio-inspired ferromagnetic graphene oxide/magnetic ionic liquid membrane for highly efficient CO2 separation.* Applied Materials Today, 2021. **24**: p. 101164.
37. Leistner, K., *Electrochemical approaches to room temperature magnetoelectric materials.* Current Opinion in Electrochemistry, 2021. **25**: p. 100636.
38. Ghosh, S.K., et al., *Rollable Magnetoelectric Energy Harvester as a Wireless IoT Sensor.* ACS Sustainable Chemistry & Engineering, 2020. **8**(2): p. 864-873.
39. Dias, J.C., et al., *Improved response of ionic liquid-based bending actuators by tailored interaction with the polar fluorinated polymer matrix.* Electrochimica Acta, 2019. **296**: p. 598-607.
40. Siponkoski, T., et al., *A printable P(VDF-TrFE)-PZT Composite with Very High Piezoelectric Coefficient.* Applied Materials Today, 2020. **20**: p. 100696.
41. Meira, R.M., et al., *Ionic-Liquid-Based Electroactive Polymer Composites for Muscle Tissue Engineering.* ACS Applied Polymer Materials, 2019. **1**(10): p. 2649-2658.
42. He, L., et al., *Facile and effective promotion of β crystalline phase in poly(vinylidene fluoride) via the incorporation of imidazolium ionic liquids.* Polymer International, 2013. **62**(4): p. 638-646.
43. Shi, Y., et al., *Enhanced magnetoelectric response in nanostructures due to flexoelectric and flexomagnetic effects.* Journal of Magnetism and Magnetic Materials, 2021. **521**: p. 167523.
44. PourhosseiniAsl, M., et al., *Effective enhancement of piezomagnetic effect in core/shell structured cobalt/manganese-zinc nanocomposite.* Applied Materials Today, 2020. **21**: p. 100834.
45. Vopson, M.M., et al., *Measurement Techniques of the Magneto-Electric Coupling in Multiferroics.* Materials (Basel), 2017. **10**(8).
46. Piedrahita, C.R., et al., *Flexoelectricity in Flexoionic Polymer Electrolyte Membranes: Effect of Thiosiloxane Modification on Poly(ethylene glycol) Diacrylate and Ionic Liquid Electrolyte Composites.* ACS Applied Materials and Interfaces, 2020. **12**(14): p. 16978-16986.
47. Almomani, A., et al., *Influence of temperature on the electromechanical properties of ionic liquid-doped ionic polymer-metal composite actuators.* Polymers, 2017. **9**(8).

48. Feng, C., C.P. Hemantha Rajapaksha, and A. Jákli, *Ionic Elastomers for Electric Actuators and Sensors.* Engineering, 2021.
49. Costa, C.M., et al., *Effect of degree of porosity on the properties of poly(vinylidene fluoride–trifluorethylene) for Li-ion battery separators.* Journal of Membrane Science, 2012. **407-408**: p. 193-201.
50. Costa, C.M., et al., *Composition-dependent physical properties of poly[(vinylidene fluoride)-co-trifluoroethylene]–poly(ethylene oxide) blends.* Journal of Materials Science, 2013. **48**(9): p. 3494-3504.
51. Wu, L., et al., *Power generation by PVDF-TrFE/graphene nanocomposite films.* Composites Part B: Engineering, 2019. **164**: p. 703-709.
52. Bhatt, A.S., D.K. Bhat, and M.S. Santosh, *Crystallinity, conductivity, and magnetic properties of PVDF-Fe3O4 composite films.* Journal of Applied Polymer Science, 2011. **119**(2): p. 968-972.
53. Zhang, J.X., et al., *The effect of magnetic nanoparticles on the morphology, ferroelectric, and magnetoelectric behaviors of CFO/P(VDF-TrFE) 0–3 nanocomposites.* Journal of Applied Physics, 2009. **105**(5): p. 054102.
54. Costa, C.M., et al., *Novel poly(vinylidene fluoride-trifluoroethylene)/poly(ethylene oxide) blends for battery separators in lithium-ion applications.* Electrochimica Acta, 2013. **88**: p. 473-476.
55. Wong, C.C.Q., A.Y. Yap, and C.-W. Liew, *The effect of ionic liquid on the development of poly(vinyl alcohol) (PVA)-based ion conductors for electric double layer capacitors application.* Journal of Electroanalytical Chemistry, 2021. **886**: p. 115146.
56. Gabal, M.A., Y.M. Al Angari, and F.A. Al-Agel, *Cr-substituted Ni–Zn ferrites via oxalate decomposition. Structural, electrical and magnetic properties.* Journal of Magnetism and Magnetic Materials, 2015. **391**: p. 108-115.
57. Yadav, R.S., et al., *Impact of grain size and structural changes on magnetic, dielectric, electrical, impedance and modulus spectroscopic characteristics of $CoFe_2O_4$ nanoparticles synthesized by honey mediated sol-gel combustion method.* Advances in Natural Sciences: Nanoscience and Nanotechnology, 2017. **8**(4): p. 045002.
58. Bhatt, A.S. and D.K. Bhat, *Crystallinity, magnetic and electrochemical studies of PVDF/Co_3O_4 polymer electrolyte.* Materials Science and Engineering: B, 2012. **177**(2): p. 127-131.
59. Martins, P., et al., *Dielectric and magnetic properties of ferrite/poly(vinylidene fluoride) nanocomposites.* Materials Chemistry and Physics, 2012. **131**(3): p. 698-705.
60. Kulkarni, A., et al., *Giant magnetoelectric effect at low frequencies in polymer-based thin film composites.* Applied Physics Letters, 2014. **104**(2): p. 022904.
61. Huang, P., et al., *Carbon quantum dots inducing formation of β phase in PVDF-HFP to improve the piezoelectric performance.* Sensors and Actuators A: Physical, 2021. **330**: p. 112880.
62. Shahzad, A., et al., *Piezoelectric pressure sensors based on GO-modified P(VDF-TrFE) fibers for vacuum applications.* Journal of Materials Science: Materials in Electronics, 2020. **31**(21): p. 18627-18639.
63. Gonçalves, R., et al., *Synthesis of highly magnetostrictive nanostructures and their application in a polymer-based magnetoelectric sensing device.* European Polymer Journal, 2016. **84**: p. 685-692.
64. Reis, S., et al., *Fabrication and Characterization of High-Performance Polymer-Based Magnetoelectric DC Magnetic Field Sensors Devices.* IEEE Transactions on Industrial Electronics, 2017. **64**(6): p. 4928-4934.
65. Rupf, R., et al., *Original article: Validity of measuring wheelchair kinematics using one inertial measurement unit during commonly used testing protocols in elite wheelchair court sports.* J Biomech, 2021. **127**: p. 110654.
66. Mateev, V. and I. Marinova *Magnetic Elastomer Sensor for Dynamic Torque and Speed Measurements*. Electronics, 2021. **10**, DOI: 10.3390/electronics10030309.
67. Giebeler, C., et al., *Robust GMR sensors for angle detection and rotation speed sensing.* Sensors and Actuators A: Physical, 2001. **91**(1): p. 16-20.
68. Khan, M.A. and S.F. Khan. *IoT based framework for Vehicle Over-speed detection*. in *2018 1st International Conference on Computer Applications & Information Security (ICCAIS)*. 2018.

8 Humidity sensors based on magnetic ionic liquids blended in poly (vinylidene fluoride-co-hexafluoropropylene)

ILs sharing a magnetic anion are commonly used in the development of humidity sensors. So, in this chapter, IL/P(VDF-HFP) composite films were prepared by solvent casting by combining several imidazolium-based ILs with different chain lengths and distinct anions, namely, $[FeCl_4]^-$, $[(SCN)_4Co]^{2-}$, and $[CoCl_4]^{2-}$, within a P(VDF-HFP) polymer matrix. The influence of the anion and cation chain length in the different P(VDF-HFP)/IL composites was analyzed, and their potential as humidity sensors was demonstrated.

This chapter is based on the following publication: Serra, J.P., Fernandes, L.C., Pereira, N., Fidalgo-Marijuan, A., Porro, J.M., Costa, C.M., Correia, D.M., Lanceros-Méndez., S., *Humidity sensors based on magnetic ionic liquids blended in poly (vinylidene fluoride-co-hexafluoropropylene).* ACS Applied Polymer Materials, 2023. **5**: p:109–119

8.1 Introduction

Due to ILs hygroscopic nature, they are natural susceptible to water/humidity. However, this is still an area in development. To the best of our knowledge, few works have shown the potential of combining ILs with polymers as a platform for humidity sensing [1-5]. Due to its hydrophobicity, the IL 1-ethyl-3-methylimidazolium bis(trifluoromethylsulfonyl)imide ([Emim][TFSI]) was evaluated using P(VDF-HFP) as polymer matrix, by two different preparation methods (spin coating and electrospinning) showing a high sensitivity, linear response, and small hysteresis with humidity variation [2]. The hygroscopic magnetic IL [Bmim][$FeCl_4$] combined with PVDF was also evaluated as humidity sensor with varying MIL content up to 40 wt. % [1]. It was observed that the sensors showed a linear response with humidity changes between 35 and 90 %, and their sensitivity increased with increasing MIL content.

As it was demonstrated, ILs sharing a magnetic anion are commonly used in the development of humidity sensors. So, in the present work, P(VDF-HFP)/IL composite films were prepared by solvent casting by combining several imidazolium-based ILs with different chain lengths and distinct anions, namely $[FeCl_4]^-$, $[(SCN)_4Co]^{2-}$ and $[CoCl_4]^-$, within a P(VDF-HFP) polymer matrix. Thus, the influence of anion and cation chain length in the different P(VDF-HFP) composites was analysed and their potential as humidity sensors demonstrated.

8.2 Experimental section

8.2.1 Preparation of the samples

Neat P(VDF-HFP) and P(VDF-HFP) incorporating 40 wt. % of the different ILs were prepared by a solvent casting method. The 40 wt. % IL content was selected based on the highest concentration commonly used for IL-polymer based materials [6, 7].

Neat P(VDF-HFP) films were obtained in two steps (**Figure 8.1**). In a first step, the polymer was dissolved into DMF (15/85 wt. %) under magnetic stirring at 40 °C. In a second step, the polymer dissolution was spread onto a glass substrate, followed by solvent evaporation at 210°C for 10 minutes in an oven (P-Selecta). For P(VDF-HFP)/IL composites, previous to the polymer addition, the different ILs (40 wt. %) were added to the DMF solvent. Samples with a thickness between 35-84 μm were obtained.

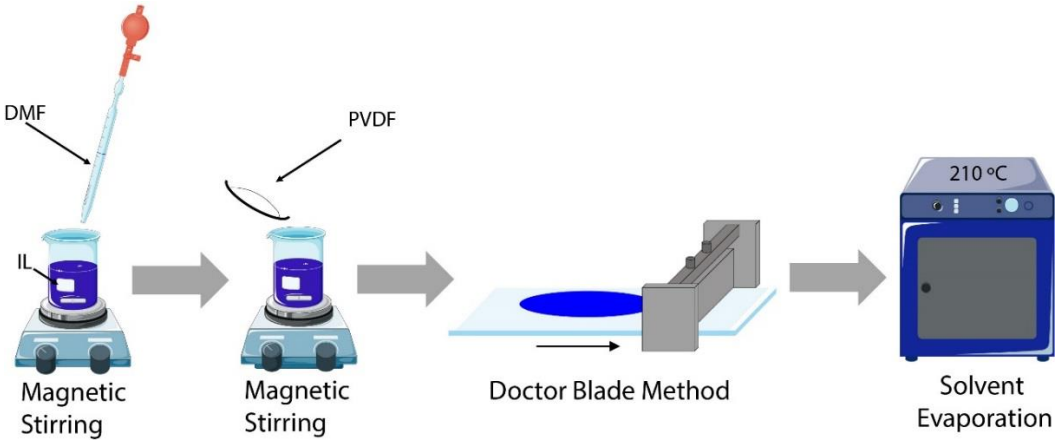


Figure 8.1 - Schematic representation of the procedure used to develop the IL/P(VDF-HFP) composites.

8.2.2 Sample characterization

The SEM technique was utilized to analyse the morphology of both net PVDF-HFP and IL/PVDF-HFP composites. The physical-chemical properties were investigated using the FTIR-ATR technique, while the thermal properties were examined through DSC and TGA techniques. The evaluation of mechanical properties involved stress-strain measurements, and magnetic properties were studied using VSM. Additionally, the electrochemical and ionic conductivity of the samples were assessed. Chapter 2 contains detailed information on all parameters related to the characterization techniques.

8.2.3 Humidity sensor response characterization

A custom-built humidity chamber was used for humidity sensing response characterization of the samples (**Figure 8.2**). The chamber is composed by a nebulizer (Medisana IN 500) that introduces humidity in the chamber. A combination of two fans, one for introducing air and another one to remove it, works to clear the humidity from the chamber. The samples were placed in the centre of the chamber with a commercial humidity and temperature data logger (Amprobe TR200-A). The samples were connected to a Quadtech 1920 LCR precision meter.

A screen printed interdigit was printed in the samples, thus allowing for the impedance measurements. The designed interdigit structure, consisting in 15 fingers with a 0.5 mm gap (inset of **Figure 8.2a**), allows the evaluation of the impedance variation upon relative humidity changes. The interdigit structure was screen printed with a mesh of 100 threads

per centimetre, with conductive silver paste DT1201 (from Hunan LEED electronics Ink), cured during 30 minutes at 120 °C on an electric forced convection oven (JP selecta 2005165). A poly(ethylene terephthalate) (PET) film tape was placed on top of the interdigit for protection from direct contact with the humidity variation.

For the characterization of the variation of the impedance with the relative humidity, the samples were connected to a LCR Meter with the function of impedance measurement at a sampling rate of 0.5 seconds. An amprobe TR200-A humidity and temperature sensor was used for the comparison of the impedance of the samples with the corresponding humidity value. All the data are saved in a txt. file by a custom-built python-based application. The experiment lasted 3000 s, with an acquisition time of 500 ms for the impedance measurements and of 1 s for the reference relative humidity-RH (Amprobe TR200-A). The number of cycles was different for the different samples due to the time needed to lower the RH from the chamber, the RH on the chamber being dependent of the ambient RH on the room.

The humidity response of the samples was assessed by the impedance variation by changing the relative humidity from 30% to 85% (**Figure 8.2b**).

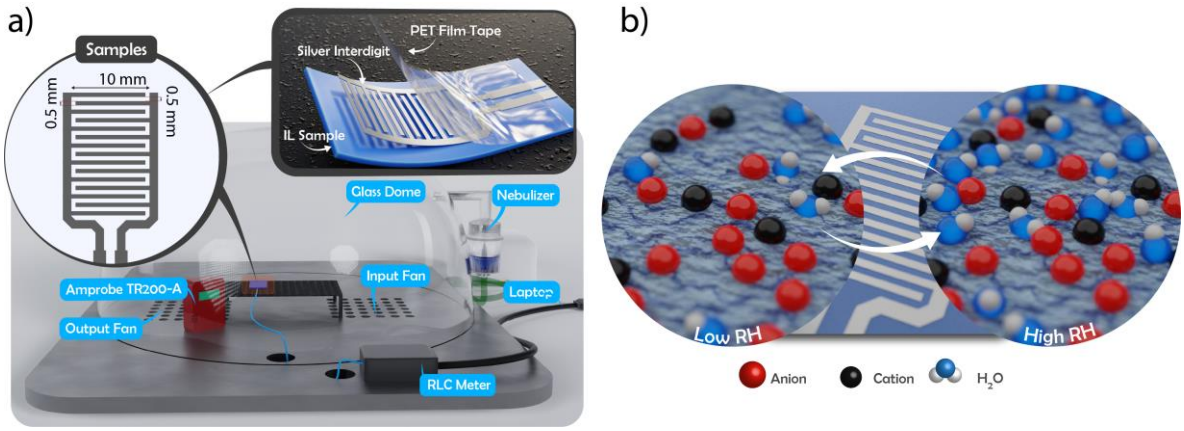


Figure 8.2 - a) Custom-built humidity characterization setup b) Representation of the humidity ionic and water content varation with the variation of RH.

8.3 Results and discussion

8.3.1 Morphology

The morphology of both neat and P(VDF-HFP)/IL composites was analysed from representative cross-section images (**Figure 8.3**) for P(VDF-HFP) and for the P(VDF-HFP)/IL samples comprising different ILs.

As reported in related studies [8] the used processing conditions (solvent evaporation at 210 °C) leads to homogenous and non-porous P(VDF-HFP) films as demonstrated in the surface and cross-section images of **Figure 8.3a and 8.3b**.

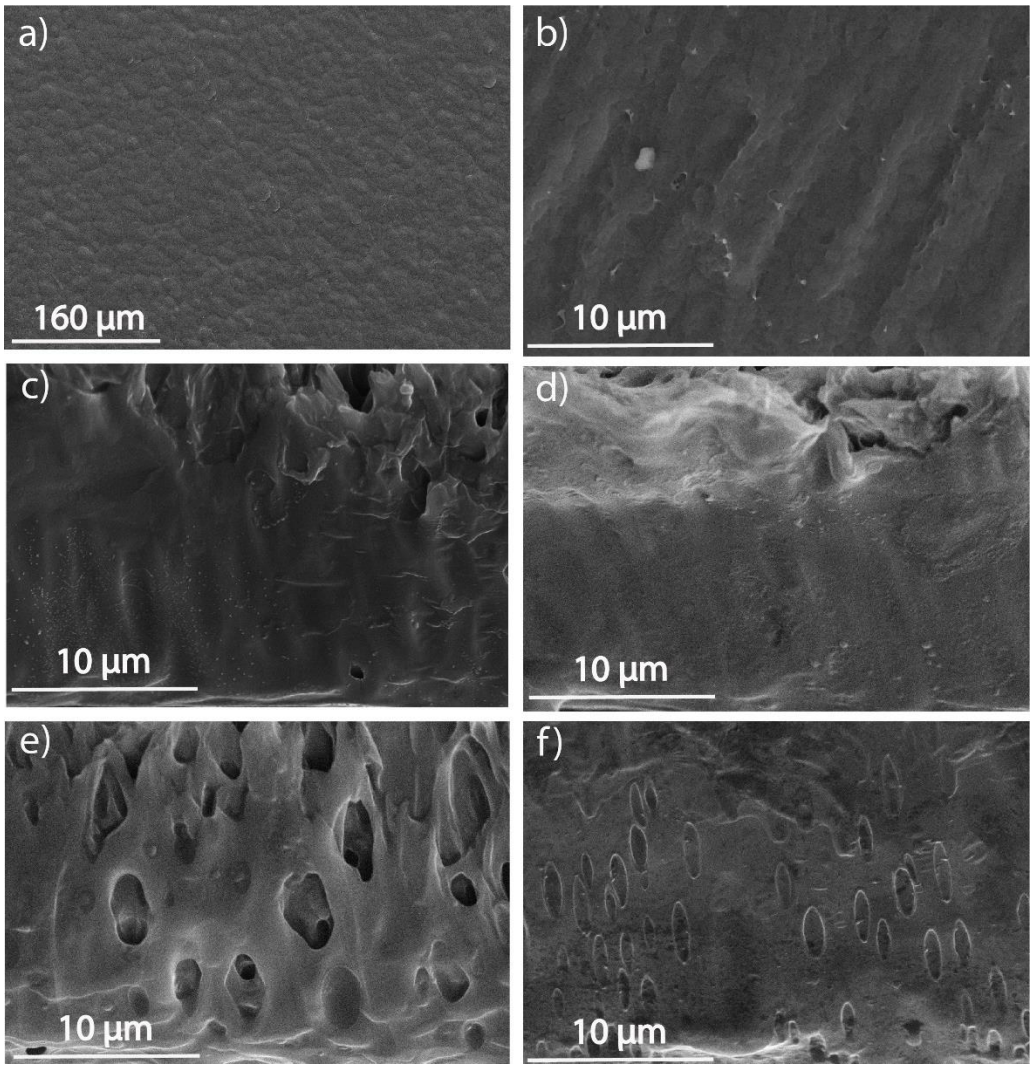


Figure 8.3 – SEM images of the different IL/P(VDF-HFP) composites: a) P(VDF-HFP) surface; b) P(VDF-HFP) cross section; c) $[Bmim]_2[CoCl_4]$; d) $[Bmim][FeCl_4]$; e) $[Bmim]_2[Co(SCN)_4]$; and f) $[Emim]_2[Co(SCN)_4]$.

Upon the incorporation of the ILs, a modification of the main morphological features occurs. **Figure 8.3c-8.3e** show that, independently of the IL anion type, the incorporation of the ILs into the polymer matrix leads to the formation of a porous structure, being this porosity more noticeable for the samples incorporating the $[Co(SCN)_4]^-$ anion, as shown in the cross-section images. Further, it is also observed a small influence of the cation chain length in the morphology. By comparing Figures 3e and 3f, it is observed that a decrease in the cation chain length from $[Bmim]_2[Co(SCN)_4]$ to $[Emim]_2[Co(SCN)_4]$ induces a decrease in the porosity of the samples. The presence of a porous structure results from a liquid-liquid polymer-solvent phase separation process during polymer crystallization, that is influenced by the incorporation of the different ILs' incorporation into the polymer matrix. Due to the strong interaction of the different ILs with the DMF solvent, the ILs migrates together with the solvent to the areas from which the solvent is latter evaporated, leading the porous structure [9]. The higher porosity of the samples incorporating the IL sharing the same $[Co(SCN)_4]^-$ anion comparatively to the other IL/polymer based samples are an indication of the stronger IL-polymer interactions, weakening the polymer-solvent interaction and, therefore, facilitating the liquid-liquid phase separation process.

A SEM-EDX analysis was performed to verify the incorporation and distribution of the ILs into the P(VDF-HFP) matrix, as presented in **Figure 8.4**.

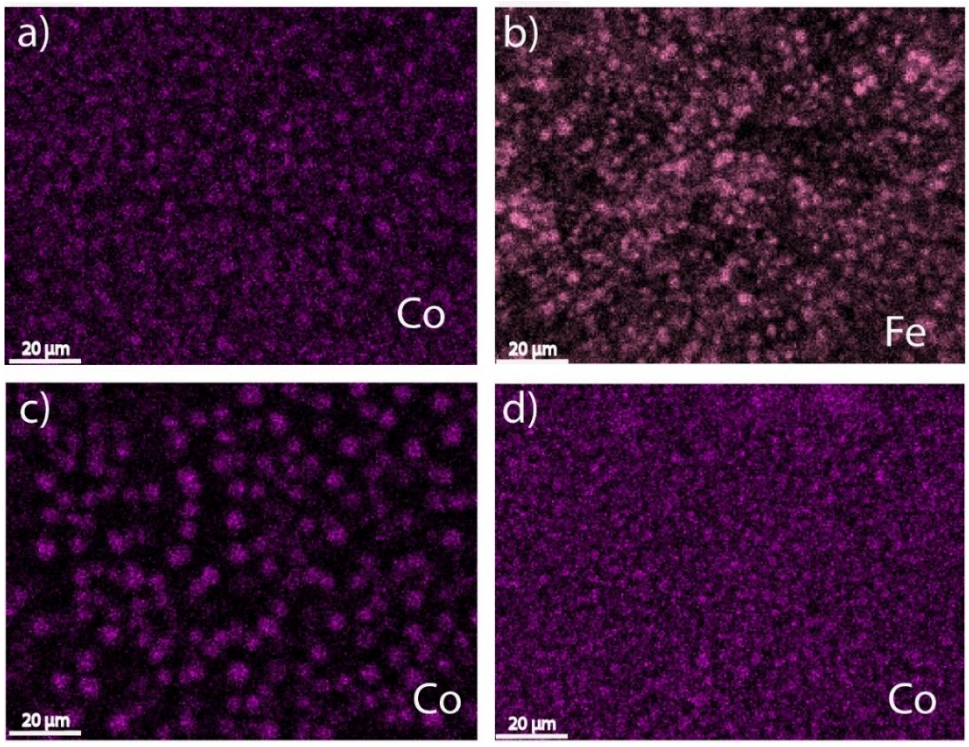


Figure 8.4 - SEM-EDX images showing the dispersion of Co and Fe elements into the different P(VDF-HFP)/IL composites a) $[Bmim]_2[CoCl_4]$, b) $[Bmim][FeCl_4]$, c) $[Bmim]_2[Co(SCN)_4]$ and d) $[Emim]_2[Co(SCN)_4]$.

From the SEM-EDX samples it is observed that the Co belonging to the $[Bmim]_2[CoCl_4]$, $[Bmim]_2[Co(SCN)_4]$ and $[Emim]_2[Co(SCN)_4]$ ILs is present in the P(VDF-HFP)/IL samples, as well as the Fe in the sample incorporating the $[BMIM][FeCl_4]$ IL. Small IL clusters are homogeneously distributed along the samples, related to the pores formed during sample processing.

8.3.2 Polymer phase content, thermal and mechanical properties

The influence of IL anion type and cation chain length on the P(VDF-HFP) vibration spectra was evaluated by FTIR. **Figure 8.5a** shows the FTIR-ATR spectra for neat P(VDF-HFP) and the different PVDF-HFP/IL composites.

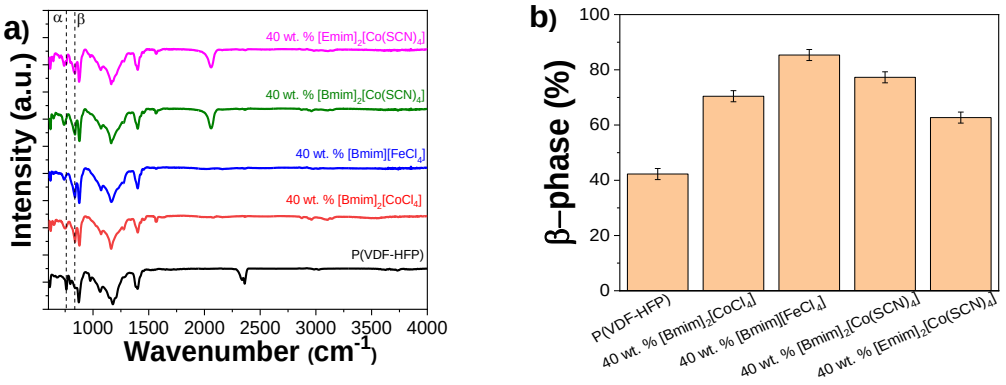


Figure 8.5 - a) FTIR-ATR spectra for neat P(VDF-HFP) and for the different P(VDF-HFP)/IL composites incorporating imidazolium based ILs with different anions. b) Corresponding β-phase content for the samples.

PVDF-HFP is characterized by the presence of the absorption bands corresponding to the stretching vibrations of the CH_2 and CF_2 groups. From the FTIR-ATR spectra it is possible to identify the polymer chain conformation in both the non-polar trans–gauche–trans–gauche´ (TGTG´) conformation, ascribed as P(VDF-HFP) α-phase, and the presence of the polar crystalline β-phase, characterized by a zig-zag (all trans) PVDF-HFP conformation. The α-phase is identified by the absorption bands at 764, 796 and 976 cm^{-1} and the polar β-phase by the bands at 840 and 878 cm^{-1} [10]. The characteristic bands at 1069, 1179 and 1402 cm^{-1} correspond to CF_3 out-of-plane deformation, antisymmetric CF_2 stretch and CH_2 wagging, respectively [11-13].

The presence of ILs into P(VDF-HFP) matrix is also identified in the FTIR-ATR spectra. The imidazolium cations $[Bmim]^+$ and $[Emim]^+$ are identified at 1275, 1450 and 1564 cm^{-1}

corresponding to stretching C-C and C-N vibrations characteristic of the NC(H)N and CCH groups of the imidazolium ring [14-16]. The absorption bands at 2061 cm^{-1} in both P(VDF-HFP)/IL composites comprising the ILs $[Emim]^+$ and $[Bmim]^+$ cations sharing the same anion, $[Co(SCN)_4]^{2-}$, are attributed to the C-N vibration modes [17, 18].

Upon the IL incorporation, and independently of the IL type, the intensity of the absorption band at 840 cm^{-1} increases being accompanied by a decrease in the intensity of the absorption band at 764 cm^{-1}, indicating that the ILs lead to a conformation change of P(VDF-HFP) from the α- to the β-phase. The quantification of the β-phase content in the P(VDF-HFP)/IL composites was performed using **Equation 2.1** [19] and the results are shown in **Figure 8.5b**. Independently of the IL type, the β-phase content increases in the composites with respect to neat P(VDF-HFP). This increase is more noticeable for P(VDF-HFP)/[Bmim][$FeCl_4$] displaying an increase from 42 % to 85 %, followed by the $[Bmim]_2[Co(SCN)_4]$ PVDF-HFP (77 %), $[Bmim]_2[CoCl_4]$/ PVDF-HFP (70 %), and $[Emim]_2[Co(SCN)_4]$ P(VDF-HFP) (63 %). The observed differences indicate strong ion-dipole electrostatic interactions during polymer crystallization between the highly polar P(VDF-HFP) polymer chains with the cation and anion from the IL $[Bmim]_2[Co(SCN)_4]$, comparatively to the other incorporated ILs studied [7, 17]. Further, it is also noticeable the cation chain length influence from $[Emim]^+$ to $[Bmim]^+$ into the β-phase content, being the polar phase content enhanced by increasing the size ring as a result of the decrease of the attractive forces between the cation and anion from the IL, which favours the IL-P(VDF-HFP) chain interactions in [20].

The influence of the incorporation of the ILs on the thermal properties of the samples was evaluated by DSC and TGA analysis (**Figure 8.6**).

Figure 8.6a shows the DSC thermograms of the samples, in which a single endothermic peak between 120 and 160 °C is observed, corresponding to the melting temperature of the polymer. Independently of the IL type, no variations are detected in the melting temperature. However, a decrease in the intensity of the melting peak is observed for the P(VDF-HFP)/IL composites, indicating a decrease in the degree of crystallinity, quantitatively evaluated using **Equation 2.3** (**Table 8.1**). The P(VDF-HFP)/[Bmim][$FeCl_4$] composite shows the same degree of crystallinity of neat P(VDF-HFP) (17 %), whereas a reduction of the degree of crystallinity to values between 11 and 13 %, are observed after incorporation of $[Bmim]_2[CoCl_4]$, $[Bmim]_2[Co(SCN)_4]$, and $[Emim]_2[Co(SCN)_4]$ in the polymer matrix. This decrease indicates that the presence of the IL acts

as a defect during polymer crystallization, leading to a decrease in the lamellar spherulite size [20].

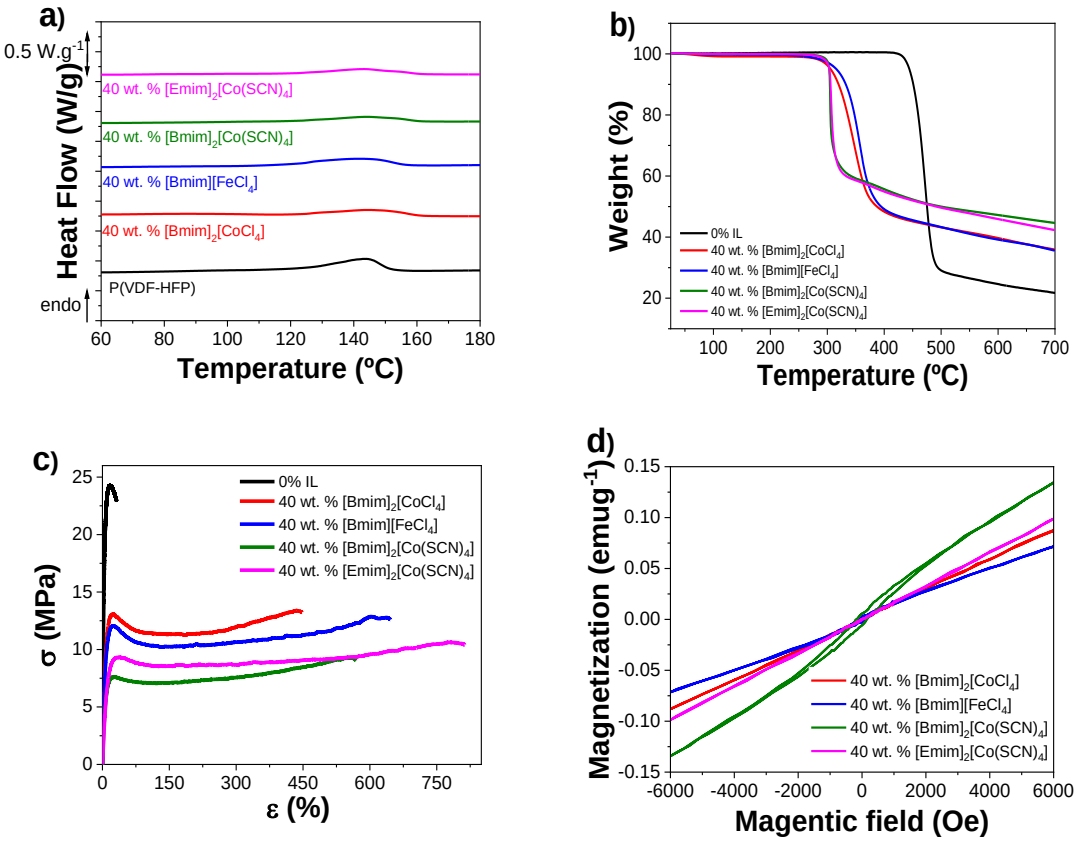


Figure 8.6 - a) DSC curves, b) TGA thermograms, c) Stress-strain mechanical curves and d) magnetic room-temperature hysteresis loops for neat P(VDF-HFP) and for the different P(VDF-HFP)/IL composites incorporating imidazolium based ILs with different anions.

Table 8.1- Degree of crystallinity ($\Delta\chi$), stress at yield (σ_y) and Young modulus (E') for the P(VDF-HFP)/IL samples

Sample	**$\Delta\chi$ / ± 2%**	σ_y (± 5 MPa)	**E' / ± 10 MPa**
P(VDF-HFP)	17	24.4	880
$[Bmim]_2[CoCl_4]$/P(VDF-HFP)	13	13.2	170
[Bmim][$FeCl_4$]/P(VDF-HFP)	18	11.9	148
$[Bmim]_2[Co(SCN)_4]$/ P(VDF-HFP)	11	7.6	75
$[Emim]_2[Co(SCN)_4]$/ P(VDF-HFP)	12	9.3	84

The influence of the different imidazolium based ILs on the thermal stability of P(VDF-HFP) was evaluated by TGA measurements (**Figure 8.6b**). The thermal degradation of P(VDF-HFP) occurs

in a single degradation step (T_{onset} ~ 442 °C) due to the scission of the C-C, C-H and C-F bonds [21]. Upon the ILs incorporation into the PVDF-HFP matrix, two mass loss steps are observed: the lower temperature one, between 25 and 100 °C and representing a mass loss between 1-2 %, is attributed to the absorbed water loss as a result of the hygroscopic character of imidazolium based ILs [17], whereas the higher temperature one identifies the thermal degradation of both the IL and the P(VDF-HFP) polymer chain. The observed results indicate that, independently of the IL type and cation chain length, the incorporation of ILs into P(VDF-HFP) matrix results in a reduction of the thermal stability, being this decrease more noticeable for the composites incorporating the $[Co(SCN)_4]^{2-}$ anion. This is a consequence of the strong ion-dipole interactions of the ILs, particularly for the ILs sharing the $[Co(SCN)_4]^{2-}$ anion with the P(VDF-HFP) matrix, which demonstrated that the anions and cations from the ILs catalytically affects the P(VDF-HFP) thermal degradation [17].

With respect to $[Emim]^+$ and $[Bmim]^+$ cations sharing the same anion $[Co(SCN)_4]^{2-}$, no changes are observed in the T_{onset} of both P(VDF-HFP)/$[Bmim]_2[Co(SCN)_4]$ and P(VDF-HFP)/$[Emim]_2[Co(SCN)_4]$ composites, starting the thermal degradation to occur at ~303 °C. P(VDF-HFP)/$[Bmim]_2[CoCl_4]$ starts the degradation at 311 °C and the composite P(VDF-HFP)/$[Bmim][FeCl_4]$ a Tonset of 322 °C.

The mechanical properties of P(VDF-HFP) and the P(VDF-HFP)/IL composites were evaluated by stress vs strain measurements as shown in **Figure 8.6c**. The characteristic stress-strain mechanical response of thermoplastic polymers are observed for all the samples, and is characterized by linear region, a yielding region and fracture at an ultimate stress. Regardless of the IL type, its addition to a composite sample affects the mechanical properties compared to neat P(VDF-HFP). The Young modulus was evaluated in the elastic region by the tangent method at 3% of maximum elongation and is presented in **Table 8.1**. Independently of the IL type, the Young modulus of the IL/P(VDF-HFP) composites decreases when compared to neat PVDF-HFP due to a plasticizing effect of the IL [20]. Additionally, with the ILs incorporation, the yield strength (σ_y) decreases with respect to neat P(VDF-HFP), being this decrease more noticeable for the composite P(VDF-HFP)/$[Bmim]_2[Co(SCN)_4]$, followed by the composites P(VDF-HFP)/$[Emim]_2[Co(SCN)_4]$, P(VDF-HFP)/$[Bmim][FeCl_4]$ and P(VDF-HFP)/$[Bmim]_2[CoCl_4]$. The observed decrease in both Young modulus and σ_y occur is a result of the ILs plasticizing effect in the polymer matrix, being this effect more noticeable for the composite P(VDF-

HFP)/$[Bmim]_2[Co(SCN)_4]$ due to the presence of strong ion-dipole interactions between the IL and the polymer matrix [17].

8.3.3 Magnetic response and ionic conductivity

Due to the magnetic nature of the used ILs, the magnetic properties of the developed composites were evaluated by VSM. **Figure 8.6d** shows the magnetic response of the P(VDF-HFP)/IL composites evaluated from VSM, characterized by a linear behaviour typical of paramagnetic materials for all of the samples but one, P(VDF-HFP)/$[Bmim]_2[Co(SCN)_4]$, which is showing an incipient ferromagnetic behaviour. Among the different samples, the composites P(VDF-HFP)/$[Bmim]_2[Co(SCN)_4]$ and P(VDF-HFP)/$[Bmim][FeCl_4]$ developed a higher magnetization response with the applied magnetic field due to stronger covalence of the Fe-Cl bond and Co-SCN bond when compared with the Co-Cl bond [22].

The effect of the different ILs on the ionic conductivity of the P(VDF-HFP)/IL composites was determined by impedance spectroscopy (**Figure 8.7**). **Figure 8.7a** shows the Nyquist plot of 40 wt. % P(VDF-HFP)/IL composites with $[Bmim][FeCl_4]$ at different temperatures. Regardless of the temperature, the Nyquist plot is composed of a semicircle located in the high-medium frequency range related to the charge transfer process and a straight line at lower frequencies that corresponds to a diffusion process [23, 24]. In addition, the semicircle decreases with increasing temperature due to the increase of ion mobility, improving charge transfer and diffusion processes. This behaviour is also observed for the rest of the P(VDF-HFP)/IL composites.

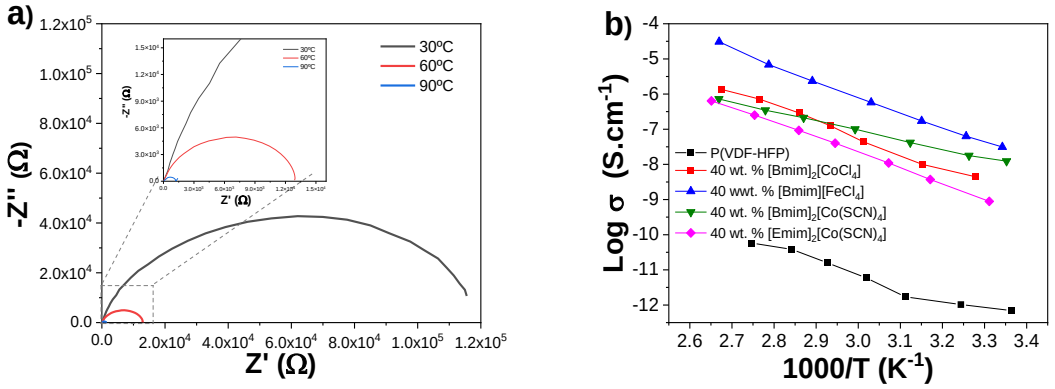


Figure 8.7 - a) Nyquist plots of the 40 wt. % P(VDF-HFP)/IL composites with $[Bmim][FeCl_4]$ at different temperatures (30, 60 and 90 °C) and b) Arrhenius plots for the ionic conductivities of the P(VDF-HFP)/IL composites with different ILs.

The ionic conductivity value was calculated from **Equation 2.7** and the temperature behaviour of the ionic conductivity for the P(VDF-HFP)/IL composites is shown in **Figure 8.7b**. Regardless of the IL type, the ionic conductivity increases with temperature, due to both the increase of the mobility of the ions and to the faster internal modes of the polymer chains, the segmental motions supporting inter-chain hopping and intra-chain ion movements [25, 26]. It is also observed a strong increase of the ionic conductivity of the composites with respect to neat P(VDF-HFP), as the addition of IL in the polymer matrix increases the ionic charge content [27].

The highest ionic conductivity value was obtained for [Bmim][$FeCl_4$] due to the high ionic conductivity (4.37 $mS.cm^{-1}$) and low viscosity (43 mPa.s) of this IL (data from the iolitec provider).

8.3.4 Humidity sensing response and proof of concept device

Due to their hygroscopic nature, ILs have been explored in humidity sensing systems [28]. In this context, the influence of the IL anion and cation chain length into the humidity sensing response of the P(VDF-HFP)/IL composites was evaluated by the resistance variation with the relative humidity varying from 35 % to 85 % at a temperature of 25 °C.

Figure 8.8a-8.8d shows the cycling impedance variation with varying humidity for the different P(VDF-HFP)/IL composites upon an applied frequency of 10 kHz as the samples displays a low impedance at this frequency.

Independently of the IL type, all the P(VDF-HFP)/IL composites shows a variation in the impedance with the relative humidity in the 30 to 85 % range, with a fast response and recovery times. In terms of cycling stability, P(VDF-HFP)/[Bmim][$FeCl_4$] shows a decreasing response during the first six cycles attributed to the high surface porosity observed in SEM images, which promotes the water absorption and entrapping, becoming then stable over time. It is also observed the influence of the imidazolium alkyl chain length for the samples comprising the $[Bmim]^+$ and $[Emim]^+$ cations sharing the same anion $[Co(SCN)_4]^{2-}$. Besides presenting similar impedance values, the P(VDF-HFP)/$[Bmim]_2[Co(SCN)_4]$ composite displayed a lower recovery time when compared to the P(VDF-HFP)/$[Emim]_2[Co(SCN)_4]$ composite. Among the different samples, the better sensor cycling response is observed for the P(VDF-HFP)/$[Bmim]_2[CoCl_4]$

composite, presenting the lowest impedance values as a result of their higher hygroscopic behaviour, as demonstrated by TGA measurements and a more stable and repeatable response.

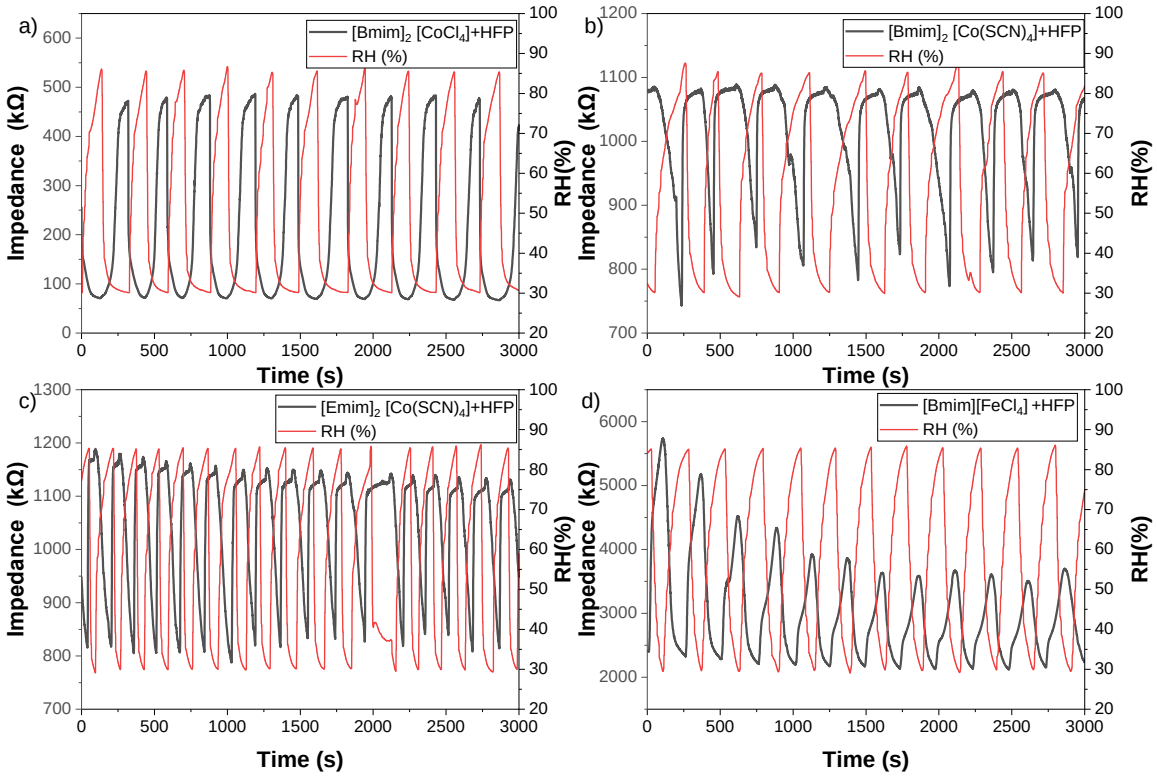


Figure 8.8 - Cycling sensing response for varying relative humidities between 35 and 85 % for the different P(VDF-HFP)/IL composites incorporating imidazolium based ILs with different anions: a) P(VDF-HFP)/$[Bmim]_2[CoCl_4]$, b) P(VDF-HFP)/$[Bmim]_2[Co(SCN)_4]$, c) P(VDF-HFP)/$[Emim]_2[Co(SNC)_4]$ and d) P(VDF-HFP)/[Bmim][$FeCl_4$].

Due to the best response of the P(VDF-HFP)/$[Bmim]_2[CoCl_4]$ composite, its sensitivity was evaluated from the linear regime of the impedance vs humidity (**Figure 8.9**), showing a sensitivity value of -2245 ±240 Ω in the 35 % to 85 % RH range.

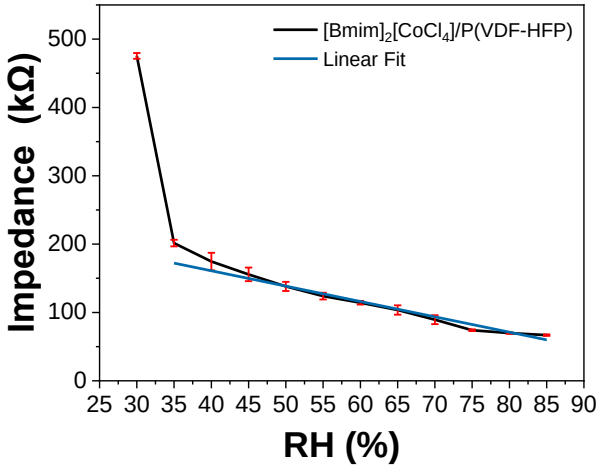


Figure 8.9 - Humidity sensing sensitivity of the P(VDF-HFP)/$[Bmim]_2[CoCl_4]$ composite.

As the composite with $[Bmin]_2[CoCl_4]$ exhibited a more stable and repeatable response with a lower impedance, a fast response and high sensitivity, a functional proof of concept concerning the monitorization of human breathing was developed. For this purpose, the sensing material was attached to a cylindrical tube due to its mechanical flexibility (**Figure 8.10a**). Real time monitoring of the human breathing was carried out through the signal acquisition board (**Figure 8.10b and 8.10c**). The electronic system sends a square wave from the microcontroller to the voltage divider in which, depending on the impedance value of the humidity sensor, the amplitude changes.

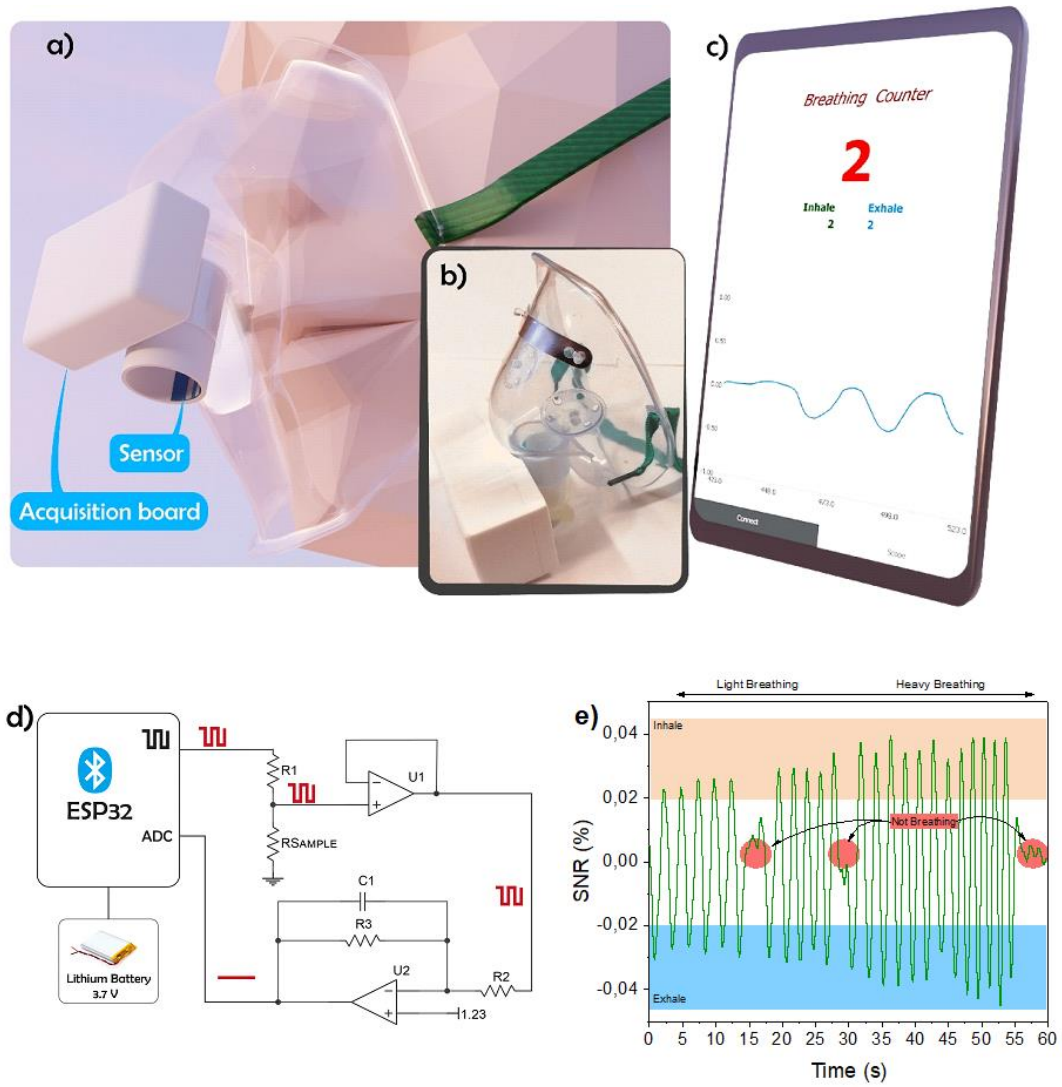


Figure 8.10 - a) Schematic representation of the breathing monitoring prototype, b) real photography of the breathing mask with component identification, including electronic system and humidity sensor, c) screen print of the Bluetooth application for breathing detection, d) schematic representation of the electronic acquisition board and e) response of the P(VDF-HFP)/$[Bmim]_2[CoCl_4]$ composite based monitoring device at different breathing rates.

The low pass filter was dimensioned to a low cut off frequency (15.9 Hz) to reduce the high frequency component and transform the high frequency signal to a low frequency signal read by the ADC of the microcontroller (**Figure 8.10d**). Further, the signal is sent by Bluetooth communication to an application built on Qt modelling language (QML). The application allows monitoring real time breathing events and based on a predefined threshold count the inhalations, exhalations, and the total breathing cycle (inhale to exhale) as shown by the one-minute

monitoring of the breathing of a person going from a light to heavy breathing rhythm, with some no breathing events (**Figure 8.10e**).

8.4 Conclusions

PVDF-HFP films incorporating imidazolium based ILs with different anion types ($[FeCl_4]^-$, $[Co(SCN)_4]^{2-}$ and $[CoCl_4]$)) and a cation chain length were developed by a solvent casting method for humidity sensing applications.

Independently of the anion type and cation size, the inclusion of the different ILs leads to the formation of a porous structure. Additionally, all the composites reveal an increase in the amount of the polar electroactive β-phase of the polymer with respect to neat P(VDF-HFP), with the composite P(VDF-HFP)/[Bmim][$FeCl_4$] displaying the maximum polar phase content of 85 %. No changes occur in the degree of crystallinity of the P(VDF-HFP)/[Bmim][$FeCl_4$] composite with respect to the pristine polymer (17 %), being observed a decrease down to 11 % for the rest of the composites. The inclusion of the ILs act a plasticizer in the polymer matrix, with a reduction of the Young modulus from 880 to 840 for the P(VDF-HFP)/$[Emim]_2[Co(SCN)_4]$ composite. The magnetic properties, as a result of the presence of magnetic anions, were evaluated, increasing the magnetization response with the applied magnetic field for all composites.

The potential of the developed materials to be applied as humidity sensors was accessed, by measuring the resistance variation with the relative humidity varying from 30% to 85 %, displaying the composite P(VDF-HFP)/$[Bmim]_2[CoCl_4]$ the best humidity response.

A proof-of-concept device concerning a real time monitoring of human breathing was developed demonstrating the potential of the P(VDF-HFP)/$[Bmim]_2[CoCl_4]$ composite for actual humidity sensing applications.

8.5 References

1. Fernandes, L., et al., *Highly sensitive humidity sensor based on ionic liquid-polymer composites.* ACS Applied Polymer Materials, 2019.
2. Zhao, X., et al., *Hydrophobic ionic liquid-in-polymer composites for ultrafast, linear response and highly sensitive humidity sensing.* Nano Research, 2021. **14**(4): p. 1202-1209.
3. Wu, K., et al., *A humidity Sensor Based on Ionic Liquid Modified Metal Organic Frameworks for Low Humidity Detection.* Sensors and Actuators B: Chemical, 2021: p. 131136.

4. Mendes-Felipe, C., et al., *Photocurable temperature activated humidity hybrid sensing materials for multifunctional coatings.* Polymer, 2021. **221**: p. 123635.
5. Li, S., et al., *Voltage response of three ionic polymer pressure sensors based on ion migration at different ambient humidities.* Smart Materials and Structures, 2020. **30**(2): p. 025004.
6. Correia, D.M., et al., *Low-field giant magneto-ionic response in polymer-based nanocomposites.* Nanoscale, 2018. **10**(33): p. 15747-15754.
7. Fernandes, L.C., et al., *Ionic-Liquid-Based Printable Materials for Thermochromic and Thermoresistive Applications.* ACS Applied Materials & Interfaces, 2019. **11**(22): p. 20316-20324.
8. Ribeiro, C., et al., *Electroactive poly(vinylidene fluoride)-based structures for advanced applications.* Nature Protocols, 2018. **13**(4): p. 681-704.
9. Correia, D.M., et al., *Low-field giant magneto-ionic response in polymer-based nanocomposites.* Nanoscale, 2018. **10**(33): p. 15747-15754.
10. Bouhamed, A., et al., *A hybrid piezoelectric composite flexible film based on PVDF-HFP for boosting power generation.* Composites Science and Technology, 2021. **208**: p. 108769.
11. Sim, L., S.R. Majid, and A.K. Arof, *FTIR studies of PEMA/PVdF-HFP blend polymer electrolyte system incorporated with LiCF3SO3 salt.* Vibrational Spectroscopy, 2012. **58**: p. 57-66.
12. Gregorio, J., Rinaldo and M. Cestari, *Effect of crystallization temperature on the crystalline phase content and morphology of poly (vinylidene fluoride).* Journal of Polymer Science Part B: Polymer Physics, 1994. **32**(5): p. 859-870.
13. Li, Z., et al., *Effect of Al2O3 nanoparticles on the electrochemical characteristics of P (VDF-HFP)-based polymer electrolyte.* Electrochimica acta, 2004. **49**(26): p. 4633-4639.
14. Chen, K., et al., *Mechanical and thermal properties of all-wood biocomposites through controllable dissolution of cellulose with ionic liquid.* Polymers, 2020. **12**(2): p. 361.
15. Serra, J., et al., *Ionic liquid based Fluoropolymer solid electrolytes for Lithium-ion batteries.* Sustainable Materials and Technologies, 2020. **25**: p. e00176.
16. Kiefer, J., J. Fries, and A. Leipertz, *Experimental vibrational study of imidazolium-based ionic liquids: Raman and infrared spectra of 1-ethyl-3-methylimidazolium bis (trifluoromethylsulfonyl) imide and 1-ethyl-3-methylimidazolium ethylsulfate.* Applied spectroscopy, 2007. **61**(12): p. 1306-1311.
17. Correia, D., et al., *All printed soft actuators based on ionic liquid/polymer hybrid materials.* Applied Materials Today, 2021. **22**: p. 100928.
18. Peñalber, C.Y., et al., *Surface characterization of imidazolium-based ionic liquids with cyano-functionalized anions at the gas–liquid interface using sum frequency generation spectroscopy.* Physical Chemistry Chemical Physics, 2012. **14**(15): p. 5122-5131.
19. Martins, P., A.C. Lopes, and S. Lanceros-Mendez, *Electroactive phases of poly(vinylidene fluoride): Determination, processing and applications.* Progress in Polymer Science, 2014. **39**(4): p. 683-706.
20. Correia, D., et al., *Ionic liquid cation size-dependent electromechanical response of ionic liquid/poly (vinylidene fluoride)-based soft actuators.* The Journal of Physical Chemistry C, 2019. **123**(20): p. 12744-12752.
21. Dias, J.C., et al., *Thermal degradation behavior of ionic liquid/ fluorinated polymer composites: Effect of polymer type and ionic liquid anion and cation.* Polymer, 2021. **229**: p. 123995.
22. García-Saiz, A., et al., *A Magnetic Ionic Liquid Based on Tetrachloroferrate Exhibits Three-Dimensional Magnetic Ordering: A Combined Experimental and Theoretical Study of the Magnetic Interaction Mechanism.* 2014. **20**(1): p. 72-76.
23. Chang, B.-Y. and S.-M. Park, *Electrochemical Impedance Spectroscopy.* Annual Review of Analytical Chemistry, 2010. **3**(1): p. 207-229.
24. Park, M., et al., *A review of conduction phenomena in Li-ion batteries.* Journal of Power Sources, 2010. **195**(24): p. 7904-7929.
25. Baril, D., C. Michot, and M. Armand, *Electrochemistry of liquids vs. solids: Polymer electrolytes.* Solid State Ionics, 1997. **94**(1): p. 35-47.

26. Cameron, G.G., *Polymer electrolyte reviews-I edited by J. R. MacCallum and C. A. Vincent, Elsevier Applied Science Publishers, London, 1987. pp. x + 351, price £48.00. ISBN 1-85166-07 1-2.* 1988. **20**(3): p. 299-300.
27. Leones, R., et al., *Effect of Ionic Liquid Anion Type in the Performance of Solid Polymer Electrolytes Based on Poly (Vinylidene fluoride-trifluoroethylene).* Electroanalysis, 2015. **27**(2): p. 457-464.
28. Correia, D.M., et al., *Ionic Liquid–Polymer Composites: A New Platform for Multifunctional Applications.* Advanced Functional Materials, 2020. **30**(24): p. 1909736.

9 Photocurable temperature activated humidity hybrid sensing materials for multifunctional coatings

Due to the current evolution of society, the necessity for sustainable alternatives to conventional polymers, such as solvent free or natural polymers, for the development of smart materials is increasing. In this chapter, photocurable thermochromic and humidity responsive materials based on PUA and $[Bmim]_2[NiCl_4]$ IL have been prepared. Their fundamental properties were studied as well as the use of these composites as humidity thermochromic sensors.

This chapter is based on the following publication: Mendes-Felipe, C., Salado, M., Fernandes, L.C., Correia, D.M., Ruiz-Rubio, L., Tariq, M., Esperança, J.M.S.S., Vilas-Vilela, J.L., Lanceros-Méndez., S., *Photocurable temperature activated humidity hybrid sensing materials for multifunctional coatings.* Polymer, 2021 **221**: p.123635

9.1 Introduction

Vat photopolymerization (VP) is mainly composed by UV or visible light curable processes in which the light activates the photopolymerization process [1, 2]. The use of UV curable materials is increasing rapidly because the fast curing method, from seconds to minutes, at room temperature, and without using volatile organic compounds, as it occurs in solvent based processes. In addition, this technique reduces the overall energy consumption, based on space and energy efficiency, and allows the fabrication of high-resolution patterns [3]. However, a small range of materials can be used, with limited functionality, and supporting materials are often required during fabrication [4].

Different polymers were used as a matrix to develop ILs based hybrid polymer composites, such as PVDF and its copolymers, poly (methyl methacrylate) (PMMA), poly (N-isopropylacrylamide) (PNIPAM), PUA, polyethylene (PE) and poly (lactic acid) (PLA), among others [5]. Different and very diverse applications have been demonstrated for these nanocomposites, from sensors and actuators or batteries and fuel cells to air and water remediation or biomedical applications [5]. Furthermore, ILs/polymer hybrid materials were obtained based on UV curable materials such as PNIPAM with phosphonium-based ILs for ionogels fabrication [6] or methacrylic oligomer with imide salt type IL to be applied as electrolytes in lithium-based batteries [7]. Further, UV cured IL/polymer hybrid materials were prepared by 3D printing, using photosensitive commercial photoresist (IP-L 780 or SU-8) combined with dicyanamide salt and printed by two-photon nanolithography to obtain good optical transparent and down to 200 nm resolution 3D structures [8]; or phosphonium polymerized ILs structures for emerging electro-active membrane technologies printed by microstereolithography [9].

UV-curable polymers are particularly suited for smart coating applications, namely as coatings for corrosion protection, inks and adhesives [10]. However, besides the large potential of these materials, few studies are dedicated to the development of smart coatings curing by UV light, being PU coatings the most commonly employed. In this sense, PU coatings produced by UV curing presents many advantages, being related with their low environmental impact, energy and time saving processing and an efficient polymerization. Smart coatings based on PU and fluorated octavinyl polyhedral oligomeric silsesquioxane (F-OV-POSS) developed by UV curing revealed a self-cleaning ability and durability, based on their superhydrophobicity. These

interesting results demonstrate their strong potential to be used in the still to develop area of smart and multifunctional coatings [10].

With the capability of reversibly changing colour with varying temperature, thermochromic materials, in particular IL/polymer materials have been gained special attention in the field of sensors, such as level sensors [11]. This thermochromic behaviour is present in halide complexes, different transition-metal complexes, including nickel or copper, due to the interaction of the transition metal with a donor solvent by the energy alteration of the d-d transitions and consequent configuration changes [12]. Systems based on thermochromic materials are being applied in areas such as energy [13], flexible electronics [14] or sensors [15], among others. In this sense, thermochromic materials and, particularly, ILs based ones, are the focus of increasing attention [5, 11]. Besides the high interest in thermochromic materials, few studies reported on the IL/polymer based thermochromism. Printable level sensors based on the IL $[Bmim]_2[NiCl_4]$ and the polymer PVDF able to change colour from transparent to a dark blue, have been reported [11].

Besides the great advantages of the ILs for the development of multifunctional materials and the advantages of UV curable polymers for additive manufacturing and protective and functional coatings [16], no studies concerning thermochromic IL-based UV curable hybrid materials able to change the colour with the temperature and to detect relative humidity variations (humidity sensor) have been reported.

Thus, UV curable ILs/polymer thermochromic and humidity responsive material are presented in this work, based on PUA and $[Bmim]_2[NiCl_4]$ able to be implemented as multifunctional materials or coatings with thermochromic and for humidity sensing capability.

9.2 Experimental section

9.2.1 Preparation of composite films

Samples with varying $[Bmim]_2[NiCl_4]$ content (0, 5, 10, 20 and 40 wt. %) were prepared by mixing the IL with the corresponding volume of the photoresin. To ensure a good mixture of the resin and the IL, the samples were dispersed under ultrasonication (ATU® ATM series Model ATM3L) for 1 h at 30 °C and magnetically stirred for 2 h at 45°C. After the completely homogeneous photoresin-IL mixture, flexible films were obtained by doctor blade spreading the mixture on a

glass substrate. The samples were cured at room temperature for 90 seconds (UVACUBE 400, Honle UV America, Inc., mercury lamp 1000 W/m² of irradiance). Finally, the films were peeled off from the glass substrates, washed in a 2-propanol bath during 5 minutes, dried, and finally, stored in the dark at room temperature for the subsequent characterization. PUA/IL hybrid materials with a thickness around 150 µm, determined by an electronic digital caliper of Powerfix®, were obtained. **Figure 9.1** shows a scheme of the preparation process for PUA and IL/PUA films.

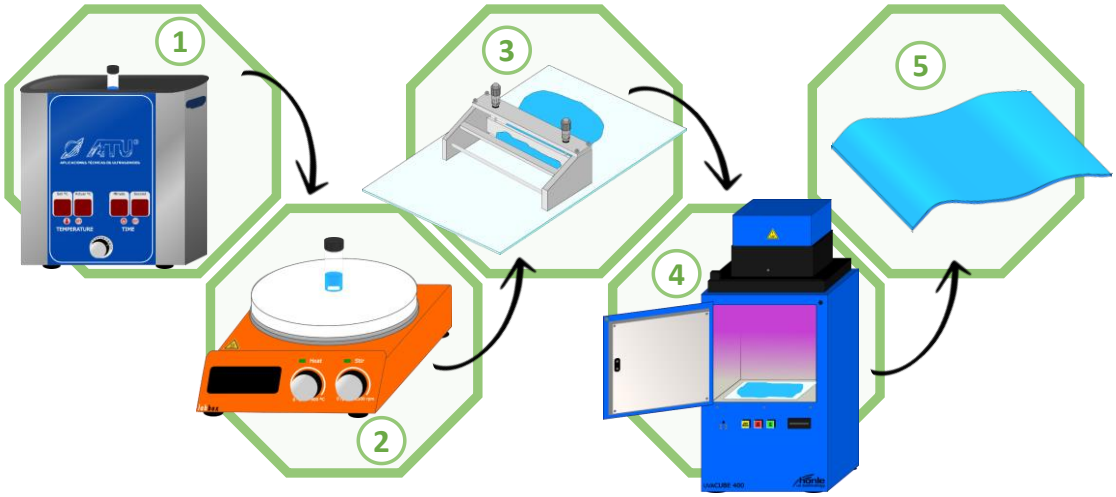


Figure 9.1 - Representation of the development of the PUA and PUA/IL composite films (5, 10, 20 and 40 wt.%): 1 – ultrasonication, 2 – magnetic stirring at 45 °C, 3 – film processing by Doctor Blade, 4 – UV cure, 5 – flexible films.

9.2.2 Sample characterization

The impact of incorporating the IL into the polymer during the UV curing process was quantified using photo-DSC. SEM was utilized to assess the morphology of the samples. Chemical interactions within the samples were investigated through FTIR-ATR. Thermal properties were examined using DSC. Hydrophobic/hydrophilic behaviour was analysed using the contact angle technique. Additionally, mechanical properties and electrical conductivity were evaluated. Chapter 2 contains comprehensive details on the employed characterization techniques.

The thermochromic response was investigated by ultraviolet–visible (UV-Vis) spectroscopy as a function of temperature. UV–Vis spectra were recorded with an Agilent Cary 60 UV/vis spectrophotometer with an external temperature controller. The spectra were obtained in the

range of 300-800 nm, with a resolution of 1 nm, from 30 to 70 °C (temperature range in which sample colour changes) every 5 °C after 2 min stabilization before each measurement. Further, the effect of temperature and relative humidity (RH) variation on the colour of the films was measured within a climate chamber Challenge 250E from ACS Company by recording photographs while RH and temperature were varied as indicated in **Table 9.1**. This analysis was carried out for the PUA/IL sample (2.5 x 2.5 cm square) with 20 wt.% IL content. In order to obtain the blue (dehydrated) initial state, the sample was kept at 70 °C for 5 minutes, while for the colourless (hydrated) state, the sample was kept under ambient conditions during 24 hours.

Table 9.1 - Experimental details for thermochromic and relative humidity (RH) variation assays.

Experiment	Initial state	Constant parameter and value	Variable parameter and interval	Studied intervals	Time of interval
1	Blue (dehydrated)	Temperature at 25 °C	Relative humidity 15 – 85 %	10 %	20 minutes at constant value and 15 minutes increasing to the next step
2	Blue (dehydrated)	Temperature at 45 °C	Relative humidity 15 – 85 %	10 %	
3	Blue (dehydrated)	Temperature at 10 °C	Relative humidity 20 – 85 %	10 %	
4	Colourless (hydrated)	Relative humidity at 60 %	Temperature 25 – 75 °C	10 °C	
5	Colourless (hydrated)	Relative humidity at 40 %	Temperature 25 – 75 °C	–10 °C	

9.3 Results and discussion

9.3.1 UV curing process

UV curing process for the samples is depicted in **Figure 9.2**. The photopolymerization conversion, C(α), as a function of time is shown in Figure 2a and the photopolymerization rate (R_p) in **Figure 9.2b**. **Table 9.2** presents the main values that characterize the UV curing process, C(α), $\mathbf{R}_p^{max}$ and tmax, of the different samples, as a function of IL content.

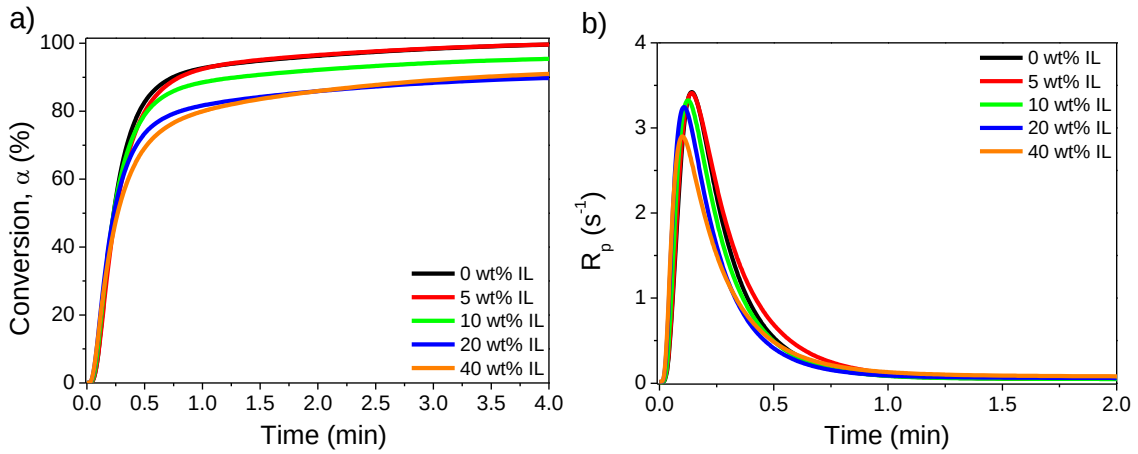


Figure 9.2 - Curing conversion (C(α)) as a function of time of the pristine photoresin and the PUA/IL samples (a), and photopolymerization rate (R_p)(b).

Table 9.2 - UV curing process characteristic parameters of the pristine resin and the PUA/IL samples for the different IL contents.

Sample	C(α) (%)	R_p^{max} (s^{-1})	t^{max} (s)
0 wt. %	100	3.4	8.0 ± 0.1
5 wt. %	99	3.4	8.0 ± 0.2
10 wt. %	95	3.3	7.4 ± 0.1
20 wt. %	89	3.2	7.0 ± 0.3
40 wt. %	88	2.9	6.2 ± 0.4

Figure 9.2a shows that a decrease on the conversion degree occurs with increasing IL content. Neat photoresin shows a 100% conversion after approximately 4 minutes that becomes 95 % for the 10 wt. % IL content sample. Similar trend is further observed for the 20 wt. % and 40 wt. % IL content samples, the total conversion decreasing to around 88% for the 40 wt. % IL content sample after 4 minutes. In addition, photopolymerization rate is also slightly affected by the incorporation of $[Bmim]_2[NiCl_4]$, changing from 3.4 s^{-1} for neat PUA to 2.9 s^{-1} for 40 wt. % IL/PUA sample. In relation to the t_{max}, a slight decrease is observed with increasing IL content, varying between 8.0 s for the 0 wt. % PUA/IL sample to 6.2 s for the sample that contains the highest amount of IL.

The UV light absorption by the photoinitiator has significant influence in the conversion of the C=C double bonds and, therefore, in the UV curing process [17]. The functionality and chemical structure of the employed oligomer influences in the reactivity of the photocurable ink and as

consequence in the final degree of conversion [1]. Further, the viscosity of the liquid curable ink/resin also plays a relevant role on the photopolymerization and is affected by the addition of additives [18]. Further, the fillers could absorb UV light, competing with the photoinitiator and, as a consequence, influencing the photopolymerization reaction and the characteristic photopolymerization parameters [19].

In the present case, UV absorption by $[Bmim]_2[NiCl_4]$ competes with absorption of light by the photoinitiator [20, 21], reducing photoinitiator efficiency and, thus, lower amount of initiating radicals are obtained. As a consequence, the final conversion and the rate at which the polymerization occurs are reduced when IL is added to the PUA resin. Despite the ability of UV light absorption by the IL, according to its chemistry, it does not generate any species further interfering with the curing process.

Furthermore, increasing viscosity influences the photopolymerization by decreasing the rate and increasing the time to obtain the maximum curing degree [22]. Hence, two factors have to be taken into account: a) when the photopolymerization is taking place, the viscosity increases and b) the presence of IL also increases the viscosity of the photocurable material [6]. Thus, different viscosities could be obtained for two materials with the same degree of cure but different amount of IL content, being observed a decrease in the R_p and t_{max} with increasing $[Bmim]_2[NiCl_4]$ content.

9.3.2 Morphological and contact angle characterization

Figure 9.3 shows the cross-sectional SEM images of neat PUA and PUA/IL samples in order to evaluate morphology variations due to the $[Bmim]_2[NiCl_4]$ inclusion within the polymer.

The filler induced morphological variations have significant influence over mechanical and electrical properties of the prepared samples [18, 19], which depends on IL type and content [6]. **Figure 9.3** shows that the presence of $[Bmim]_2[NiCl_4]$ modifies the PUA polymer morphology: whereas pristine PUA (**Figure 9.3a**) shows a smooth and flat structure, without any visible crack, pores or patters, the incorporation of the IL leads to spherical or porous like structures within the sample. This trend increases with increasing IL content within the PUA matrix and the pore distribution is homogeneous throughout the films. When IL content increases, the spherical (bubble type) structures appear in a greater extent and the pores seem to be larger [23].

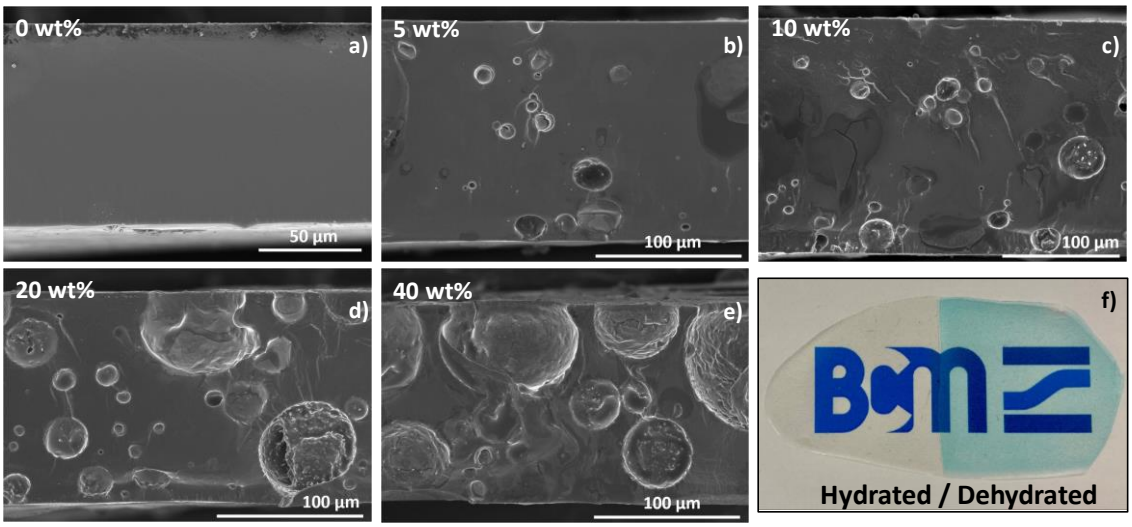


Figure 9.3 - Representative SEM images of the PUA (a) and PUA/IL hybrid samples comprising different IL contents (b-e) at magnification of 300×. Thermochromism resulting from the dehydration process of PUA/IL with 10 wt. % IL content (f).

The obtained SEM results are in agreement with elated studies with $[Bmim]_2[NiCl_4]$ within different polymer matrix [11, 24]. Further, as the IL $[Bmim]_2[NiCl_4]$ is known by its thermochromic properties upon a hydration and dehydration process, an important property for the development of multifunctional materials for smart coatings and/or sensor applications, the thermochromism upon a hydration process was evaluated. **Figure 9.3f** shows the thermochromism occurring as a result of a hydration/dehydration process for the sample with 10 wt. % IL content, as demonstrated by a colour change from colourless/whitish to light blue, respectively. This effect will be quantitatively analysed in this work.

The surface wettability of the PUA and PUA/$[Bmim]_2[NiCl_4]$ was evaluated by contact angle measurements (**Figure 9.4**). Attending to the contact angle values, the hydrophobic/hydrophilic behaviour of each sample can be evaluated.

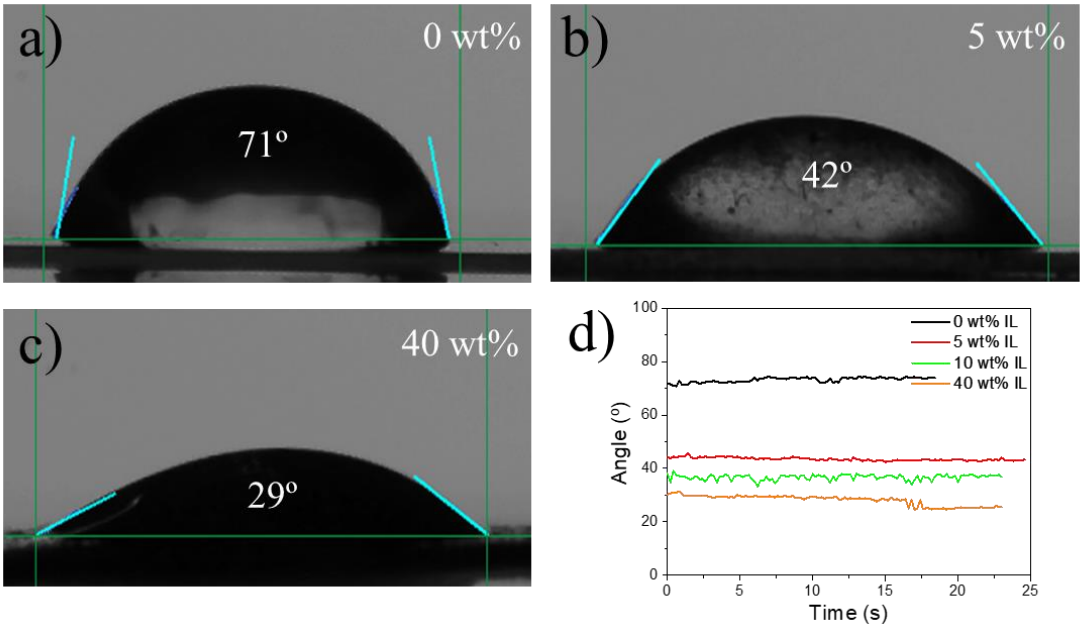


Figure 9.4 - Representative images of the water surface contact angle for neat PUA film (a) and PUA/IL samples containing 5 wt. % (b), 10 wt. % (c), 20 wt. % (d) and 40 wt. % (e). Evolution of the contact angle values as a function of time for the mentioned samples (f).

Figure 9.4 shows that the contact angle for neat PUA films present a value of 71° and that when the IL is added to the polymer matrix, the contact angle value decreases to 42° for the 5 wt. % IL/PUA sample and to a minimum value of 29° for the 40 wt. % IL content sample. The improvement of the surface wettability of the samples with increasing $[Bmim]_2[NiCl_4]$ content shows that the inclusion of the IL into the polymer matrix improves the water absorption capability, increasing the absorbed water per unit mass in the PUA/IL samples [25]. The results are in agreement with the larger porosity of the samples with increasing IL content presented in **Figure 9.3**, as higher porosity allows a larger contact between film and water drop and increased water absorption [23].

9.3.3 Thermal and chemical characterization

The thermal properties of pristine and PUA/IL samples were evaluated by the DSC thermograms shown in **Figure 9.5**. Only a change (a step) in the base line is observed for neat PUA in the first and second scans, corresponding to the glass transition temperature (T_g). The glass transition temperatures of the samples are indicated in **Table 9.3**.

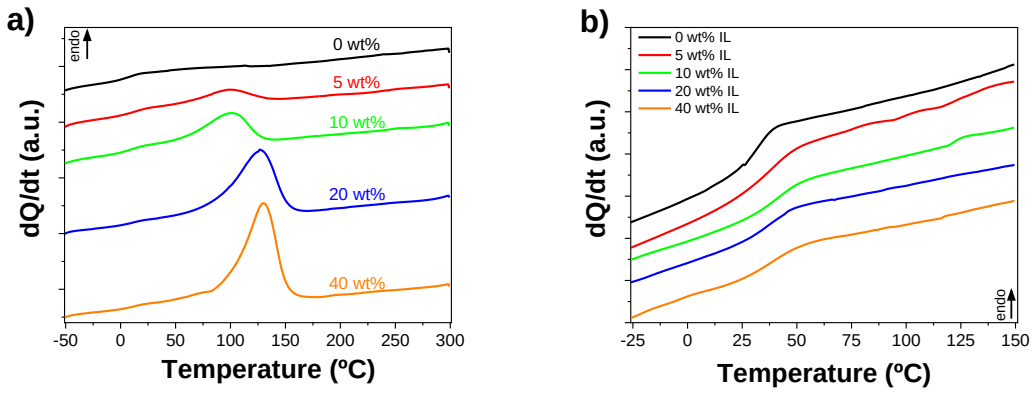


Figure 9.5 - DSC thermograms of neat PUA and PUA/IL samples for the first (a) and second (b) scans.

Table 9.3 - Glass transition temperature for first (T_{g1}) and second (T_{g2}) scans, strain at break (ε_b) and elastic modulus (E) for PUA and IL/PUA films.

Sample	T_{g1} (ºC)	T_{g2} (ºC)	ε_b (%)	E (MPa)
0 wt.%	20.2	41.2	45.8 ± 3.2	4.04 ± 0.35
5 wt.%	24.1	52.8	54.3 ± 4.4	4.87 ± 0.37
10 wt.%	23.5	53.3	29.1 ± 2.1	4.20 ± 0.13
20 wt.%	23.7	50.9	27.0 ± 2.5	4.27 ± 0.31
40 wt.%	23.6	56.7	32.9 ± 5.3	3.45 ± 0.02

For neat PUA the glass transition is located around room temperature (Tg = 20 °C). With the incorporation of the IL $[Bmim]_2[NiCl_4]$ an endothermic peak is observed between 60 and 150 °C that increases with IL content. This endothermic peak is related to water desorption and can appears at different temperature ranges depending on the H_2O molecular interactions [26], being indicative in the present case of a reversible water desorption on Ni (II) compounds in which H_2O molecules are coordinated to the metal [15, 27]. The increase of the endothermic peak with increasing IL content is in agreement with contact angle results, where a higher wettability is observed for samples with higher IL content. Further, higher values at which the endothermic peak appears can be ascribed to the high heating rate used during the DSC scans.

Figure 9.5a also shows that T_{g1} for neat PUA and PUA/IL samples (**Table 9.3**) slightly increases from 20 to ~24 °C when $[Bmim]_2[NiCl_4]$ is added. This small change on the T_g value can be associated to experimental errors (selection of the temperature or measurement uncertainties). In addition, this slightly increase can be also associated to a possible interaction

between the IL and the polymer that hinders the polymer chains, reducing the free volume and therefore increasing the T_g. In any case, it can be concluded that no relevant differences are observed for the different samples.

After the heating process up to 300 °C and the subsequent cooling to -50 °C the peak corresponding to the water absorption does not appear (**Figure 9.5b**), indicating that the hydration process does not occur. Related to PUA, T_g increases compared with the first scan from 20 °C (T_{g1}) to 41 °C (T_{g2}), increasing further for samples with IL content up to 40 wt. %, being 53 °C for 5 wt. % IL content sample and 56 °C for the one with 40 wt. % IL. The increase of the T_{g1} of PUA with the IL incorporation indicates that the IL actually interacts with the polymer, reducing its mobility [28]. Thus, after the heating process and water evaporation (second scan), the increase of T_g indicative of the polymer mobility reduction that can be ascribed to IL and PUA interactions when dehydration has occurred [28]. Furthermore, a possible heat-activated post-curing process could occur [19], increasing T_g of the samples from the first to the second scan. This process could be appreciated in the DSC thermogram of the first scan as an exothermic peak, but probably is not observed due to the high values of the endothermic peaks.

The IL-polymer physical-chemical interactions as well as the conformational variations of the PUA/IL samples after the hydration and dehydration processes were evaluated by FTIR-ATR. **Figure 9.6** shows both the room temperature, 25 °C, (hydrated) and 80 °C (dehydrated) FTIR spectra.

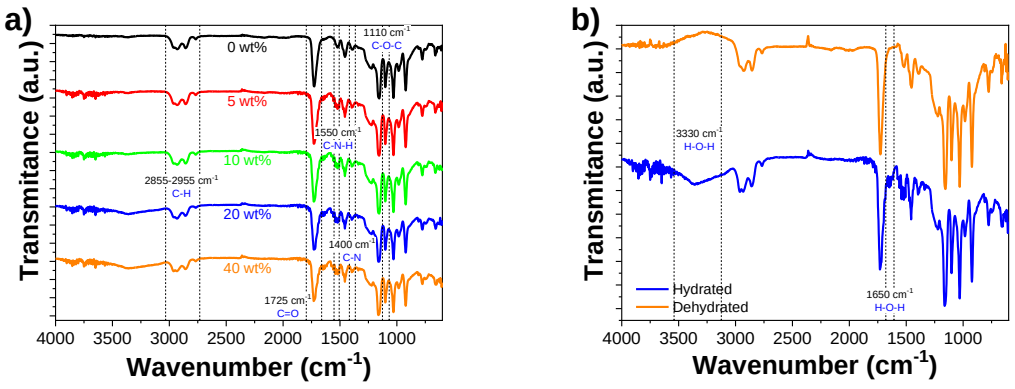


Figure 9.6 - FTIR spectra of neat PUA and PUA/IL samples containing different IL contents (a) and FTIR spectra at room temperature (hydrated) and at 80 °C (dehydrated) of 20 wt.% PUA/IL sample (b).

Figure 9.6a allows to identify the characteristic absorption bands of neat PUA. The absorption band at 1550 cm^{-1} is related to the stretching vibrations of C-N and N-H bonds of the urethane group. C-N and C-O-C absorption bands appear at 1400 cm^{-1} and 1110 cm^{-1}, respectively. The C=O stretching vibrations are observed at 1725 cm^{-1} and the CH_2 and CH_3 vibrations are observed between 2855 cm^{-1} and 2955 cm^{-1} [18]. No chemical changes are identified in the PUA FTIR-ATR spectra upon the IL incorporation within the polymer matrix. Additionally, it is also to notice that the characteristic IL imidazolium CH_2, CH_3 and C-N absorption bands of the cation $[Bmim]^+$ are overlapping with the polymer absorption bands [11, 24]. Apart from that, no band displacement or new absorption bands are observed upon the addition of IL, showing that no relevant intermolecular interactions occur between the IL and PUA polymer [18].

Comparing samples before (hydrated) and after (dehydrated) the heating process, it is to notice the presence of two absorption bands at 1650 and 3330 cm^{-1} in the hydrated samples, which correspond to water molecules stretching and bending modes [11]. These results indicate that the change in colour from light blue to colourless (**Figure 9.3f**) can be attributed to the presence or absence of water molecules within the coordination structure of the IL within the PUA/IL samples, as it will be analysed in detail latter.

9.3.4 Mechanical and electrical properties

The mechanical characterization of the PUA/IL films was performed by stress vs. strain measurements in tensile mode (**Figure 9.7a**) and the corresponding elastic modulus (**Figure 9.7b**) and strain at breaks (**Table 9.3**) were evaluated.

According to **Figure 9.7a**, all samples exhibit a linear elastic response up to a breaking point. The maximum strain for the PUA film is ~ 45 % decreasing down to ~ 27 % for the PUA/IL film with a [Bmim]2[NiCl4] content of 20 wt. %. The Young's modulus (**Figure 9.7b**) has a value of 4.04 ± 0.35 MPa for the PUA photoresin film and slightly increase to 4.87 ± 0.37 MPa for the 5 wt. % IL composite. However, for concentrations higher than 5 wt. %, a reduction in the Young modulus is observed, being 4.20 ± 0.13 MPa and 4.27 ± 0.31 MPa for the composites containing 10 and 20 wt. % of $[Bmim]_2[NiCl_4]$, respectively. The PUA/IL film with 40 wt. % of $[Bmim]_2[NiCl_4]$ shows a Young modulus of 3.45 ± 0.02 MPa. The decrease in the Young modulus

is mainly attributed to the plasticizing effect of the $[Bmim]_2[NiCl_4]$ as well as to the observed morphology variations increasing $[Bmim]_2[NiCl_4]$ content, appreciated in the SEM images [28].

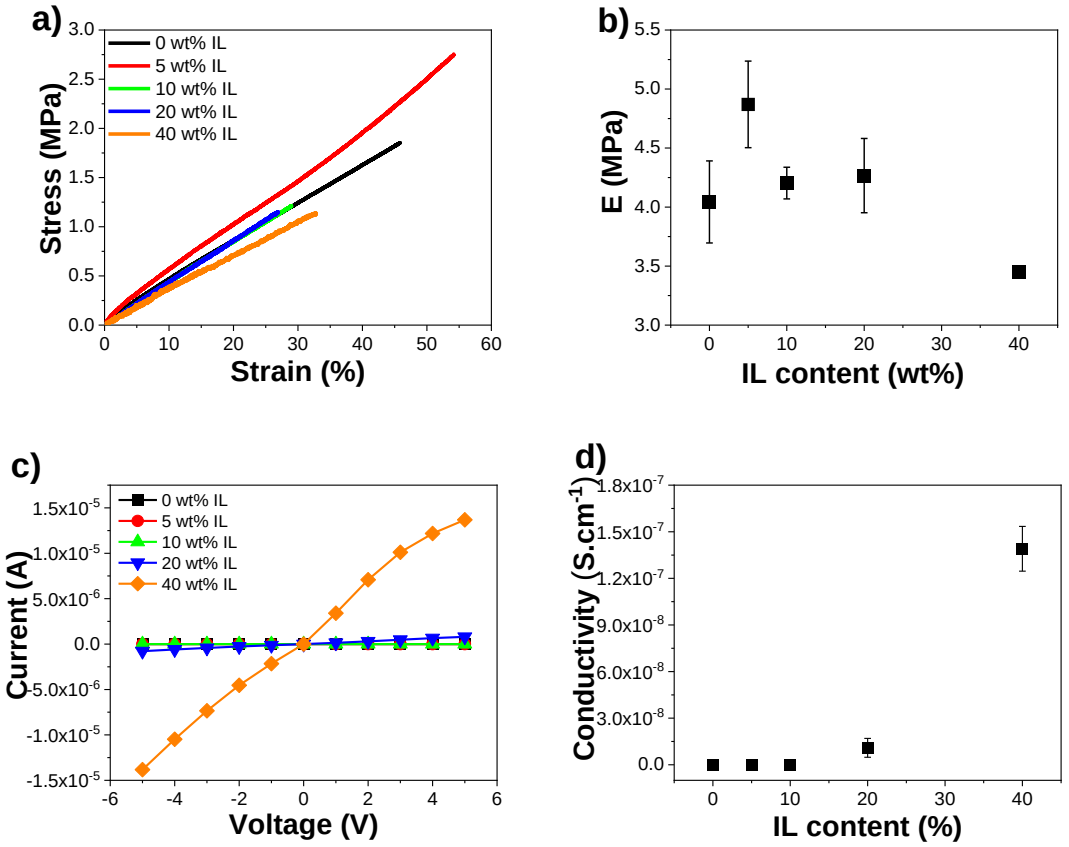


Figure 9.7 - Stress vs. strain mechanical characteristic curves (a) and Young modulus (b) for neat PUA and for PUA/IL samples containing different $[Bmim]_2[NiCl_4]$ contents. I-V curves (c) and electrical conductivity (d) for the same samples.

Attending to the elongation level of the material, the addition of IL increases the maximum elongation of the materials for the lower IL contents being 45.8 ± 3.2 % for neat PUA and 54.3 ± 4.4 % for the 5 wt. % sample. When higher amounts of IL are added, the maximum elongation decreases down to 27.0 ± 2.5 % for the 20 wt. % sample. As shown before, the addition of IL induces variations on the morphology of the obtained polymer hybrids resulting in increasingly porous structures and, as consequence, the materials show lower levels of stretchability [29]. Interestingly, all films present bending ability and do not become fragile with the introduction of different amounts of the IL, being therefore suitable materials for flexible applications.

The electrical properties of the samples are shown in **Figure 9.7c and 9.7d**. **Figure 9.7c** shows the characteristic I-V curves and the corresponding volume electrical conductivity of the films is presented in **Figure 9.7d**.

All samples exhibit a typical I-V linear behaviour independent of the IL content, with the slope increasing with increasing IL content (**Figure 9.7c**). The electrical conductivity of the samples **Equation 2.6** shows a strong increase with increasing IL content (**Figure 9.7d**), the electrical conductivity of the PUA film being around 2.92 x 10^{-12} S·m^{-1} and the highest electrical conductivity being obtained for the sample with 40 wt. % $[Bmim]_2[NiCl_4]$ IL content: 5.51x10^{-6} S·m-1. This increase results from the ionic characteristics of the ILs and to ion-dipole interactions, that occurs between the IL and the PUA being the electrical conductivity governed by the increase in the number and mobility of the ions, ionic charge and viscosity of the $[Bmim]_2[NiCl_4]$ [30]. By increasing the $[Bmim]_2[NiCl_4]$ concentration in the polymeric matrix, the ion transport and dissociation of IL is promoted, increasing the number of ionic carriers. Further, it has been reported that the IL-polymer interaction may decrease as the IL content increases, promoting a more rapid ionic transport [11].

9.3.5 Temperature-activated humidity-sensitive materials

9.3.5.1 UV-Vis characterization

The thermochromic effect of the PUA/$[Bmim]_2[NiCl_4]$ films was evaluated by UV-Vis spectroscopy at different temperatures (**Figure 9.8**). **Figure 9.8a** shows the UV–Vis spectra for PUA/$[Bmim]_2[NiCl_4]$ composite with 20 wt. % of $[Bmim]_2[NiCl_4]$ content in the temperature range from 30 to 70 °C. **Figure 9.8b** shows the UV-Vis curves for the composites with different IL contents at 70 °C.

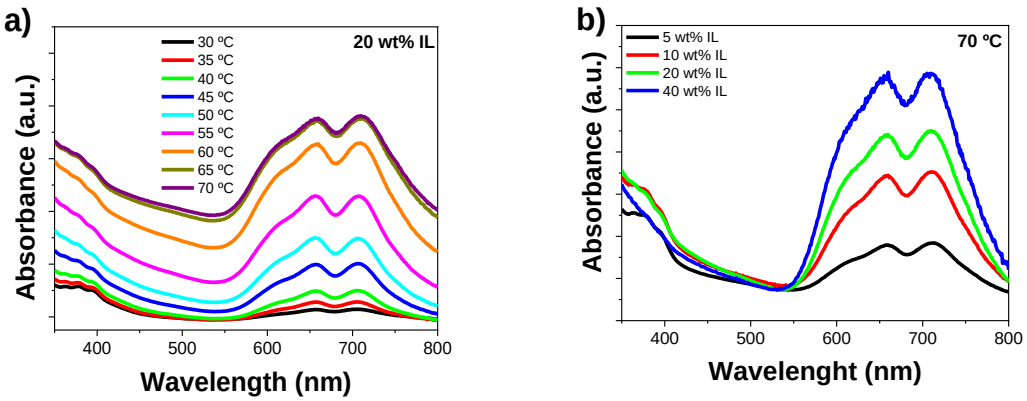


Figure 9.8 - UV-Vis spectra for the IL/PUA samples containing 20 wt. % of $[Bmim]_2[NiCl_4]$ content in the temperature range from 30 to 70 °C (a) and UV-Vis curves for the different samples at 70 °C (b).

Upon the processing, and independently of the IL content, the films are colourless, changing their colour to blue upon the heating up to 70 °C, being the colour change a reversible and temperature-dependent process.

Figure 9.8a shows that the increase in temperature from 30 to 70 °C induces the appearance and subsequent increase of two absorption bands at 660 and 710 nm. Comparing these two peaks among them, similar intensity and shape is obtained regardless of the temperature. Furthermore, this process is observed for all IL/PUA samples, independently of the $[Bmim]_2[NiCl_4]$ content, reaching maximum absorption at temperatures between 60 and 70 °C in all cases. In addition, an increase of the IL content from 5 to 40 wt. % induces an increase in the absorption bands, as presented in **Figure 9.8b**.

The appearance of the two absorption bands with increasing temperature indicates colour change of the films from colourless to blue. As indicated, the absorption peaks appear at wavelengths between 600 and 750 nm, ascribed to the blue region of the UV-Vis spectrum. In addition, these peaks reach a maximum absorption value that corresponds to the most intense blue colour obtained in the films and this colour is dependent on the IL content of the composite, increasing the peak intensity, and in this sense the colour intensity, with the IL content. The observed peaks of similar intensities are related to the $[NiCl_4]^{2-}$ complex in its tetrahedral conformation [21], being thus responsible for the colour variation. Therefore, the colour change of the composites is related to the modification of the coordination reaction [11].

9.3.5.2 Temperature-humidity-colour change characterization

As the composites are thermally and humidity responsive, they show a strong potential for smart and multifunctional coatings and/or sensing materials. **Figure 9.9** shows the evolution of the colour with varying relative humidity (RH) at constant temperature, and with varying temperature at constant humidity.

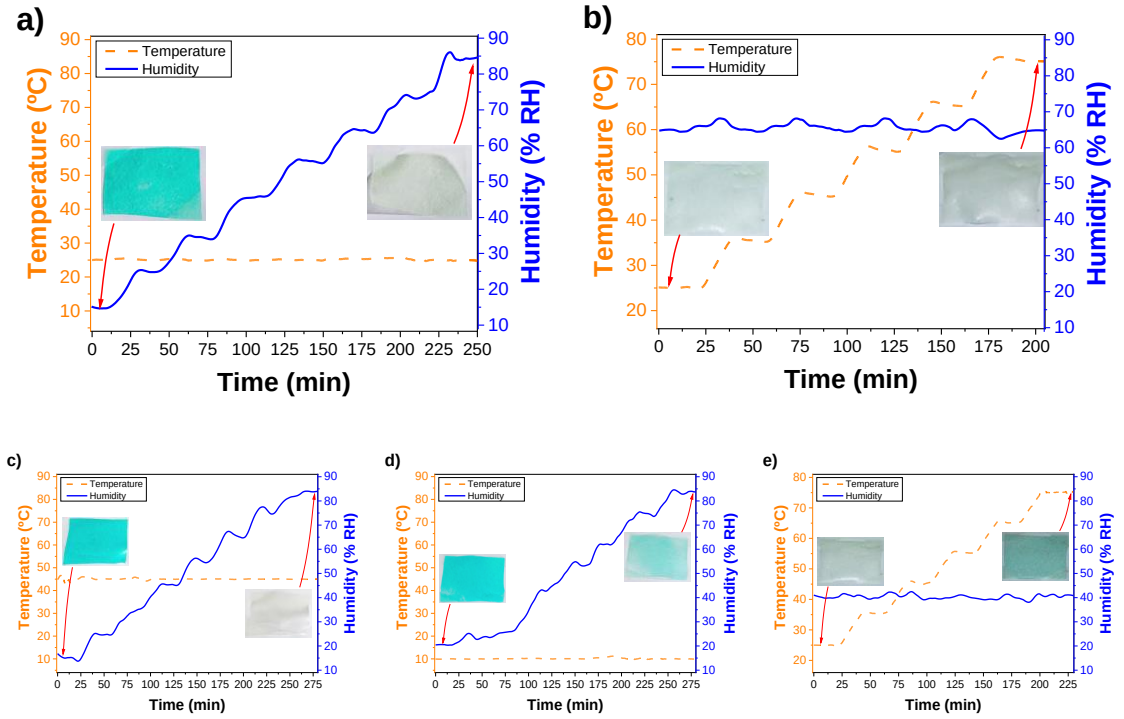


Figure 9.9 - Colour variation of the films (initial and final state) with increasing relative humidity at constant temperature of 25 °C (a) and with increasing temperature at constant relative humidity of 60 % (b), increasing relative humidity at constant temperature of 45 °C (d) and 10 °C (e), and with increasing temperature at constant relative humidity of 40 % (f).

Attending to **Figure 9.9a**, as the RH increases, keeping the temperature constant, the film remains completely blue until 55 % of RH. At this moment, the film starts to change its colour to a lighter blue. When a RH of 75 % is reached, the film becomes colourless, defining the "range of colour change" from 55 to 75 % of RH.

These results also indicate a reversible response of the film in which blue films can recover the transparency/whitish colour at room temperature, confirming the reversible thermochromism, which is explained by an abrupt change in the chemical structure as indicated in section 9.3.5 [31].

Further, when the RH increases, keeping the temperature constant (**Figure 9.9c**), the film remains completely blue. When a RH of 40 % is achieved, the film starts to change its colour to a lighter blue (similarly to the first test at room temperature). Finally, when a RH of 55 % is reached, the film becomes colourless, defining the range of colour change from 40 to 55 % RH. Thus, temperature has a strong influence on the range of colour change, a decrease from 55% to 40 % of RH being observed for the beginning of the colour change when the tests are performed at constant temperature of 25 °C or 45 °C, respectively.

When the temperature is maintained at 10 °C (**Figure 9.9d**), a similar result is obtained. However, in this case, the film has not turned completely colourless at the end of the experiment, remaining slightly blue. In addition, the colour change begins at higher RH, around 65 % of RH, than in the previous test indicating that the water absorption (hydration of $[Bmim]_2[NiCl_4]$) is slower than when temperature is 25 °C or 45 °C. Thus, the variation on the moisture absorption by the ILs with temperature and RH is confirmed [32]. The ILs structure (cation and anion type or cation alkyl chain length) and external factors (relative humidity, temperature or impurities) have an influence on the hydration of ILs [33] demonstrating that is a process sensitive to and stimulated by temperature [34].

Figure 9.9b shows that the colourless sample does not undergo any change during the heating process under the defined test conditions (temperature variation from 25 °C to 75 °C under constant RH of 60 %). Thus, when there is enough humidity, the temperature has not influence for the colouring process.

Finally, as shown in **Figure 9.9e**, when the temperature reaches 65 °C, the film begins to undergo a colour change. This result indicates that the water evaporation occurs when temperature reaches the mentioned value and, as a result, a hydrothermochromatic coordination reaction occurs (from the colourless octahedral complex to the blue tetrahedral). Thus, when humidity is lower than 55 %, temperature induces water evaporation and, therefore, substitution of water molecules by Cl^- atoms in the Ni (II) complex [35].

Thus, it is shown that the chromic phenomenon is humidity governed as at each temperature the humidity sets the colour change (directly dependence on the humidity of the system) and is thermally activated as the humidity limit value for the colour change depends on the temperature of the system. Thus, these humidity hybrid sensing materials present a temperature limit of 10 °C below which colour change is not clearly observed. At room temperature, colour change

occurs at 55 % of RH, setting this value as limit for thermochromic effect upon temperature variation.

9.3.5.3 Colour changing mechanism

The colour changes observed by both the UV-Vis (**Figure 9.8**) and the climate chamber assays (**Figure 9.9**), are related to the $[NiCl_4]^{2-}$ complex in its tetrahedral conformation [21]. Therefore, the colour change of the films is related to the modification of the coordination reaction as reported in **Figure 9.10** [11].

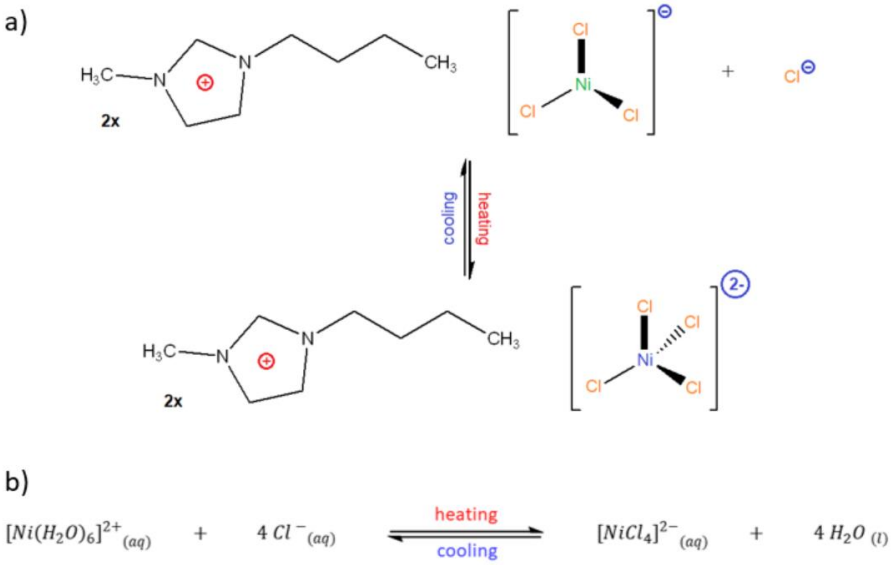


Figure 9.10 - Chemical modifications occurring during the heating and cooling process of the $[Bmim]_2[NiCl_4]$ IL (a) and changes in the coordination number of Ni(II) from octahedral to tetrahedral structure (b). Reproduced with permission [11]. Copyright 2019, ACS Publications.

$[Bmim]_2[NiCl_4]$ is a hygroscopic salt capable of absorbing water molecules from ambient humidity. The afore discussed experiments show that the observed colour change is attributed to an absorption/dehydration process of the IL [11]. The coordination number of Ni (II) in the IL structure undergoes a change, varying its structure form tetrahedral (blue colour) to octahedral (not colour) without change in the cationic structure (see Scheme 9.10a) [36]. At room temperature, the Cl^- ions of the nickel complex are replaced by water molecules from ambient humidity as a result of H-bond interactions with the IL anion $[NiCl_4]^{2-}$ [21], corroborating the DSC endothermic peak results [27] (section 9.3). Therefore, the colouring process is dependent on the environmental humidity as demonstrated in the scheme 9.10b.

Therefore, the thermochromic effect of the IL/PUA composite is an effect due to the water absorption/dehydration of the $[NiCl_4]^{2-}$, i.e. a change on the coordination number of the Ni(II) from octahedral to tetrahedral depending on the hydrated ($[Ni(H_2O)_6]^{2+}$) or dehydrated ($[NiCl_4]^{2-}$) state.

9.4 Conclusions

Flexible electronic devices and smart and multifunctional coatings are one of the cornerstones of the current technological advances. In this work, a flexible and cost-effective dual humidity and temperature sensor and/or coating material has been successfully developed. After the incorporation of IL in a UV-curable polymer matrix, a porous network structure is obtained without relevant chemical changes neither in the IL or in the polymer matrix. In addition, the incorporation of the IL slightly influences the UV curing process of the polymer obtaining in all cases a polymer curing conversion of 88 % or above. Further, the inclusion of the IL influences the electrical and mechanical properties of the samples for the higher IL contents obtaining an increase in the electrical conductivity and a decrease on the Young modulus.

Thermochromic effect was observed even at low IL loads. It was observed that humidity has a strong influence in the thermochromic effect up to 55 % RH and that this process is thermally influenced. This effect is due to the water absorption/dehydration of $[NiCl_4]^{2-}$, which is related to a variation in the coordination number of the Ni(II) from octahedral to tetrahedral depending the hydrated ($[Ni(H_2O)_6]^{2+}$) or dehydrated ($[NiCl_4]^{2-}$) state.

Thus, the present work demonstrated the suitability of UV curable hybrid materials for smart and multifunctional coatings processable by additive manufacturing technologies, paving the way to cost-effective sensing coatings with a low carbon footprint due to it solvent-less process.

9.5 References

1. Endruweit, A., M.S. Johnson, and A.C. Long, *Curing of composite components by ultraviolet radiation: A review.* Polymer Composites, 2006. **27**(2): p. 119-128.
2. Xiao, P., et al., *Visible light sensitive photoinitiating systems: Recent progress in cationic and radical photopolymerization reactions under soft conditions.* Progress in Polymer Science, 2015. **41**: p. 32-66.
3. Mendes-Felipe, C., et al., *State-of-the-Art and Future Challenges of UV Curable Polymer-Based Smart Materials for Printing Technologies.* Advanced Materials Technologies, 2019. **4**(3): p. 1800618.

4. Gibson, I., et al., *Additive manufacturing technologies*. Vol. 17. 2021: Springer.
5. Correia, D.M., et al., *Ionic Liquid–Polymer Composites: A New Platform for Multifunctional Applications.* Advanced Functional Materials, 2020. **30**(24): p. 1909736.
6. Ziółkowski, B., et al., *Mechanical Properties and UV Curing Behavior of Poly(N-Isopropylacrylamide) in Phosphonium-Based Ionic Liquids.* Macromolecular Chemistry and Physics, 2013. **214**(7): p. 787-796.
7. Gerbaldi, C., et al., *UV-cured polymer electrolytes encompassing hydrophobic room temperature ionic liquid for lithium batteries.* Journal of Power Sources, 2010. **195**(6): p. 1706-1713.
8. Bakhtina, N.A., et al., *Two-Photon Nanolithography Enhances the Performance of an Ionic Liquid–Polymer Composite Sensor.* Advanced Functional Materials, 2015. **25**(11): p. 1683-1693.
9. Schultz, A.R., et al., *3D Printing Phosphonium Ionic Liquid Networks with Mask Projection Microstereolithography.* ACS Macro Letters, 2014. **3**(11): p. 1205-1209.
10. Chen, K., et al., *Smart UV-curable fabric coatings with self-healing ability for durable self-cleaning and intelligent oil/water separation.* Colloids and Surfaces A: Physicochemical and Engineering Aspects, 2019. **565**: p. 86-96.
11. Fernandes, L.C., et al., *Ionic-Liquid-Based Printable Materials for Thermochromic and Thermoresistive Applications.* ACS Applied Materials & Interfaces, 2019. **11**(22): p. 20316-20324.
12. Yu, L. and G.Z. Chen, *Cryo-solvatochromism in ionic liquids.* RSC Advances, 2014. **4**(76): p. 40281-40285.
13. Perez, G., et al., *Smart reversible thermochromic mortar for improvement of energy efficiency in buildings.* Construction and Building Materials, 2018. **186**: p. 884-891.
14. Kim, H., et al., *Flexible Thermochromic Window Based on Hybridized VO_2/Graphene.* ACS Nano, 2013. **7**(7): p. 5769-5776.
15. Baron, M.G. and M. Elie, *Temperature sensing using reversible thermochromic polymeric films.* Sensors and Actuators B: Chemical, 2003. **90**(1): p. 271-275.
16. Decker, C., *New developments in UV radiation curing of protective coatings.* Surface Coatings International Part B: Coatings Transactions, 2005. **88**(1): p. 9-17.
17. Mendes-Felipe, C., et al., *High dielectric constant UV curable polyurethane acrylate/indium tin oxide composites for capacitive sensing.* Composites Science and Technology, 2020. **199**: p. 108363.
18. Mendes-Felipe, C., et al., *UV curable nanocomposites with tailored dielectric response.* Polymer, 2020. **196**: p. 122498.
19. Mendes-Felipe, C., et al., *Stimuli responsive UV cured polyurethane acrylated/carbon nanotube composites for piezoresistive sensing.* European Polymer Journal, 2019. **120**: p. 109226.
20. Zhong, C., et al., *Syntheses, Structures, and Properties of a Series of Metal Ion-Containing Dialkylimidazolium Ionic Liquids.* Bulletin of the Chemical Society of Japan, 2007. **80**(12): p. 2365-2374.
21. Wei, X., et al., *Thermo-solvatochromism of chloro-nickel complexes in 1-hydroxyalkyl-3-methyl-imidazolium cation based ionic liquids.* Green Chemistry, 2008. **10**(3): p. 296-305.
22. Llorente, O., et al., *Study of the crosslinking process of waterborne UV curable polyurethane acrylates.* Progress in Organic Coatings, 2016. **99**: p. 437-442.
23. Gong, X., J. Zhang, and S. Jiang, *Ionic liquid-induced nanoporous structures of polymer films.* Chemical Communications, 2020. **56**(20): p. 3054-3057.
24. Fernandes, L., et al., *Highly sensitive humidity sensor based on ionic liquid-polymer composites.* ACS Applied Polymer Materials, 2019.
25. Behera, P.K., et al., *A novel ionomeric polyurethane elastomer based on ionic liquid as crosslinker.* RSC Advances, 2016. **6**(101): p. 99404-99413.
26. Fernández de Luis, R., et al., *Short-Range and Long-Range Magnetic Ordering, in Third Generation Brannerite Type Inorganic−Organic Vanadates: [{Mn(Bpy)}$(VO_3)_2$]≈(H_2O)1.16 and [{Mn(Bpy)0.5}(VO3)2]≈(H2O)0.62.* Chemistry of Materials, 2010. **22**(19): p. 5543-5553.

27. Fernández de Luis, R., et al., *Reversible Solid-State Transformation in {Ni2(H2O)2(Bpa)2}(V6O17) Proved by Synchrotron Radiation: Color and Magnetic Properties Change.* Crystal Growth & Design, 2014. **14**(2): p. 658-670.
28. Correia, D.M., et al., *Ionic Liquid Cation Size-Dependent Electromechanical Response of Ionic Liquid/Poly(vinylidene fluoride)-Based Soft Actuators.* The Journal of Physical Chemistry C, 2019. **123**(20): p. 12744-12752.
29. Reizabal, A., et al., *Tailoring silk fibroin separator membranes pore size for improving performance of lithium ion batteries.* Journal of Membrane Science, 2020. **598**: p. 117678.
30. Dias, J.C., et al., *Electromechanical actuators based on poly(vinylidene fluoride) with N-1112(OH) NTf_2 and C_2mim C_2SO_4.* Journal of Materials Science, 2016. **51**(20): p. 9490-9503.
31. Sone, K. and Y. Fukuda, *Thermochromism of Transition Metal Complexes in the Solid State*, in *Inorganic Thermochromism*, K. Sone and Y. Fukuda, Editors. 1987, Springer Berlin Heidelberg: Berlin, Heidelberg. p. 104-131.
32. Chen, Y., et al., *Water collection from air by ionic liquids for efficient visible-light-driven hydrogen evolution by metal-free conjugated polymer photocatalysts.* Renewable Energy, 2020. **147**: p. 594-601.
33. Cao, Y., et al., *Water sorption in ionic liquids: kinetics, mechanisms and hydrophilicity.* Physical Chemistry Chemical Physics, 2012. **14**(35): p. 12252-12262.
34. Freire, M.G., et al., *Hydrolysis of Tetrafluoroborate and Hexafluorophosphate Counter Ions in Imidazolium-Based Ionic Liquids.* The Journal of Physical Chemistry A, 2010. **114**(11): p. 3744-3749.
35. Cammarata, L., et al., *Molecular states of water in room temperature ionic liquids.* Physical Chemistry Chemical Physics, 2001. **3**(23): p. 5192-5200.
36. Wei, X., et al., *Solar-thermochromism of Pseudocrystalline Nanodroplets of Ionic Liquid–NiII Complexes Immobilized inside Translucent Microporous PVDF Films.* Advanced Materials, 2009. **21**(7): p. 776-780.

10 Environmental-friendly carrageenan based ionic-liquid driven soft actuators

A naturally derived polymer based on iota carrageenan and different ammonium and imidazolium based ILs are used for the development of environmentally friendly soft actuators. In this chapter, the influence of IL content and type and solvent evaporation temperature on the morphological and physical-chemical properties of the materials was evaluated, together with the effect on actuator functional response.

This chapter is based on the following publication: Serra, J.P., Fernandes, L.C., Correia, D.M., Tubio, C.R., Vilas-Vilela, J.L., Tariq, M., Esperança, J.M.S.S., Costa, C.M., Lanceros-Méndez, S., *Environmental-friendly carrageenan based ionic-liquid driven soft actuators.* Materials Advances, 2022. **3**: p.937-945

10.1 Introduction

Most IL/polymer based actuators are composed by synthetic polymers derived from fossil fuels, such as PVDF and its copolymers [1], PEO [2], and PLA [3], among others [4-6], mainly based on their mechanical, thermal, and chemical stability. However, industry and society demand for a new generation of materials in the scope of sustainable and circular economy paradigms [7]. In fact, environmental problems such as global warming related issues, may be aggravated in the next decades and several of those problems are caused by a lifestyle strongly dependent on fossil fuels [8]. In this scope, a reduction of the dependence on fossil fuel derived products is necessary [9]. In this sense, replacement of synthetic polymers by natural and biopolymers is an urgent need.

However, besides the great interest on soft actuators, natural polymers and ILs, is still an emergent one, with a lack of studies concerning the suitable combination of natural polymers and ILs, despite its great potential in tuning materials properties and functional performance [10, 11]. Imidazolium-based ILs and epoxidized natural rubber (ENR), able to improve the polymers heat resistance and electrical conductivity showed potential in application as elastomeric sensors and actuators [12]. In another work, Migliorini et al. [13] combined the bioplastic poly (3-hydroxybutyrate) (PHB) with the IL 1-butyl-3-methylimidazolium bis(trifluoromethylsulfonyl)imide ([Bmim][TFSI]) producing soft actuators with a working window from 0.1 to 7 V and a displacement ranging from 0.2 to 17 mm, respectively [13]. Other natural polymers, such as cellulose incorporating [Ch][DHP], have been also developed for actuators applications, displaying a displacements of 9 mm at 8 V_{pp} [14]. Related to carrageenan, electromechanical actuators have been developed based on poly (3-hexylthiophene)/carrageenan conductive hydrogels, the ι- hydrogel showing a deflection distance of 12.70 ± 0.1 mm and a deflection angle of 77.62 ± 0.35 at an electric field strength of 600 $V.mm^{-1}$ [15]. Thus, it seems interesting to explore the potential of carrageenan-based actuators, by the development of blends with IL to tune electrical conductivity, mechanical properties and, therefore, functional response.

In the present work IL/carrageenan hybrid materials have been developed containing different ILs and produced at different solvent evaporation temperatures (25 and 80 °C). The effect of both IL type and content and solvent evaporation temperature into the morphological and physical-chemical of the materials was evaluated, together with the functional electromechanical actuator response. This study represents a contribution to the development of natural polymer

based soft actuators, with strong potential for soft robotics and biomedical applications, among others.

10.2 Experimental section

10.2.1 Preparation of the neat and IL/carrageenan films

Neat carrageenan thin films were obtained by solvent casting after the dissolution of the polymer in ultrapure water (15/85 w/w %.) under magnetic stirring. For IL/carrageen composites, different amounts of [Ch][DHP] (10, 20 and 40 wt %) were first dispersed in ultrapure water for 10 minutes. Subsequently, carrageenan was added to the solution (15/85 w/w %.) and magnetically stirred at 40 °C. After complete polymer dissolution, the solution was spread on petri dishes followed by solvent evaporation at different drying temperatures: 25 °C (3 days) and 80 °C (4 hours) in an oven (P-Selecta) (Barcelona, Spain) (**Figure 10.1**). The thickness of the films is shown in **Table 10.1**.

Table 10.1 - Thickness of the IL/carrageenan films

IL/Carrageenan	wt % IL	Solvent evaporation temperature	Thickness ± 1μm
[Ch][DHP]	0	25 °C	85
	10		105
	20		92
	40		165
[Ch][$FeCl_4$]	40	80 °C	119
[Bmim][$FeCl_4$]	40		182
[Bmim][$C(CN)_3$]	40		215
	40		247

To study the effect of IL type in the characteristics and actuator performance of these materials, different ILs ([Bmim][$FeCl_4$], [Bmim][$C(CN)_3$] and [Ch][$FeCl_4$]) were used at a 40 wt. % concentration. In order to evaluate the effect of cation and anion on the hybrid materials physical-chemical characteristics, two ILs have been selected with different cations but a common anion, while other two share a common cation but with different anions. IL/carrageen films based on these ILs were prepared following the solvent evaporation temperature of 80 °C.

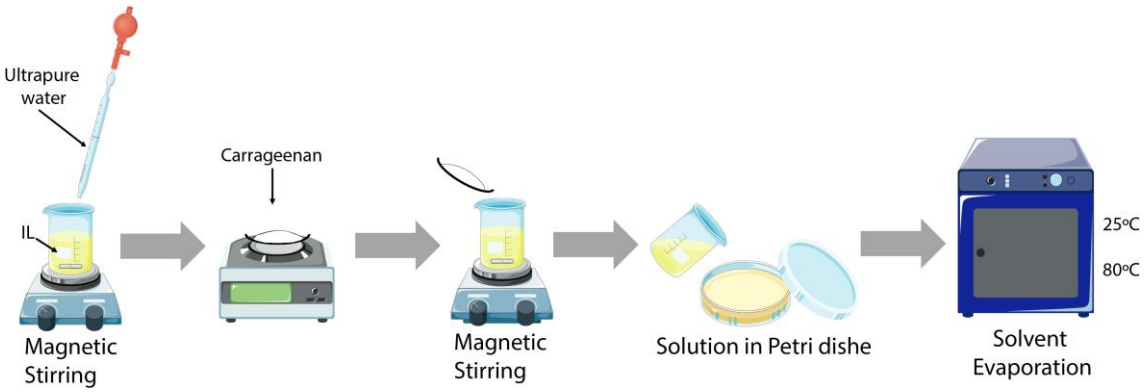


Figure 10.1 - Schematic representation of the procedure used for the preparation of the carrageenan/IL hybrid materials.

10.2.2 Sample characterization

The SEM technique was employed to assess the morphology of the samples. FTIR-ATR was utilized to analyse the characteristic vibrational bands of the samples. Thermal properties were investigated using DSC and TGA. Additionally, mechanical stress-strain tests and the ionic conductivity of the samples were studied. Chapter 2 offers comprehensive details on the applied characterization techniques and parameters.

The electromechanical response of the IL/carrageenan films was evaluated by bending measurements using a PC connected to a Logitech HD 1080p Webcam camera (Lausanne, Switzerland). In the actuators design, two gold electrodes were deposited by magnetron sputtering, on both sides of the samples (dimensions of 2 mm x 12 mm), using a Polaron SC502 equipment (Göttingen, Germany). For the displacement measurements, the actuators were clamped with two needles and connected to an Agilent 33220A function generator (California, USA). The performance of the samples as actuators was evaluated in DC mode for applied voltages ranging from 4 V to 9 V.

10.3 Results and discussion

10.3.1 Morphological features

The morphology of neat carrageenan and the carrageenan/IL films was evaluated by SEM. The influence of IL content, type and solvent evaporation temperature were evaluated. **Figure 10.2a** shows that neat carrageenan films present a non-porous structure with a cratered morphology as

a result of its semicrystalline structure [16]. The incorporation of [Ch][DHP] leads to a more homogeneous cross-section surface, with irregularities in the films surface attributed to IL aggregation during the drying process. It is also to notice that increasing IL content up to 40 wt. % lead to a more compact structure, indicating that, independently of the [Ch][DHP] concentration, the IL is embedded into the carrageenan matrix.

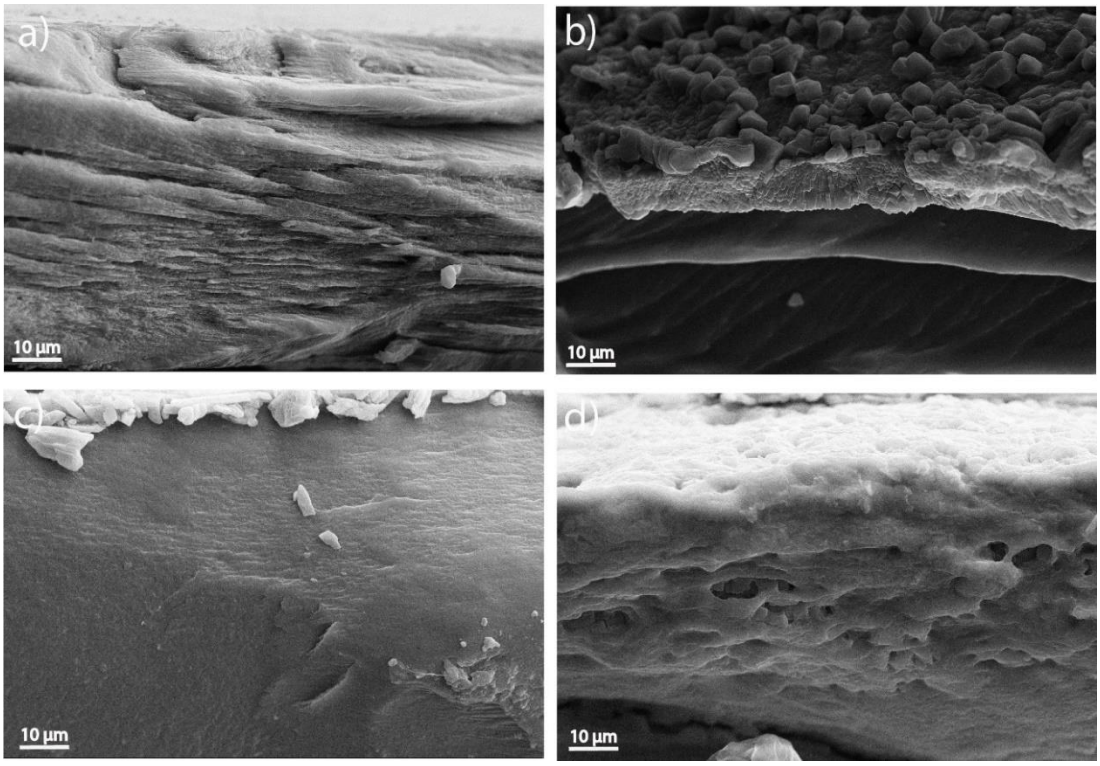


Figure 10.2 – Cross-section images of the IL/carrageenan composites with different IL contents obtained at different solvent evaporation temperatures: a) 0 wt. % at 25 °C, b) 20 wt.% of [Ch][DHP] at room temperature, c) 40 wt.% of [Ch][DHP] at 80 °C and d) 40 wt. % of [Bmim][$FeCl_4$] at 80°C.

The effect of the IL type and solvent evaporation temperature (25 °C and 80 °C) were also accessed. Similarly, as for the carrageenan/[Ch][DHP] samples, the incorporation of the [Bmim][$FeCl_4$] (**Figure 10.2d**) induces a compact internal structure, when compared to neat carrageenan. Similar results are also observed upon the incorporation of 40 wt. % of [Ch][$FeCl_4$] and [Bmim][$C(CN)_3$]. It is to notice that for all samples, no significant differences are observed in their morphology when subjected to the different drying temperatures. Thus, we have mostly concentrated in the samples prepared at 80 °C based on the faster preparation.

The presence of ILs into the carrageen matrix was also accessed by EDX analysis. **Figure 10.3** shows the EDX cross section images for the different carrageenan/IL samples, comprising 40 wt.

% of each IL type obtained at a solvent evaporation temperature of 80°C. For the sample containing [Ch][DHP] the phosphor (P) chemical element is identified through a yellow colour (**Figure 10.3a**). Similarly, for [Ch][$FeCl_4$], [Bmim][$FeCl_4$] and [Bmim][$C(CN)_3$], Iron (Fe) and nitrogen (N) are identified, respectively. It is confirmed that, independently of the IL type, all the EDX images shows a uniform IL distribution along the carrageenan matrix. Similar results were observed for the [Ch][DHP]/carrageenan samples comprising different IL contents obtained at 25 °C. It is also to notice the presence of the element P in the surface of the [Ch][DHP]/carrageenan sample (**Figure 10.3a**), indicating that some IL remains at the surface of the material.

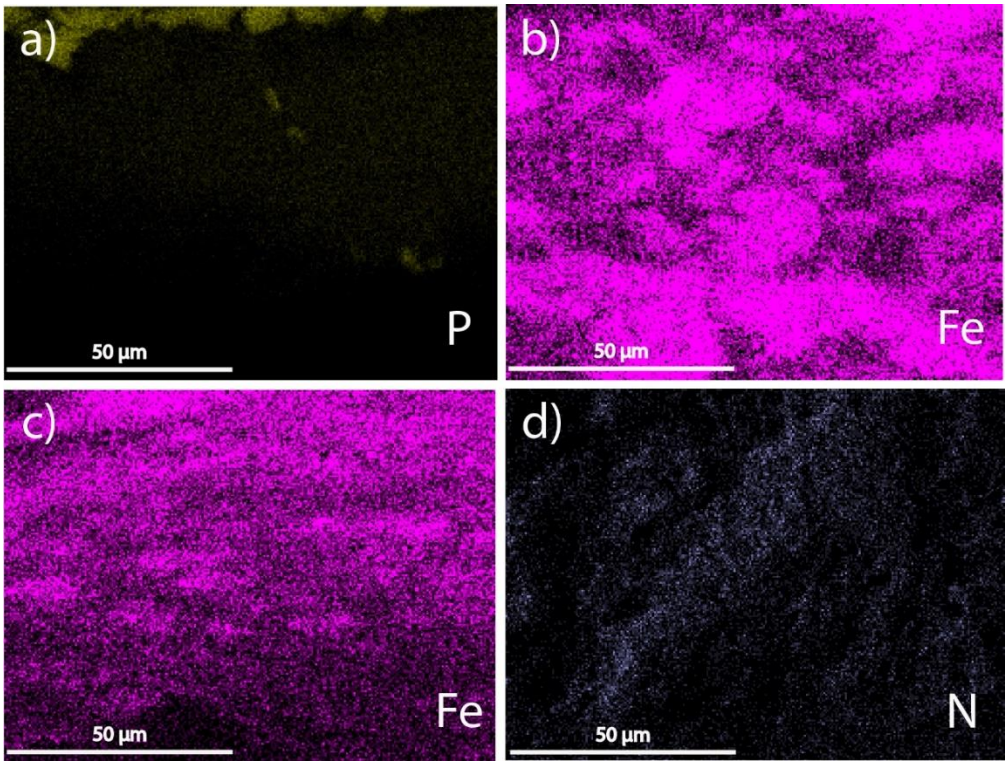


Figure 10.3 - EDS cross section images for the carrageenan/IL samples containing different ILs: (a) 40 wt. % of [Ch][DHP], b) 40 wt. % of [Ch][$FeCl_4$], b) 40 wt. % of [Bmim][$FeCl_4$] and d) 40 wt. % of [Bmim][$C(CN)_3$]). All the samples were obtained at a solvent evaporation temperature of 80 °C.

10.3.2 Infrared vibrational bands and mechanical properties

The influence of the incorporation of different ILs into the chemical properties of the carrageenan matrix have been studied by FTIR-ATR measurements (**Figure 10.4a-b**). Additionally, the effect of solvent evaporation temperature during the sample's preparation was also evaluated.

Figure 10.4a shows the FTIR spectra of carrageenan/[Ch][DHP] samples with different IL contents obtained at different solvent drying temperatures. Independently of IL content and

solvent evaporation temperature, the main carrageenan absorption bands are observed in the FTIR spectra. The absorption bands at 805, 845 and 905 cm^{-1} are attributed to the C-O-SO_3 bonds at C_2 of 3,6-anyhydrogalactose and to C4 and C6 of the galactose unit, respectively. The absorption bands that appear at 930 and 1070 cm^{-1} are attributed to the C-O bond of 3,6-anhydroglactose. The galactose groups are also identified at 970-975 cm^{-1} and the band appearing between 1240 and1260 cm^{-1} is ascribed to S=O bond of sulphate esters [17]. The band at 1635 cm^{-1} corresponds to the C=O asymmetric stretch/N-H deformation and at 3400 cm-1 to the OH/NH stretching [18]. The absorption bands of the IL [Ch][DHP] are observed at 1479 and 1644 cm^{-1}, corresponding to the CH_3 vibration and the band at 1644 cm^{-1} to the ν(O–H) stretching vibration [19, 20]. It is to notice a decrease in the stretching [Ch][DHP] vibration observed at 1479 cm^{-1} with increasing solvent drying temperature from 25 to 80 °C, and also in the carrageenan absorption bands due to that the water molecules enhanced the structural stability by connecting the sulfate groups to the neighbouring hydroxymethyl group [21].

The absorption band observed at 2164 cm^{-1} for the [Bmim][$C(CN)_3$] sample (**Figure 10.4b**) is attributed to the C-N stretching vibration characteristic of the [$C(CN)_3$]$^-$ anion [22, 23]. For [Bmim][$FeCl_4$]/carrageenan composites, the absorption band at 1163 cm^{-1} is assigned to the aromatic C-H vibrations of the [Bmim]$^+$ cation and the bands at 829 and 1459 cm^{-1} correspond to the aliphatic C-H vibrations of the [Bmim]$^+$ cation [24, 25].

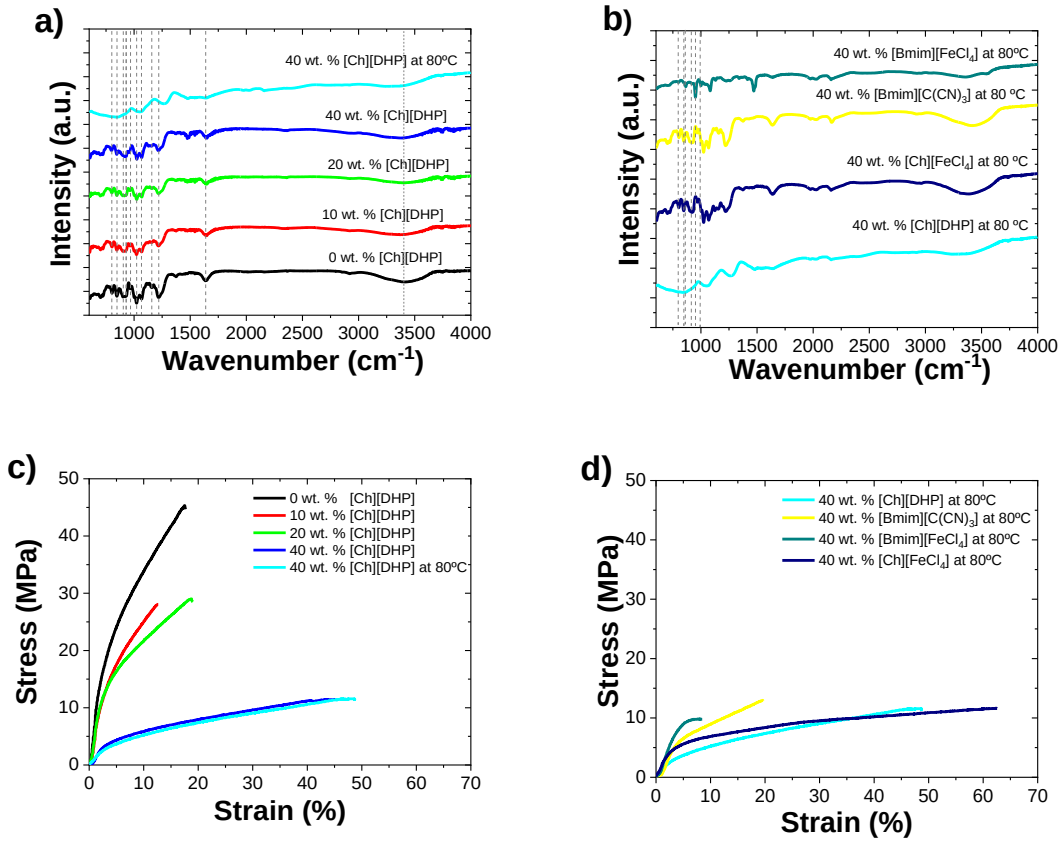


Figure 10.4 - a-b) FTIR-ATR spectra and c-d) stress-strain curves for: carrageenan/[Ch][DHP] samples containing different IL contents (10, 20 and 40 wt. %) obtained at different drying temperatures (25 and 80 °C) and for carrageenan/IL samples comprising different ILs obtained at a solvent evaporation temperature of 80 °C, respectively.

The influence of IL content, type and processing temperature on the mechanical properties of the IL/carrageenan samples are presented in **Figure 10.4c and 10.4d**.

Figure 10.4c shows that neat carrageenan presents a mechanical behaviour characteristic of a thermoplastic polymer [26], characterized by an elastic region, corresponding to elastic deformation. Upon the incorporation of [Ch][DHP] into the carrageenan matrix and using a solvent evaporation temperature of 25 °C, a noticeable plastic deformation is observed, decreasing the films stiffness, being this behavior more noticeable for larger IL contents, indicating a plasticizing effect of ILs. Thus, [Ch][DHP] seems to act as a nucleating agent leading to a crystallinity decrease of the samples [20] and in this sense to a decrease in the maximum tensile strength (σ_y). As shown in **Figure 10.4c**, a decrease in the σ_y occurs with the IL content increase being independent of the solvent temperature, displaying the carrageenan a σ_y of 45.58 MPa and [Ch][DHP]/carrageenan 40 wt. %, a σ_y of 11.56 MPa. Further, a small increase in the

elastic region is observed for the samples processed at 80 °C, which may be attributed to the plasticizing effect of the IL. The extension of plastic deformation region is IL type dependent as observed in **Figure 10.4d**. The more noticeable plastic deformation is observed for the carrageenan samples comprising the cation cholinium ([Ch][$FeCl_4$] and [Ch][DHP]), followed by the samples incorporating the ILs [Bmim][$C(CN)_3$] and [Bmim][$FeCl_4$] as a result of the higher cation size of the methylimidazolium based ILs when compared to the cholinium cation, being the cation/anion-carrageenan interactions favoured for cholinium-based ILs. Attending to values obtained for the Young Modulus (E´) values, obtained from the linear regime at 2 % of maximum elongation in the elastic region by the tangent method (**Table 10.2**), it is observed that the increase in the elastic region is accompanied by a decrease in E´, the yield strength also decreasing and increasing the yielding strain.

As shown in **Table 10.2**, for the samples obtained at 25 °C, E' decreases from 748 MPa for neat carrageenan to 145 MPa for the carrageenan/[Ch][DHP] sample with an IL content of 40 wt. %. This decrease is IL content dependent, decreasing the E' with increasing IL content. Further, the mechanical properties are also drying temperature dependent, E' decreasing from 145 MPa (at 25°C) to 91 MPa (80 °C) for the carrageenan/[Ch][DHP] sample with 40 wt. % IL content because of the higher chain mobility as a result of the temperature increase. The type of IL also influences the mechanical properties of the hybrid samples: smaller choline anions leading to a higher decrease of E' with respect to the neat polymer. Thus, E' decreases in the following order, [Ch][DHP], 91 MPa < [Ch][$FeCl_4$], 261 MPa indicating that polymer-anions interactions are predominant in the determination of the mechanical properties. This behaviour is not so prominent for the carrageenan comprising the imidazolium based ILs in which no significant differences are observed, presenting [Bmim][$FeCl_4$]/carrageenan a E´ of 207 MPa and carrageenan/[Bmim][$C(CN)_3$] a E´ of 210 MPa.

Table 10.2 - Young modulus and glass transition temperature of the different carrageenan/IL composites.

IL/Carrageenan	wt. % IL	Solvent evaporation temperature	E´ ± 15 MPa	T_g ± 2 (ºC)
[Ch][DHP]	0 wt. %	25 °C	748	105
	10 wt. %		667	104
	20 wt. %		673	104
	40 wt. %		145	106
	40 wt. %	80 °C	91	100
[Ch][$FeCl_4$]	40 wt. %		261	97
[Bmim][$FeCl_4$]	40 wt. %		207	96
[Bmim][$C(CN)_3$]	40 wt. %		210	100

10.3.3 Thermal properties

The influence of IL content and type and solvent evaporation temperature on the thermal characteristics of the carrageenan/IL samples was evaluated by DSC and TGA measurements (**Figure 10.5**).

Figure 10.5a and 10.5b shows the DSC curves for all carrageenan/[Ch][DHP] samples comprising different IL contents and obtained at a solvent evaporation of 25 and 80 °C. Independently of the IL content and drying temperature, neat and carrageenan/[Ch][DHP] samples display a single endothermic peak between 60 and 140 °C attributed to the sol-gel transition temperature (T_g) [27]. This endothermic peak also occurs in the same range for the hybrid materials, indicating no influence of the IL s in type or content on this peak of carrageenan (**Table 10.2**). On the other hand, for a given IL content but varying drying temperature, a decrease in this peak is observed when solvent evaporation takes place at 80 °C. This fact is attributed to the transformation of carrageenan molecules from random coils to a double helix structure [14].

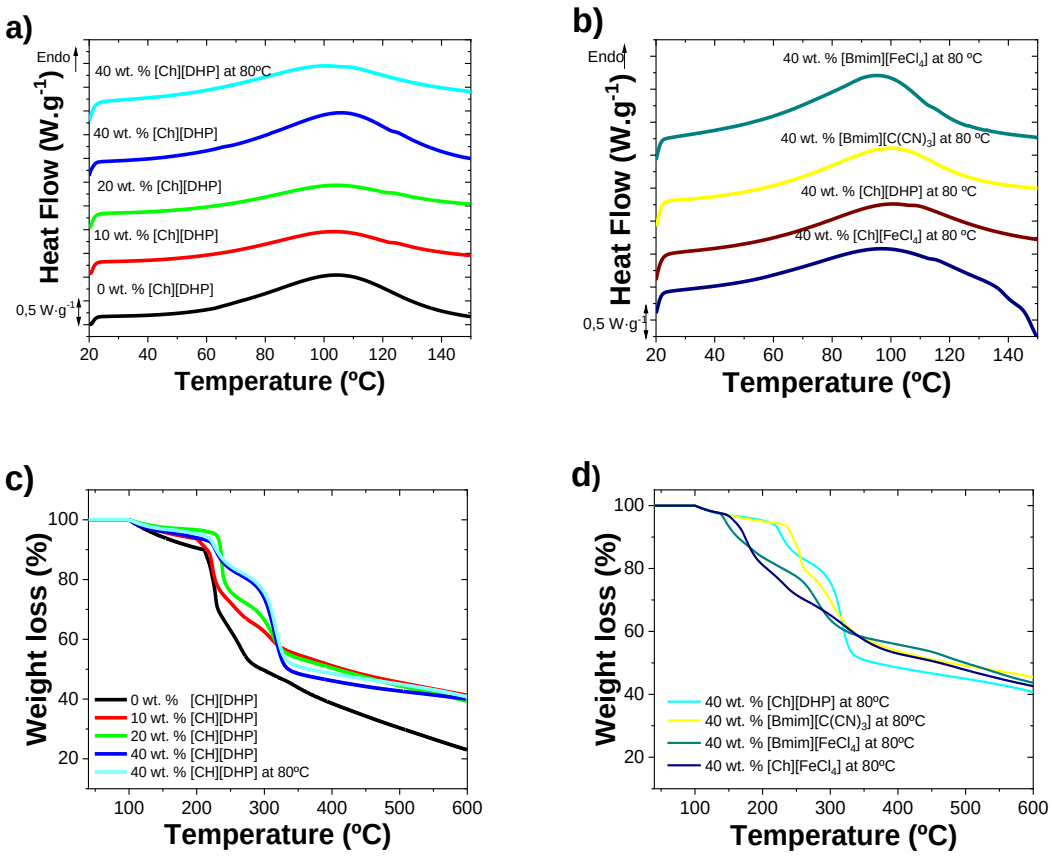


Figure 10.5 - a-b) DSC and c-d) TGA thermograms for: carrageenan/[Ch][DHP] samples containing different IL contents (10, 20 and 40 wt. %) and obtained at different drying temperatures (25 and 80 °C) and for carrageenan/IL samples comprising different ILs obtained at a solvent evaporation temperature of 80 °C, respectively.

The thermal stability of the carrageenan/IL samples were evaluated by TGA measurements, as presented in **Figure 10.5c and 10.5d**. For neat carrageenan, three main weigh loss steps are observed. The first stage occurs between 25 and 100 °C and is associated with the adsorbed and bound water loss of the samples [28]. The second degradation step is observed in the range 210 to 330 °C and is attributed to the polymeric backbone -OSO_3- decomposition [29]. The third and last stage is observed at ~750 °C and correspond to the decomposition of the carrageenan [30]. Attending to [Ch][DHP]/carrageenan samples (**Figure 10.5**), it is observed that, independently of the IL content and solvent evaporation temperature, all samples display the same three degradation steps with no significant changes in the decomposition temperatures. However, a decrease in the weight loss occurs when compared no neat carrageenan probably as a result of the IL-carrageenan interactions. The influence of the IL anion type was also evaluated for the samples obtained at a solvent drying temperature of 80 °C (**Figure 10.5d**), being

observed the same three degradation. However, for the imidazolium-based carrageenan films, the onset temperature (T_{onset}, calculated from the partial peak resulting from the decomposition of the films), of each individual degradation stage decreases, indicating a decrease in the thermal stability of the films indicating that the higher size of $[Bmim]^+$ cations promote weaker IL-polymer interactions, resulting in a thermal stability decrease.

10.4 Ionic conductivity

The ionic conductivity is an essential parameter determining actuator performance. The ionic conductivity of the developed materials, comprising the different ILs and obtained at room temperature and 80 °C, was obtained from the Nyquist plots obtained in the temperature range from 25 °C to 70 °C (**Figure 10.6**).

Regardless of the composite, the Nyquist plot shows three different regions: a semi-circle located in the high frequency range that corresponds to a charge transfer process, a straight line at lower frequencies, characteristic of a charge diffusion process, and finally, the transition between these two phenomena [31]. It only shows the results of the Arrhenius plots for the ionic conductivity of IL/carrageenan composites due for neat carrageenan, the ionic conductivity is very low in comparison to the composites. Regardless to the composite type, increasing temperature, leads to an increase in the ion diffusion caused by an increase in the charge transfer process. The ionic conductivity was calculated from **Equation 2.7** and the typical Arrhenius plots for the different IL/carrageenan composites are shown in **Figure 10.7**.

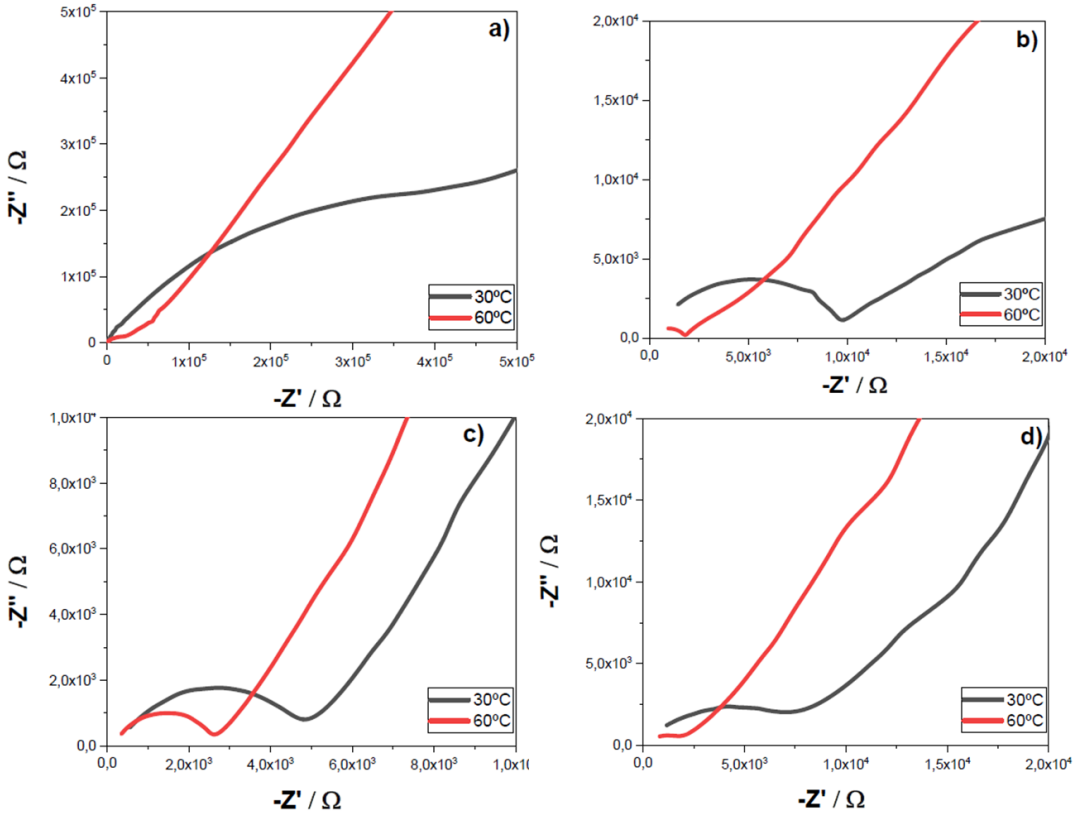


Figure 10.6 - Nyquist plots at 30 and 60 °C for the IL/carrageenan samples comprising 40 wt .% of the different ILs: (a) [Ch][DHP], b) [Ch][$FeCl_4$], c) [Bmim][$FeCl_4$] and d) [Bmim][$C(CN)_3$]). All the samples were obtained at a solvent evaporation temperature of 80 ◦C.

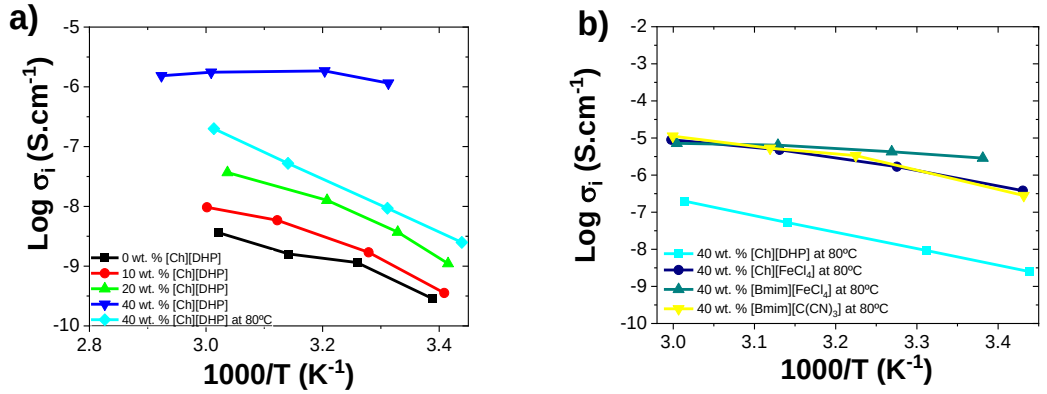


Figure 10.7 - Arrhenius plots for the ionic conductivity of the Carrageenan/IL composites: a) carrageenan/[Ch][DHP] samples containing different IL contents (10, 20 and 40 wt. %) and obtained at different drying temperatures (25 and 80 °C) and b) carrageenan/IL samples comprising different ILs obtained at a solvent evaporation temperature of 80 °C.

Figure 10.7a shows the ionic conductivities values of the carrageenan and carrageenan/[Ch][DHP] composites with different IL contents (10, 20 and 40 wt. %) in the temperature range from 25 °C to 70 °C. Regardless to the IL content, the ionic conductivity increases with the IL incorporation into carrageenan matrix and with increasing temperature due to improvement of the segmental motion of the polymer chains and of the ionic mobility [32]. It is also observed that the IL content and solvent evaporation temperature affects ionic conductivity, the conductivity increasing with increasing IL content due to the larger ionic charge content. At room temperature, the highest ionic conductivity is 1.2×10^{-6} $S.cm^{-1}$ for [Ch][DHP] with 40 wt. % prepared at 25 °C, probably attributed to the presence of intrinsically water.

Figure 10.7b shows the ionic conductivities of 40 wt. % carrageenan/IL composites in the same temperature range but obtained after processing at 80 °C. All 40 wt. % IL composites show a similar ionic conductivity, independently of the anion type, response excepting for the composite with 40 wt. % [Ch][DHP] which shows a lower ionic conductivity as a result of the lowest ionic conductivity of this IL type (<0.4 $mS.cm^{-1}$).

Thus, the ionic conductivity is mainly affected by IL content due to increases the carrier concentration inside the composites but also on the solvent evaporation temperature, as it affects the carrageenan final conformation correlated to the double helix conformation [21].

10.4.1 Electromechanical functional response

Due to their ionic properties as a result of the presence of cations and anions into the polymer matrix, the potential of the developed materials to be applied as actuators was accessed through electromechanical measurements. The results presented in **Figure 10.8** correspond to the carrageenan/[Ch][DHP] samples comprising different 10, 20 and 40 wt. % IL contents, obtained at different solvent drying temperatures (25 and 80 °C) as no bending displacement was observed for the other carrageenan/IL samples comprising [Ch][$FeCl_4$], [Bmim][$FeCl_4$] and [Bmim][$C(CN)_3$] indicating that the carrageenan matrix favours the ion diffusion and mobility as a result of the high ion-dipole interactions between the [Ch][DHP] with the carrageenan polymer chain, namely the negatively SO^{3-} groups of carrageenan with the $[Ch]^+$ cations from the IL. For the samples comprising the imidazolium cation $[Bmim]^+$ the absence of bending response

results, as above mentioned, from the lower IL-carrageenan interactions in these type of composites as a result of the cation size.

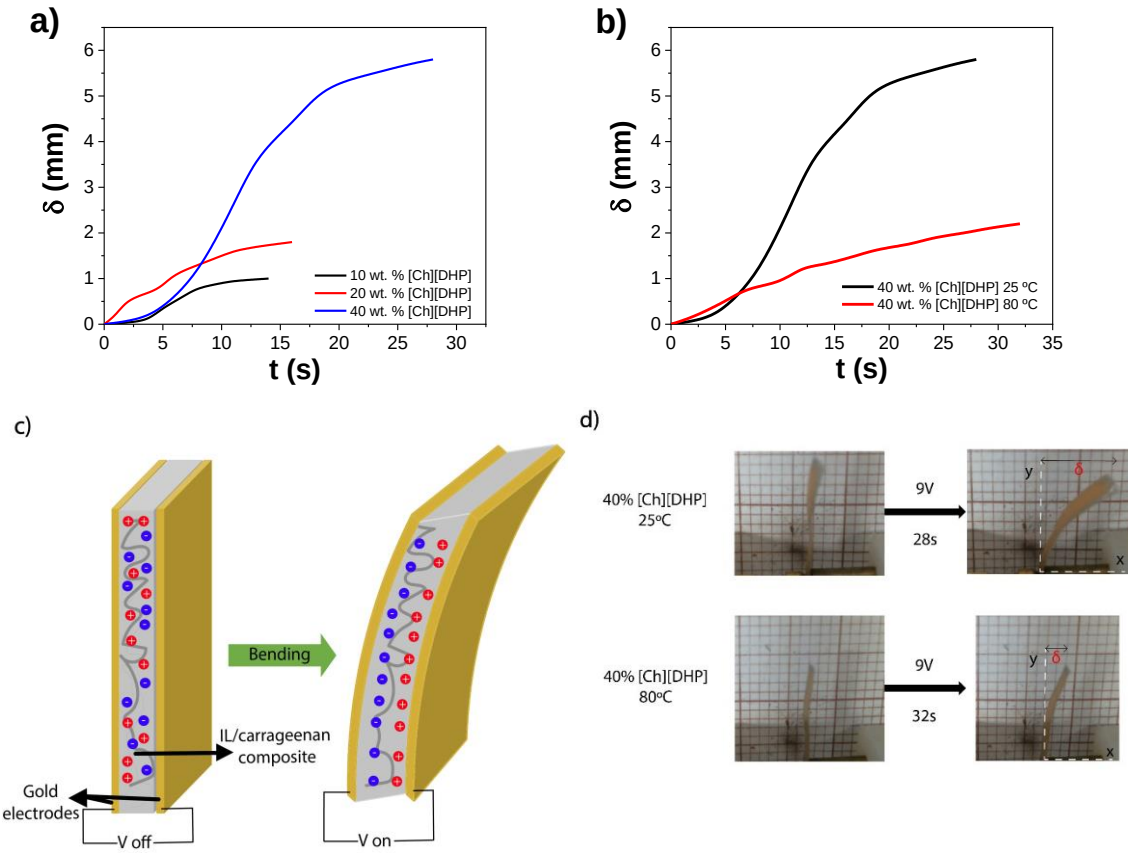


Figure 10.8 - a) Displacement of the carrageenan/[Ch][DHP] composites containing 10, 20 and 40 wt. % of IL at same maximum applied voltage (9 V) under an DC field. b) Bending motion as a function of time for 40 wt. % [Ch][DHP]/carrageenan films prepared at solvent evaporation temperatures of 25 °C and 80 °C for an applied voltage of 9 V at. c) Schematic representation of bending actuation mechanism and d) optical pictures of the [Ch][DHP]/carrageenan films prepared at solvent evaporation temperatures of 25 °C and 80 °C for an applied voltage of 9V.

Figure 10.8a shows the displacement developed by the sample obtained at 25 °C comprising 10, 20 and 40 wt. % of [Ch][DHP] and at 80 °C (**Figure 10.8b**) at applied voltage of 9 V in a DC mode as a function of time. The observed bending response with the applied voltage results from the different sizes of cations and anions and their movement and diffusion to the negative and positive electrode layers, respectively [22, 33] (**Figure 10.8c**). As a result, the cations and anions from the IL migrate and redistribute near to the electrodes, leading to a electromechanical response [33]. The maximum displacement was developed by the sample carrageenan/[Ch][DHP] comprising 40 wt. % of IL with a maximum displacement of 5.8 mm upon an applied voltage of 9 V, followed by 20 wt. % of [Ch][DHP] (1.65 mm) and 10 wt. %

[Ch][DHP] (0.95 mm). These results are explained from the lower Young Modulus obtained for carrageenan/[Ch][DHP] comprising 40 wt. %, comparatively to the other carrageenan/[Ch][DHP] comprising 10 and 20 wt. %, and in this sense in a higher ions density, resulting in a higher bending response.

The sample processing temperature also influences the bending motion response. As shown in **Figure 10.8b and 10.8d** through the representative images of the bending motion as a function of time for 40 wt. % carrageenan/[Ch][DHP] films for an applied voltage of 9 V at solvent evaporation temperatures of 25 °C and 80 °C, the maximum displacement is obtained for the sample 40 wt. % of carrageenan/[Ch][DHP] obtained at 25 °C due to the double helix conformation resulting the interaction between water and carrageenan chains. Thus, the displacement is governed by the electrical properties of the samples but also by their mechanical properties. For a solvent evaporation temperature of 25 °C, the sample containing 40 wt. % of [Ch][DHP] shows the lowest E' (145 MPa), when compared to the samples comprising 10 and 20 wt. % of IL, favouring the bending response as a result of ions accumulation. On the other hand, this sample show a displacement of 2 mm when the solvent evaporation occurs at 80 °C.

The obtained results demonstrate that carrageenan/[Ch][DHP]-based materials are suitable to be applied as soft bending actuators.

10.5 Conclusions

In the present work, novel naturally derived materials based on iota-carrageenan and different ammonium and imidazolium based ILs were developed for actuators applications. Carrageenan/[Ch][DHP] samples comprising different [Ch][DHP] contents (10, 20 and 40 wt. %) and carrageenan/[Ch][$FeCl_4$], [Bmim][$FeCl_4$] and [Bmim][$C(CN)_3$] samples incorporating 40 wt. % of IL were developed.

A non-porous structure was obtained for all samples, being independent of the IL content, type, and solvent evaporation temperature. Increasing [Ch][DHP] content up to 40 wt. % leads to a more compact structure, indicating that, independently of the [Ch][DHP]concentration, the IL is embedded into the carrageenan matrix. Similar results were observed for the other carrageenan/IL samples comprising different ILs. The mechanical properties evaluated from tensile measurements revealed a plasticizing effect as a result of the IL incorporation into the

carrageenan matrix, resulting in a decrease of the Young Modulus for all the produced composites with respect to the neat polymer. This reduction is IL content dependent, being observed a decrease from 748 MPa for carrageenan to 145 MPa for the sample with 40 wt. % of [Ch][DHP]. On the other hand, no significant difference is observed in the thermal stability of the samples.

The ionic conductivity depends on IL content and solvent evaporation temperature, but it is nearly independent on IL type. For carrageenan/[Ch][DHP] composites, the highest ionic conductivity at room temperature is 1.2×10^{-6} $S.cm^{-1}$ observed for an IL content 40 wt. % processed at 25°C.

The successful performance of the materials as electromechanical actuators was demonstrated, being the maximum electromechanical bending displacement (5.8 mm upon an applied voltage of 9 V) obtained by the carrageenan/[Ch][DHP] sample containing 40 wt. % of IL and processed at 25 °C. The obtained results demonstrate the suitability of the developed natural based bending actuator for environmental friendlier soft robotic applications, among others.

10.6 References

1. Barbosa, J.C., et al., *Recent advances in poly (vinylidene fluoride) and its copolymers for lithium-ion battery separators.* Membranes, 2018. **8**(3): p. 45.
2. Xue, Z., D. He, and X. Xie, *Poly (ethylene oxide)-based electrolytes for lithium-ion batteries.* Journal of Materials Chemistry A, 2015. **3**(38): p. 19218-19253.
3. Correia, D., et al., *Superhydrophilic poly (l-lactic acid) electrospun membranes for biomedical applications obtained by argon and oxygen plasma treatment.* Applied Surface Science, 2016. **371**: p. 74-82.
4. Bar, H., R. Ikan, and Z. Aizenshtat, *Fossil fuels and synthetic polymers: isothermal pyrolysis kinetics as indication of structural resemblance.* Journal of analytical and applied pyrolysis, 1988. **14**(1): p. 73-79.
5. Worsfold, P., et al., *Encyclopedia of analytical science*. 2019: Elsevier.
6. C. M. Costa, M.N.T.M., J. L. Gomez Ribelles, S. Lanceros-Méndez, *Composition-dependent physical properties of poly[(vinylidene fluoride)- co -trifluoroethylene]–poly(ethylene oxide) blends.* Journal of Materials Science, 2013(9).
7. Hysa, E., et al., *Circular Economy Innovation and Environmental Sustainability Impact on Economic Growth: An Integrated Model for Sustainable Development.* 2020. **12**(12): p. 4831.
8. Harper, C. and M. Snowden, *Environment and society: Human perspectives on environmental issues*. 2017: Taylor & Francis.
9. OECD, *Global material resources outlook to 2060.* 2019.
10. Correia, D.M., et al., *Ionic Liquid–Polymer Composites: A New Platform for Multifunctional Applications.* Advanced Functional Materials, 2020. **30**(24): p. 1909736.
11. Martins, P., et al., *Polymer-based actuators: back to the future.* Physical Chemistry Chemical Physics, 2020. **22**(27): p. 15163-15182.
12. Matchawet, S., et al., *Effects of imidazolium ionic liquid on cure characteristics, electrical conductivity and other related properties of epoxidized natural rubber vulcanizates.* European Polymer Journal, 2017. **87**: p. 344-359.

13. Migliorini, L., et al., *Bioplastic electromechanical actuators based on biodegradable poly(3-hydroxybutyrate) and cluster-assembled gold electrodes.* Sensors and Actuators B: Chemical, 2019. **286**: p. 230-236.
14. Correia, D.M., et al., *Cellulose Nanocrystal and Water-Soluble Cellulose Derivative Based Electromechanical Bending Actuators.* 2020. **13**(10): p. 2294.
15. Tanusorn, N., et al., *Influence of carrageenan molecular structures on electromechanical behaviours of poly(3-hexylthiophene)/carrageenan conductive hydrogels.* International Journal of Biological Macromolecules, 2018. **118**: p. 2098-2107.
16. Ghani, N.A.A., et al., *Incorporating 1-butyl-3-methylimidazolium Chloride Ionic Liquid into Iota Carrageenan Solid Biopolymer Electrolyte for Electrochemical Devices Application.* Sains Malaysiana, 2020. **49**(2): p. 305-313.
17. Pereira, L., et al., *Identification of selected seaweed polysaccharides (phycocolloids) by vibrational spectroscopy (FTIR-ATR and FT-Raman).* Food Hydrocolloids, 2009. **23**(7): p. 1903-1909.
18. Rajasulochana, N.G., *Analysis on the Seasonal Variations in Carrageenans of Hypnea flagelliformis and Sarconema filiforme by FTIR Spectroscopy. .* Asian Journal of Chemistry. , 2009. **21**: p. 4547-4552.
19. Du, C., et al., *Effect of water presence on choline chloride-2urea ionic liquid and coating platings from the hydrated ionic liquid.* Scientific reports, 2016. **6**(1): p. 1-14.
20. Meira, R.M., et al., *Ionic-Liquid-Based Electroactive Polymer Composites for Muscle Tissue Engineering.* ACS Applied Polymer Materials, 2019. **1**(10): p. 2649-2658.
21. Ghani, N.A.A., et al., *Impact of purification on iota carrageenan as solid polymer electrolyte.* Arabian Journal of Chemistry, 2019. **12**(3): p. 370-376.
22. Correia, D., et al., *All printed soft actuators based on ionic liquid/polymer hybrid materials.* Applied Materials Today, 2021. **22**: p. 100928.
23. Peñalber, C.Y., et al., *Surface characterization of imidazolium-based ionic liquids with cyano-functionalized anions at the gas–liquid interface using sum frequency generation spectroscopy.* Physical Chemistry Chemical Physics, 2012. **14**(15): p. 5122-5131.
24. Xie, Z.-L., et al., *Transparent, flexible, and paramagnetic ionogels based on PMMA and the iron-based ionic liquid 1-butyl-3-methylimidazolium tetrachloroferrate (III)[Bmim][FeCl$_4$].* Journal of Materials Chemistry, 2010. **20**(42): p. 9543-9549.
25. Correia, D., et al., *Magnetic ionic liquid/polymer composites: Tailoring physico-chemical properties by ionic liquid content and solvent evaporation temperature.* Composites Part B: Engineering, 2019. **178**: p. 107516.
26. Costa, C.M., et al., *Microscopic origin of the high-strain mechanical response of poled and non-poled poly (vinylidene fluoride) in the β-phase.* Journal of non-crystalline solids, 2008. **354**(32): p. 3871-3876.
27. Alnaief, M., R. Obaidat, and H. Mashaqbeh, *Effect of processing parameters on preparation of carrageenan aerogel microparticles.* Carbohydrate Polymers, 2018. **180**: p. 264-275.
28. Sadeghi, M., *Synthesis of a biocopolymer carrageenan-g-poly(AAm-co-IA)/montmorilonite superabsorbent hydrogel composite.* Brazilian Journal of Chemical Engineering, 2012. **29**(2): p. 295-305.
29. Jumaah, F.N., et al., *Derivative of iota-carrageenan as solid polymer electrolyte.* Ionics, 2015. **21**(5): p. 1311-1320.
30. Ma, S., et al., *Thermal Behavior of Carrageenan: Kinetic and Characteristic Studies.* International Journal of Green Energy, 2012. **9**(1): p. 13-21.
31. Chang, B.-Y. and S.-M. Park, *Electrochemical Impedance Spectroscopy.* Annual Review of Analytical Chemistry, 2010. **3**(1): p. 207-229.
32. Leones, R., et al., *Effect of Ionic Liquid Anion Type in the Performance of Solid Polymer Electrolytes Based on Poly (Vinylidene fluoride-trifluoroethylene).* Electroanalysis, 2015. **27**(2): p. 457-464.
33. Correia, D.M., et al., *Ionic Liquid Cation Size-Dependent Electromechanical Response of Ionic Liquid/Poly(vinylidene fluoride)-Based Soft Actuators.* The Journal of Physical Chemistry C, 2019. **123**(20): p. 12744-12752.

11 Conclusions and future work

This chapter summarizes main conclusions of the work and provides some suggestions for future work.

11.1 Conclusions

In today's digitally driven society, anchored in the principles of the Internet of Things and Industry 4.0, the demand for universal and multifunctional sensing and actuating technologies is on the rise. This surge in demand has fuelled an increased interest in developing devices that are flexible, lightweight, cost-effective, and efficient. Consequently, there is a growing imperative to explore a diverse range of smart materials with the capability to respond to various external stimuli in a controlled and repetitive manner. With this in perspective, advanced multifunctional composites based on MILs with synthetic and natural polymers have been developed. These materials were processed for being processable by additive manufacturing printing technologies for application in the area of sensors and actuators.

First, the solvent evaporation temperature and MIL content influence on the composites properties was evaluated for PVDF-TrFE/[Bmim][$FeCl_4$] composite films. It was observed that the morphology of the composites is dependent on the evaporation temperature, with no changes in P(VDF-TrFE) chemical structure. Further, it was also observed that the inclusion of the MIL into the P(VDF-TrFE) matrix induced a decrease in the crystallinity degree from 28 % for pristine P(VDF-TrFE) to the lowest being 12 % for the sample with 20 wt. % of MIL content with solvent evaporation at 210 °C. The good miscibility between the polymer and MIL was confirmed by thermal characterization, increasing the thermal stability with MIL content. Additionally, the magnetic susceptibility increased with MIL content and solvent evaporation temperature with all samples exhibiting a paramagnetic behaviour.

Then the effect of IL type in the structural, physical-chemical and ILs structural organization into PVDF was studied, using several imidazolium based ILs to better understand the IL-polymer matrix chain interactions, stability, and macroscopic response. The composites morphology was dependent on the IL type and interactions during solvent evaporation and, SANS technique revealed different nanoscale structural organizations, namely, just single polydisperse objects with Rg = 4.2 nm were detected after addition of [Pmim][TFSI] or [Pmpip][TFSI] to PVDF and more complex structures were obtained for the composites with the MILs. These complex structures are indicative of a strong interaction with the DMF solvent during the evaporation process, resulting in the presence of a porous structure.

The influence of the alkyl chain length was studied in PVDF/[$C_n$mim][$FeCl_4$] (n=2, 4, 8 and 14) films to evaluate their potential as multifunctional MI sensors and electromechanical actuators.

For all cases, an increased β-phase from ~33% for neat PVDF up to 87% (PVDF/[C_{14}mim][$FeCl_4$]), and paramagnetic behaviour was observed. The highest magnetoionic (MI) response (1.06±0.02 V cm^{-1} Oe^{-1}) was obtained for the composite with the lowest alky chain length and the maximum displacement of 1.1 mm for PVDF/[C_4mim][$FeCl_4$] composite.

Exploring the potential of MILs as magnetic sensors and actuators, films based on the magnetic IL [Bmim][$FeCl_4$] and P(VDF-TrFE) were prepared using different solvent evaporation temperatures tuning samples' morphologies. The developed materials exhibit a double functional response: a MI and electromechanical, which were maximized for the samples with the larger average pore size of ~35 μm a MI coefficient of ~14.1 V cm^{-1} Oe^{-1} and magnetic bending displacement of 2.1 mm.

Regarding the development of materials with magnetic properties, a different approach was explored with a non-magnetic IL and CFO nanoparticles to study the performance as magnetic sensors. The prepared composite exhibited a uniform structure, suitable thermal properties (IL leads to a reduction of the polymer melting temperature from 149 ◦C to 139 ◦C and the Curie temperature from 112 ◦C to 103 ◦C), and improved ionic conductivity, reaching a maximum of 1.5x10^{-3} S.m^{-1}. Regarding their performance as sensors, they demonstrated a good magnetoelectric (ME) response (≈0.6 V.cm^{-1}.Oe^{-1}) with potential for a speedometer showing high linearity(r^2= 0.998).

The potential applicability of ILs in the field of humidity sensing was explored by developing P(VDF-HFP)-based composite films with different MILs. Independently of the MIL, porous structures were observed, as well as increase in electroactive β-phase (with the composite P(VDF-HFP)/[Bmim][$FeCl_4$] displaying the maximum content of 85 %), and plasticizing effect with a decrease in the crystallinity from 17 % to 11 %. The composite films also showed a magnetic response with a paramagnetic behaviour typical in these materials, and their potential as humidity sensors was showcased with the best results for the P(VDF-HFP)/[Bmim]$_2$[$CoCl_4$] composite showing a sensitivity value of −2245±240 Ω in the 35 to 85% RH range. As a final proof of concept showcasing their potential as humidity sensor was developed by real time monitoring of human breathing.

Thermochromic materials with potential to change its colour both with temperature and humidity were also developed. Aiming a more sustainable solvent free approach, the MIL [Bmim]$_2$[$NiCl_4$] was incorporated in a UV-curable polymer matrix, where a porous network structure is obtained

without relevant chemical changes neither in the IL or in the polymer matrix. The MIL incorporation influenced the electrical and mechanical properties of the composites, increasing the electrical conductivity and elasticity with increasing IL content. The thermochromic effect was observed even at low IL loads (5 wt. %) with the humidity strongly influencing this behaviour.

Finally, showing the suitability of the implementation of ILs in natural polymeric matrices, novel naturally derived materials based on iota-carrageenan and different ammonium and imidazolium based ILs were developed for actuators applications. The composites were successfully processed showing a non-porous structure, with a plasticizing effect arising from the ILs. As a proof of concept, it was demonstrated their potential to be applied in the field of electromechanical actuation, being the maximum electromechanical bending displacement, 5.8 mm upon an applied voltage of 9 V, obtained with the carrageenan/[Ch][DHP] sample containing 40 wt. % of IL and processed at 25 °C.

In conclusion, novel multifunctional materials have been developed in this study exhibiting significant potential for sensors and actuators. They present further opportunities for the sustainable solvent-free and natural polymer matrix approaches, being also suitable for application by additive manufacturing techniques.

11.2 Future work

The present study has demonstrated the feasibility of employing MIL/polymer composites as multifunctional materials in the field of sensors and actuators. This paves the way for future research, including:

- Investigating the various interactions between different ionic species and the polymeric matrix using molecular dynamics (MD) to optimize material design.
- Synthesizing a new generation of MILs with improved magnetic response and assessing their compatibility with various polymeric matrices.
- Synthesizing multifunctional ionic liquids with tailored optical responses and assessing their compatibility with various polymeric matrices
- Evaluating the applicability by additive manufacturing by different printing techniques